Journal of Fluids Engineering

Published Monthly by ASME

VOLUME 129 • NUMBER 12 • DECEMBER 2007

SPECIAL ISSUE ON COMPUTING TURBULENT FLOW DYNAMICS WITH IMPLICIT LARGE EDDY SIMULATION

GUEST EDITORIAL

1481 Computing Turbulent Flow Dynamics With Implicit Large Eddy Simulation
Fernando F. Grinstein and Dimitris Drikakis

RESEARCH PAPERS

1483 On Flux-Limiting-Based Implicit Large Eddy Simulation
Fernando F. Grinstein and Christer Fureby

1493 Effective Subgrid Modeling From the ILES Simulation of Compressible Turbulence
William J. Rider

1497 Assessment of Very High Order of Accuracy in Implicit LES models
Andrew Mosedale and Dimitris Drikakis

1504 Large-Eddy Simulation of Shock-Wave-Induced Turbulent Mixing
Ben Thornber and Dimitris Drikakis

1514 ILES and LES of Complex Engineering Turbulent Flows
C. Fureby

1524 Large Scale Urban Contaminant Transport Simulations With Miles
Gopal Patnaik, Jay P. Boris, Theodore R. Young, and Fernando F. Grinstein

1533 Implicit Large-Eddy Simulation in Meteorology: From Boundary Layers to Climate
Piotr K. Smolarkiewicz, Len G. Margolin, and Andrzej A. Wyszogrodzki

1540 Prediction of Leading-Edge Sheet Cavitation Inception on Hydrofoils at Low to Moderate Reynolds Number Flows
Zvi Rusak, Wallace J. Morris, II, and Yoav Peles

1547 Flow Past a Sphere With Surface Blowing and Suction
Prosenjit Bagchi

1559 A Generalized Neural Network Model of Refrigerant Mass Flow Through Adiabatic Capillary Tubes and Short Tube Orifices
Ling-Xiao Zhao, Chun-Lu Zhang, Liang-Liang Shao, and Liang Yang

(Contents continued on inside back cover)

This journal is printed on acid-free paper, which exceeds the ANSI Z39.48-1992 specification for permanence of paper and library materials. ♾™
♲ 85% recycled content, including 10% post-consumer fibers.

FLUIDS ENGINEERING DIVISION

Editor
J. KATZ (2009)

Assistant to the Editor
L. MURPHY (2009)

Associate Editors
M. J. ANDREWS (2009)
S. BALACHANDAR (2008)
A. BESKOK (2008)
S. L. CECCIO (2009)
D. DRIKAKIS (2008)
P. A. DURBIN (2008)
I. EAMES (2010)
A. GOTO (2007)
C. HAH (2009)
T. J. HEINDEL (2007)
H. JOHARI (2009)
J. KOMPENHANS (2009)
Y. T. LEE (2007)
J. A. LIBURDY (2007)
P. LIGRANI (2008)
R. MITTAL (2009)
T. J. O'HERN (2008)
U. PIOMELLI (2007)
S. ROY (2007)
D. SIGINER (2008)
S. P. VANKA (2007)
Y. ZHOU (2008)

PUBLICATIONS COMMITTEE
Chair, **B. RAVANI**

OFFICERS OF THE ASME
President, **SAM Y. ZAMRIK**
Executive Director, **V. R. CARTER**
Treasurer, **T. D. PESTORIUS**

PUBLISHING STAFF

Managing Director, Publishing
P. DI VIETRO

Manager, Journals
C. MCATEER

Production Coordinator
A. HEWITT

Transactions of the ASME, Journal of Fluids Engineering (ISSN 0098-2202) is published monthly by The American Society of Mechanical Engineers, Three Park Avenue, New York, NY 10016. Periodicals postage paid at New York, NY and additional mailing offices.
POSTMASTER: Send address changes to Transactions of the ASME, Journal of Fluids Engineering, c/o THE AMERICAN SOCIETY OF MECHANICAL ENGINEERS, 22 Law Drive, Box 2300, Fairfield, NJ 07007-2300.
CHANGES OF ADDRESS must be received at Society headquarters seven weeks before they are to be effective. Please send old label and new address.
STATEMENT from By-Laws. The Society shall not be responsible for statements or opinions advanced in papers or ... printed in its publications (B7.1, Par. 3).
COPYRIGHT © 2007 by the American Society of Mechanical Engineers. Authorization to photocopy material for internal or personal use under those circumstances not falling within the fair use provisions of the Copyright Act, contact the Copyright Clearance Center (CCC), 222 Rosewood Drive, Danvers, MA 01923, tel: 978-750-8400, www.copyright.com. Request for special permission or bulk copying should be addressed to Reprints/Permission Department.
Canadian Goods & Services Tax Registration #126148048.

Downloaded 03 Jun 2010 to 171.66.16.159. Redistribution subject to ASME license or copyright; see http://www.asme.org/terms/Terms_Use.cfm

(**Contents continued**)

Journal of Fluids Engineering **Volume 129, Number 12** **DECEMBER 2007**

1565 Flow Field Characterization at the Onset of Gas Entrainment in a Single Downward Discharge Using Particle Image Velocimetry
R. C. Bowden and I. G. Hassan

1577 Flow Regimes and Drag Characteristics of Yawed Elliptical Cavities With Varying Depth
Thomas Hering and Eric Savory

1584 Author Index

The ASME Journal of Fluids Engineering is abstracted and indexed in the following:

Applied Science & Technology Index, Chemical Abstracts, Chemical Engineering and Biotechnology Abstracts (Electronic equivalent of Process and Chemical Engineering), Civil Engineering Abstracts, Computer & Information Systems Abstracts, Corrosion Abstracts, Current Contents, Ei EncompassLit, Electronics & Communications Abstracts, Engineered Materials Abstracts, Engineering Index, Environmental Engineering Abstracts, Environmental Science and Pollution Management, Excerpta Medica, Fluidex, Index to Scientific Reviews, INSPEC, International Building Services Abstracts, Mechanical & Transportation Engineering Abstracts, Mechanical Engineering Abstracts, METADEX (The electronic equivalent of Metals Abstracts and Alloys Index), Petroleum Abstracts, Process and Chemical Engineering, Referativnyi Zhurnal, Science Citation Index, SciSearch (The electronic equivalent of Science Citation Index), Shock and Vibration Digest, Solid State and Superconductivity Abstracts, Theoretical Chemical Engineering

Downloaded 03 Jun 2010 to 171.66.16.159. Redistribution subject to ASME license or copyright; see http://www.asme.org/terms/Terms_Use.cfm

Journal of Fluids Engineering

Guest Editorial

Computing Turbulent Flow Dynamics With Implicit Large Eddy Simulation

The Navier-Stokes equations (NSE) can be solved directly for laminar flows, but the wide range of eddy scales to be captured prohibits direct numerical simulation for the high Reynolds-number turbulent flows of technological interest. The prevalent remedy to this resolution problem has traditionally involved the Reynolds-averaged Navier-Stokes (RANS) approach, with averaging typically carried out over time or across an ensemble of equivalent flows. The applicability of RANS typically requires that time scales associated with organized unsteady motion be substantially larger than those of turbulent motion. Such statistically steady flow assumptions can be satisfied in many (e.g., low-frequency dominated) unsteady flow applications, but most turbulent flows of interest do not fall into this category.

A more viable approach is the large eddy simulation (LES) approach [1]. LES is based on the expectation that the physically meaningful scales of turbulence can be split into two groups: one consisting of the resolved geometry and regime specific scales, and the other associated with the unresolved smallest eddies in the flow, for which the presumably more-universal dynamics is represented with subgrid scale (SGS) closure models. Scale separation is achieved by solving the low-pass filtered NSE, and using explicit SGS models introduced for closure prior to discretization. In the absence of an accepted universal theory of turbulence to solve the problem of SGS modeling, the development and improvement of such models has been driven by pragmatic practice dependent on the rational use of empirical information. In addition to the physics based difficulties in developing and validating SGS models, one is faced with simulations where contributions from numerical truncation terms can be as significant as those from SGS models in typical LES strategies. LES resolution requirements can thus become prohibitively expensive for practical flows and regimes of interest. Implicit LES (ILES) effectively addresses the seemingly insurmountable issues posed to LES by under-resolution, by relying on the use of SGS modeling and filtering provided implicitly by physics-capturing numerics of a broad class of high-resolution, non-linear finite-volume methods.

Increasing interest in ILES techniques is reflected in recent dedicated sections in archival journals [2,3], dedicated chapters in CFD textbooks [4], and by the publication of the first comprehensive book synthesizing our current understanding of the theoretical basis and accomplishments of ILES [5]. Timely ILES issues were addressed in two very-well attended minisymposia on “Computing Turbulent Flow Dynamics with ILES” at the 2006 ECCOMAS CFD conference at Egmond aan Zee, Netherlands, September 5–8, 2006. Five papers selected from the invited sessions and two other separately invited papers were assembled in the present special issue of JFE to provide a broad state-of-the-art perspective.

The first four papers deal with fundamental studies using modified equation analysis and tests in basic cases for which good reference data are available. Grinstein and Fureby discuss a class of flux-limiting methods used for ILES in both, incompressible and compressible regimes, focusing on their commonalities and basic performance. Comparative verification tests of ILES and classical LES are used to address performance of the various strategies in predicting transition and turbulence decay. Mosedale and Drikakis present an assessment of very high-order ILES models for multi-component compressible flows using WENO methods with fifth- and ninth-order of accuracy. Rider addresses SGS modeling issues arising from the application of ILES in the simulation of compressible turbulent flows, focusing on the form of the effective SGS model for the conservation of mass equations. Thornber and Drikakis report on ILES studies of multi-component compressible turbulent mixing featuring complex flow physics such as Richtmyer-Meshkov instability and transition to turbulence, including detailed comparisons against shock-tube experiments.

The last three papers address issues in simulations of extremely complex flows of interest in engineering, threat reduction management, and geophysics, for which whole-domain scalable laboratory (or field) studies are typically impossible or very difficult. Deterministic simulation studies are very expensive and critically constrained by difficulties in modeling and validating all the relevant physical sub-processes, as well as in acquiring all the necessary and relevant boundary condition information. Fureby first discusses the application of ILES to a variety of complex engineering-type applications ranging from incompressible external flows around typical naval applications to external and internal supersonic flows in aerospace applications. Large scale urban simulations are then discussed by Patnaik et al. Airborne contaminant transport in cities presents challenging new requirements for computational fluid dynamics. Turbulence is one of the most important of these phenomena and yet the overall problem is sufficiently difficult that the turbulence must be included efficiently with an absolute minimum of extra memory and computing time. Finally, Smolarkiewicz et al. present studies of geophysics using the ILES methodology. The difficulties of modeling the dynamics of the global ocean and atmosphere are compounded by the broad range of significant length scales and by the relative smallness of the vertical height of these boundary layers in comparison to their horizontal extent, which accentuates the importance of the backscatter of energy to the larger scales of motion.

The authors contributing to this special issue are grateful to the JFE editors for their careful and expeditious handling of the manuscripts, in turn making possible timely publication of these works. All involved would like to thank the JFE editor, Joe Katz, for recognizing the timeliness and importance of this subject, and offer sincere thanks to Laurel Murphy for her patience and skill in coordinating various aspects of the review and processing of the papers.

Fernando F. Grinstein
Los Alamos National Lab., Los Alamos, NM
Dimitris Drikakis
Cranfield University, England, UK
Guest Editors

Downloaded 03 Jun 2010 to 171.66.16.156. Redistribution subject to ASME license or copyright; see http://www.asme.org/terms/Terms_Use.cfm

References

[1] Sagaut, P., 2006, *Large Eddy Simulation for Incompressible Flows*, 3rd ed., Springer, NY.

[2] Drikakis, D., ed., 2002, "Very Large Eddy Simulation," Special Issue of Int. J. Numer. Methods Fluids, **39**, pp. 763–864.

[3] Grinstein, F. F., and Karniadakis, G. Em., eds., 2002, "Alternative LES and Hybrid RANS/LES," Special Issue of ASME J. Fluids Eng., **124**, pp. 821–942.

[4] Drikakis, D., and Rider, W., 2005, *High-Resolution Methods for Incompressible and Low-Speed Flows*, Springer.

[5] Grinstein, F. F., Margolin, L. G., and Rider, W. J., eds., 2007, *Implicit Large Eddy Simulation: Computing Turbulent Fluid Dynamics*, Cambridge University Press.

Downloaded 03 Jun 2010 to 171.66.16.156. Redistribution subject to ASME license or copyright; see http://www.asme.org/terms/Terms_Use.cfm

On Flux-Limiting-Based Implicit Large Eddy Simulation

Fernando F. Grinstein
Applied Physics Division,
Los Alamos National Laboratory,
MS B259,
Los Alamos, NM 87545
e-mail: fgrinstein@lanl.gov

Christer Fureby
The Swedish Defence Research Agency,
FOI, SE-172 90 Stockholm, Sweden
e-mail: fureby@foi.se

Recent progress in understanding the theoretical basis and effectiveness of implicit large eddy simulation (ILES) is reviewed in both incompressible and compressible flow regimes. We use a modified equation analysis to show that the leading-order truncation error terms introduced by certain hybrid high resolution methods provide implicit subgrid scale (SGS) models similar in form to those of conventional mixed SGS models. Major properties of the implicit SGS model are related to the choice of high-order and low-order scheme components, the choice of a flux limiter, which determines how these schemes are blended locally depending on the flow, and the designed balance of the dissipation and dispersion contributions to the numerical solution. Comparative tests of ILES and classical LES in the Taylor–Green vortex case show robustness in capturing established theoretical findings for transition and turbulence decay.

[DOI: 10.1115/1.2801684]

Keywords: LES, implicit LES, limiting, nonoscillatory, modified equation

1 Introduction

In nearly every area of fluid mechanics, our understanding is limited by the presence of turbulence. Although many experimental and theoretical studies in the past have significantly helped to increase our physical understanding, a predictive closed theory of turbulent flows has not yet been established and is unlikely to emerge in the foreseeable future. Moreover, even with the capabilities of today's supercomputers, it is not possible to compute most high Reynolds (Re) number turbulent flows directly by fully resolving all relevant scales of motions in space and time. Instead, at least part of the unsteady turbulent motion must be approximated to make these calculations feasible. The grand challenge is to develop simulation models that, although they may not explicitly incorporate all dynamic scales, will still give accurate and reliable results for at least the larger energy-containing scales of flow motion.

In large eddy simulation (LES) [1], the large energy-containing structures are resolved whereas the smaller, presumably more isotropic, structures are filtered out, and their unresolved subgrid scale (SGS) effects are modeled. This gives LES a much higher generality than industrial-standard Reynolds averaged Navier-Stokes (NS) approaches, which solve equations averaged over time, in spatially homogeneous directions, or across an ensemble of equivalent flows, and for which the entire turbulent spectrum is effectively modeled. LES has emerged as the next generation simulation tool for handling complex engineering, geophysical, and astrophysical flows. Different approaches are available for deriving the LES equations and the associated SGS models required to handle the effects of the unresolved flow physics. In the absence of a universal theory of turbulence, the construction of SGS models is based primarily on the rational use of empirical information and pragmatic practice. We distinguish between conventional LES and implicit LES (ILES) strategies.

Classical LES approaches range from using inherently limited SGS eddy-viscosity formulations to using more sophisticated and accurate dynamic and mixed models [1]. Eddy-viscosity models are able to reproduce the SGS dissipation quite well but not the SGS forces entering the momentum equation, thereby making this approach less suited for complex high-Re flows, which by necessity are usually poorly resolved. The more recent efforts have focused on developing mixed models, combining in essence dissipative eddy-viscosity models with more accurate but less stable scale-similarity models, thus providing a more accurate SGS force approximation. The results from such mixed models have been mostly satisfactory, but their implementation and computational complexity have limited their popularity. Adding to the inherent physics-based difficulties in developing and validating SGS models, truncation terms due to discretization are comparable to SGS models in the typical LES strategies [2], and LES resolution requirements become prohibitively expensive for practical flows and regimes. In fact, because of the need to distinctly separate (i.e., resolve) the effects of explicit filtering and SGS reconstruction models from those implicitly due to discretization, carrying out a *well-resolved* LES can typically amount in practice to performing *coarse* direct numerical simulation (DNS).

ILES [3–5] effectively addresses the seemingly insurmountable issues posed to LES by under-resolution by focusing on the use of SGS modeling and filtering provided implicitly by *physics capturing* numerics [5]. In ILES, the effects of the SGS physics on the resolved scales are incorporated through a functional reconstruction of the convective fluxes with high resolution (HR) finite-volume (FV) algorithms (as defined in [6]), including popular methods such as the flux-corrected transport (FCT), the piecewise parabolic method (PPM), and total variation diminishing algorithms. The original proposal, namely, the monotone integrated LES approach (MILES)—the particular class of ILES strategies based on using locally monotonic methods—was due to Boris [7] and Boris et al. [8]. Boris made the crucial early connection [7], namely, that truncation errors of such algorithms could, in fact, serve as LES SGS models. Later theoretical studies [9,10] used modified equation analysis (MEA) to show that certain FV algorithms with dissipative leading-order terms provide effective built-in (implicit) SGS models of a mixed tensorial (generalized) eddy-viscosity type. ILES uses locally adaptive (dynamic) physics capturing FV numerics to emulate (1) the small-scale anisotropy of high-Re turbulent flows (e.g., worm vortices and shocks), (2) the viscosity-independent dissipation characteristic of the turbulent cascade dynamics, and (3) the dynamics of finite scale laboratory observables. ILES has been successfully applied to a broad range of free and wall-bounded flows, ranging from canonical benchmark flows to extremely complex flows at the frontiers of current flow simulation capabilities [3,5].

In this paper, we review our recent progress in understanding the theoretical basis of ILES and fundamental features relating to

---

Contributed by the Fluids Engineering Division of ASME for publication in the Journal of Fluids Engineering. Manuscript received February 20, 2007; final manuscript received July 19, 2007. Review conducted by Dimitris Drikakis.

Copyright © 2007 by ASME

Downloaded 03 Jun 2010 to 171.66.16.156. Redistribution subject to ASME license or copyright; see http://www.asme.org/terms/Terms_Use.cfm

its performance. We use MEA to show that the leading-order truncation error terms introduced by a particular class of hybrid HR methods provide *mixed* implicit SGS models similar in form to those used in classical LES. Major properties of the implicit SGS model are related to (i) the choice of high- and low-order scheme components—where the former is well behaved in smooth flow regions and the latter is well behaved near sharp gradients; (ii) the choice of a flux limiter, which determines how these schemes are blended locally, depending on the flow; (iii) the balance of the dissipation and dispersion contributions to the numerical solution, which depend on the design details of each numerical method. The possibility of achieving ILES performance improvement through a special design of the SGS physics capturing capabilities of the HR methods is emphasized in this context.

Various hybrid HR algorithms suitable for ILES are tested in the case of the Taylor–Green vortex (TGV) problem [11]. The TGV has been used as a fundamental prototype for vortex stretching and consequent production of small-scale eddies to address the basic dynamics of transition to turbulence based on DNS. As such, it can also be effectively used to test the capabilities of a SGS model to simulate the two basic empirical laws of turbulence, namely, the existence of an inertial subrange on the kinetic energy spectra for sufficiently high Re and the finite (viscosity-independent) energy dissipation limit law. We review results from our recent tests [12] showing the robustness of ILES in capturing established theoretical findings for transition and turbulence decay in terms of the characteristic evolution of the kinetic energy dissipation, energy spectra, and enstrophy.

2 Modified Equation Analysis

We proceed with our formal study using the MEA introduced by Hirt [13]. Briefly stated, given the partial differential equations (PDEs) of interest and the numerical method to be employed, MEA uses Taylor series expansion techniques to yield differential equations solved more accurately than the original PDE by the numerical solution. These modified differential equations thus include the actual PDE terms plus additional terms related to the truncation *errors* of the numerical method. One key aspect of the MEA compared with other approaches is that truncation terms include relevant nonlinear aspects related to either the differential equation or the numerical method. More precisely, if the PDE of interest are

$$\partial_t(\mathbf{U}) + \nabla \cdot (\mathbf{F}(\mathbf{U})) = \mathbf{s}(\mathbf{U})$$

the modified PDE, satisfied by the numerical solution, is

$$\partial_t(\mathbf{U}) + \nabla \cdot (\mathbf{F}(\mathbf{U})) = \mathbf{s}(\mathbf{U}) + \mathcal{T}(\mathbf{U},\mathbf{d})$$

where $\mathcal{T}(\mathbf{U},\mathbf{d})$ is the truncation error associated with the selected spatial discretization, time integration, and flux reconstruction process. This clearly resembles the appearance of additional terms (requiring modeling) in the LES equations after explicit filtering is applied to the original flow equations. The objective here is to exploit this analogy to identify the leading-order terms of the implicit (built-in) SGS models associated with the numerical method and to explain their properties and relation to explicit SGS models used in conventional LES.

2.1 Incompressible Navier–Stokes Equations. The MEA for the incompressible NS equations is best illustrated, and most easily executed, when the equations are discretized in space only and when the convective and diffusive flux terms are explicitly expressed in terms of the dependent variables. It is important to note that different treatments of the convective fluxes employed by different solvers result in different modified equations. Thus, as much algorithmic details as possible should be included in the analysis if the aim is to analyze the performance of a particular scheme. The fully three-dimensional (3D) analysis presented here is used to emphasize the tensorial properties of the implicit SGS models, this being a key property for marginally resolved flows and for flows in complex geometries in which the anisotropy of the smallest resolved scales is important. For the sake of the presentation, however, we will omit here the time-integration details since we are primarily interested in *comparing* explicit LES and ILES, which usually use similar, or even identical, time-integration schemes. Earlier versions of our MEA were reported in [9,14].

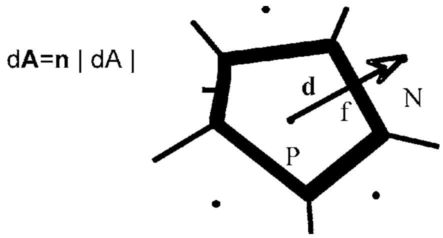

Fig. 1 Grid schematic

The standard first stage procedure in the MEA involves generating a semidiscretized version of the NS equations. Discrete FV approximations to the differential operators can be derived by combining the divergence theorem [15] with a localization theorem [16]. For example, the gradient of f in the form $\nabla f = \lim_{r\to 0}(1/\delta V)\int_{\partial\Omega}(f)d\mathbf{A}$, where $d\mathbf{A}=\mathbf{n}dA$ is the area element of integration and $\mathbf{n}$ is the outward pointing unit normal to Ω (Fig. 1). If we identify Ω with the control volume W_P, located around point $\mathbf{x}_P$, and replace the surface integrals with a discrete summation over the cell faces enclosing the control volume W_P, it follows that $\nabla f \approx 1/\delta V_P \Sigma_f [f d\mathbf{A}]_f$. Similarly, if $\mathbf{f}$ is a vector field and $\mathbf{F}$ a tensor field, then $\nabla \mathbf{f} \approx 1/\delta V_P \Sigma_f [\mathbf{f} \otimes d\mathbf{A}]_f$, $\nabla \cdot \mathbf{f} \approx 1/\delta V_P \Sigma_f [\mathbf{f} \cdot d\mathbf{A}]_f$, $\nabla \cdot \mathbf{F} \approx 1/\delta V_P \Sigma_f [\mathbf{F} d\mathbf{A}]_f$, and $\nabla \times \mathbf{f} \approx 1/\delta V_P \Sigma_f [\mathbf{f} \times d\mathbf{A}]_f$. Here, · denotes the scalar product, ⊗ the tensor product, and × the cross product. Given the vectors $\mathbf{a}$, $\mathbf{b}$ and $\mathbf{c}$, expressed as $\mathbf{a}=a_i\mathbf{e}_i$, $\mathbf{b}=b_i\mathbf{e}_i$, and $\mathbf{c}=c_i\mathbf{e}_i$ in a Cartesian basis $\{\mathbf{e}_i\}$, the scalar product is defined as $\mathbf{a}\cdot\mathbf{b}=a_ib_i$, the tensor product is defined through the transformation $(\mathbf{a}\otimes\mathbf{b})\mathbf{c}=(\mathbf{b}\cdot\mathbf{c})\mathbf{a}$, which implies that $(\mathbf{a}\otimes\mathbf{b})_{ij}=a_ib_j$ and the vector product is defined as $\mathbf{a}\times\mathbf{b}=a_ib_j\cdot\varepsilon_{ijk}\mathbf{e}_k$, where ε_{ijk} is the Levi-Civita $\mathbf{e}$ tensor [15].

Proceeding in this way, we can derive semidiscretized versions of the NS equations in the form

$$\partial_t(\mathbf{v}_P) + \frac{1}{\delta V_P}\sum_f [(\mathbf{v}\otimes\mathbf{v})_f d\mathbf{A}_f - \nu(\nabla\mathbf{v})_f d\mathbf{A}_f] = -(\nabla p)_P + \mathbf{f}_P \tag{1}$$

where p is the pressure and $\mathbf{f}$ denotes an eventual body force.

In order to close the discretization, the numerical flux functions that approximate the exact convective, diffusive, and additional fluxes must be specified. These are typically defined at the cell faces f, whereas the values of the dependent variables are stored at the cell centers, P and N, according to Fig. 1. In order to obtain a complete FV method, rules must be prescribed for how these numerical flux functions are to be reconstructed from the stored dependent variable data. Since information propagates at finite speed, it is reasonable to first assume that we can obtain these fluxes based only on the values at P and N, bracketing the cell face f.

Here, we distinguish between flux reconstruction of the convective and diffusive fluxes since these fluxes describe different physical processes: Diffusion is represented by the viscous stress tensor $\mathbf{S}=\frac{1}{3}\mu(\nabla\cdot\mathbf{v})\mathbf{I}+\mu(\nabla\mathbf{v}+\nabla\mathbf{v}^T)$. Ideally, the numerical treatment could be regarded as a tool separated from the physics. This viewpoint can be accomplished by choosing numerical methods with very high order of accuracy and fine grids, which can become too expensive for practical problems. Alternatively, the flux reconstruction step can be seen as one in which physical interpre-

Downloaded 03 Jun 2010 to 171.66.16.156. Redistribution subject to ASME license or copyright; see http://www.asme.org/terms/Terms_Use.cfm

tation and modeling cross paths with numerical methods; this is the view pioneered by Boris [7] and Boris et al. [8], and provides the basis of the implicit approach to LES.

We are interested in discussing how ILES models the convective fluxes in (1) using a hybrid flux function to reconstruct interface (f) values based on center values (P and N). Specifically, the hybrid fluxes are defined (for a generic *velocity component* ρ) as

$$\begin{aligned}\mathbf{F}_f^{C,\rho,\text{hybrid}} &= \mathbf{F}_f^{C,\rho,H} - (1-\Psi_f)[\mathbf{F}_f^{C,\rho,H} - \mathbf{F}_f^{C,\rho,L}] \\ &= F_f^C(\rho_f^H - (1-\Psi_f)(\rho_f^H - \rho_f^L)) \\ &= F_f^C((\ell_f\rho_P + (1-\ell_f)\rho_N) - (1-\Psi_f)[(\ell_f\rho_P + (1-\ell_f)\rho_N) \\ &\quad - (\beta^+\rho_P + \beta^-\rho_N)])\end{aligned}$$

based on a local combination of the linear flux function,

$$\mathbf{F}_f^{C,\rho,\text{linear}} = F_f^C\rho_f^{\text{linear}} \approx F_f^C(\ell_f\rho_P + (1-\ell_f)\rho_N)$$

where $\ell_f=|\mathbf{x}_f-\mathbf{x}_P|/|\mathbf{x}_N-\mathbf{x}_P|$, and the upwind-biased flux function,

$$\mathbf{F}_f^{C,\rho,\text{upwind}} = F_f^C\rho_f^{\text{upwind}} \approx F_f^C(\beta^+\rho_P + \beta^-\rho_N)$$

where $\beta_f^{\pm}=\frac{1}{2}(\text{sgn}(F_f^C)\pm 1)$. The blending parameter or flux limiter $\Psi=\Psi(\mathbf{U},\mathbf{d})$ for the particular equation

$$\partial_t(\mathbf{U}) + \nabla\cdot(\mathbf{F}(U)) = \mathbf{s}(\mathbf{U})$$

is being considered. The flux limiter Ψ behaves as a switch between the underlying flux reconstruction schemes; it can be a function of the dependent variables, making the switch nonlinear—i.e., the entire algorithm becomes nonlinear, even for linear equations, in order to achieve second-order accuracy simultaneously with monotonicity. Depending on the local value of Ψ, the properties of the leading-order truncation error can be adjusted to give the algorithm certain desired features, thus adapting the numerical algorithm based on the behavior of the local solution. The fundamental aspect of methods based on the flux-limiting approach is the goal of producing a nonoscillatory solution. This means that the method does not produce (significant) unphysical oscillations in the numerical solution. This blending parameter is often erred to as the flux (or slope) limiter [17,18] and is the general nonlinear mechanism that distinguishes modern methods from classical linear schemes. A survey of these methods was recently put together by Drikakis and Rider [19]. Review papers discussing the original as well as the more recent FCT formulations and applications can be found in [20].

For convenience, we note the particular flux functions and remainders of interest for the analysis discussed here (further details can be found in [21]),

$$\mathbf{v}_f^{\text{hybrid}} = \mathbf{v}_f^{\text{linear}} - (1-\Psi_f)[\mathbf{v}_f^{\text{linear}} - \mathbf{v}_f^{\text{upwind}}]$$

$$\mathcal{R}_f^{\text{hybrid}} = (1-\Psi_f)[(1-l_f)\beta_f^+ - l_f\beta_f^-](\nabla\mathbf{v})_f\mathbf{d} + \frac{1}{8}(\nabla^2\mathbf{v})_f(\mathbf{d}\otimes\mathbf{d}) + \cdots$$

$$(\nabla\mathbf{v})_f d\mathbf{A}_f \approx |d\mathbf{A}_f|(\mathbf{v}_N - \mathbf{v}_P)/|\mathbf{d}|$$

$$\mathcal{J}_f \approx -\frac{1}{24}[(\nabla^3\mathbf{v})_f d\mathbf{A}_f](\mathbf{d}\otimes\mathbf{d}) + \cdots \tag{2}$$

where $\mathbf{v}_f^{\text{linear}}\approx\ell_f\mathbf{v}_P+(1-\ell_f)\mathbf{v}_N$ and $\mathbf{v}_f^{\text{upwind}}\approx\beta_f^+\mathbf{v}_P+\beta_f^-\mathbf{v}_N$. For the hybrid approximation to the convective term $\mathbf{v}_f\otimes\mathbf{v}_f$ in Eq. (1), we have

$$\begin{aligned}\mathbf{v}_f^{\text{hybrid}}\otimes\mathbf{v}_f^{\text{hybrid}} = (\mathbf{v}_f - \mathcal{R}_f^{\text{hybrid}})\otimes(\mathbf{v}_f - \mathcal{R}_f^{\text{hybrid}}) &= \mathbf{v}_f\otimes\mathbf{v}_f \\ &- [\mathbf{C}_f(\nabla\mathbf{v})_f^T + (\nabla\mathbf{v})_f\mathbf{C}_f^T] + \chi_f^2((\nabla\mathbf{v})_f\mathbf{d})\otimes((\nabla\mathbf{v})_f\mathbf{d}) \\ &+ \frac{1}{64}((\nabla^2\mathbf{v})_f(\mathbf{d}\otimes\mathbf{d}))\otimes((\nabla^2\mathbf{v})_f(\mathbf{d}\otimes\mathbf{d})) \\ &- \frac{1}{8}[\mathbf{v}_f\otimes((\nabla^2\mathbf{v})_f(\mathbf{d}\otimes\mathbf{d})) \\ &+ ((\nabla^2\mathbf{v})_f(\mathbf{d}\otimes\mathbf{d}))\otimes\mathbf{v}_f] + \frac{1}{8}\chi_f[((\nabla^2\mathbf{v})_f(\mathbf{d}\otimes\mathbf{d})) \\ &\otimes((\nabla\mathbf{v})_f\mathbf{d}) + ((\nabla\mathbf{v})_f\mathbf{d})\otimes((\nabla^2\mathbf{v})_f(\mathbf{d}\otimes\mathbf{d}))] + \cdots\end{aligned} \tag{3}$$

where $\chi_f=(1-\Psi_f)((1-\ell_f)\beta_f^+-\ell_f\beta_f^-)$ and $\mathbf{C}_f=\chi_f(\mathbf{v}_f\otimes\mathbf{d})$. Inserting Eqs. (3) and (2) into Eq. (1) results in the semidiscretized modified incompressible NS equation

$$\begin{aligned}&\partial_t(\mathbf{v}_P) + \frac{1}{\delta V_P}\sum_f[(\mathbf{v}_f\otimes\mathbf{v}_f)d\mathbf{A}_f - \nu((\nabla\mathbf{v})_f d\mathbf{A}_f)] \\ &+ \frac{1}{\delta V_P}\sum_f[(-[\mathbf{C}_f(\nabla\mathbf{v})_f^T + (\nabla\mathbf{v})_f\mathbf{C}_f^T] + \chi_f^2((\nabla\mathbf{v})_f\mathbf{d}) \\ &\otimes((\nabla\mathbf{v})_f\mathbf{d}))d\mathbf{A}_f] - \frac{1}{\delta V_P}\sum_f\left[\left(\frac{1}{8}[\mathbf{v}_f\otimes((\nabla^2\mathbf{v})_f(\mathbf{d}\otimes\mathbf{d}))\right.\right. \\ &\left.\left.+ ((\nabla^2\mathbf{v})_f(\mathbf{d}\otimes\mathbf{d}))\otimes\mathbf{v}_f]\right)d\mathbf{A}_f\right] + \frac{1}{\delta V_P}\sum_f\left[\left(\frac{1}{64}((\nabla^2\mathbf{v})_f(\mathbf{d}\right.\right. \\ &\left.\left.\otimes\mathbf{d}))\otimes((\nabla^2\mathbf{v})_f(\mathbf{d}\otimes\mathbf{d}))\right)d\mathbf{A}_f\right] + \frac{1}{\delta V_P}\sum_f\left[\left(\frac{1}{8}\chi_f[((\nabla^2\mathbf{v})_f(\mathbf{d}\right.\right. \\ &\left.\left.\otimes\mathbf{d}))\otimes((\nabla\mathbf{v})_f\mathbf{d}) + ((\nabla\mathbf{v})_f\mathbf{d})\otimes((\nabla^2\mathbf{v})_f(\mathbf{d}\otimes\mathbf{d}))]\right)d\mathbf{A}_f\right] \\ &- \frac{1}{\delta V_P}\sum_f\left[\frac{1}{24}\nu[(\nabla^3\mathbf{v})_f d\mathbf{A}_f](\mathbf{d}\otimes\mathbf{d})\right] + \cdots = -(\nabla p)_P + \mathbf{f}_P.\end{aligned} \tag{4}$$

We now convert the semidiscrete modified equation (Eq. (4)) to the corresponding continuous modified equation using the Gauss theorem in combination with the localization theorem [16],

$$\begin{aligned}\partial_t(\mathbf{v}) + \nabla\cdot(\mathbf{v}\otimes\mathbf{v}) = \nabla\cdot(\nu\nabla\mathbf{v}) - \nabla p + \mathbf{f} + \nabla\cdot(\mathbf{C}(\nabla\mathbf{v})^T &+ (\nabla\mathbf{v})\mathbf{C}^T \\ - \chi^2((\nabla\mathbf{v})\mathbf{d})\otimes((\nabla\mathbf{v})\mathbf{d})) &+ \nabla\cdot\left(\frac{1}{8}[\mathbf{v}\otimes((\nabla^2\mathbf{v})\right. \\ &\left.\times(\mathbf{d}\otimes\mathbf{d})) + ((\nabla^2\mathbf{v})(\mathbf{d}\otimes\mathbf{d}))\otimes\mathbf{v}]\right) \\ &- \nabla\cdot\left(\frac{1}{8}\chi[((\nabla^2\mathbf{v})(\mathbf{d}\otimes\mathbf{d}))\otimes((\nabla\mathbf{v})\mathbf{d})\right. \\ &\left.+ ((\nabla\mathbf{v})\mathbf{d})\otimes((\nabla^2\mathbf{v})(\mathbf{d}\otimes\mathbf{d}))]\right) \\ &- \nabla\cdot\left(\frac{1}{64}((\nabla^2\mathbf{v})(\mathbf{d}\otimes\mathbf{d}))\otimes((\nabla^2\mathbf{v})(\mathbf{d}\otimes\mathbf{d}))\right) \\ &+ \nabla\cdot\left(\frac{1}{24}\nu(\nabla^3\mathbf{v})(\mathbf{d}\otimes\mathbf{d})\right) + \cdots\end{aligned} \tag{5}$$

where we note that gridding features directly affect the various terms in Eq. (5) through the vector field $\mathbf{d}$ and the tensor field $\mathbf{d}\otimes\mathbf{d}$. In particular, anisotropies introduced by eventual nonuniform (e.g., adaptive) gridding will directly lect as contributions to the implicit SGS tensor $\mathbf{T}$ through the grid tensor $\mathbf{d}\otimes\mathbf{d}$; clearly, this is an additional way in which *good or bad* SGS physics can be implicitly designed. We note that for a uniform Cartesian grid, with mesh spacing Δx, Δy, and Δz, the grid tensor $\mathbf{d}\otimes\mathbf{d}$ degenerates into a diagonal tensor with components Δx^2, Δy^2, and Δz^2.

In the limit of perfectly smooth conditions $\Psi=1$, $\chi=0$, and $\mathbf{C}=\mathbf{0}$, and we recover the modified equations for the high-order scheme, i.e.,

Downloaded 03 Jun 2010 to 171.66.16.156. Redistribution subject to ASME license or copyright; see http://www.asme.org/terms/Terms_Use.cfm

$$
\begin{aligned}
\partial_t(\mathbf{v}) + \nabla\cdot(\mathbf{v}\otimes\mathbf{v}) = {} & \nabla\cdot(\nu\,\nabla\,\mathbf{v}) - \nabla p + \mathbf{f} + \nabla\cdot\left(\frac{1}{8}[\mathbf{v}\otimes((\nabla^2\mathbf{v})(\mathbf{d} \right. \\
& \left. \otimes\,\mathbf{d})) + ((\nabla^2\mathbf{v})(\mathbf{d}\otimes\mathbf{d}))\otimes\mathbf{v}]\right) \\
& - \nabla\cdot\left(\frac{1}{64}((\nabla^2\mathbf{v})(\mathbf{d}\otimes\mathbf{d}))\otimes((\nabla^2\mathbf{v})(\mathbf{d}\otimes\mathbf{d}))\right) \\
& + \nabla\cdot\left(\frac{1}{24}\nu(\nabla^3\mathbf{v})(\mathbf{d}\otimes\mathbf{d})\right) + \cdots
\end{aligned}
\tag{6}
$$

commonly used in explicit LES. From the leading-order terms in Eq. (5), we can identify the built-in SGS model appearing in ILES when using algorithms based on the hybrid flux function,

$$
\begin{aligned}
\mathbf{T} = {} & \mathbf{C}(\nabla\mathbf{v})^T + (\nabla\mathbf{v})\mathbf{C}^T - \chi^2((\nabla\mathbf{v})\mathbf{d})\otimes((\nabla\mathbf{v})\mathbf{d}) \\
& + \frac{1}{8}[\mathbf{v}\otimes((\nabla^2\mathbf{v})(\mathbf{d}\otimes\mathbf{d})) + ((\nabla^2\mathbf{v})(\mathbf{d}\otimes\mathbf{d}))\otimes\mathbf{v}]
\end{aligned}
\tag{7}
$$

where we note that the last term on the right of Eq. (7), present in both Eqs. (5) and (6), is independent of the limiter and due only to the second order FV discretization.

Other than discussing the perfectly smooth solution case ($\Psi=1$) above, we have made no specific assumptions on Ψ or, equivalently, on c and $\mathbf{C}$. This is a particularly sensitive aspect of the analysis given that (1) MEA relies on the existence and use of Taylor series expansions (for which solution smoothness is, *in principle*, a requirement) and (2) the local grid-dependent flow-adaptive features of Ψ (and their contribution to the series expansion) are intimately connected not only with its specific nature but also with its 3D implementation in the algorithm under consideration. We will discuss in detail such properties of the implicit (or built-in) SGS model (Eq. (7)) implied by specific assumptions in Sec. 2.3 below. However, it is readily apparent that $\mathbf{T}$ has similarities with the commonly used SGS viscosity models of explicit LES, but with grid properties entering in a tensorial form rather than in the common scalar form.

2.2 Compressible Navier–Stokes Equations.

The analysis of the compressible NS equations (Eq. (2)) follows the above outlined procedure, but is technically more involved due to a larger number of terms as compared to the incompressible NSE. The results are, however, similar in structure. The semidiscretized compressible NS equations are

$$
\begin{aligned}
& \partial_t(\rho_P) + \frac{1}{\delta V_P}\sum_f [(\rho\mathbf{v})_f\cdot d\mathbf{A}_f] = 0 \\
& \partial_t(\rho_P\mathbf{v}_P) + \frac{1}{\delta V_P}\sum_f \left[(\rho\mathbf{v}\otimes\mathbf{v})_f d\mathbf{A}_f - (\mu\,\nabla\,\mathbf{v})_f d\mathbf{A}_f + \left(\frac{1}{3}\mu(\nabla\cdot\mathbf{v})\right)_f d\mathbf{A}_f\right] = -(\nabla p)_P + (\rho\mathbf{f})_P \\
& \partial_t(\rho_P E_P) + \frac{1}{\delta V_P}\sum_f \left[(\rho\mathbf{v}E)_f\cdot d\mathbf{A}_f - \left(\frac{\kappa}{C_V}\nabla E\right)_f d\mathbf{A}_f - (p\mathbf{v})_f d\mathbf{A}_f + \left(\frac{1}{3}\mu(\nabla\cdot\mathbf{v})\mathbf{I} - \mu(\nabla\mathbf{v}+\nabla\mathbf{v}^T)\right)_f d\mathbf{A}_f\right] = (\rho\sigma)_P
\end{aligned}
\tag{8}
$$

In order to be able to discuss both explicit LES and ILES we model the convective fluxes in Eq. (8) using the hybrid flux function, which is based on a local combination of the linear flux function and the upwind-biased flux function using the blending parameter or flux limiter Ψ. The diffusive fluxes in Eq. (8) are modeled using the linear flux function,

$$
\mathbf{F}_f^{D,v,\text{linear}} \approx \nu(\nabla\mathbf{v})_f d\mathbf{A} = \nu|d\mathbf{A}_f|(\mathbf{v}_N - \mathbf{v}_P)/|\mathbf{d}|
$$

which is based on central differencing of the inner gradient in the diffusive fluxes. Performing the same analysis as described in Sec. 2.1, we find that the modified equations for the compressible NS equations becomes

$$
\begin{aligned}
\partial_t(\rho) + \nabla\cdot(\rho\mathbf{v}) = {} & \nabla\cdot\left(\rho\chi(\nabla\mathbf{v})\mathbf{d} + \frac{1}{8}\rho(\nabla^2\mathbf{v})(\mathbf{d}\otimes\mathbf{d})\right) + \cdots \\
\partial_t(\rho\mathbf{v}) + \nabla\cdot(\rho\mathbf{v}\otimes\mathbf{v}) = {} & -\nabla p + \nabla\cdot\left(\frac{1}{3}\mu(\nabla\cdot\mathbf{v})\mathbf{I} - \mu(\nabla\mathbf{v}+\nabla\mathbf{v}^T)\right) \\
& + \rho\mathbf{f} + \nabla\cdot(\rho[\mathbf{C}(\nabla\mathbf{v})^T + (\nabla\mathbf{v})\mathbf{C}^T - \chi^2(\nabla\mathbf{v})\mathbf{d} \\
& \otimes(\nabla\mathbf{v})\mathbf{d}]) + \nabla\cdot\left(\frac{1}{8}\rho[\mathbf{v}\otimes((\nabla^2\mathbf{v})(\mathbf{d}\otimes\mathbf{d})) \right. \\
& \left. + ((\nabla^2\mathbf{v})(\mathbf{d}\otimes\mathbf{d}))\otimes\mathbf{v}]\right) - \nabla\cdot\left(\frac{1}{8}\rho\chi[((\nabla^2\mathbf{v}) \right. \\
& \times(\mathbf{d}\otimes\mathbf{d}))\otimes((\nabla\mathbf{v})\mathbf{d}) + ((\nabla\mathbf{v})\mathbf{d})\otimes((\nabla^2\mathbf{v}) \\
& \left. \times(\mathbf{d}\otimes\mathbf{d}))]\right) - \nabla\cdot\left(\frac{1}{64}\rho((\nabla^2\mathbf{v})(\mathbf{d}\otimes\mathbf{d})) \right. \\
& \left. \otimes((\nabla^2\mathbf{v})(\mathbf{d}\otimes\mathbf{d}))\right) + \nabla\cdot\left(\frac{1}{24}\mu(\nabla^3\mathbf{v})(\mathbf{d} \right. \\
& \left. \otimes\,\mathbf{d})\right) + \cdots \\
\partial_t(\rho E) + \nabla\cdot(\rho\mathbf{v}E) = {} & \nabla\cdot\left(-p\mathbf{v} + \frac{\kappa}{C_V}(\nabla E)\mathbf{v} + \frac{1}{3}\mu(\nabla\cdot\mathbf{v})\mathbf{v} \right. \\
& \left. - \mu(\nabla\mathbf{v}+\nabla\mathbf{v}^T)\mathbf{v}\right) + \rho\sigma + \nabla\cdot(\rho[\mathbf{C}\,\nabla\,E \\
& + E\chi(\nabla\mathbf{v})\mathbf{d} - \chi^2(\nabla E\cdot\mathbf{d})(\nabla\mathbf{v})\mathbf{d}]) \\
& + \nabla\cdot\left(\frac{1}{8}\rho[(\nabla^2 E)(\mathbf{d}\otimes\mathbf{d})\mathbf{v} + (\nabla^2\mathbf{v})(\mathbf{d}\otimes\mathbf{d})E]\right) \\
& + \nabla\cdot\left(\frac{1}{8}\rho\chi[(\nabla^2 E)(\mathbf{d}\otimes\mathbf{d})(\nabla\mathbf{v})\mathbf{d} + (\nabla^2\mathbf{v})(\mathbf{d} \right. \\
& \left. \otimes\,\mathbf{d})(\nabla E)\mathbf{d}]\right) - \nabla\cdot\left(\frac{1}{64}\rho[(\nabla^2\mathbf{v})(\mathbf{d}\otimes\mathbf{d})(\nabla^2 E) \right. \\
& \left. \times(\mathbf{d}\otimes\mathbf{d})]\right) + \nabla\cdot\left(\frac{1}{24}\kappa(\nabla^3 E)(\mathbf{d}\otimes\mathbf{d})\right) + \cdots
\end{aligned}
\tag{9}
$$

If $\Psi=1$ (and $c=0$, $\mathbf{C}=0$), we again recover the modified equations of the high-order linear scheme. From the leading-order terms in Eq. (9), we can identify the built-in SGS model in the hybrid flux function based ILES.

We note that implicit SGS models are present not only on the right-hand side of the momentum and energy equations, but also in the continuity equation, as a consequence of the flux reconstruction of the velocity field. This is in contrast with classical approaches to LES of compressible flow (e.g., [1]), where use of mass weighted filtered velocities prevents the appearance of SGS terms in the continuity equation. The term on the right-hand side of the continuity equation in Eq. (9) is particularly interesting from two perspectives. First, it has the potential of providing a useful model for the effects of SGS mass-density fluctuations—the role of which becomes increasingly more important for high-Mach-number flow regimes (e.g., [22]). Moreover (on a still controversial note at present), recent arguments on the *kinematics of volume transport* [23] have led to the recognition that (finite scale) mass diffusion effects, which should be clearly absent in the

Downloaded 03 Jun 2010 to 171.66.16.156. Redistribution subject to ASME license or copyright; see http://www.asme.org/terms/Terms_Use.cfm

strictly incompressible limit, could, however, be expected in the continuity equation in compressible regimes; in this context, the implicitly provided source term in the mass equation can be viewed as providing some necessary SGS modeling for simulations involving high (but finite) Reynolds numbers—based on mass diffusion, much like when we formally base ILES on the Euler equations to investigate nominally inviscid regimes. Further research is required to assess these possibilities.

Otherwise, focusing on the momenta and energy equations, the leading terms in the implicit counterparts of the (conventional LES) SGS flux vector and stress tensors are given as follows:

$$\mathbf{T} = \rho[\mathbf{C}(\nabla\mathbf{v})^T + (\nabla\mathbf{v})\mathbf{C}^T - \chi^2(\nabla\mathbf{v})\mathbf{d} \otimes (\nabla\mathbf{v})\mathbf{d}]$$

$$\times\frac{1}{8}\rho[\mathbf{v} \otimes ((\nabla^2\mathbf{v})(\mathbf{d} \otimes \mathbf{d})) + ((\nabla^2\mathbf{v})(\mathbf{d} \otimes \mathbf{d})) \otimes \mathbf{v}]$$

$$\mathbf{t} = \rho[\mathbf{C}\,\nabla E + E\chi(\nabla\mathbf{v})\mathbf{d} - \chi^2(\nabla E \cdot \mathbf{d})(\nabla\mathbf{v})\mathbf{d}]$$

$$\times\frac{1}{8}\rho[(\nabla^2 E)(\mathbf{d} \otimes \mathbf{d})\mathbf{v} + (\nabla^2\mathbf{v})(\mathbf{d} \otimes \mathbf{d})E] \qquad (10)$$

which have the same mathematical structure and physical interpretation, as the implicit SGS model in Eq. (7) for the incompressible ILES model. In particular, we note, as before, that the last terms in the expressions of **T** and **t** in Eq. (9) depend only on the second order FV discretization (and not on the limiter).

2.3 Detailed Properties of the Built-In Subgrid Scale Models of Implicit Large Eddy Simulation. Next, we will discuss some key properties of the built-in (or implicit) SGS model in ILES. For this purpose, we focus, for simplicity, on the incompressible flow model (Eq. (3)). The built-in SGS tensor (Eq. (7)) can be split into three components: $\mathbf{T}^1 = \mathbf{C}(\nabla\mathbf{v})^T + (\nabla\mathbf{v})\mathbf{C}^T$, $\mathbf{T}^2 = \chi^2((\nabla\mathbf{v})\mathbf{d} \otimes (\nabla\mathbf{v})\mathbf{d})$, and $\mathbf{T}^3 = \frac{1}{8}[\mathbf{v} \otimes ((\nabla^2\mathbf{v})(\mathbf{d} \otimes \mathbf{d})) + ((\nabla^2\mathbf{v})(\mathbf{d} \otimes \mathbf{d})) \otimes \mathbf{v}]$. The first component is symmetric and linear in the velocity gradient tensor $\nabla\mathbf{v}$ and can theore be viewed as the implicit counterpart to a generalized conventional SGS viscosity model used in explicit LES [1]. The second component is also symmetric but quadratic in $\nabla\mathbf{v}$ and can be interpreted as an implicit counterpart to the model of Clark et al. [24], which has been generalized by Aldama [25]. These two terms ($\mathbf{T}^1 + \mathbf{T}^2$) provide an implicit analog of a mixed (SGS viscosity + scale similar) model. The third component ($\mathbf{T}^3$) is symmetric, and, as already noted, it is associated with the high-order part of the numerical scheme and would thus also be present in a comparable explicit LES framework (competing with the explicit SGS model). The decomposition in $\mathbf{T}^1$, $\mathbf{T}^2$, and $\mathbf{T}^3$ is also attractive, considering the decomposition into rapid and slow parts [26]. In ILES, the rapid part that cannot be captured by isotropic models relates to $\mathbf{T}^2$, while the slow part relates to $\mathbf{T}^1$. Borue and Orszag [27] presented evidence that a $\mathbf{T}^2$-type term improves the correlations between the exact and modeled SGS stress tensor.

2.3.1 Implications of a Specific Model for the Limiter. Up to this point, we have made no explicit use in the analysis of any specifics on the nature of the flux limiter Ψ. As noted, the impact of the local features of Ψ on the MEA is intimately connected with their nature and actual implementation in the algorithm under consideration; in particular, this information must be specified to determine the actual contribution of the limiter to the Taylor series expansions used in the analysis.

In order to assess the possible implications of including such detailed limiter information, let us assume a simple model for the limiter at the smooth end of its range, i.e., assume, $\Psi \approx 1 - \theta|\mathbf{d}|$, where $\theta > 0$ has dimensions of reciprocal length. Such a model is relevant, in particular, when using directional split integrations since it can be realized in one dimension. Specifically, for the van Leer limiter [28], we have $\Psi = \Psi(r) = 2r/(1+r)$, with $r = (\rho_i - \rho_{i-1})/(\rho_{i+1} - \rho_i) > 0$. Assuming smooth conditions in the neighborhood of $x = x_i$, $r \approx 1 - h\partial_{xx}\rho/\partial_x\rho$ and $\Psi \approx 1 - \frac{3}{2}h\partial_{xx}\rho/\partial_x\rho$ (Margolin [29]), where $h = x_{i+1} - x_i = x_i - x_{i-1}$ and $\theta = \frac{3}{2}\partial_{xx}\rho/\partial_x\rho$ are associated with large-scale variations of ρ. We note here that when ρ is the streamwise velocity and x denotes a cross-stream variable, this particular θ^{-1} has the form of a mixing length used in conjunction with a classical similarity hypothesis (e.g., [30]).

We now consider the inclusion of this simple model ($\Psi \approx 1 - \theta|\mathbf{d}|$) into our MEA, and focus on the lowest-order implied approximations, i.e., $\chi \approx \theta|\mathbf{d}|((1-1)\beta^+ - 1\beta^-)$ and $\mathbf{C} \approx \theta|\mathbf{d}|((1-1)\beta^+ - 1\beta^-)(\mathbf{v} \otimes \mathbf{d})$, which in turn lead to the following estimates of the implicit SGS tensor:

$$\mathbf{T}^1 \approx [\theta|\mathbf{d}|((1-1)\beta^+ - 1\beta^-)(\mathbf{v} \otimes \mathbf{d})](\nabla\mathbf{v})^T$$

$$+ (\nabla\mathbf{v})[\theta|\mathbf{d}|((1-1)\beta^+ - 1\beta^-)(\mathbf{v} \otimes \mathbf{d})]^T$$

$$\mathbf{T}^2 \approx [\theta|\mathbf{d}|((1-1)\beta^+ - 1\beta^-)]^2((\nabla\mathbf{v})\mathbf{d} \otimes (\nabla\mathbf{v})\mathbf{d})$$

$$\mathbf{T}^3 = \frac{1}{8}[\mathbf{v} \otimes ((\nabla^2\mathbf{v})(\mathbf{d} \otimes \mathbf{d})) + ((\nabla^2\mathbf{v})(\mathbf{d} \otimes \mathbf{d})) \otimes \mathbf{v}] \qquad (11)$$

From Eq. (11), we find that in regimes of smooth flow, the leading $O(|\mathbf{d}|^2)$ contribution to the implicit SGS model T comes from $\mathbf{T}^1 + \mathbf{T}^3$ (dissipative and dispersive terms, proportional to $|\nabla\mathbf{v}|$ and $|\nabla^2\mathbf{v}|$, respectively), whereas $\mathbf{T}^2$ is $O(|\mathbf{d}|^4)$ and is proportional to $|\nabla\mathbf{v}|^2$. The latter (higher-order) $\mathbf{T}^2$ term is a dispersive implicit analog of a (rapid) scale-similar component, which (as noted) is known to improve on the anisotropic predictions of SGS models.

In closing, we note the main limitation of the above analysis. Associated with our smooth flow assumption $\Psi \approx 1 - \theta|\mathbf{d}|$, the MEA results presented here do not provide insights regarding behaviors on the other end of the limiter range, i.e., in the nonsmooth flow regime largely impacted by the low-order component of the hybrid scheme—where the leading-order terms in the Taylor series expansions are likely not very meaningful by themselves. Alternative procedures for processing information in a series expansion, e.g., based on using Padé approximants (e.g., [31]), typically have much larger convergence domains and could provide greater applicability of MEA. Such appropriate techniques have not yet been evaluated in the MEA context, and their use might allow for a better understanding of how HR FV methods work when the limiters are active. This is clearly an area where the analysis has to be extended and improved.

3 Taylor-Green Vortex Problem

The TGV system is a well-defined flow that has been used as a prototype for vortex stretching, instability, and production of small-scale eddies to examine the dynamics of transition to turbulence based on DNS [11]. As such, it can also be effectively used (as done recently in [12] and reviewed here) as a convenient case to test the ability of explicit and implicit SGS modeling to allow the simulation of the basic empirical laws of turbulence (e.g., [32]), namely, the existence of an inertial subrange on the energy spectra for sufficiently high Re number and the finite (viscosity-independent) energy dissipation limit law.

The TVG case is also used here to revisit the ability of ILES to reproduce established features of decaying turbulence. Such positive evaluations of ILES in the turbulence decaying case have been previously reported by Porter et al. [33] and Fureby and Grinstein [14] using locally monotonic HR (FCT and PPM) methods, respectively, and by Domaradzki et al. using a sign-preserving HR algorithm [34]. On the other hand, poor performances in this fundamental context noted by Garnier et al. [35] using other popular HR schemes are extensively discussed by Margolin and Rider [36] as an example of *unsuitable implementations* of HR methods for ILES.

It is important to note here that the conventional wisdom (classical LES) is that numerical diffusion effects at the convection stage are undesirable and should be avoided. Specifically, the kinetic energy can be damped only by resolved (large-scale) viscous

Downloaded 03 Jun 2010 to 171.66.16.156. Redistribution subject to ASME license or copyright; see http://www.asme.org/terms/Terms_Use.cfm

effects or by those introduced through the explicit SGS models. Kinetic energy should otherwise be conserved. In this context, integral measures in the TVG case have been previously used as a erence to assess (the presumably unwanted) effects of numerical dissipation (see, e.g., Shu et al. [37]). This is in contrast with the ILES perspective as presented here, where the view is that convective numerical diffusion effects of certain algorithms can be effectively used *by themselves* to emulate the dominant SGS physics in the high-Re applications.

The TGV configuration considered here involves triple-periodic boundary conditions enforced on a cubical domain with box side length 2π cm using 64^3, 128^3, or 256^3 evenly spaced computational cells. The flow is initialized with the solenoidal velocity components,

$$u = u_0 \sin(x)\cos(y)\cos(z)$$

$$v = -\, u_0 \cos(x)\sin(y)\cos(z)$$

$$w = 0$$

with pressure given by a solution of the Poisson equation for the above given velocity field, i.e.,

$$p = p_0 + [\rho(u_0)^2/8][1 + \cos(2z)][\cos(2x) + \cos(2y)]$$

where we further select $p_0 = 1.0$ bar, mass density $1.178\ \mathrm{kg/m^3}$, $u_0 = 100\ \mathrm{m/s}$ (corresponding to a Mach number of $\mathrm{Ma} = 0.28$), and an ideal gas equation of state for air.

Using truncated series analysis techniques, an inviscid instability for the TGV system was identified by Morf et al. [38], with an estimated onset at a nondimensional time $t^* = ku_0t \approx 5.2$ (the wave number k is unity here). These results were later questioned in [14], where it was pointed out that accuracy in the analytic continuation procedure used in [39] deteriorates too quickly to lead to a definite conclusion regarding their early prediction. Further estimates of t^* based on the DNS of Brachet et al. [11] and Brachet [39] reported a fairly consistent dissipation peak at $t^* \approx 9$, for $\mathrm{Re} = 800$, 1600, 3000, and 5000, where Re was based on the integral scale. The almost indistinguishable results for $\mathrm{Re} = 3000$ and 5000 (e.g., Fig. 4(*a*)), suggested that they may be close to the viscosity-independent limit. Whether or not this finite-time singularity exists for the purely inviscid case remains unsettled and controversial (e.g., [37]).

The mathematical flow simulation model used here is based on the conservation and balance equations of mass, momentum, and energy for the flow conditions in [12]. By design, ILES emulates the dynamics of convectively dominated flows characterized by high (but finite) Re ultimately determined by the nonvanishing residual dissipation of the numerical algorithms. In the present work, ILES models nominally inviscid flow (when Euler based) or a linear viscous flow for which SGS effects are neglected (when NS based). ILES was tested on this TGV case using various algorithms, including FCT, characteristics-based (CB) Godunov, and Lagrange-remap (LR) methods. The FCT schemes considered involved the standard fourth-order FCT algorithm [17], the fourth-order 3D monotone limiter FCT [40], and a second-order FCT using hybridization of first-order upwind and second-order central differences [13]. The CB schemes [41,42] used are of the Godunov type [19,43] and of the hybrid TVD type [41,42]. The fluxes are discretized at the cell faces using the values of the conservative variables along the characteristics. Third-order variants of the fluxes can be obtained through flux limiting based on the squares of second-order pressure or energy derivatives. Examples of flux limiting in connection with the CB scheme can be found in [19,43]. The LR method by Youngs [44] uses a nondissipative finite difference method plus quadratic artificial viscosity in the Lagrange phase and a third-order van Leer monotonic advection method [28] in the remap phase. Table 1 summarizes the ILES models. Typical Courant numbers used in the present simulations were 0.25 (LES and second-order FCT), 0.4 (fourth-order FCT and LR), or in the range of 0.5–0.7 (CB Godunov (CBG)).

Table 1 ILES methods

	Low/high type	High order	Convective flux function
FCT B&B	Multistep	Fourth	Directional split limiter
FCT DeVore	Multistep	Fourth	Monotonic, unsplit limiter
Second FCT	Upwind/central	Second	Boris and Book limiter
CBG	Second/third	Third	MUSCL, slope limiting
LR	Lagrange-remap	Third	Split monotonic remap phase

Two different codes were used for the conventional LES calculations: (a) an incompressible finite-volume code based on central differencing of the convective and diffusive fluxes, Crank–Nicholson time integration, and a pressure-implicit operator-splitting type of algorithm, which is used to handle the pressure-velocity coupling; (b) a fully compressible explicit finite-volume code based on central differencing of the convective and diffusive fluxes and a fourth-order accurate Runge-Kutta time integration. Almost identical results were obtained on the 64^3 and 128^3 grids, and hence only results from the incompressible code studies will be presented and discussed hereafter. The SGS modeling is performed by means of (i) the dynamic Smagorinsky viscosity model [45] (DSMG), (ii) the one-equation eddy-viscosity model [46] (OEEVM), and (iii) the mixed model [47] (MM), combining the OEEVM and the scale-similarity model. Table 2 summarizes the conventional LES models, as a function of the resolved strain rate tensor $\bar{\mathbf{D}}$, SGS viscosity ν_k, mesh spacing D, SGS kinetic energy k, and model coefficients c_D, c_k, and c_e. Further details can be found in [13].

Figure 2(*a*) shows the TGV flow dynamics based on instantaneous visualizations from the present TGV simulations. The figure shows the initial TGV at $t^* = 0$ and depicts the later transition to increasingly smaller-scale (but organized) vortices (top row) and then to the fully developed (disorganized) decaying worm-vortex dominated flow regime (bottom row), as characteristic of developed turbulence. Being representative of all methods discussed, the results shown here were generated with ILES using the fourth-order 3D monotone FCT on the 128^3 grid. The snapshots are based on (ray tracing) volume renderings of λ_2—the second-largest eigenvalue of the velocity gradient tensor [48], with hue and opacity maps chosen to be the same for all times, except for peak magnitude values (normalized by its value at $t^* = 0$), indicated at the lower right of each frame. Figure 2(*b*) shows comparable volume visualizations of the vorticity magnitude for the later time—representative of the developed turbulence phase, showing

Table 2 Conventional LES models. In the OEEVM and MM, *k* is provided by a modeled transport equation, and in the DSMG, the model coefficient is determined dynamically with averaging performed over the entire computational model such that $c_D = c_D(t)$

	SGS model term	SGS viscosity ν_k	Coefficients
DSMG	$-2\nu_k\bar{\mathbf{D}}$	$c_D\Delta^2\lVert\bar{\mathbf{D}}\rVert$	c_D determined dynamically
OEEVM	$-2\nu_k\bar{\mathbf{D}}$	$c_k\Delta\sqrt{k}$	$c_k = 0.07$, $c_e = 1.05$
MM	$-2\nu_k\bar{\mathbf{D}} + (\overline{\bar{\mathbf{v}} \otimes \bar{\mathbf{v}}} - \bar{\bar{\mathbf{v}}} \otimes \bar{\bar{\mathbf{v}}})$	$c_k\Delta\sqrt{k}$	$\mathrm{c_k} = 0.07$, $\mathrm{c_e} = 1.05$

Downloaded 03 Jun 2010 to 171.66.16.156. Redistribution subject to ASME license or copyright; see http://www.asme.org/terms/Terms_Use.cfm

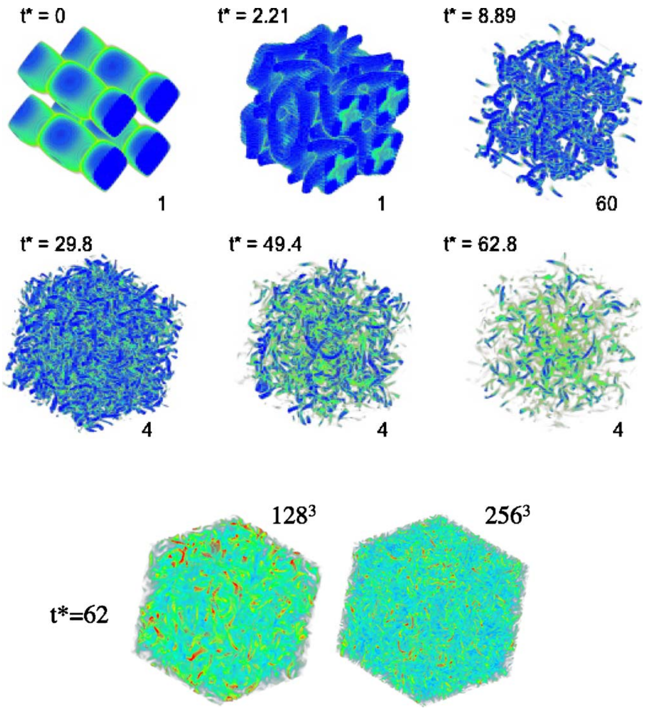

Fig. 2 (*a*) Flow visualizations of the TGV flow using volume renderings of λ_2—the second-largest eigenvalue of the velocity gradient tensor on the 128^3 grid; (*b*) volume visualizations of the vorticity magnitude are shown on the right at $t^*=62$ for 128^3 (top left) and 256^3 resolutions. The results shown here, being representative of all methods discussed, are from the fourth-order 3D monotone FCT.

that characteristic cross sections of the smallest resolved vortical worm structures scale with the ILES cutoff (determined by grid spacing).

The evolution in time of the kinetic energy dissipation $-dK/dt$, where $K=\frac{1}{2}\langle \mathbf{v}^2\rangle$ and $\langle\cdot\rangle$ denotes mean (volumetric average), is demonstrated in Fig. 3, including DNS results [12,40] (Fig. 3(*a*)) and the 128^3 resolution ILES for FCT, CBG, and LR (Fig. 3(*b*)); corresponding conventional LES results on the 128^3 grid are shown in Fig. 3(*c*), including DSMG, OEEVM, and MM—combining OEEVM and the scale-similarity model. Fastest K decay at the dissipation peak (and peak mean enstrophy Ω^* in Fig. 3(*d*)) corresponds to the onset of the inviscid TG instability at $t^*\approx 9$. The observed qualitative agreement between ILES, MM LES, and previous high-Re DNS is quite good in predicting both the time and height of the dissipation peak for the large-Re limit; agreement is particularly good when comparing the (present) 128^3 results with the highest-Re DNS cases.

Studies of sensitivity of ILES to grid resolution carried out on the 64^3, 128^3, and 256^3 cases are exemplified in Fig. 3(*e*). Similarly, in Fig. 3(*f*), we present a resolution study of LES runs on 64^3 and 128^3 grids, together with corresponding results from a selected erence ILES case. Actual values of Re characterizing the flow at the smallest resolved scales (e.g., based on the Taylor microscale) are not a priori available in LES or ILES. Our previously reported [9] comparisons of instantaneous probability density functions (PDFs) of *explicit and implicit SGS viscosities* in the context of forced isotropic turbulence simulations showed similar qualitative PDF behaviors, sensitive to actual SGS models involved. The present predictions for the TGV dissipation rate of the kinetic energy further indicate that (explicit *or* implicit) SGS models act very similarly in predicting some sort of Re-independent regime asymptotically attained with increasing grid resolution. On the other hand, Re-dependent effects are clearly suggested associated with the lower predicted characteristic t^* at dissipation peaks (as well as the wider peaks) with the coarser-grid simulations, a trend that is consistently exhibited by the DNS results as Re is lowered (Fig. 3(*e*)). Moreover, we also find a noticeable correlation between profiles of mean kinetic energy dissipation rates $-dK^*/dt^*$ (Figs. 3(*b*) and 3(*c*)) and mean resolved enstrophy Ω^* (Fig. 3(*d*)) from various different MILES, LES, and grids, with actual peak Ω^* values increasing with grid resolution. This observed correlation is qualitatively consistent with the relation $dK^*/dt^*=-\Omega^*/\mathrm{Re}$ for an incompressible NS fluid with Reynolds number Re. Thus, the relevance of using a characteristic Re that effectively increases with grid resolution (for both ILES and conventional LES) is suggested by our analysis.

Differences between the various ILES methods are tied with specifics of the various limiting algorithms and/or their implementations; a more systematic analysis of these features and further exploration of their possible parametrization in terms of a suitably defined Re is required. For example, the double-peaked structure of the dissipation near $t^*\approx 9$ predicted by the LR method (Fig. 3(*b*)) is likely due to the dispersive properties of this scheme compared to the less dispersive FCT and CBG-type schemes. On the other hand, the LR method is also the least dissipative of the compared methods, especially at the early stages of the flow development, exhibiting a relatively slower decay rate of K; this is apparent in Figs. 3(*b*), 3(*d*), and 5 (discussed further below), suggesting that 128^3 LR predictions are *comparable* to the 256^3 3D-FCT data.

Three-dimensional velocity spectra $E(k)$ for the 128^3 resolution are exemplified in Fig. 4(*a*), based on the 3D-FCT data. Corresponding compensated spectra $k^{+5/3}E(k)$ for the later times and two grid resolutions are shown in Fig. 4(*b*). The peak in the velocity spectra around the $k=\sqrt{3}$ wave number shell in Fig. 4(*a*) corresponds to the chosen initial (TGV) conditions. Higher wave-number modes are populated in time through the virtually inviscid cascading process. As the size of the smallest scale structures approaches the cutoff resolution, the kinetic energy is removed at the grid level through numerical dissipation. Figure 4(*a*) (and the compensated velocity spectra in Fig. 4(*b*)) show that the spectra consistently emulates a $(-5/3)$ power-law inertial subrange and self-similar decay for the times $t^*>6$. Figure 4(*b*) indicates that the length of the simulated inertial subrange consistently becomes longer with increasing resolution (and presumably larger associated effective Re). As the Kolmogorov spectra becomes more established in time (e.g., $t^*>15$ in Fig. 4(*a*)), it is associated at the smallest resolved scale with the more disorganized worm-vortex dominated flow regime (bottom row frames of Figs. 2(*a*) and 2(*b*))—as characteristic of developed turbulence (e.g., [49]).

The depicted self-similar decay in Figs. 4(*a*) and 4(*b*) suggests that the removal of kinetic energy by numerical dissipation may occur at a physically suitable rate. The decay rates are examined with more details based on selected representative 128^3 data in Fig. 5, where, for reference, we have indicated slopes corresponding to power laws with exponents -1.2 and -2 through the mean value of K at the observed dissipation peaks (Fig. 3(*b*)). Despite the unavoidable degree of subjectivity introduced by choice of origin times when such power-law fits are attempted, all compared methods show decay rates consistent with each other, with the -1.2 law for times immediately after that of the dissipation peak at $t^*\approx 9$, and with the -2 exponent for much later times. The power law—with a -1.2 exponent, is the one generally accepted as characteristic of decaying turbulence (e.g., [50]). Figure 5(*b*) uses the FCT-based ILES data to illustrate the consistency of the latter power-law behavior versus grid resolution. The *later* -2 exponent can be understood in terms of the expected saturation of the energy-containing length scales lecting that eddies larger than the simulation box side length cannot exist [51].

Downloaded 03 Jun 2010 to 171.66.16.156. Redistribution subject to ASME license or copyright; see http://www.asme.org/terms/Terms_Use.cfm

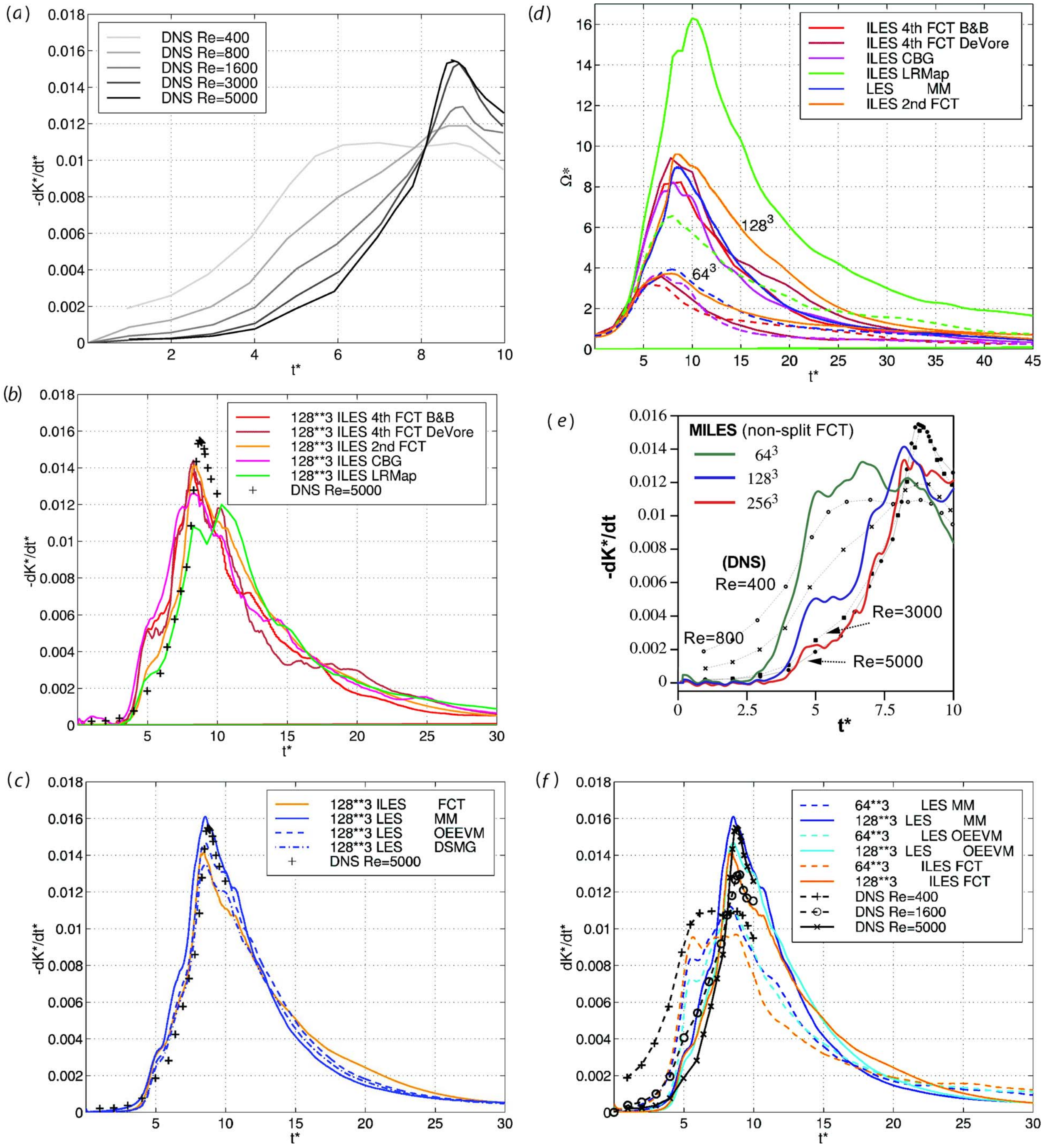

Fig. 3 Temporal evolution of the kinetic energy dissipation rate $-dK/dt$ from (*a*) the DNS [14,38], (*b*) the 128^3 ILES and MM LES simulations, and (*c*) comparative representative conventional LES; (*d*) evolution of the mean enstrophy on 64^3 and 128^3 simulations for second-order FCT ILES and LES (from [11]); (*e*) $-dK/dt$ predictions from 64^3, 128^3, and 256^3 3D-FCT, and DNS data; (*f*) $-dK/dt$ predictions from DNS data, second-order FCT ILES, and various LES.

4 Concluding Remarks

In ILES, the effects of the SGS physics on the resolved scales are incorporated in the functional reconstruction of the convective fluxes using HR methods. MEA shows that ILES based on a particular class of such flux-limiting schemes provides implicitly implemented anisotropic SGS models dependent on the specifics of the numerical scheme considered, i.e., on the flux limiter, on the choice of low- and high-order schemes, on the implementation specifics, and on the gridding. In this context, MEA provides a framework to reverse engineer physically desirable features into the numerics design (e.g., [52]).

We discussed the behavior of ILES based on various different HR monotonic schemes in the simulation of the fundamental TGV case study, previously used as a canonical test case to address the transition to turbulence. Comparisons were established with available DNS results, as well as with conventional LES methods. The results show that all numerical schemes tested here can provide a fairly robust LES computational framework to capture the physics of flow transition and turbulence decay without resorting to an explicit SGS model and using relatively coarse grids. The results show that the mean kinetic energy dissipation rate and enstrophy specifics depend somewhat on the detailed aspects of the SGS

Downloaded 03 Jun 2010 to 171.66.16.156. Redistribution subject to ASME license or copyright; see http://www.asme.org/terms/Terms_Use.cfm

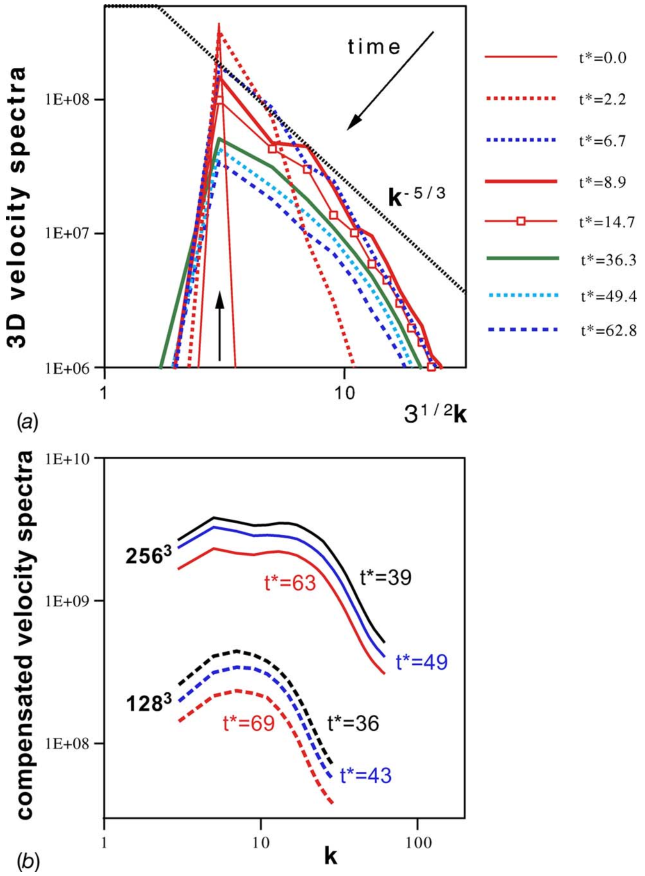

Fig. 4 (*a*) Evolution of the 3D velocity spectra *E*(*k*); (*b*) compensated spectra, $k^{+5/3}E(k)$

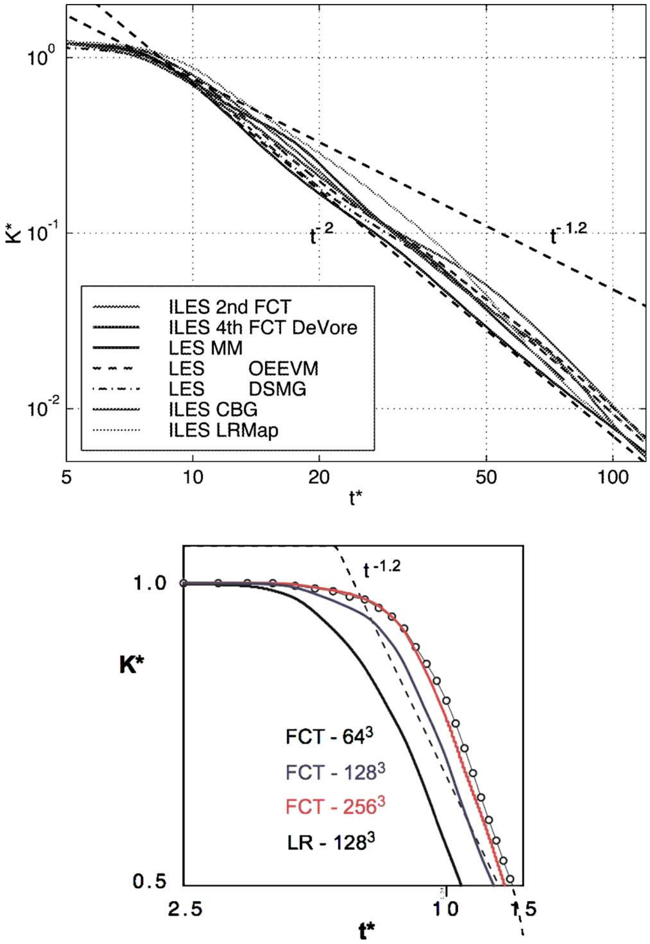

Fig. 5 Volumetrically averaged kinetic energy decay in time. (*a*) Comparative power-law behaviors versus various ILES methods and the MM LES; (*b*) kinetic energy decay versus grid resolution based on the fourth-order FCT (128^3 and 256^3) and LR (128^3) simulation data; all scales are logarithmic.

model provided implicitly by the various HR algorithms (or explicitly by the conventional LES methods) and by their actual implementations. The performance of representative LES and ILES approaches appears to be equally good for this application, and there is no discriminating characteristic favoring one or another. Looking toward practical complex flows and regimes, however, the ability of ILES to offer a simpler computational environment should be clearly emphasized.

Most flows of practical interest feature coupled processes that introduce additional physical length sales and time scales to those of convection. These may occur strictly in the context of hydrodynamics, e.g., compressibility, rotation, and stratification. Alternatively, these may include additional regimes of physics where the flow features are not necessarily dominated by large-scale convection, such as material mixing, combustion, radiation transport, plasma physics, and magnetohydrodynamics. Implicit SGS models provided by certain HR methods work well in emulating the (inherently incompressible) physical dynamics of turbulent velocity fluctuations. However, the presence of new physical scales will likely require adding specialized explicit SGS models to ILES (e.g., interface treatments), *as with any other conventional LES approach*. Formal and test studies need to be extended to establish how ILES treat turbulent mass-density and species-concentration fluctuations, the role of which is crucial for, e.g., Kelvin–Helmholtz, Rayleigh–Taylor, and Ritchmyer–Meshkov driven mix instabilities and increasingly important for the higher Mach number regimes (e.g., [22]).

Challenges for ILES include improving on MEA (the mathematical and physical framework for its analysis and development), further understanding the connections between implicit SGS model and numerical scheme, and, in particular, addressing how to build SGS physics into the numerical scheme to improve on the global ILES performance, i.e., on the implicitly implemented SGS dissipation and backscatter features. ILES performance enhancements are possible through an improved design of the SGS physics capturing capabilities. Further investigations seeking a better understanding of specific dissipation and dispersion properties of HR schemes—and suitable testing and validation frameworks to establish a physical basis for the various possible choices—are clearly warranted in this context.

References

[1] Sagaut, P., 2005, *Large Eddy Simulation for Incompressible Flows*, 3rd ed., Springer, New York.

[2] Ghosal, S., 1996, “An Analysis of Numerical Errors in Large-Eddy Simulations of Turbulence,” J. Comput. Phys., **125**, pp. 187–206.

[3] Grinstein, F. F., and Fureby, C., 2004, “From Canonical to Complex Flows: Recent Progress on Monotonically Integrated LES,” Comput. Sci. Eng., **6**, pp. 37–49.

[4] Margolin, L. G., Rider, W. G., and Grinstein, F. F., 2006, “Modeling Turbulent Flow With Implicit LES,” J. Turbul., **7**, pp. 1–27.

[5] *Implicit Large Eddy Simulation: Computing Turbulent Fluid Dynamics*, F. F. Grinstein, L. G. Margolin, and W. J. Rider, eds., Cambridge University Press, Cambridge, England.

[6] Harten, A., 1983, “High Resolution Schemes for Hyperbolic Conservation Laws,” J. Comput. Phys., **49**, pp. 357–393.

[7] P. J. Boris, 1990, “On Large Eddy Simulation Using Subgrid Turbulence Models,” in *Whither Turbulence? Turbulence at the Crossroads*, J. L. Lumley, ed., Springer, New York, p. 344.

[8] Boris, J. P., Grinstein, F. F., Oran, E. S., and Kolbe, R. L., 1992, “New Insights Into Large Eddy Simulation,” Fluid Dyn. Res., **10**, pp. 199–228.

[9] Fureby, C., and Grinstein, F. F., 1999, “Monotonically Integrated Large Eddy

Downloaded 03 Jun 2010 to 171.66.16.156. Redistribution subject to ASME license or copyright; see http://www.asme.org/terms/Terms_Use.cfm

Simulation of Free Shear Flows," AIAA J., **37**, pp. 544–556.
[10] Margolin, L. G., and Rider, W. J., 2002, "A Rationale for Implicit Turbulence Modeling," Int. J. Numer. Methods Fluids, **39**, pp. 821–841.
[11] Brachet, M. E., Meiron, D. I., Orszag, S. A., Nickel, B. G., Morg, R. H., and Frisch, U. J., 1983, "Small-Scale Structure of the Taylor-Green Vortex," J. Fluid Mech., **130**, pp. 411–452.
[12] Drikakis, D., Fureby, C., Grinstein, F. F., and Youngs, D. 2007, "Simulation of Transition and Turbulence Decay in the Taylor-Green Vortex," J. Turbul. **8**(020), pp. 1–12.
[13] Hirt, C. W., 1968, "Heuristic Stability Theory for Finite Difference Equations," J. Comput. Phys., **2**, pp. 339–355.
[14] Fureby, C., and Grinstein, F. F., 2002, "Large Eddy Simulation of High Reynolds-Number Free and Wall Bounded Flows," J. Comput. Phys., **181**, pp. 68–97.
[15] Gurtin, M. E., 1981, *An Introduction to Continuum Mechanics*, Academic, Orlando.
[16] Kellogg, O. D., 1929, *Foundations of Potential Theory*, Springer, New York.
[17] Boris, J. P., and Book, D. L., 1973, "Flux-Corrected Transport I. SHASTA, A Fluid Transport Algorithm That Works," J. Comput. Phys., **11**, pp. 38–69.
[18] Sweby, P. K., 1985, "Flux Limiters," in *Numerical Methods for the Euler Equations of Fluid Dynamics*, F. Angrand, A. Dervieux, J. A. Desideri, and R. Glowinski, eds., Siam, Philadelphia, pp. 48–65.
[19] Drikakis, D., and Rider, W., 2004, *High-Resolution Methods for Incompressible and Low-Speed Flows*, Springer, New York.
[20] Kuzmin, D., Lohner, R., and Turek, S., 2005, *High-Resolution Schemes for Convection Dominated Flows:* 30 Years *of FCT*, Springer, New York.
[21] Drikakis, D., Hahn, M., Grinstein, F. F., DeVore, C. R., Fureby, C., Liefvendahl, M., and Youngs, D. L., 2007, "Limiting Algorithms," in *Implicit Large Eddy Simulation: Computing Turbulent Fluid Dynamics*, F. F. Grinstein, L. G. Margolin, and W. J. Rider, eds., Cambridge University Press, Cambridge, England.
[22] Van der Bos, F., and Geurts, B. J., 2006, "Computational Turbulent Stress Closure for Large-Eddy Simulation of Compressible Flow," J. Turbul., **7**(9), pp. 1–16.
[23] Brenner, H., 2005, "Kinematics of Volume Transport," Physica A, **349**, pp. 11–59.
[24] Clark, R. A., Ferziger, J. H., and Reynolds, W. C., 1979, "Evaluation of Sub-Grid Scale Models Using an Accurately Simulated Turbulent Flow," J. Fluid Mech., **118**, pp. 1–16.
[25] Aldama, A. A., 1993, "Leonard and Cross-Term Approximations in the Anisotropically Filtered Equations of Motion," in *Large Eddy Simulation of Complex Engineering and Geophysical Flows*, B. Galperin and S. A. Orszag, eds., Cambridge University Press, New York.
[26] Shao, L., Sarkar, S., and Pantano, C., 1999, "On the Relationship Between the Mean Flow and Subgrid Stresses in Large Eddy Simulation of Turbulent Shear Flows," Phys. Fluids, **11**, pp. 1229–1248.
[27] Borue, V., and Orszag, S. A., 1998, "Local Energy Flux and Subgrid-Scale Statistics in Three Dimensional Turbulence, J. Fluid Mech., **366**, pp. 1–31.
[28] van Leer, B., 1977, "Towards the Ultimate Conservative Difference Scheme IV. A New Approach to Numerical Convection," J. Comput. Phys., **23**, pp. 276–299.
[29] Margolin, L., 2005, private communication.
[30] Schlichting, H., 1979, *Boundary Layer Theory*, McGraw-Hill, New York, p. 585.
[31] Baker, G. A., 1975, *Essentials of Padé Approximants*, Academic, New York.
[32] Frisch, U., 1995, *Turbulence*, Cambridge University Press, Cambridge, England, p. 57.
[33] Porter, D. H., Pouquet, A., and Woodward, P. R., 1994, "Kolmogorov-Like Spectra in Decaying Three-Dimensional Supersonic Flows," Phys. Fluids, **6**, pp. 2133–2142.
[34] Domaradzki, J. A., Xiao, Z., and Smolarkiewicz, P. K., 2003, "Effective Eddy Viscosities in Implicit Modeling of Turbulent Flows," Phys. Fluids, **15**, pp. 3890–3893.
[35] Garnier, E., Mossi, M., Sagaut, P., Comte, P., and Deville, M., 1999, "On the Use of Shock-Capturing Schemes for Large Eddy Simulation," J. Comput. Phys., **153**, pp. 273–311.
[36] Margolin, L. G., and Rider, W. J., 2007, "Numerical Regularization: The Numerical Analysis of Implicit Subgrid Models," in *Implicit Large Eddy Simulation: Computing Turbulent Fluid Dynamics*, F. F. Grinstein, L. G. Margolin, and W. J. Rider, eds., Cambridge University Press, Cambridge, England.
[37] Shu, C.-W., Don, W.-S., Gottlieb, D., Schilling, O., and Jameson, L. 2005, "Numerical Convergence Sudy of Nearly Incompressible, Inviscid Taylor-Green Vortex Flow," J. Sci. Comput., **24**, pp. 1–27.
[38] Morf, R. H., Orszag, S. A., and Frisch, U., 1980, "Spontaneous Singularity in Three-Dimensional, Inviscid, Incompressible Flow," Phys. Rev. Lett., **44**, pp. 572–575.
[39] Brachet, M. E., 1991, "Direct Numerical Simulation of Three-Dimensional Turbulence in the Taylor-Green Vortex," Fluid Dyn. Res., **8**, pp. 1–8.
[40] DeVore, C. R., 1998, "An Improved Limiter for Multidimensional Flux-Corrected Transport," NRL, Report No. NRL-MR-6440-98-8330.
[41] Zoltak, J., and Drikakis, D., 1998, "Hybrid Upwind Methods for the Simulation of Unsteady Shock-Wave Diffraction Over a Cylinder," Comput. Methods Appl. Mech. Eng., **162**, pp. 165–185.
[42] Bagabir, A., and Drikakis, D., 2004, "Numerical Experiments Using High-Resolution Schemes for Unsteady, Inviscid, Compressible Flows," Comput. Methods Appl. Mech. Eng., **193**, pp. 4675–4705.
[43] Eberle, A., 1987, "Characteristic Flux Averaging Approach to the Solution of Euler's Equations," *VKI Lecture Series*, Computational Fluid Dynamics Report No. 1987-04.
[44] Youngs, D. L., 1991, "Three-Dimensional Numerical Simulation of Turbulent Mixing by Rayleigh-Taylor Instability," Phys. Fluids A, **3**, pp. 1312–1320.
[45] Germano, M., Piomelli, U., Moin, P., and Cabot, W. H., 1994, "A Dynamic Sub Grid Scale Eddy Viscosity Model," Phys. Fluids A, **3**, pp. 1760–1765.
[46] Schumann, U., 1975, "Subgrid Scale Model for Finite Difference Simulation of Turbulent Flows in Plane Channels and Annuli," J. Comput. Phys., **18**, pp. 376–404.
[47] Bardina, J., Ferziger, J. H., and Reynolds, W. C., 1980, "Improved Subgrid Scale Models for Large Eddy Simulations," AIAA Paper No. 80-1357.
[48] Jeong, J., and Hussain, F., 1995, "On the Identification of a Vortex," J. Fluid Mech., **285**, pp. 69–94.
[49] Jimenez, J., Wray, A., Saffman, P., and Rogallo, R., 1993, "The Structure of Intense Vorticity in Isotropic Turbulence," J. Fluid Mech., **255**, pp. 65–90.
[50] Lesieur, M., and Ossia, S., 2000, "3D Isotropic at Very High Reynolds Numbers: EDQNM Study," J. Turbul., **1**(007), pp. 1–25.
[51] Skrbek, L., and Stalp, S. R., 2000, "On the Decay of Homogeneous Isotropic Turbulence," Phys. Fluids, **12**, pp. 1997–2019.
[52] Margolin, L. G., and Rider, W. J., 2005, "The Design and Construction of Implicit Subgrid Scale Models," Int. J. Numer. Methods Fluids, **47**, pp. 1173–1179.

Downloaded 03 Jun 2010 to 171.66.16.156. Redistribution subject to ASME license or copyright; see http://www.asme.org/terms/Terms_Use.cfm

Effective Subgrid Modeling From the ILES Simulation of Compressible Turbulence

William J. Rider
Computational Shock and Multiphysics,
Sandia National Laboratories,
Albuquerque, NM 87185-0385
e-mail: wjrider@sandia.gov

*Implicit large eddy simulation (ILES) has provided many computer simulations with an efficient and effective model for turbulence. The capacity for ILES has been shown to arise from a broad class of numerical methods with specific properties producing nonoscillatory solutions using limiters that provide these methods with nonlinear stability. The use of modified equation has allowed us to understand the mechanisms behind the efficacy of ILES as a model. Much of the understanding of the ILES modeling has proceeded in the realm of incompressible flows. Here, we extend this analysis to compressible flows. While the general conclusions are consistent with our previous findings, the compressible case has several important distinctions. Like the incompressible analysis, the ILES of compressible flow is dominated by an effective self-similarity model (Bardina, J., Ferziger, J. H., and Reynolds, W. C., 1980, "Improved Subgrid Scale Models for Large Eddy Simulations," AIAA Paper No. 80–1357; Borue, V., and Orszag, S. A., 1998, "Local Energy Flux and Subgrid-Scale Statistics in Three Dimensional Turbulence," J. Fluid Mech., **366**, pp. 1–31; Meneveau, C., and Katz, J., 2000, "Scale-Invariance and Turbulence Models for Large-Eddy Simulations," Annu. Rev. Fluid. Mech., **32**, pp. 1–32). Here, we focus on one of these issues, the form of the effective subgrid model for the conservation of mass equations. In the mass equation, the leading order model is a self-similarity model acting on the joint gradients of density and velocity. The dissipative ILES model results from the limiter and upwind differencing resulting in effects proportional to the acoustic modes in the flow as well as the convective effects. We examine the model in several limits including the incompressible limit. This equation differs from the standard form found in the classical Navier–Stokes equations, but generally follows the form suggested by Brenner (2005, "Navier-Stokes Revisited," Physica A, **349**(1–2), pp. 60–133) in a modification of Navier–Stokes necessary to successfully reproduce some experimentally measured phenomena. The implications of these developments are discussed in relation to the usual turbulence modeling approaches.*

[DOI: 10.1115/1.2801680]

Keywords: implicit large eddy simulation, modified equation, Navier–Stokes, finite-volume equations

1 Introduction

Implicit large eddy simulation (ILES) has provided both a powerful and a practical approach to modeling turbulence in a broad variety of circumstances. Successful ILES modeling has been conducted with a variety of high-resolution methods. The first observation of an effective modeling of turbulence without explicit modeling is credited to Boris [4], who called the methodology monotonically ILES (MILES). Boris applied the flux-corrected transport method that he had developed to produce MILES. Other researchers also found the same capacity with other methods. Porter and Woodward applied the Godunov-type method (piecewise parabolic method (PPM)) to astrophysical problems and discovered effective turbulence modeling [25]. Linden et al. found similar results with an entirely different class of methods using a Lagrange-remap methodology [19]. More recently, success has been had with total variation diminishing (TVD) methods for engineering flows [14]. These methods have now been documented in several review articles [9,10] and two books [11,15]. These two articles and books catalog the large variety of methods and applications where ILES has had success.

Going back to the origins of numerical fluid dynamics provides more compelling evidence that ILES and classical LES are connected. The original shock capturing method developed by Von Neumann and Richtmyer [30] used a nonlinear artificial viscosity to stabilize the computation of shock waves. This same nonlinear viscosity was then applied in weather modeling by Smagorinsky, albeit in three dimensions [28,29]. Smagorinsky's viscosity was the original subgrid modeling used for LES. Thus, classical LES has its origins with the first nonlinear shock capturing method that has ultimately developed into the same class of methods now associated with ILES.

We have examined a number of high-resolution methods using the technique known as modified equation analysis (MEA) [20–22,26]. MEA produces the differential equation more accurately solved by a numerical method than the original intended equation. For example, first-order upwind differencing of the simple advection equation produces the solution to a specific advection-diffusion equation. Through MEA, we have uncovered the form of the implicit model from which ILES's modeling success is derived. In the following sections, we will describe the MEA analysis of compressible flow and discuss the implications for the form of the implicit model. The differences with classical modeling is most acute in the mass equation. This allows us to focus on how ILES provides a unique and powerful modeling technique.

Contributed by the Fluids Engineering Division of ASME for publication in the JOURNAL OF FLUIDS ENGINEERING. Manuscript received February 11, 2007; final manuscript received May 21, 2007. Review conducted by Dimitris Drikakis. Paper presented at the ECCOMAS 2006.

Downloaded 03 Jun 2010 to 171.66.16.156. Redistribution subject to ASME license or copyright; see http://www.asme.org/terms/Terms_Use.cfm

2 Modified Equation Analysis

MEA was first developed to assess the stability of numerical algorithms [17]. Basically, the analysis consists of Taylor series expansion about a relevant mesh spacing $\Delta x \rightarrow 0$ applied to the discrete terms of the algorithm as if the equation (and its solution) were continuous. We note that the limit of $\Delta x \rightarrow 0$ cannot be achieved in reality (not to mention the violation of the continuum hypothesis that the equations themselves are based on). This immediately raises the issue of the dynamics at finite scales, which we examined in the paper [22]. We found that the physics of finite volumes of fluid evolve by different evolution equations than the Navier–Stokes equations. This is predicated on the presence of dissipation that enforces the smoothness of the flow at small scales. A renormalization procedure allows the smoothness to insure the applicability of the Taylor series expansion at each succeeding scale. We note that numerical viscosity insures that a comparable result will apply to ILES solutions. The techniques that produce the nonlinear stability of the methods also work to insure that the solutions are smooth enough for the Taylor series expansion to have an explanatory power undiluted by the presence of discontinuities and unresolved layer in a flow field.

The main assumption is the use of Taylor analysis itself, which implies restrictions on the smoothness of the function. In particular, the Taylor analysis produces an infinite series of terms, but the modified equation is formed by truncating this series and keeping only the lowest order terms, which are assumed to dominate the numerical effects. Our analysis indicates that numerical dissipation is sufficient to keep the flow field regular enough for the Taylor series expansion to have meaning. A discussion of the uses of MEA and caveats of its use can be found in Ref. [20].

The modified equation for a *consistent* algorithm consists of the modeled PDE plus additional terms, each proportional to a power of the computational time step Δt or of the computational cell size Δx, or possibly both. The smallest power among these terms determines the order of accuracy of the scheme. In general, if the partial differential equation (PDE) has the form

$$\frac{\partial \mathbf{U}}{\partial t} + \nabla \cdot \mathbf{F}(\mathbf{U}) = 0 \tag{1}$$

then the modified equation of a consistent algorithm will have the form

$$\frac{\partial \mathbf{U}}{\partial t} + \nabla \cdot \mathbf{F}(\mathbf{U}) = \mathbf{T}(\mathbf{U}, \Delta x, \Delta t) \tag{2}$$

where $\mathbf{T}$ is the truncation term. More specifically, when finite-volume differencing [31] is employed, then the modified equation will have the form

$$\frac{\partial \mathbf{U}}{\partial t} + \nabla \cdot \mathbf{F}(\mathbf{U}) = \nabla \cdot \tau(\mathbf{U}, \Delta x, \Delta t) \tag{3}$$

This produces the result in a form similar to that found in standard constitutive modeling with a stress tensor. Thus, all algorithms based on finite-volume differencing have a truncation term in the form of the divergence of a "subgrid scale" model. The conditions under which this form is useful for ILES is the main subject of this paper. We will focus on the compressible form of the stress tensor associated with the mass (or continuity) equation.

3 Multidimensional Modified Equation Analysis

It is straightforward to extend the one-dimensional analysis to fully three-dimensional algorithms. In this section, we will show the general results, assuming the use of a second-order, but otherwise unspecified flux limiters for both incompressible and compressible flows in three dimensions. First, the 3D incompressible Euler equations will be presented using a general limiter that provides a nonlinear combination of a first-order and second-order methods. We follow this with a presentation of the modified equation for the fully compressible version of the same method.

We will derive the modified equation using a symbolic algebra software, specifically the MATHEMATICA program. We will use tensor notation with implied summation over repeated indices. For the case of incompressible flow, we will then specialize our results to the two-dimensional case on a rectangular mesh of cells $\Delta x \times \Delta y \times \Delta z$. This will allow detailed comparisons of our results with those in Ref. [22] for the finite scale equations and for the modified equation of the multidimensional positive difinite advection transport algorith (MPDATA).

The incompressible Euler equations can be written compactly as

$$\frac{\partial u_m}{\partial t} + \frac{\partial u_n u_m}{\partial x_n} + \frac{\partial p}{\partial x_m} = 0 \tag{4}$$

where the indices $m, n = 1, 2, 3$ indicate summation over those indices. The constraint of incompressibility is expressed by

$$\frac{\partial u_n}{\partial x_n} = 0 \tag{5}$$

The compressible equations can also be written abstractly. Our notation will employ the vector flux function of a vector of conserved quantities,

$$\frac{\partial \mathbf{u}}{\partial t} + \frac{\partial \mathbf{f}_n(\mathbf{u})}{\partial x_n} = 0 \tag{6}$$

This represents a system of conservation laws.

In the analysis that follows, the pressure field is defined as a potential field that acts to ensure that the velocity field is divergence free (i.e., solenoidal). Our algorithm will consist of the combination of a first-order and a second-order accurate method, with relative weights of the two schemes determined by a flux-limiter function. We construct a second-order accurate method by defining a set of edge variables as the averages of the cell-centered values across a cell edge, i.e.,

$$\begin{aligned} u_{m,i+1/2,j,k} &= \tfrac{1}{2}(u_{m,i,j,k} + u_{m,i+1,j,k}) \\ u_{m,i,j+1/2,k} &= \tfrac{1}{2}(u_{m,i,j,k} + u_{m,i,j+1,k}) \\ u_{m,i,j,k+1/2} &= \tfrac{1}{2}(u_{m,i,j,k} + u_{m,i,j,k+1}) \end{aligned} \tag{7}$$

Here, i, j, and k are the grid indices associated with the cell centers. The numerical approximation for the divergence is

$$\frac{u_{1,i+1/2,j,k} - u_{1,i-1/2,j,k}}{\Delta x_1} + \frac{u_{2,i,j+1/2,k} - u_{2,i,j-1/2,k}}{\Delta x_2} + \frac{u_{3,i,j,k+1/2} - u_{3,i,j,k-1/2}}{\Delta x_3} = 0 \tag{8}$$

The second-order expression for the nonlinear product that appears in the advective terms is simply constructed as the product of the edge values, e.g.,

$$(u_1 u_2)^{\text{2nd}}_{i+1/2,j,k} = u_{1,i+1/2,j,k} u_{2,i+1/2,j,k} \tag{9}$$

With our second-order approximations defined, we need to define the first-order approximations. This is done using the donor cell method where the numerical definition of the edge value is biased by the normal velocity. For example, in direction 1 for the two motion equations, we need to define the product $u_1 u_2$ at cell boundaries,

$$(u_1 u_2)^{\text{1st}}_{i+1/2,j,k} = (u_1 u_2)^{\text{2nd}}_{i+1/2,j,k} - \tfrac{1}{2}|u_{1,i+1/2,j,k}|(u_{2,i+1,j,k} - u_{2,i,j,k}) \tag{10}$$

We will define our limiter abstractly as a function, ϕh, that depends on the mesh spacing $h = \Delta x_m$ (we assume that the mesh spacing is constant, but not necessarily equal, in all three directions for simplicity). Although the flux limiter is itself dimensionless, we have explicitly factored out the cell dimension in antici-

Downloaded 03 Jun 2010 to 171.66.16.156. Redistribution subject to ASME license or copyright; see http://www.asme.org/terms/Terms_Use.cfm

pation of future results. A number of limiters could fit this general form, including the MPDATA method, Sweby's form of TVD methods, high-order Godunov methods, and flux-corrected transport to mention but a few.

With the limiter defined, we can simply express our high-resolution method using a combination of the two previous expressions,

$$(u_1u_2)^{\text{hi res}}_{i+1/2,j,k} = \phi_1 h_1 (u_1u_2)^{\text{1st}}_{i+1/2,j,k} + (1-\phi_1 h_1)(u_1u_2)^{\text{2nd}}_{i+1/2,j,k} \tag{11}$$

where the limiter is constructed to produce second-order or higher accuracy. With our basic numerical method defined, we introduce our numerical approximations into the discrete incompressible Euler equations and expand using a Taylor series in each of the three coordinate directions. After some simplification, our results are compactly written notation as

$$\begin{aligned}\frac{\partial u_m}{\partial t} + \frac{\partial u_n u_m}{\partial x_n} + \frac{\partial p}{\partial x_m} = h_n^2\Bigg[&\frac{1}{2}\phi_n|u_n|\left(\frac{1}{u_n}\frac{\partial u_n}{\partial x_n}\frac{\partial u_m}{\partial x_n} + \frac{\partial^2 u_m}{\partial x_n^2}\right)\\ &+ \frac{1}{2}|u_n|\frac{\partial \phi_n}{\partial x}\frac{\partial u_m}{\partial x_n} - \frac{1}{4}\left(\frac{\partial u_m}{\partial x_n}\frac{\partial^2 u_n}{\partial x_n^2} + \frac{\partial u_n}{\partial x_n}\frac{\partial^2 u_m}{\partial x_n^2}\right)\\ &- \frac{1}{6}\left(u_n\frac{\partial^3 u_m}{\partial x_n^3} + u_m\frac{\partial^3 u_n}{\partial x_n^3}\right)\Bigg] + \mathcal{O}(h_n^3)\end{aligned} \tag{12}$$

where again the pressure gradient is simply the gradient of the potential function that enforces the discrete divergence condition (Eq. (9)). This form is similar to the one-dimensional forms in the presence of the self-similar terms[1,3,23] and in the leading order impact of the limiter on the dissipation.

The entire approach has been successfully validated using detailed data from high Reynolds number decaying turbulence [18]. The validation has included integral behavior such as kinetic energy decay and energy spectra, as well as velocity probability distribution functions (PDFs) [22,26]. In all cases, the ILES methods produced exceptional results despite the relatively coarse grids. Furthermore, the ILES methods produced a far better reproduction of the intermittency measured in the experiment than the classical LES methods tested in Ref. [18]. In an overall sense, the ILES models appear to have achieved a favorable validation against experimental data.

4 Analysis of Compressible Implicit Large Eddy Simulation

We can apply the same basic differencing for compressible flows. The key differences are the lack of the divergence-free constraint and the application of the differencing to a vector function with an abstractly defined flux function. The high-order flux (second-order) is defined using the face-averaged value as before, but now it is written as

$$\mathbf{f}^{\text{2nd}}_{i+\text{half},j,k} = \mathbf{f}(\mathbf{u}_{i+1/2,j,k}) \tag{13}$$

The first-order flux is defined with the help of the flux Jacobian, $\mathbf{f}' = \partial\mathbf{f}/\partial\mathbf{u}$ as,

$$\mathbf{f}^{\text{1st}}_{i+\text{half},j,k} = \mathbf{f}^{\text{2nd}}_{i+\text{half},j,k} - \tfrac{1}{2}|\mathbf{f}'|(\mathbf{u}_{i+1,j,k} - \mathbf{u}_{i,j,k}) \tag{14}$$

The use of an eigenvalue decomposition of the flux Jacobian can be used to produce the absolute value, $|\mathbf{f}'| = R|\lambda|R^{-1}$, where R are the right eigenvectors. Substituting these expressions combined using our abstractly defined limiter that blends the first- and second-order fluxes and expanding the expression in a three-dimensional Taylor series produces

$$\frac{\partial \mathbf{u}}{\partial t} + \frac{\partial \mathbf{f}(\mathbf{u})}{\partial x_n} = h_n^2\frac{\partial}{\partial x_n}\left[\frac{1}{2}\phi_n|\mathbf{f}'|\frac{\partial \mathbf{u}}{\partial x_n} - \frac{1}{6}\mathbf{f}'\frac{\partial^2 \mathbf{u}}{\partial x_n^2} - \frac{1}{24}\mathbf{f}''\left(\frac{\partial \mathbf{u}}{\partial x_n}\right)^2\right] + \mathcal{O}(h_n^3) \tag{15}$$

Of course, this expression is only formally accurate away from discontinuities. This form is also similar to the one-dimensional compressible analysis having the self-similar terms proportional to the convexity of the flux function ($\mathbf{f}''$). The limiter enters into the analysis, as expected, at second order.

By substituting our defined high-resolution method, specifically for the mass (continuity) equation, we produce the following form:

$$\begin{aligned}\frac{\partial \rho}{\partial t} + \frac{\partial \rho u_n}{\partial x_n} = h_n^2\frac{\partial}{\partial x_n}\Bigg[&\frac{\phi_n|u_n|}{2}\frac{\partial(\rho - p/a^2)}{\partial x_n}\\ &+ \frac{\phi_n|u_n - a|}{4}\frac{\partial(\rho u_n/a - p/a^2)}{\partial x_n}\\ &+ \frac{\phi_n|u_n + a|}{4}\frac{\partial(\rho u_n/a + p/a^2)}{\partial x_n} - \frac{u_n}{6}\frac{\partial^2 \rho}{\partial x_n^2} - \frac{\rho}{6}\frac{\partial^2 u_n}{\partial x_n^2}\\ &- \frac{\gamma+1}{48}\frac{\partial \rho}{\partial x_n}\frac{\partial u_n}{\partial x_n}\Bigg] + \mathcal{O}(h_n^3)\end{aligned} \tag{16}$$

Here, a is the sound speed.

Note that the form has the self-similarity term and a nonlinear dissipation from the upwind differencing, which, upon further analysis, comes directly from the acoustic waves. For the mass equation, the effective subgrid model is quite unlike that found in classical LES modeling. Specifying the above analysis for the mass equation and providing an upwinding mechanism that operates characteristic by characteristic (for a gamma law gas) gives the modified equation below. If we take the limit where the sound speed becomes very large in comparison to the fluid velocity, the dissipation remains,

$$\frac{\partial \rho}{\partial t} + \frac{\partial \rho u_n}{\partial x_n} = h_n^2\frac{\partial}{\partial x_n}\left[\frac{1}{2}\phi_n\rho\frac{\partial u_n}{\partial x_n} - \frac{\rho}{6}\frac{\partial^2 u_n}{\partial x_n^2} - \frac{\gamma+1}{48}\frac{\partial \rho}{\partial x_n}\frac{\partial u_n}{\partial x_n}\right] + \mathcal{O}(h_n^3) \tag{17}$$

Thinking about the mixing of fluids of different densities, the right hand side makes physical sense. The stretching for fluid elements by the velocity field will act to mix the fluid at the large scale, bringing fluids of differing density into contact on the scale of fluid volumes parametrized by h. It is notable that Brenner's analysis produces dissipation that is not proportional to γ, but comes from normal gradient diffusion processes. The terms derived above are generated by the hyperbolic (advection) terms in the equations, and the diffusion is necessary to produce entropy satisfying solutions.

The bottom line is that the mass equation has both a nonlinear dissipative model and a self-similar model under all relevant circumstances. As a specific example, the shock capturing LES model by Cook and Cabot [8] has a zero right hand side for the mass equation (Florina and Lele modified this method to include a nonzero right hand side [12]). Cook and Cabot followed a tried principle of connecting the turbulent closure's form to that of the Navier–Stokes. As such, the physical interpretation remains firmly connected to our understanding of the basic PDEs and laminar flow.

We will relay recent developments regarding the form of the mass equation in the Navier–Stokes equation. These developments have been spearheaded by Brenner of MIT and have reformulated the Navier–Stokes equations in terms of a volumetric velocity rather than a mass velocity. The bottom line of this reformulation is to introduce a diffusive component into the mass equation. In addition, we might be tempted to ask whether the effective governing equations for turbulent flows in finite volumes

Downloaded 03 Jun 2010 to 171.66.16.156. Redistribution subject to ASME license or copyright; see http://www.asme.org/terms/Terms_Use.cfm

of fluid ought to have the same form as the equations governing the laminar flow at a point. Our suggestion is that they should not, for several important and valid reasons.

5 Discussion of the Modified Equation Analysis of the Mass Equation

Unlike most classical turbulence models, the continuity equation has a nonzero right hand side. We note that techniques, such as Favre averaging, usually produce a form for the continuity equation that is identical to the standard continuity equation with a zero right hand side. It is notable that many of the early applications of ILES have been to material mixing, where there are clearly nonlinear effects from density and velocity fluctuations. These effects are notably lacking from standard turbulence modeling approaches although many models will include these effects in the momentum and energy balances. Until recently, the modeling approach ILES could be criticized for having a form so different from the Navier–Stokes equation. A common approach is to have the constitutive modeling follow the same form as physical properties. Evidence now exists that calls this critique into question.

It is notable that the form of the continuity equation has been the subject of vigorous debate recently. The challenges to the classical form have been summarized in a remarkable sequence of papers by Brenner [2,5–7]. In these papers, compelling evidence is presented that the Navier–Stokes equations for compressible flows are missing a key physical mechanism for mass transfer. This is a diffusive mechanism that is necessary to provide a systematic explanation of experimental data. In simple terms, the convective fluxes of mass exchange atoms or molecules with the surrounding fluid; thus, variations in the rate of exchange would naturally lead to diffusive fluxes. This explanation is equivalent to the classical explanation of diffusion rates in gases and liquids. A zero diffusion rate would only be physical under the conditions that the material were solid and the flux volumes were impermeable.

We make a particular point of concentrating on this result in that our analysis systematically produces a continuity equation with a nonzero right hand side. This is true for all methods that have been useful as ILES techniques and has its basis in the form for the equations controlling the evolution of volumes of fluid [22]. Bringing the recent developments to mind shows that the ILES approach follows directly from parallel physical arguments. One stems from the small scale physics leading to diffusion through a random motion of the constituent particles comprising the flow. The other stems from the nature of the evolution of finite volumes of fluid. These finite volumes are a natural state to examine fluid flows due to the existence of finite scales of observation associated with experimental techniques. The closure to these ideas follows the association of finite scales of observation with the use of finite-volume (or conservative) methods. Finite-volume methods also need to employ some sort of instantiation of the second law of thermodynamics to guarantee physical solutions. The second law of thermodynamics follows from a dissipative or diffusive impact on the large scale solution to equations (via a vanishing viscosity solution).

Acknowledgment

This work was performed under the auspices of the U.S. Department of Energy under Contract No. W-7405-ENG-36.

References

[1] Bardina, J., Ferziger, J. H., and Reynolds, W. C., 1980, "Improved Subgrid Scale Models for Large Eddy Simulations," AIAA Paper No. 80-1357.
[2] Bielenberg, J. R., and Brenner, H., 2006, "A Continuum Model of Thermal Transpiration," J. Fluid Mech., **546**, pp. 1–23.
[3] Borue, V., and Orszag, S. A., 1997, "Local Energy Flux and Subgrid-Scale Statistics in Three Dimensional Turbulence," J. Fluid Mech., **366**, pp. 344–353.
[4] Boris, J. P., 1989, "Comments," *Whither Turbulence? Turbulence at the Crossroads*, J. Lumley, ed., Springer-Verlag, Berlin.
[5] Brenner, H., 2005, "Navier-Stokes Revisited," Physica A, **349**(1-2), pp. 60–132.
[6] Brenner, H., 2005, "Nonisothermal Brownian Motion: Thermophoresis as the Macroscopic Manifestation of Thermally Biased Molecular Motion," Phys. Rev. E, **72**(6), p. 061201.
[7] Brenner, H., and Bielenberg, J. R., 2005, "A Continuum Approach to Phoretic Motions: Thermophoresis," Physica A, **355**(2–4), pp. 251–273.
[8] Cook, A. W., and Cabot, W. H., 2004, "A High-Wavenumber Viscosity for High-Resolution Numerical Methods," J. Comput. Phys., **195**(2), pp. 594–601.
[9] Drikakis, D., 2003, "Advances in Turbulent Flow Computations Using High-Resolution Methods," Prog. Aerosp. Sci., **39**(6–7), pp. 405–424.
[10] Drikakis, D., Grinstein, F., and Youngs, D., 2005, "On the Computation of Instabilities and Symmetry-Breaking in Fluid Mechanics," Prog. Aerosp. Sci., **41**(8), pp. 609–641.
[11] Drikakis, D., and Rider, W., 2004, *High-Resolution Methods for Incompressible and Low-Speed Flows*, Springer-Verlag, Berlin.
[12] Florina, B., and Lele, S. K., 2005, "An Artificial Nonlinear Diffusivity Method for Shock-Capturing in Supersonic Reacting Flows," Annual Research Briefs for the Center for Turbulence Research, Stanford University.
[13] Frisch, U., 1995, *Turbulence: The Legacy of A. N. Kolmogorov*, Cambridge University Press, Cambridge, England.
[14] Fureby, C., and Grinstein, F. F., 2002, "Large Eddy Simulation of High Reynolds-Number Free and Wall Bounded Flows," J. Comput. Phys., **181**, pp. 68–97.
[15] Grinstein, F. F., Margolin, L. G., and Rider, W. J., 2006, *Implicit Large Eddy Simulation: Computing Complex Fluid Dynamics*, Cambridge University Press, Cambridge, England.
[16] Grinstein, F. F., and Fureby, C., 2002, "Recent Progress on MILES for High Re Flows," ASME J. Fluids Eng., **124**, pp. 848–861.
[17] Hirt, C. W., 1968, "Heuristic Stability Theory for Finite Difference Equations," J. Comput. Phys., **2**, pp. 339–355.
[18] Kang, H. S., Chester, S., and Meneveau, C., 2003, "Decaying Turbulence in an Active-Grid-Generated Flow and Comparisons With Large-Eddy Simulation," J. Fluid Mech., **480**, pp. 129–160.
[19] Linden, P. F., Redondo, J. M., and Youngs, D. L., 1994, "Molecular Mixing in Rayleigh-Taylor Instability," J. Fluid Mech., **265**, pp. 97–124.
[20] Margolin, L. G., and Rider, W. J., 2002, "A Rationale for Implicit Turbulence Modeling," Int. J. Numer. Methods Fluids, **39**, pp. 821–841.
[21] Margolin, L. G., and Rider, W. J., 2005, "The Design and Construction of Implicit Subgrid Scale Models," Int. J. Numer. Methods Fluids, **47**(10-11), pp. 1173–1179.
[22] Margolin, L. G., Rider, W. J., and Grinstein, F. F., 2006, "Modeling Turbulent Flow With Implicit LES," J. Turbul., **7**(15), pp. 1–27.
[23] Meneveau, C., and Katz, J., 2000, "Scale-Invariance and Turblence Models for Large-Eddy Simulation," Annu. Rev. Fluid Mech.
[24] Pope, S., 2000, *Turbulent Flows*, Cambridge University Press, Cambridge, England.
[25] Porter, D. H., and Woodward, P. R., 1994, "High Resolution Simulations of Compressible Convection With the Piecewise-Parabolic Method (PPM)," Astrophys. J., Suppl. Ser., **93**, pp. 309–349.
[26] Rider, W. J., 2006, "The Relationship of MPDATA to Other High-Resolution Methods," Int. J. Numer. Methods Fluids, **50**(10), pp. 1145–1158.
[27] Sagaut, P., 2003, *Large Eddy Simulation for Incompressible Flows*, Springer-Verlag, Berlin.
[28] Smagorinsky, J., 1963, "General Circulation Experiments With the Primitive Equations. I. The Basic Experiment," Mon. Weather Rev., **101**, pp. 99–164.
[29] Smagorinsky, J., 1983, "The Beginnings of Numerical Weather Prediction and General Circulation Modeling: Early Recollections," Adv. Geophys., **25**, pp. 3–37.
[30] Von Neumann, J., and Richtmyer, R., 1950, "A Method for the Numerical Calculation of Hydrodynamic Shocks," J. Appl. Phys., **21**, pp. 532–537.
[31] Finite-volume differencing is also known as conservative form and as flux form differencing. We will use these terms interchangeably.

Downloaded 03 Jun 2010 to 171.66.16.156. Redistribution subject to ASME license or copyright; see http://www.asme.org/terms/Terms_Use.cfm

Assessment of Very High Order of Accuracy in Implicit LES models

Andrew Mosedale
e-mail: a.d.mosedale@cranfield.ac.uk

Dimitris Drikakis
e-mail: d.drikakis@cranfield.ac.uk

Fluid Mechanics & Computational
Science Group,
Aerospace Sciences Department,
School of Engineering,
Cranfield University,
Cranfield MK43 0AL, United Kingdom

This paper looks at the use of high-resolution and very high-order methods for implicit large-eddy simulation (ILES), with the specific example of simulating the multicomponent two-dimensional single-mode Richtmyer–Meshkov instability for which experimental data is available. The two gases are air and SF6, making stringent demands on the models used in the code. The interface between the two gases is initialized with a simple sinusoidal perturbation over a wavelength of 59 mm*, and a shock of strength Mach 1.3 is passed through this interface. The main comparison is between the second-order monotone upwind-centered scheme for conservation law methods of van Leer (1979, "Towards the Ultimate Conservative Difference Scheme," J. Comput. Phys.* ***32****, pp. 101–136) and the current state-of-the-art weighted essentially nonoscillatory interpolation, which is presented to ninth order, concentrating on the effect on resolution of the instability on coarse grids. The higher-order methods as expected provide better resolved and more physical features than the second-order methods on the same grid resolution. While it is not possible to make a definitive statement, the simulations have indicated that the extra time required for the higher-order reconstruction is less than the time saved by being able to obtain the same or better accuracy at lower computational cost (fewer grid points). It should also be noted that all simulations give a good representation of the growth rate of the instability, comparing very favorably to the experimental results, and as such far better than the currently existing theoretical models. This serves to further indicate that the ILES approach is capable of providing accurately physical information despite the lack of any formal subgrid model.* [DOI: 10.1115/1.2801374]

1 Introduction

This paper investigates the effect of the order of accuracy of the reconstruction step in so-called "high-resolution" methods, through simulations of the multicomponent two-dimensional single-mode Richtmyer–Meshkov instability (RMI) following the experiments by Jacobs [1]. High-resolution methods can be defined as those giving second (or higher-) order accuracy in smooth regions of the flow while suppressing spurious oscillations [2]. These are intrinsically nonlinear, even for linear equations, and are commonly found in treatment of compressible flow where the hyperbolic nature of the equations can make it impossible to simply use high-order reconstructions. One way to improve accuracy without breaking the physical constraints of hyperbolicity is to use compact schemes, generating higher-order reconstruction without increasing the size of the stencil. These can be costly to compute and are still fundamentally limited in their stability. Given that a nonlinear mechanism is required for stability, it is often easier to simply use noncompact stencils and allow the limiting function to control the oscillations. The earlier second-order schemes of van Leer are discussed in Sec. 2, followed by an explanation of the more recent higher-order developments used in this paper.

Different approaches are available for deriving the large-eddy simulation (LES) equations and the associated subgrid scale (SGS) models required to handle the effects of the unresolved flow physics. In general, we need to distinguish between the classical and the implicit LES. In classical LES, the flow equations are filtered by convolving all dependent variables with a predefined filter in order to extract the large-scale components, see, e.g., Ref. [3] for a recent survey. There are various models with differing characteristics, which can be used to represent the complex small scales of turbulence. In essence, LES simply requires that all energy beyond a certain wavelength be dissipated appropriately and it can still accurately represent the flow field. Classical approaches have ranged from the inherently limited subgrid viscosity formulations to more sophisticated and accurate dynamic and mixed models, which, however, increase computational complexity. In the context of classical LES and in the absence of a universal theory of turbulence, the construction of SGS models is unavoidably pragmatic and based primarily on the rational use of empirical information. Beyond the problem of devising a subgrid model that accurately deals with the dissipation, traditional LES has to theoretically achieve zero numerical dissipation in the scheme. This is significant as the truncation error in the straightforward second-order accurate discretization of the equations is of the same order of magnitude as the dissipation required by the subgrid scale. Difficulties pertinent to classical LES have been discussed in recent surveys [4] and include commutation and aliasing errors, limitations with regard to compressible flows and masking of the SGS terms by the truncation error.

An alternative approach to LES is therefore to design a scheme with the correct amount of inherent dissipation so as to not require a separate subgrid model. The implicit large-eddy simulation (ILES) approach (see Ref. [5] for a recent survey) employs the original (unfiltered) flow equations instead of the filtered ones and the effects of the SGS physics on the resolved scales are incorporated in the functional reconstruction of the convective fluxes using high-resolution finite-volume methods (as defined by Harten [2,6]). The ILES methods discussed in this paper are flux difference splitting (FDS) schemes; however, there are other approaches to ILES notably the class of flux vector splitting (FVS) schemes typified by the flux corrected transport (FCT) method [7]. Classical FDS schemes invoke nonoscillatory constraints via nonlinear limiters to implicitly act as a filtering (and nonlinear adaptive regularization) mechanism for the small scales. Modified equation analysis indicates that the leading truncation-error terms introduced by such methods provide implicit SGS models of mixed anisotropic type and show some good agreements between truncation errors due to the numerical scheme and the required form of the subgrid terms [8–10]. Major properties of the implicit SGS model are related to (i) the choice of high- and low-order

---

Contributed by the Fluids Engineering Division of ASME for publication in the JOURNAL OF FLUIDS ENGINEERING. Manuscript received February 15, 2007; final manuscript received July 27, 2007. Review conducted by Fernando Grinstein.

Downloaded 03 Jun 2010 to 171.66.16.156. Redistribution subject to ASME license or copyright; see http://www.asme.org/terms/Terms_Use.cfm

schemes—where the former is well behaved in smooth flow regions and the latter is well behaved near sharp gradients; (ii) the choice of flux/slope limiter, which determines how these schemes should be blended locally, depending on prescribed characterization of the flow smoothness; (iii) the balance of the dissipation and dispersion contributions to the numerical solution, which strongly depends on the design details of each numerical method. Using ILES, excellent results have been gained in simulation of flows as varied as Rayleigh–Taylor and RMIs [11–13] free jets [7,14], channel flow [14], open cavity flow [15,16], geophysical flows [17,18], delta wings [19], and decaying turbulence [9,20–23].

The aim of research into ILES schemes is to design them such that their numerical errors specifically improve the realism of the result—in particular, with finely detailed turbulent flows. As a consequence of this, the order of accuracy of any part of the scheme and its attendant truncation errors must come under great scrutiny. The most recent efforts have been in weighted essentially nonoscillatory (WENO) schemes, which offer very high-order spatial accuracy in the reconstruction while avoiding the worst of the spurious oscillations such interpolations usually entail (see Ref. [8] for a recent survey and references therein). The WENO approach belongs to the Godunov class of high-resolution methods, affecting only the reconstruction of the variables prior to application of the Riemann solver in the finite-volume framework. It is an alternative limiting procedure to the traditional monotone upwind-centered scheme for conservation law (MUSCL) and allows for higher-order accuracy in the interpolation of the interface variables. This does not equate to the global order of accuracy for the scheme, merely the number of truncation terms introduced at this point to contribute to the implicit subgrid model. It has been observed that second-order monotonic interpolations are overly dissipative, which is the motivation for exploring higher-order methods, but it should be noted that there are still other sources of error in the scheme; indeed, as directionally splitting is used the global order of the scheme for multidimensional problems is limited to second order in any case. However, it is our contention that using a higher-order interpolation in the reconstruction does have a positive effect on the overall result. Thus far, very little work has been done applying these schemes to multicomponent physical problems of the nature presented in this paper. Here, the spatial scheme is supported by a third-order accurate total variation diminishing (TVD) Runge–Kutta time stepping, and implemented with the HLLC Riemann Solver of Toro [24]. All these elements combine to give as sophisticated an ILES method as currently exists for these types of problems.

Modeling of compressible turbulent mixing is a challenging business. It makes most of the toughest demands on a solver - the ability to accurately capture shock waves and model other compressibility effects while still giving accurate solutions in the incompressible regime where most of the turbulent energy dissipation occurs. While it is relatively easy to compute a single instability on a fine enough grid to resolve the features, in reality an unstable flow will have hundreds or thousands of small features facilitating the transition to turbulence, and so it is important for large-scale applications that these features can be reliably and accurately resolved over as few grid cells as possible, as this is what ultimately limits what can be considered a resolved LES.

2 Computational Model and High-Order Godunov Methods

Given the presence of shock waves and compressible mixing, it is necessary to employ a compressible method. With a Reynolds number on the order of 10^6, the Kolmogorov length scale is significantly below the grid scale, and the effect of viscosity on the scales resolved by the grid is considered negligible. Thus, the governing equations chosen are the Euler equations plus two additional equations for the multicomponent model. The following are the full three-dimensional governing equations including the additional two equations for total enthalpy conservation of multicomponent flow proposed by Wang et al. [25]:

$$\frac{\partial \mathbf{U}}{\partial t} + \frac{\partial \mathbf{E}}{\partial x} + \frac{\partial \mathbf{F}}{\partial y} + \frac{\partial \mathbf{G}}{\partial z} = 0$$

where

$$\mathbf{U} = \left[\rho, \rho u, \rho v, \rho w, e, \frac{\rho\chi}{M}, \frac{\rho}{M}\right]^T$$

$$\mathbf{E} = \left[\rho u, \rho u^2 + p, \rho u v, \rho u w, (e+p)u, \frac{\rho u\chi}{M}, \frac{\rho u}{M}\right]^T$$

$$\mathbf{F} = \left[\rho v, \rho u v, \rho v^2 + p, \rho v w, (e+p)v, \frac{\rho v\chi}{M}, \frac{\rho v}{M}\right]^T$$

$$\mathbf{G} = \left[\rho w, \rho u w, \rho v w, \rho w^2 + p, (e+p)w, \frac{\rho w\chi}{M}, \frac{\rho w}{M}\right]^T$$

$$e = \rho i + 0.5\rho q^2$$

and ρ, i, u, v, w are the density, internal energy, and Cartesian velocity components, respectively, and q is the total magnitude of the velocity. M is molecular weight, and χ is defined as

$$\chi = \frac{\rho i}{p} + 1$$

At the pressures and temperatures considered, both SF_6 and air are approximated well by the ideal gas equation of state and are miscible.

With the introduction of nonlinear dynamics and discontinuities such as shock waves, the simplest central difference approximations fail immediately to correctly capture the physics of hyperbolic equations such as the Euler equations. An inevitable and well-observed consequence of this is spurious oscillation arising around a discontinuity. To counter this, "upwind" schemes can be employed to provide numerical stability. One approach is to split the flux vector into positive and negative components according to the eigenvectors, and then propagate only the appropriate flux in each direction. Such methods are known as FVS schemes. A generally more refined alternative, employed here, that allows for even greater physical information to be taken advantage of is FDS based on the Godunov scheme. Godunov achieved the first extension of the basic Courant-Isaacson-Rees (CIR) flux scheme [26] to systems of equations using the assumption that the flow variables were piecewise constant in each cell and then dictated that the value used for the flux calculation at each interface be the solution of the resulting Riemann problem, between cells. This then captures the basic physics of any flow, allowing for a stable and conservative solution of shocked flows. There are two major drawbacks to Godunov's method, one is the analytic solution of the Riemann problems, which has been largely overcome—all simulations for this paper utilized the HLLC Riemann Solver of Toro [24]. The other problem is the loss of information caused by the assumption of piecewise constant data, and this will be addressed in the rest of this paper.

According to the Godunov's theorem, "There are no monotone, linear schemes…of second or higher order accuracy." Monotonicity is the requirement that cell variable updates are bounded by the neighboring cells. It is essentially what we mean by removing the spurious oscillations that occur around shock waves; no new minima or maxima can be created. Godunov's theorem explicitly states that monotonicity and accuracy are contradictory aims. Naturally people have been trying to circumvent this for years, and the key to this effort is in the assumption of a linear method. It is perhaps not surprising that in order to fully engage with the highly nonlinear governing equations, a nonlinear solver can be used. In many schemes, this nonlinearity is introduced through

Downloaded 03 Jun 2010 to 171.66.16.156. Redistribution subject to ASME license or copyright; see http://www.asme.org/terms/Terms_Use.cfm

artificial viscosity (the high-order accurate central schemes have dissipation added artificially where necessary to damp out the inherent oscillations). Thus far, the Godunov method is inherently free of oscillations but restricted to first order. To improve this requires a nonlinear extension that will increase the order of accuracy in smooth parts of the flow but not interfere with the region of any discontinuity—quite the opposite requirement to artificial viscosity. The first major attempt at this was the work of van Leer [27].

The MUSCL approach of van Leer was an obvious extension to Godunov's method. Instead of assuming piecewise constant data, van Leer assumed piecewise linear data thereby achieving second-order accuracy. The values used for either side of the Riemann problem are a much better approximation of the real interface value. The nonlinearity is introduced through "slope limiters," functions that restrict the slope imposed on each cell in the vicinity of the discontinuity in order to maintain monotonicity. These were developed as TVD schemes, which for one-dimensional linear advection is synonymous with preserving monotonicity. The basic aim of these restrictions was that maxima would decrease in value and minima increase, thereby avoiding the creation of spurious oscillations. The basic consequence was that in the region of a shockwave the scheme defaulted to first-order accuracy. Various limiters have been developed with varying degrees of dissipation; there is a clear correlation between improved resolution of discontinuities and increase in oscillations. Sweby [28] covers and standardizes all the traditional limiters (see Refs. [8,24] for recent surveys). However, even the most dissipative of these is a definite improvement over the first-order solutions. In the past decade, there have been many attempts to push the limit of the TVD concept [29–31].

The main advance since MUSCL in this area has been the increasing development of ENO schemes [32] and more recently WENO schemes [33]. ENO and WENO aim to provide very high-order accuracy without reducing the integrity of the shock-wave region in finite-volume schemes (see also Ref. [34]). They are effectively complex polynomial interpolations to the data values at the interface based on a large support stencil; finite difference ENO and WENO interpolated the fluxes themselves to the cell interfaces. Instead of limiting functions to dissipate undesirable oscillations, ENO and WENO actually maintain the same level of accuracy in all areas of the flow by using an adaptive stencil. ENO selects its support such that it does not cross a discontinuity, whereas WENO uses a convex combination of all available stencils (with discontinuous stencils being afforded zero weight). WENO has several other advantages—it gives a smoother, more predictable flux; can obtain the optimal accuracy from its support base ($(2r-1)$ where r is the size of the stencil); and removes the logical statements necessary for ENO, which makes it twice as fast on vector supercomputers. However, to achieve a proper multidimensional high-order interpolation in finite-volume schemes on unstructured meshes can require an excessively large number of calculations. It is not necessarily practical to use these schemes for problems where there is little return for supposedly increased accuracy, but using them in split dimensions on Cartesian grids such as those used here, while limited in its effect, is fairly straightforward to implement. The weaknesses of these very high-order schemes, apart from additional computational time, are detecting the discontinuities, particularly when two discontinuities are close together. These methods are not perfect, a fact acknowledged in their name as *essentially* nonoscillatory. They are a move away from the more traditional thinking of TVD schemes, yet there are cases where further monotonicity restraints are required for stability [35,36], and various approaches to artificial compression are currently being investigated to counter unwanted diffusion [37]. For all these supposed flaws, the ability to calculate relatively stable and clear results at fifth, ninth, or potentially higher orders of accuracy has made these methods very attractive as shall be seen in the results. The extra cost of evaluating the large stencils is more than covered by the reduction in grid resolution that can be made while maintaining an accurate and well-resolved solution. Comparisons of the different high-order methods can be found in Refs. [38,39] and alternative approaches to improving the WENO concept in Refs. [40–43]. This paper shall primarily compare the second-order MUSCL approach with fifth- and ninth-order WENOs for RMI and mixing.

3 Computing Richtmyer–Meshkov Instability and Mixing

The RMI modeled here is taken from the experimental work of Jacobs [1]. The simulation has been initialized as perfect—pure gases on either side of the interface with a preshock Atwood No. of 0.692—whereas due to necessity in creating the perturbation the experiment has some diffusion leaving some air mixed with the SF6. The numerical interface between the two gases is initialized with a simple sinusoidal perturbation over a wavelength of 59 mm, and a shock of strength Mach 1.3 is passed through this interface. The experimental and numerical problems are similar enough to bear comparison, not only in the visual appearance of the instability but also the growth rates of the bubble and spike, which are appropriately nondimensionalized in any case. Simulations with a modified initial condition to allow for the experimental diffusion have been carried out along with a different two-fluid model—neither significantly affects the results or conclusions here.

The typical growth of the instability is shown in Fig. 1 for a reasonably well-resolved scheme, where the dark region represents the SF6 in a plot of volume fraction. After the initial linear growth phase, the vorticity deposited by the shock wave can be seen to be gathering at the head of the instability as it starts to pull material around the sides. This roll-up continues, establishing clear vortical structures, which then start to manifest the secondary instability seen in experiments as a series of small Kelvin–Helmoholtz features, which disturb the smooth lines of the vortex leading to an eventual breakdown into turbulence. Comparison with experiment will quickly reveal, however, that the curvature of the mushroom head is flawed in this simulation. This is due to how the initial perturbation is resolved on the Cartesian grid; indeed, there are many factors to consider in setting the initial conditions as these high-order schemes are very sensitive to small differences. While the vortex dynamics dominate the flow and can destabilize the upper surface, there is no evidence that the shape of the very tip of the instability has any major impact on the formation of the vortices or the breakdown to turbulence. Indeed, the comparison of methods conducted by Liska and Wendroff [38] in which they consider the Rayleigh–Taylor instability, which is closely related to Richtmyer–Meshkov, shows a host of unphysical and unpredictable features at the head of the instability depending on the method used. This is a manifestation of how different methods respond to "errors" in different ways. Should the initial conditions be perfectly specified as part of a continuum, then one would expect a properly rounded tip to the instability but this is one area that demands very careful approximations to be simulated accurately.

Figure 2 shows the comparison of different order accuracy methods over a range of coarse grids with 20, 40, or 80 cells per wavelength. At the coarsest resolution very little can be seen, though it is well worth noting that the overall amplitude of the instability at this time is comparable with the more highly resolved simulations. With less than 20 cells this soon ceases to be the case, so this point can be considered to be when the primary instability is resolved. It is hard to see much difference between the schemes; however, the higher-order WENO methods do give an indication that some genuine vorticity is at work at the top of the spike causing the shear layer to roll up. At 40 cells across, features are much more clearly visible. The plots (*b*) and (*h*) in Fig. 2 still appear very similar at the large scale but the ninth-order WENO interpolation shows clear vortical roll-up at this

Downloaded 03 Jun 2010 to 171.66.16.156. Redistribution subject to ASME license or copyright; see http://www.asme.org/terms/Terms_Use.cfm

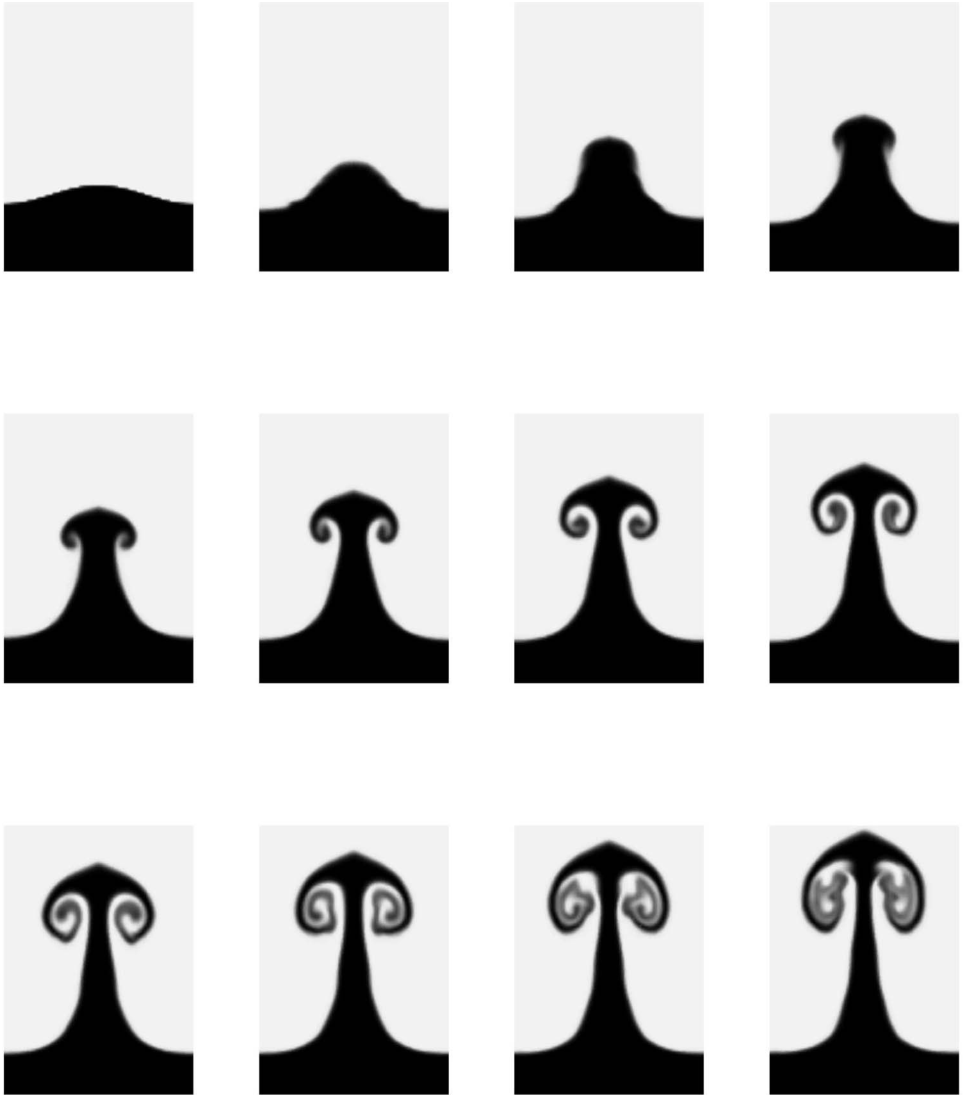

Fig. 1 Plot of volume fraction of SF6 showing the development of the instability over time, using fifth-order WENO on 80×240 grid, based on a sharp initial interface

stage and the mushroom shape compares favorably to the experimental results. Yet, increasing the resolution further allows the second-order method (plot (*c*) in Fig. 2) to start showing some kind of vortex, but still it is not qualitatively the same as the much more advanced vortex coil for the fifth-order scheme (plot (*f*) in Fig. 2) nor even highly comparable to the coarser WENO simulations (plots (*e*) and (*h*)). The most resolved picture (*i*) has already passed the secondary instability within the vortex coil (visible as "waviness" in the fifth order simulation) and has broken down into a turbulently mixed area. Also quite clearly seen is some separated fluid drawn down from the vortices, which is caused by small Kelvin–Helmholtz instabilities that form on the stem. At this resolution, only the effects of distortion can be seen. They are not found in the experiment due to the slightly diffuse nature of the initial perturbation. By contrast, these simulations had a sharp discontinuity (to the level of resolution of the grid) and the higher-order schemes do not carry sufficient dissipation to damp out the numerical errors.

As mentioned before, the growth rates seen in all the simulations are very similar. Figure 3 shows the nondimensionalized plot of amplitude over time. The points represent the experimental measurements taken from Jacobs' paper [1] and the lines show the results of the simulations for all resolutions and schemes. It is expected that if the simulations were extended to much later time there would be increasing deviation as the nonlinearity of the growth becomes dominated by the turbulent mixing—a phenomenon not captured at the lower resolutions. However, it is clear that the schemes can capture the main nonlinear growth region, which the theoretical models struggle to predict, and having validated the method against these experiments a parametric study could relatively swiftly be carried out to improve the theory of this growth via the simulations.

Table 1 shows the relative CPU cost for a given length of simulated time for the different schemes used, normalized by the runtime for the 20 cell van Leer scheme. For the very coarse grid the "fixed" costs start to dominate such that there is less difference between the different order schemes. However, what is important to note is the relative cost of, for example, the ninth-order scheme on a 40 cell grid with the second-order scheme on an 80 cell grid. The higher-order WENO methods are more expensive, but are better value for the level of fine-scale detail they provide. More refined grids and further comparison with experimental results is required to assess whether such detail is physically correct; however, it has been noticed that the higher-order schemes are particularly sensitive to very small differences in initial conditions and there is a limit to how well the experiment can be modeled to

Downloaded 03 Jun 2010 to 171.66.16.156. Redistribution subject to ASME license or copyright; see http://www.asme.org/terms/Terms_Use.cfm

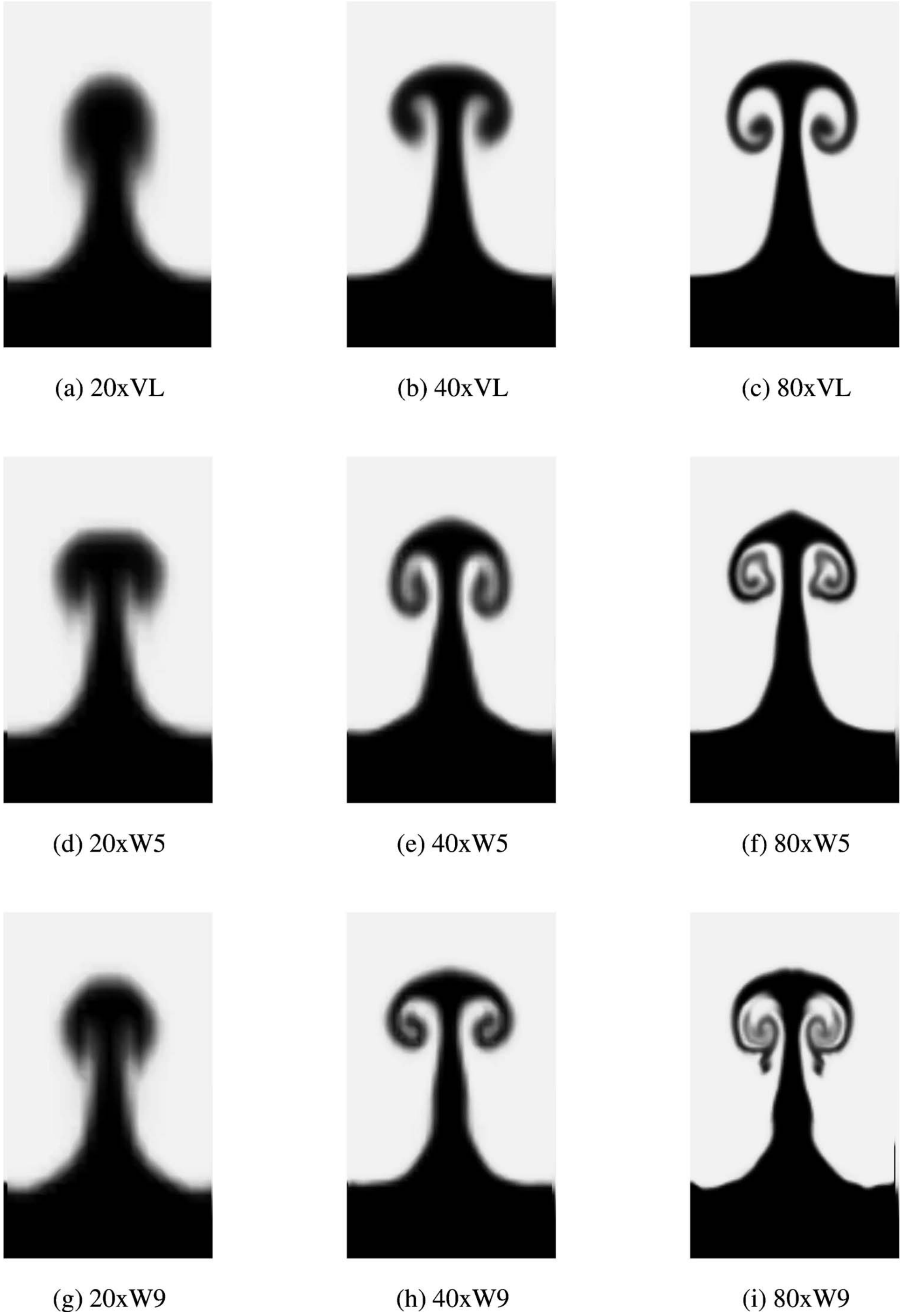
(a) 20xVL (b) 40xVL (c) 80xVL

(d) 20xW5 (e) 40xW5 (f) 80xW5

(g) 20xW9 (h) 40xW9 (i) 80xW9

Fig. 2 Volume fraction plots of Richtmyer–Meshkov simulations with No. of cells per wavelength and reconstruction method (VL: second-order van Leer, W5: fifth-order WENO, W9: ninth-order WENO) for sharp initial interface and Atwood No. of 0.692

achieve highly comparable results with simulations. Indeed, it may not be possible with this problem to identify whether the scheme is introducing spurious errors or merely reflecting discrepancies in other parts of the model. Thus far, the behavior has appeared physical, and with coarse simulations the WENO methods do well at mimicking the results of the the second-order schemes on finer grids, but it has not been definitively seen that both approaches converge to the same solution for this problem. Thus far, we can only say that the WENO methods are feasible. They are not prohibitively expensive and if the results prove sufficiently accurate for a given problem it is expected that they will be better value than the lower-order schemes.

4 Concluding Remarks

Simple ILES for RMI and mixing have been shown to provide meaningful physical information bearing good comparison to experimental results. Furthermore, high-order accuracy interpolation

Downloaded 03 Jun 2010 to 171.66.16.156. Redistribution subject to ASME license or copyright; see http://www.asme.org/terms/Terms_Use.cfm

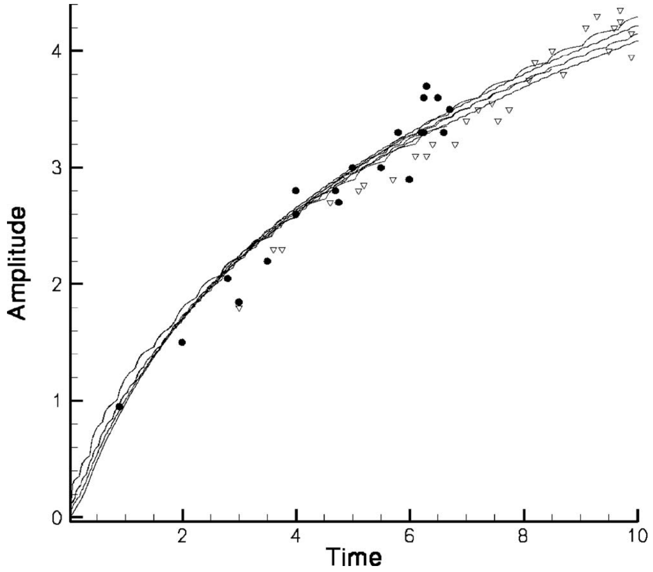

Fig. 3 Growth of instability, as predicted by different methods (lines), compared to experimental measurements (circles relate to equivalent problem, and triangles to a weaker shock case), nondimensionalized

Table 1 CPU runtime for schemes VL, W5, and W9 at grid resolutions 20, 40, and 80 for a given length of simulated time

Resolution	VL	W5	W9
20	1	1.02	1.70
40	4.1	10.4	11.5
80	18.2	45.1	53.5

schemes appear to dramatically improve the qualitative results of simulations on coarse grids. It is cheaper to use a high-order scheme on such a grid than a low-order scheme on a more refined grid to achieve comparable resolution of features. However, further work is required to assess the "reality" of results for a given problem.

Acknowledgment

The authors would like to acknowledge stimulating discussions with David Youngs and Robin Williams (AWE, Aldermaston) and Ben Thornber (Fluid Mechanics and Computational Science Group, Cranfield University). They would also like to acknowledge the financial support from EPSRC, MoD and AWE through the EPSRC (EP/C515153)-JGS (No. 971) project.

References

[1] Jacobs, J. W., and Krivets, V. V., 2005, "Experiments on the Late-Time Development of Single-Mode Richtmyer–Meshkov Instability," Phys. Fluids, **17**, p. 034105.

[2] Harten, A., 1997, "High Resolution Schemes for Hyperbolic Conservation Laws," J. Comput. Phys., **49**, pp. 357–393.

[3] Sagaut, P., *Large-Eddy Simulation for Incompressible Flows—An Introduction*, Springer-Verlag, Berlin.

[4] Pope, S. B., 2000, *Turbulent Flows*, Cambridge University Press, Cambridge.

[5] F. F. Grinstein, L. G. Margolin, and W. J. Rider, editors. *Implicit Large Eddy Simulation*, CUP, 2006.

[6] Harten, A., Engquist, B., Osher, S., and Chakravarthy, S. R., 1987, "Uniformly High Order Accurate Essentially Non-Oscillatory Schemes, III," J. Comput. Phys., **71**(2), pp. 231–303.

[7] Boris, J. P., Grinstein, F. F., Oran, E. S., and Kolbe, R. L., 1992, "New Insights into Large Eddy Simulation," Fluid Dyn. Res., **10**, pp. 199–228.

[8] Drikakis, D., and Rider, W., *High-Resolution Methods for Incompressible and Low-Speed Flows*, Springer, New York.

[9] Fureby, C., and Grinstein, F. F., 2002, "Large Eddy Simulation of High-Reynolds-Number Free and Wall-Bounded Flows," J. Comput. Phys., **181**, pp. 68–97.

[10] Margolin, L. G., Rider, W. J., and Grinstein, F. F., 2006, "Modeling Turbulent Flow With Implicit Les," J. Turbul., **7**(15), pp. 1–27.

[11] Youngs, D. L., 2003, "Application of Miles to Rayleigh–Taylor and Richtmyer–Meshkov Mixing," AIAA Paper No. 2003-4102.

[12] Youngs, D. L., 1991, "Three-Dimensional Numerical Simulation of Turbulent Mixing by Rayleigh–Taylor Instability," Phys. Fluids A, **3**(5), pp. 1312–1320.

[13] Thornber, B., and Drikakis, D., 2006, "ILES of Shock Waves and Turbulent Mixing Using High Resolution Riemann Solvers and TVD Methods," *ECCOMAS 2006, Minisymposia on Large Eddy Simulation: Theory and Applications*.

[14] Grinstein, F. F., and Fureby, C., 2002, "Recent Progress on Miles for High Reynolds Number Flows," ASME Trans. J. Fluids Eng., **848**, pp. 848–861.

[15] Drikakis, D., 2003, "Advances in Turbulent Flow Computations Using High-Resolution Methods," Prog. Aerosp. Sci., **39**, pp. 405–424.

[16] Hahn, M., and Drikakis, D., 2005, "Large Eddy Simulation of Compressible Turbulence Using High-Resolution Method," Int. J. Numer. Methods Fluids, **49**, pp. 971–977.

[17] Margolin, L. G., Smolarkiewicz, P. K., and Sorbjan, Z., 1999, "Large-Eddy Simulations of Convective Boundary Layers Using Nonoscillatory Differencing," Physica D, **133**, pp. 390–397.

[18] Smolarkiewicz, P. K., and Margolin, L. G., 1998, "Mpdata: A Finite Difference Solver for Geophysical Flows," J. Comput. Phys., **140**(2), pp. 459–480.

[19] Gordnier, R. E., and Visbal, M. R., 2005, "Compact Different Scheme Applied to Simulation of Low-Sweep Delta Wing Flow," AIAA J., **43**(8), pp. 1744–1752.

[20] Drikakis, D., Fureby, C., Grinstein, F., Hahn, M., and Youngs, D., 2006, "Miles of Transition to Turbulence in the Taylor–Green Vortex System," *ERCOFTAC Workshop on Direct and Large Eddy Simulation-6*, p. 133.

[21] Fureby, C., Tabor, F., Weller, H. G., and Gosman, A. D., 1997, "A Comparative Study of Subgrid Scale Models in Homogeneous Isotropic Turbulence," Phys. Fluids, **9**(5), pp. 1416–1429.

[22] Porter, D. H., Woodward, P. R., and Pouquet, A., 1998, "Inertial Range Structures in Decaying Compressible Turbulent Flows," Phys. Fluids, **10**(1), pp. 237–245.

[23] Margolin, L. G., Smolarkiewicz, P. K., and Wyszogrodzki, A. A., 2002, "Implicit Turbulence Modelling for High Reynolds Number Flows," ASME J. Fluids Eng., **124**, pp. 862–867.

[24] Toro, E. F., 1999, *Riemann Solvers and Numerical Methods for Fluid Dynamics*, 2nd ed., Springer, New York.

[25] Wang, S. P., Anderson, M. H., Oakley, J. G., Corradini, M. L., and Bonazza, R., 2004, "A Thermodynamically Consistent and Fully Conservative Treatment of Contact Discontinuities for Compressible Multi-Component Flows," J. Comput. Phys., **195**, pp. 528–559.

[26] Courant, R., Isaacson, E., and Rees, M., 1952, "On the Solution of Nonlinear Hyperbolic Differential Equations by Finite Differences," Commun. Pure Appl. Math., **5**, pp. 243–255.

[27] van Leer, B., 1979, "Towards the Ultimate Conservative Difference Scheme. V," J. Comput. Phys., **32**, pp. 101–136.

[28] Sweby, P. K., 1984, "High Resolution Schemes Using Flux Limiters for Hyperbolic Conservation Laws," SIAM (Soc. Ind. Appl. Math.) J. Numer. Anal., **21**(5), pp. 995–1011.

[29] Piperno, S., and Depeyre, S., 1998, "Criteria for the Design of Limiters Yielding Efficient High Resolution TVD Schemes," Comput. Fluids, **27**(2), pp. 183–197.

[30] Kadalbajoo, M. K., and Kumar, R., 2006, "A High Resolution Total Variation Diminishing Scheme for Hyperbolic Conservation Law and Related Problems," Appl. Math. Comput., **175**(2), pp. 1556–1573.

[31] Mahmood, K., Basri, S., Mokhtar, A. S., Ahmad, M. M. H. M., Asrar, W., and Omar, A. A., 2005, "Flux Limiting With High-Order Compact Schemes," *43rd AIAA Aerospace Sciences Meeting and Exhibit*.

[32] Harten, A., Engquist, B., Osher, S., and Chakravarthy, S. R., 1987, "Uniformly High Order Accurate Essentially Non-Oscillatory Schemes, III," J. Comput. Phys., **71**(2), pp. 231–303.

[33] Jiang, G.-S., and Shu, C.-H., 1996, "Efficient Implementation of Weighted ENO Schemes," J. Comput. Phys., **126**, pp. 202–228.

[34] Titarev, V. A., and Toro, E. F., 2004, "Finite-Volume WENO Schemes for Three-Dimensional Conservation Laws," J. Comput. Phys., **201**, pp. 238–260.

[35] Balsara, D. S., and Shu, C.-H., 2000, "Monotonicity Preserving Weighted Essentially Non-Oscillatory Schemes With Increasingly High Order of Accuracy," J. Comput. Phys., **160**, pp. 405–452.

[36] Suresh, A., and Huynh, H. T., 1997, "Accurate Monotonicity-Preserving Schemes With Runge–Kutta Time Stepping," J. Comput. Phys., **136**, pp. 83–99.

[37] Xu, Z., and Shu, C.-H., 2005, "Anti-Diffusive Flux Corrections for High-Order Finite Difference WENO Schemes," J. Comput. Phys., **205**, pp. 458–485.

Downloaded 03 Jun 2010 to 171.66.16.156. Redistribution subject to ASME license or copyright; see http://www.asme.org/terms/Terms_Use.cfm

[38] Liska, R., and Wendroff, B., 2002, “Comparison of Several Difference Schemes on 1D and 2D Test Problems for the Euler Equations,” available at http://www-troja.fjfi.cvut.cz/liska/CompareEuler/compare8/

[39] Shu, C.-W., 2003, “High-Order Finite Difference and Finite Volume WENO Schemes and Discontinuous Galerkin Methods for CFD,” Int. J. Comput. Fluid Dyn., **17**(2), pp. 107–118.

[40] Pirozzoli, S., 2002, “Conservative Hybrid Compact-WENO Schemes for Shock-Turbulence Interaction,” J. Comput. Phys., **178**, pp. 81–117.

[41] Kim, K. H., and Kim, C., 2005, “Accurate, Efficient and Monotonic Numerical Methods for MultiDimensional Compressible Flows. Part I: Spatial Discretization,” J. Comput. Phys., **208**, pp. 527–569.

[42] Kim, K. H., and Kim, C., 2005, “Accurate, Efficient and Monotonic Numerical Methods for Multi-Dimensional Compressible Flows. Part II: Multi-Dimensional Limiting Process,” J. Comput. Phys., **208**, pp. 570–615.

[43] Deng, X., and Zhang, H., 2000, “Developing High-Order Weighted Compact Non-Linear Schemes,” J. Comput. Phys., **165**, pp. 22–44.

Downloaded 03 Jun 2010 to 171.66.16.156. Redistribution subject to ASME license or copyright; see http://www.asme.org/terms/Terms_Use.cfm

Ben Thornber
e-mail: b.j.r.thornber@cranfield.ac.uk

Dimitris Drikakis
e-mail: d.drikakis@cranfield.ac.uk

Fluid Mechanics and Computational
Science Group,
Aerospace Sciences Department,
School of Engineering,
Cranfield University,
Cranfield MK43 0AL, UK

Large-Eddy Simulation of Shock-Wave-Induced Turbulent Mixing

The paper presents implicit large-eddy simulation (ILES) simulation of a shock tube experiment involving compressible turbulent mixing. A new characteristic-based approximate Riemann solver is derived, and employed in a second-order and fifth-order finite volume Godunov-type ILES framework. The methods are validated against (qualitative) experimental data and then compared and contrasted in terms of resolved turbulent kinetic energy and mixing parameters as a function of grid resolution. It is concluded that both schemes represent the experiment with good accuracy. However, the fifth-order results are approximately equivalent to results gained on double the grid size at second order, whereas the fifth-order method requires only approximately 20% extra computational time. [DOI: 10.1115/1.2801367]

1 Introduction

Recent experimental results by Holder and Barton [1] permit validation of numerical methods for multicomponent compressible turbulent mixing of two miscible gas species. The Reynolds number at the final time instant has been computed for the primary flow feature. This is a vortex of radius 0.05 m, velocity magnitude of the order of 10^2 m/s, and mean density of 7 kg/m^3. The viscosity of air at room temperature is ($\mu = 1.82 \times 10^{-5}$ Pa s), which is higher than SF$_6$ ($\mu = 1.51 \times 10^{-5}$ Pa s), hence giving a conservative estimate. Thus the Reynolds number based on these quantities is on the order of 5×10^6, thus given current computations power the simulations cannot be fully resolved. The shock tube experiment consists of an incident shock wave of Mach 1.26 in air passing through a square block of sulfur hexaflouride (SF$_6$). As it passes through the block, initially small perturbations on the gas interface create both Richtmyer–Meshkov instabilities (vorticity deposition as the shock passes) [2,3] and Kelvin–Helmholtz rollups. These perturbations grow rapidly in size leading to turbulent transition of the flow and inviscid mixing of the two gas components.

It is a great challenge to accurately simulate such a rich physical problem, and it is necessary to employ numerical methods, which have sufficient dissipation to maintain monotonicity across shock waves, yet allow the growth of the initially small perturbations and capture contact surfaces with good accuracy. Large-eddy simulation (LES) is emerging as a viable alternative in flows of industrial interest where the time dependent behavior of the flow must be resolved. Conventional LES [4] has been employed successfully in many prototype flows; however it is known to provide excessive dissipation in flows where the growth of an initially small perturbation to fully turbulent flow must be resolved [5,6]. However, there is as yet no subgrid model developed, which can capture shock waves, track multiple materials without oscillations, and model turbulent flows accurately, as the majority of subgrid models have been developed for incompressible flows.

It has been recognized that some numerical schemes gain good results in complex flows without the explicit addition of a subgrid model [4,5,7]. This methodology is called implicit large-eddy simulations, or ILES. It has been applied to a variety of flows, such as shock induced turbulent mixing, for example [8–10], free jets [11], convection of plumes, channel flow [11], cavity flow [12], geophysical flows [13], and decaying turbulence [12,14–16].

The good agreement of the simulations with turbulent flow physics stems from the "natural" form of the finite volume system. The properties evolved from one time step to the next are cell averaged, essentially filtered by a top hat filter. To compute the fluxes at the cell interface the filtered quantities are interpolated using a reconstruction method to recover the subgrid variations. This is to leading order a deconvolution approach, the approximations being in the order of accuracy of the numerical scheme and the one-dimensional nature of the reconstruction method. This has advantages in the simplicity of the method, and in previous papers ILES has been shown to capture the behavior of the large scales accurately (see references in the previous paragraph).

In this paper, a new characteristic-based Riemann solver is derived for the "total enthalpy conservation of the mixture" (THCM) model proposed by Wang et al. [17]. The governing equations, derivation of the fully coupled Riemann solver, and extensions to higher order of accuracy are detailed in Sec. 2. Section 3 discusses the initialization of the flowfield and presents the results obtained for both second- and fifth-order accuracies, on two different grid sizes. The paper finishes with some conclusions and discussion of future development.

2 Computational Approach

2.1 Governing Equations. Given the presence of shock waves and compressible mixing, it is necessary to employ a compressible method. With a Reynolds number on the order of 10^8, the Kolmogorov length scale is significantly below the grid scale, and the effect of viscosity on the scales resolved by the grid is considered negligible. Thus the governing equations chosen are the Euler equations plus two additional equations for the multicomponent model. At the pressures and temperatures considered, both SF$_6$ and air are approximated well by the ideal gas equation of state and are miscible. The three-dimensional compressible Euler equations for a Cartesian coordinate system can be written in conservative variables as

$$\frac{\partial \mathbf{U}}{\partial t} + \frac{\partial \mathbf{E}}{\partial x} + \frac{\partial \mathbf{F}}{\partial y} + \frac{\partial \mathbf{G}}{\partial z} = 0 \tag{1}$$

where

$$\mathbf{U} = [\rho,\ \rho u,\ \rho v,\ \rho w,\ E]^T \tag{2}$$

$$\mathbf{E} = [\rho u,\ \rho u^2 + p,\ \rho uv,\ \rho uw,\ (E+p)u]^T \tag{3}$$

Contributed by the Fluids Engineering Division of ASME for publication in the JOURNAL OF FLUIDS ENGINEERING. Manuscript received February 7, 2007; final manuscript received June 29, 2007. Review conducted by Fernando Grinstein. Paper presented for special issue on Implicit Large Eddy Simulation.

Copyright © 2007 by ASME

Downloaded 03 Jun 2010 to 171.66.16.156. Redistribution subject to ASME license or copyright; see http://www.asme.org/terms/Terms_Use.cfm

$$\mathbf{F} = [\rho v,\ \rho uv,\ \rho v^2 + p,\ \rho vw,\ (E+p)v]^T \tag{4}$$

$$\mathbf{G} = [\rho w,\ \rho uw,\ \rho vw,\ \rho w^2 + p,\ (E+p)w]^T \tag{5}$$

$$E = \rho\epsilon + 0.5\rho q^2 \tag{6}$$

and ρ, ϵ, u, v, w are the density, internal energy, and Cartesian velocity components, respectively. The subscripts $(.)_x, (.)_y, (.)_z$ indicate a partial derivative with respect to x, y, and z. The system of equations is completed with the specification of an equation of state (EOS), which for an ideal gas would be

$$p = \rho\epsilon(\gamma - 1) \tag{7}$$

The multicomponent model proposed by Wang et al. is based on the conservation of total enthalpy within the fluid mixture. The initial model derived requires two additional equations:

$$\frac{\partial}{\partial t}\left(\frac{\rho\chi}{M}\right) + \frac{\partial}{\partial x}\left(\frac{\rho u\chi}{M}\right) + \frac{\partial}{\partial y}\left(\frac{\rho v\chi}{M}\right) + \frac{\partial}{\partial z}\left(\frac{\rho w\chi}{M}\right) = 0 \tag{8}$$

$$\frac{\partial}{\partial t}\left(\frac{\rho}{M}\right) + \frac{\partial}{\partial x}\left(\frac{\rho u}{M}\right) + \frac{\partial}{\partial y}\left(\frac{\rho v}{M}\right) + \frac{\partial}{\partial z}\left(\frac{\rho w}{M}\right) = 0 \tag{9}$$

where M is the molecular mass of the mixture, and the variable χ is defined as

$$\chi = \frac{\gamma}{\gamma - 1} \tag{10}$$

for a perfect gas. This system is chosen as it is more rapid to compute than a full system of equations for each component, it is fully conservative (hence has very good shock capturing abilities), and reduces greatly the pressure oscillations at material interfaces compared to employing only the mass or volume fraction model. The resulting governing equations are solved using the Godunov method [18], which for a one-dimensional hyperbolic equation can be written in conservative form as

$$U_j^{n+1} = U_j^n + \frac{\Delta t}{\Delta x}(F_{j-1/2} - F_{j+1/2}) \tag{11}$$

$$F_{j+1/2} = F(U_{j+1/2}(0)) \tag{12}$$

$$F_{j-1/2} = F(U_{j-1/2}(0)) \tag{13}$$

where the intercell numerical fluxes $F_{j+1/2}$ and $F_{j-1/2}$ are computed based on the solution to the Riemann problems using (U_j^n, U_{j+1}^n) and (U_j^n, U_{j-1}^n), respectively. Time advancement is achieved using the third-order Runge–Kutta method [19],

$$U_i^1 = U_i^n + \frac{1}{2}\frac{\delta t}{\delta x} f(U_i^n) \tag{14}$$

$$U_i^2 = U_i^n + \frac{1}{2}\frac{\delta t}{\delta x}[f(U_i^1)] \tag{15}$$

$$U_i^{n+1} = \frac{1}{3}\left(2U_i^2 + U_i^n + \frac{\delta t}{\delta x}[f(U_i^2) + f(U_i^1)]\right) \tag{16}$$

where $f(U_j^n)$ indicates the net flux into the cell evaluated using the array of conserved variables at time n in cell position j (see also Ref. [20]).

2.2 Characteristic-Based Approximate Riemann Solver. To derive an approximate Riemann solver for each flux, dimensional splitting is applied. Dimensional splitting is used *only* for deriving characteristic-based formulas, for the intercell variables (denoted by a tilde in the text) according to which the advective fluxes are calculated. The numerical time integration is obtained for the complete system of equations after adding all the discretized fluxes. Thus, for the flux **E**

$$\frac{\partial \tilde{\mathbf{U}}}{\partial t} + \frac{\partial \tilde{\mathbf{E}}}{\partial x} = 0 \tag{17}$$

where the $\tilde{\mathbf{U}}$ denotes the reconstructed conservative variables and $\tilde{\mathbf{E}}$ the corresponding flux. Expanding Eq. (17) for each of the governing equations and reducing to primitive variables give

$$\frac{\partial \tilde{\rho}}{\partial t} + \tilde{u}\frac{\partial \tilde{\rho}}{\partial x} + \tilde{\rho}\frac{\partial \tilde{u}}{\partial x} = 0 \tag{18}$$

$$\tilde{\rho}\frac{\partial \tilde{u}}{\partial t} + \tilde{\rho}\tilde{u}\frac{\partial \tilde{u}}{\partial x} + \tilde{\rho}\frac{\partial \tilde{p}}{\partial x} = 0 \tag{19}$$

$$\tilde{\rho}\frac{\partial \tilde{v}}{\partial t} + \tilde{\rho}\tilde{u}\frac{\partial \tilde{v}}{\partial x} = 0 \tag{20}$$

$$\tilde{\rho}\frac{\partial \tilde{w}}{\partial t} + \tilde{\rho}\tilde{u}\frac{\partial \tilde{w}}{\partial x} = 0 \tag{21}$$

$$\frac{\partial \tilde{p}}{\partial t} + \tilde{u}\frac{\partial \tilde{p}}{\partial x} + \tilde{\rho}c^2\frac{\partial \tilde{u}}{\partial x} = 0 \tag{22}$$

$$\tilde{\rho}\frac{\partial \tilde{\chi}}{\partial t} + \tilde{\rho}\tilde{u}\frac{\partial \tilde{\chi}}{\partial x} = 0 \tag{23}$$

$$\tilde{\rho}\frac{\partial}{\partial t}\frac{1}{\tilde{M}} + \tilde{\rho}\tilde{u}\frac{\partial}{\partial x}\frac{1}{\tilde{M}} = 0 \tag{24}$$

where c is the speed of sound. The Riemann invariant is a transformation of the nonconservative Euler equations on the characteristic directions [21]. These invariants are given by

$$(\tilde{p} - p_0) - c^2(\tilde{\rho} - \rho_0) = 0 \tag{25}$$

$$(\tilde{v} - v_0) = 0 \tag{26}$$

$$(\tilde{w} - w_0) = 0 \tag{27}$$

$$(\tilde{\chi} - \chi_0) = 0 \tag{28}$$

$$\left(\frac{1}{\tilde{M}} - \frac{1}{M_0}\right) = 0 \tag{29}$$

$$(\tilde{p} - p_1) + \tilde{\rho}c(\tilde{u} - u_1) = 0 \tag{30}$$

$$(\tilde{p} - p_2) - \tilde{\rho}c(\tilde{u} - u_2) = 0 \tag{31}$$

where $(.)_1$ and $(.)_2$ indicate values evaluated along the λ_1 and λ_2 characteristic lines, respectively. Thus there are now six characteristic equations for the six unknown averaged flow values needed to determine the flux at the cell face. As this derivation has made use of the homogeneity property, the invariants have to be inverted to conserved variables. From the definition of the conservative flow variables, we have

$$u = \frac{\rho u}{\rho} \tag{32}$$

$$v = \frac{\rho v}{\rho} \tag{33}$$

$$w = \frac{\rho w}{\rho} \tag{34}$$

$$p = (\gamma - 1)\left(E - \frac{(\rho u)^2 + (\rho v)^2 + (\rho w)^2}{2\rho}\right) \tag{35}$$

Downloaded 03 Jun 2010 to 171.66.16.156. Redistribution subject to ASME license or copyright; see http://www.asme.org/terms/Terms_Use.cfm

$$\chi = \frac{\rho\chi/M}{\rho/M} \tag{36}$$

$$M = \frac{\rho}{\rho/M} \tag{37}$$

The differences can be expressed using the chain rule of differentiation [for example, $\rho\Delta u + u\Delta\rho = \Delta(\rho u)$]:

$$\Delta u = \frac{\Delta(\rho u) - u\Delta\rho}{\rho} \tag{38}$$

$$\Delta v = \frac{\Delta(\rho v) - v\Delta\rho}{\rho} \tag{39}$$

$$\Delta w = \frac{\Delta(\rho w) - w\Delta\rho}{\rho} \tag{40}$$

$$\Delta\chi = \frac{\Delta(\rho\chi/M) - \chi\Delta\rho/M}{\rho/M} \tag{41}$$

$$\Delta\left(\frac{1}{M}\right) = \frac{\Delta(\rho/M) - 1/M\Delta/M}{\rho} \tag{42}$$

For the pressure equation, we must take extra care, as in a multicomponent flow the ratio of specific heats can vary across an interface. Adapting a methodology utilized in Drikakis and Tsangaris [22] for an arbitrary equation of state, the pressure difference is expressed as

$$\Delta p = p_\epsilon \Delta\epsilon + p_\rho \Delta\rho + p_\chi \Delta\chi \tag{43}$$

From Eq. (6) the difference in internal energy i can be written as

$$\rho\Delta\epsilon = \Delta e - [u\Delta(\rho u) + v\Delta(\rho v) + w\Delta(\rho w)] - \epsilon\Delta\rho \tag{44}$$

Substituting Eq. (44) into Eq. (43),

$$\begin{aligned}\Delta p = Q\Delta\rho &+ \frac{p_\epsilon}{\rho}[\Delta e - (u\Delta(\rho u) + v\Delta(\rho v) + w\Delta(\rho w))] \\ &+ \frac{p_\chi}{\rho}(\Delta(\rho\chi) - \chi\Delta\rho)\end{aligned} \tag{45}$$

$$Q = p_\rho + 0.5q^2\frac{p_\epsilon}{\rho} - \epsilon\frac{p_\epsilon}{\rho}$$

$$q = u^2 + v^2 + w^2$$

Next, these differences are substituted into Eqs. (25)–(31), and renaming

$$(\rho u) = l \quad (\rho v) = m \quad (\rho w) = n \quad (\rho\chi/M) = o \quad (\rho/M) = q \tag{46}$$

gives

$$\begin{aligned}(\tilde\rho - \rho_0)(Q - c^2) + \frac{p_\epsilon}{\rho}[(\tilde E - E_0) - (u(\tilde l - l_0) + v(\tilde m - m_0) + w(\tilde n \\ - n_0))] + \frac{p_\chi}{q}[(\tilde o - o_0) - \chi(\tilde q - q_0)] = 0\end{aligned} \tag{47}$$

$$-(\tilde\rho - \rho_0)v + (\tilde m - m_0) = 0 \tag{48}$$

$$-(\tilde\rho - \rho_0)w + (\tilde n - n_0) = 0 \tag{49}$$

$$(\tilde o - o_0) - \chi(\tilde\rho - \rho_0) = 0 \tag{50}$$

$$\begin{aligned}(\tilde\rho - \rho_1)(Q - c\lambda_0) + (\tilde l - l_1)\left(c - u\frac{p_\epsilon}{\rho}\right) - (\tilde m - m_1)v\frac{p_\epsilon}{\rho} - (\tilde n \\ - n_1)w\frac{p_\epsilon}{\rho} + (\tilde E - E_1)\frac{p_\epsilon}{\rho} + \frac{p_\chi}{q}[(\tilde o - o_1) - \chi(\tilde q - q_1)] = 0\end{aligned} \tag{51}$$

$$\begin{aligned}(\tilde\rho - \rho_2)(Q + c\lambda_0) - (\tilde l - l_2)\left(c + u\frac{p_\epsilon}{\rho}\right) - (\tilde m - m_2)v\frac{p_\epsilon}{\rho} - (\tilde n \\ - n_2)w\frac{p_\epsilon}{\rho} + (\tilde E - E_2)\frac{p_\epsilon}{\rho} + \frac{p_\chi}{q}[(\tilde o - o_2) - \chi(\tilde q - q_2)] = 0\end{aligned} \tag{52}$$

Repeating the technique by Courant and Hilbert [23], the above equations are multiplied by the coefficients a, b, c, d, f, g, and h (omitting e as a coefficient to avoid confusion with the total energy E).

$$\begin{aligned}\tilde\rho\bar\rho + \tilde l\bar l + \tilde m\bar m + \tilde n\bar n + \tilde E\bar E + \tilde o\bar o + \tilde q\bar q = \rho_0\bar\rho + l_0\bar l + m_0\bar m + n_0\bar n + o_0\bar o \\ + q_0\bar q + e_E\bar E + 2c^2(gR_1 + hR_2)\end{aligned} \tag{53}$$

where

$$\bar\rho = a(Q - c^2) - bv - cw + g(Q - c\lambda_0) + h(Q + c\lambda_0) - \frac{f}{M} \tag{54}$$

$$\bar l = g\left(c - u\frac{p_\epsilon}{\rho}\right) - h\left(c + u\frac{p_\epsilon}{\rho}\right) - au\frac{p_\epsilon}{\rho} \tag{55}$$

$$\bar m = -(a + g + h)v\frac{p_\epsilon}{\rho} + b \tag{56}$$

$$\bar n = -(a + g + h)w\frac{p_\epsilon}{\rho} + c \tag{57}$$

$$\bar E = \frac{p_\epsilon}{\rho}[a + g + h] \tag{58}$$

$$\bar o = d + \frac{p_\chi}{q}(a + g + h) \tag{59}$$

$$\bar q = f - \frac{\chi p_\chi}{q}(a + g + h) - d\chi \tag{60}$$

$$\begin{aligned}2c^2R_1 = (\rho_0 - \rho_1)(c\lambda_0 - Q) + (l_0 - l_1)\left(u\frac{p_\epsilon}{\rho} - c\right) + (m_0 - m_1)v\frac{p_\epsilon}{\rho} \\ + (n_0 - n_1)w\frac{p_\epsilon}{\rho} - (E_0 - E_1)\frac{p_\epsilon}{\rho} - \frac{p_\chi}{q}[(o_0 - o_1) - \chi(q_0 - q_1)]\end{aligned} \tag{61}$$

$$\begin{aligned}2c^2R_2 = -(\rho_0 - \rho_2)(Q + c\lambda_0) + (l_0 - l_2)\left(u\frac{p_\epsilon}{\rho} + c\right) + (m_0 - m_2)v\frac{p_\epsilon}{\rho} \\ + (n_0 - n_2)w\frac{p_\epsilon}{\rho} - (E_0 - E_2)\frac{p_\epsilon}{\rho} - \frac{p_\chi}{q}[(o_0 - o_2) - \chi(q_0 - q_2)]\end{aligned} \tag{62}$$

This system of equations must be inverted to solve for g and h. First combining Eqs. (55) and (58),

Downloaded 03 Jun 2010 to 171.66.16.156. Redistribution subject to ASME license or copyright; see http://www.asme.org/terms/Terms_Use.cfm

$$f - g = \frac{\bar{l} + \lambda_0 \bar{E}}{c} \tag{63}$$

Next add Eqs. (54) and (55) multiplied by u, Eq. (56) multiplied by v, Eq. (57) multiplied by w, Eq. (59) multiplied by χ/M, and Eq. (60) multiplied by $1/M$,

$$g + h = \frac{\bar{\rho} + \bar{l}u + \bar{m}v + \bar{n}w + \bar{E}H + \bar{o}\chi/M + \bar{q}/M}{c^2}$$

$$H = \frac{q^2}{2} + \epsilon + \frac{p}{\rho} \tag{64}$$

$$c^2 = p\frac{p_\epsilon}{\rho^2} + p_\rho$$

Now, g and h can be obtained by subtraction and addition of Eqs. (63) and (64),

$$g = \frac{1}{2\tilde{c}^2}\left[\bar{\rho} + \bar{l}(u + c) + \bar{m}v + \bar{n}w + \bar{E}(H + c\lambda_0) + \bar{o}\frac{\chi}{M} + \frac{\bar{q}}{M}\right] \tag{65}$$

$$h = \frac{1}{2\tilde{c}^2}\left[\bar{\rho} + \bar{l}(u - c) + \bar{m}v - + \bar{n}w + \bar{E}(H - c\lambda_0) + \bar{o}\frac{\chi}{M} + \frac{\bar{q}}{M}\right] \tag{66}$$

Setting $\bar{\rho}=1$, $\bar{l}=\bar{m}=\bar{n}=\bar{e}=\bar{o}=\bar{q}=0$ an expression for the characteristic solution for $\tilde{\rho}$ can be obtained. The other characteristic interface values are given by repeating the same process. After simplification of the resulting expressions, the characteristic-based conservative variables, which can then be used to calculate the intercell flux following Godunov's method, are

$$\tilde{\rho} = \rho_0 + \bar{\rho} + r_1 + r_2 \tag{67}$$

$$\tilde{l} = l_0 + (u + c)r_1 + (u - c)r_2 + u\bar{\rho} \tag{68}$$

$$\tilde{m} = m_0 + v(r_1 + r_2 + \bar{\rho}) \tag{69}$$

$$\tilde{n} = n_0 + w(r_1 + r_2 + \bar{\rho}) \tag{70}$$

$$\tilde{E} = E_0 + (H + c\lambda_0)r_1 + (H - c\lambda_0)r_2 + H\bar{\rho} \tag{71}$$

$$\tilde{o} = o_0 + \frac{\chi}{M}(\bar{\rho} + r_1 + r_2) \tag{72}$$

$$\tilde{q} = q_0 + \frac{1}{M}(\bar{\rho} + r_1 + r_2) \tag{73}$$

$$\bar{\rho} = \frac{1}{c^2}\left[\frac{p_\epsilon}{\rho}(\bar{E} - E_0) + \frac{p_\chi}{q}(\chi q_0 - o_0) - \rho_0 Q\right] \tag{74}$$

$$\bar{E} = l_0 u + m_0 v + n_0 w \tag{75}$$

$$r_1 = \frac{1}{2c^2}\left\{\rho_1(Q - c\lambda_0) + l_1\left(c - u\frac{p_\epsilon}{\rho}\right) - m_1 v\frac{p_\epsilon}{\rho} - n_1 w\frac{p_\epsilon}{\rho} + E_1\frac{p_\epsilon}{\rho} - \frac{p_\chi}{q}(\chi q_1 - o_1)\right\} \tag{76}$$

$$r_2 = \frac{1}{2c^2}\left\{\rho_2(Q + c\lambda_0) - l_2\left(c + u\frac{p_\epsilon}{\rho}\right) - m_2 v\frac{p_\epsilon}{\rho} - n_2 w\frac{p_\epsilon}{\rho} + E_2\frac{p_\epsilon}{\rho} - \frac{p_\chi}{q}(\chi q_2 - o_2)\right\} \tag{77}$$

2.3 Extension to Higher-Order Accuracy. Higher order accuracy is achieved through van Leer's MUSCL limiting technique [24], where the left and right extrapolated states are defined as

$$\mathbf{U}^L_{i+1/2} = \mathbf{U}_i + \frac{1}{2}\phi(r^L)(\mathbf{U}_i - \mathbf{U}_{i-1}) \tag{78}$$

$$\mathbf{U}^R_{i+1/2} = \mathbf{U}_{i+1} - \frac{1}{2}\phi(r^R)(\mathbf{U}_{i+2} - \mathbf{U}_{i+1}) \tag{79}$$

where $\mathbf{U}$ is the vector of cell averaged primitive variables and

$$r^L_i = \frac{\mathbf{U}_{i+1} - \mathbf{U}_i}{\mathbf{U}_i - \mathbf{U}_{i-1}} \tag{80}$$

$$r^R_i = \frac{\mathbf{U}_{i+1} - \mathbf{U}_i}{\mathbf{U}_{i+2} - \mathbf{U}_{i+1}} \tag{81}$$

Within this paper, the second-order van Leer and a fifth-order M5 limiter [25] are used,

$$\phi_{VL} = \frac{2r}{1 + r} \tag{82}$$

$$\phi_{M5,L} = \frac{-2/r^L_{i-1} + 11 + 24r^L_i - 3r^L_i r^L_{i+1}}{30} \tag{83}$$

$$\phi_{M5,R} = \frac{-2/r^R_{i+2} + 11 + 24r^R_{i+1} - 3r^R_{i+1} r^R_i}{30} \tag{84}$$

where monotonicity is maintained by limiting the above extrapolations using

$$\phi_L = \max(0, \min(2, 2r^L_i, \phi_L)) \tag{85}$$

$$\phi_R = \max(0, \min(2, 2r^R_i, \phi_R)) \tag{86}$$

This limiter is fifth-order accurate in a one-dimensional sense and is strictly only second-order accurate in more than one dimension (as is true for all higher-order methods with one-dimensional stencils). As a guide to computational performance, employing the fifth-order limiter increased the total computational time by 18% compared to the van Leer limiter in this study.

2.4 Implicit Model. As discussed in the Introduction, each numerical method can be seen as a deconvolution of the top hat filter so an order of accuracy given by the numerical scheme. This is true for schemes above second-order of accuracy, as this is the lowest order at which such terms appear. Hence, for the fifth-order scheme, the Taylor series expansion of the truncation terms matches up to fifth order the expansion of the finite scale Euler equations as derived by Margolin et al. [16]. However, as the stencils are one dimensional then there are terms in the cross-stream direction, which are not taken into account (of second order and above). Margolin et al. [16] state that in numerical experiments these cross terms appear not to contribute greatly to the numerical subgrid model.

The prior discussion applies to modes, which can be resolved on the grid, those which are below the Nyquist frequency for the given mesh. Subgrid modes are modeled via the leading order truncation error. The finite volume fluxes for the Godunov method can be written in the following format [26]:

$$\mathbf{F}_{i+1/2} = \frac{1}{2}(\mathbf{F}_L + \mathbf{F}_R) - \frac{1}{2}|\mathbf{A}|(\mathbf{U}_R - \mathbf{U}_L) \tag{87}$$

$$|\mathbf{A}| = \mathbf{K}|\Lambda|\mathbf{K}^{-1} \tag{88}$$

where the subscripts R and L indicate the right and left sides of the interface, respectively. Note that $|\mathbf{A}|$ is not the same as the absolute of the Jacobian matrix $\mathbf{A}$. In the numerical method described above, the flux Jacobian $|\mathbf{A}|$ is computed from the average of the

Downloaded 03 Jun 2010 to 171.66.16.156. Redistribution subject to ASME license or copyright; see http://www.asme.org/terms/Terms_Use.cfm

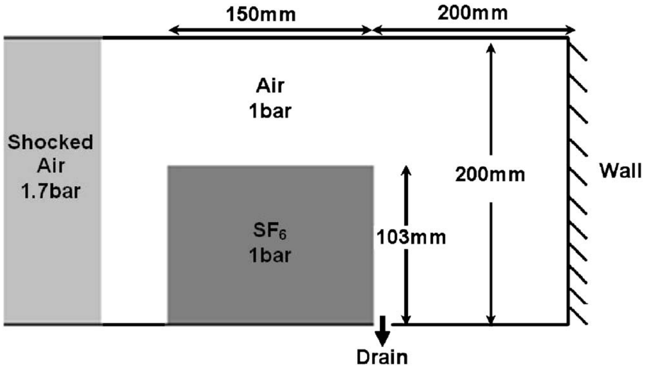

Fig. 1 Schematic of the half-height experiment; note that the shock tube is 100 mm deep

conserved variables in the left- and right-hand cells. Including this in the derivation of the modified equation gives the leading order effective subgrid model for both limiting methods as

$$\tau_{vl} = \frac{\Delta x^2}{12}\frac{\partial}{\partial x}(2M^2 u u_{xx} + p_{xx}) + M^2\frac{\Delta y^2}{12}\frac{\partial}{\partial y}(u v_{yy} + u_{yy} v) \quad (89)$$

$$\tau_{M5} = \frac{\Delta x^5}{60}[|\mathbf{A}_x|\mathbf{U}_{xxxxx} + |\mathbf{A}|\mathbf{U}_{xxxxxx}] \quad (90)$$

If it is assumed that the subgrid model should be of order Δx^2 [16], then only the van Leer method satisfies that criteria. The leading order dissipation is from the second-order accuracy of the projection when computing the average of the left- and right-hand fluxes. The M5 limiter provides dissipation at a rate proportional to Δx^5. In this case, the leading order dissipation is from the difference of the primitive variables, in the form of dissipative terms multiplied by the flux Jacobian, and dispersive terms multiplied by the derivative of the flux Jacobian at leading order.

Examining the wave number where the flux due to the finite volume method is less than 90% of the equivalent spectral flux shows that the fifth-order scheme increases the range of resolved wave numbers by 50% over the van Leer scheme [27]. This means that higher resolution modes are captured more accurately, along with their interactions with low wave number modes.

In summary, although better accuracy should be gained via the fifth-order method as it is inverting the grid filter to a higher order, the van Leer limiter could give better results as its dissipative behavior is closer to that physically expected.

3 Half-Height Experiment

3.1 Experimental Setup and Diagnostics. Figure 1 shows a schematic of the half-height experiment (see Ref. [1] for the full details). The shock tube contains air at atmospheric pressure and temperature. When the diaphragm is burst, a shock of $M=1.26$ propagates from left to right. At $x=0$, there is a "block" of SF_6, which is 5.5 times denser than air, and has $\gamma=1.076$, which is initially held in place by microfilm membrane. The speed of sound is approximately three times slower in SF_6 than in air, thus inducing a strong Kelvin–Helmholtz instability on the upper surface of the block and rapid transition to turbulence. In addition to this, there is growth of Richtmyer-Meshkov type instabilities on the vertical interfaces. The shock wave reflects off the wall at the right side of the domain and passes back through the mixing region, injecting further energy into the turbulent mixing zone. The output from the experiment was a series of images taken at specific times using a pulsed laser sheet. The SF_6 block was initially seeded with olive oil droplets; hence the intensity of the image represents the density of the SF_6 at a specific location.

3.2 Grid and Initialization. The coordinate system chosen has the x direction aligned with the initial direction of shock propagation, z in the vertical direction, and y in the homogeneous direction. The point (0,0,0) is located at the bottom left-hand interface between the SF_6 block and air.The numerical domain chosen extends from -0.45 m to 0.35 m in x and takes the shock tube dimensions in the other two directions. This is longer than the test section shown in Fig. 1 as it is necessary to track the shock front reflected off the left face of the block of SF_6. The boundary conditions are taken as reflective (inviscid wall boundary condition) on the upper-, lower-, and right-hand walls, and an extended one-dimensional domain on the left-hand interface in the x direction. The y-direction boundary conditions are periodic.

There is special treatment required for the drain hole, which is modeled as an extended one-dimensional domain. The incident shock wave can then diffract down the drain hole, entraining material in a similar manner to that seen in the experiment. At late times, this holes acts as a nozzle where high speed air/SF_6 mixture exits the shock tube. The addition of the drain hole was demonstrated as being necessary in earlier studies [10,28]. The extended one-dimensional domain is initialized as air at atmospheric pressure and density. The drain hole is located between $0.153 \text{ m} < x < 0.16$ m and $0.05 \text{ m} < y < 0.95$ m.

The block of SF_6 is initially held in place with a microfilm membrane, which is destroyed by the incident shock wave. However, this membrance imparts a perturbation onto the interface between the two gases, which must be modeled, as this perturbation is the seed that triggers growth of the instabilities. Numerically, this perturbation is modeled as a summation of random modes with rms amplitude of 0.1 mm at wavelengths between 5 mm and 50 mm satisfying a power spectra proportional to the wave number of the mode. The upper interface is not held in place by a membrane and so in the experiment it is likely that this would be a diffuse interface; however it is modeled as a sharp interface numerically.

To facilitate comparison of the two numerical methods, simulations were run at two different grid resolutions for each method. The coarse grid was $300\times80\times160$, and the fine grid $600\times160\times320$. An additional grid of $750\times200\times400$ (double the number of mesh points in the fine grid) was run with fifth-order limiting to test convergence of plane averaged statistics. Finally, the densities, of SF_6 and air were 6.34 kg/m^3 and 1.153 kg/m^3, and the ratios of specific heats γ were 1.076 and 1.4, respectively.

3.3 Comparison With Experiment. Figure 2 compares the experimental images with plane slices of SF_6 density taken from computational results. The vertical reference line on the experimental images is at $x=0.15$ m. For the first two time steps, there is very little difference between the experimental and numerical images. There is slightly more roll-up of the primary vortex (developing at the upper left corner of the block) in the fifth-order method as compared to the second-order method. At 0.37 ms, the shock wave is about a third of the way through the SF_6 block and has formed a Mach intersection. This links the plane shock transmitted through the SF_6 block with the shock, which is propagating more rapidly through the air over the top of the block.

At 1 ms, the intersecting shock waves have converged at the lower right-hand side of the block of SF_6, and reflect off the lower wall creating a region of very high pressure and density. The strong reflected shock induces a rapid postshock velocity generating the bulge in the right interface of the block. Some differences between the numerical methods and the experiment can be seen. Initial instabilities in the primary vortex can be seen in both the experiment and the fifth-order method, which takes on an oval shape. This is not seen in the second-order method as the initial perturbations have been damped more heavily. However, there are signs of small Kelvin–Helmholtz instabilities on the upper interface of the SF_6 block in the fifth-order simulation, which are not seen in the experiments. This is because in the experiments the upper interface was initially diffuse, which tends to inhibit the

Downloaded 03 Jun 2010 to 171.66.16.156. Redistribution subject to ASME license or copyright; see http://www.asme.org/terms/Terms_Use.cfm

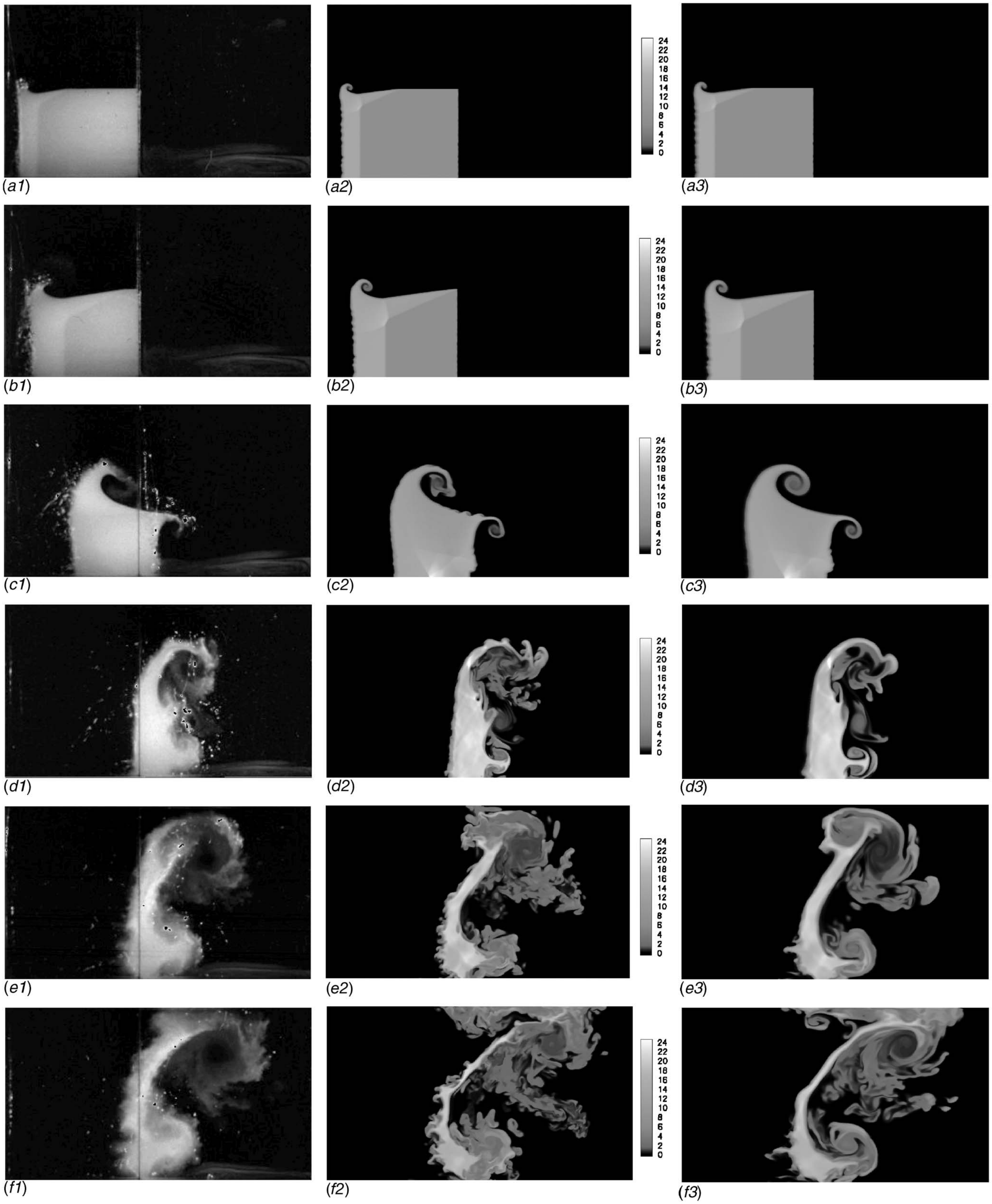

Fig. 2 Comparison of experimental images (left, © British Crown Copyright 2006/MOD) and SF_6 density (kg/m^3) for fifth order (center) and second order (right) using the grid of cross section of 600×160×320

growth of such instabilities. An example of this behavior can be seen by comparing simulations at high resolution with a sharp interfaces by Shi et al. [29], which show Kelvin–Helmholtz instabilities along the interface compared with simulations by Latini et al. [30] with a diffuse initial interface, which suppresses these features. The innate diffusivity within the second-order method also acts to suppress these features.

The shock reflects off the end of the shock wave and passes

Downloaded 03 Jun 2010 to 171.66.16.156. Redistribution subject to ASME license or copyright; see http://www.asme.org/terms/Terms_Use.cfm

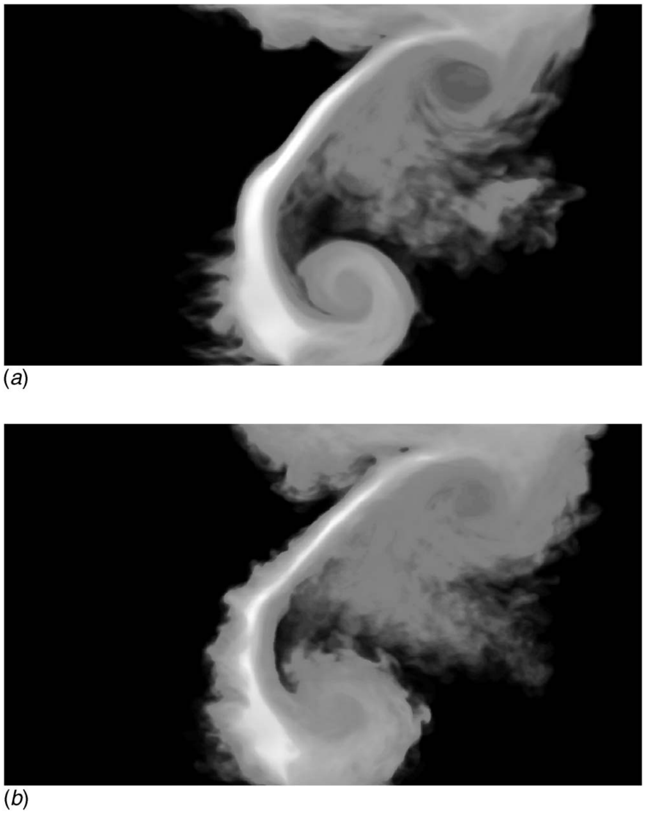

Fig. 3 Line average SF_6 density at 4 ms

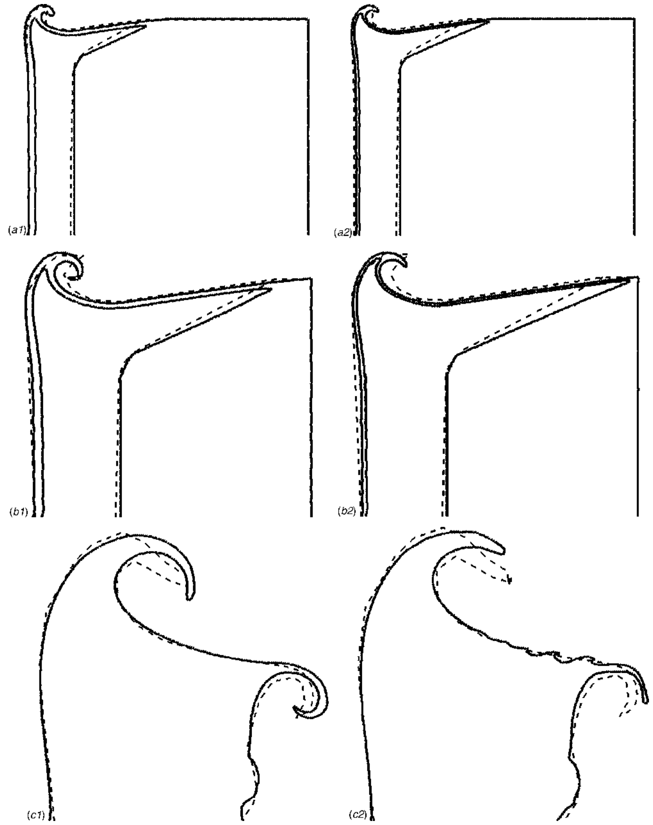

Fig. 4 Comparison of experimental shock and SF_6 positions (dashed line) and numerical results (solid line) for second order (left) and fifth order (right) using the grid of cross section of 160×320

through the developing mixing layer. By 2 ms, the shock wave has passed through the "bulge" visible on the right-hand interface at 1 ms producing a single mode "mushroom" shaped vortex. At the same time, the primary vortex has become unstable and a well mixed region is developing in the vortex core. The size and location of the main flow features are almost identical in comparing experiments and simulation; however, there is clearly more fine scale detail in the fifth-order simulation. At 3 ms, the mixing continues to evolve, with additional mixing in the thin strip of material linking the mushroom shaped feature with the primary vortex. This mixing is at a small scale relative to the grid resolution so it is not resolved at second-order accuracy; however, at fifth-order some instability can be seen.

The final images again agree very well; however, there is a region of mixed fluid traveling along the top of the shock tube in the simulation, which appears not to be present in the experiment. It is believed that this is due to the poor resolution of the experimental images as the laser sheet approaches the wall. An additional point to note is that the experimental images appear more diffuse as they do not represent a plain slice through the flow field. Although the laser sheet is extremely thin, the reflected light is subsequently scattered through additional interactions with oil droplets before reaching the imaging device. Figure 3 shows line-averaged SF_6 density, which appears more diffuse as in the experimental images. Also, it is clear that the fifth-order method captures the small scale mixing at the thin strip much better than the second-order method.

Measurements of the position of the SF_6 block and shock wave at early times have been taken. A comparison of experiment and the two numerical methods can be seen in Fig. 4. The position of the block and the shock wave was identified using contours of 0.5 and 1.5 times the initial density of SF_6. There is a slight discrepancy in position of the diffracted shock in both numerical simulations. This is due to the initial diffuse interface in the experiment, which would lead to a larger vertical distance between the shock traveling in pure air and the shock traveling in pure SF_6.

Comparing the numerical methods, it is clear that the material interface is captured significantly more sharply in the fifth-order method than in the second-order method. Also, this validates the choice of governing equations as the shock wave is captured without oscillation, and the position of the material interfaces is captured well in comparison with the experiment.

Figure 5 shows volume fraction isosurfaces at 4 ms, illustrating the highly turbulent nature of the flow, and also the presence of fine scale features in the fifth-order simulation, which are not present at second order.

3.4 Turbulent Mixing and Kinetic Energy. As a means to compare and contrast the numerical methods, the turbulent kinetic energies and plane averaged mixing quantities have been computed for two different grid resolutions for each method. Figure 6 presents plane averaged mixing $\langle f_1\rangle\langle f_2\rangle$, and Fig. 7 the quantity $\langle f_1 f_2\rangle$, which is a measure of the amount of molecular mixing in the primary vortex. f_1 is the volume fraction of air and f_2 that of SF_6.

There is excellent agreement at all grid resolutions and between the two numerical methods for the location and magnitude of the peaks of plane averaged mixing and molecular mixing. Slight differences appear at around $x=0.16$ m in the plot of plane averaged mixing, which is due to enhanced mixing at the right-hand side of the thin strip of dense material. This is visible in Fig. 3, and also

Downloaded 03 Jun 2010 to 171.66.16.156. Redistribution subject to ASME license or copyright; see http://www.asme.org/terms/Terms_Use.cfm

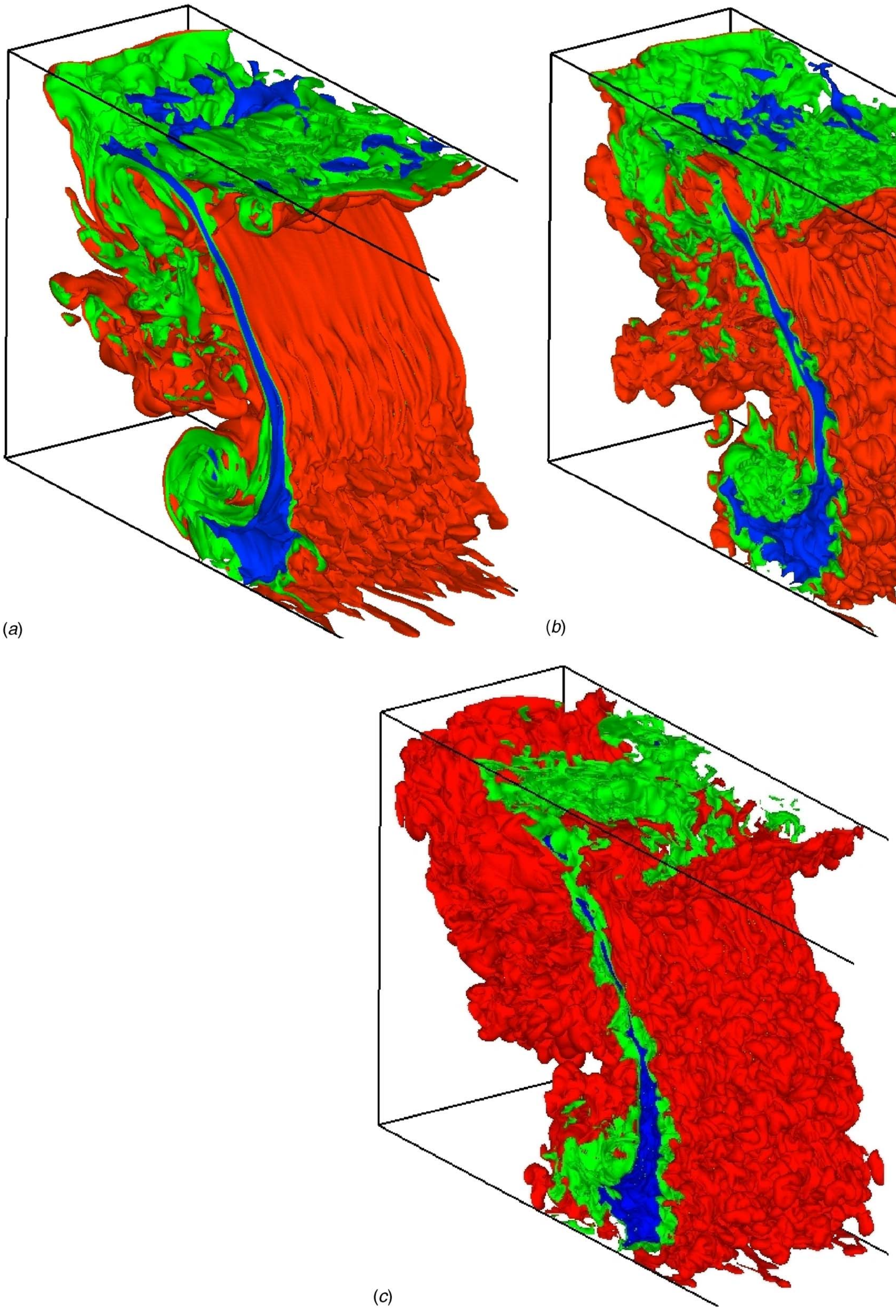

(*a*)

(*b*)

(*c*)

Fig. 5 Isosurfaces of 1%, 50%, and 99% volume fraction of air

appears in the level of molecular mixing in Fig. 7, where molecular mixing is at a local minimum in the second-order method. There is a slight "bump" at $x=0.29$ m in the coarse resolution fifth-order simulation caused by the advection of a small region of dense fluid over the top of the primary vortex, which does not occur in the finer resolution simulations, and is diffused in the coarse grid simulation at second order.

The turbulent kinetic energy per meter is defined as

Downloaded 03 Jun 2010 to 171.66.16.156. Redistribution subject to ASME license or copyright; see http://www.asme.org/terms/Terms_Use.cfm

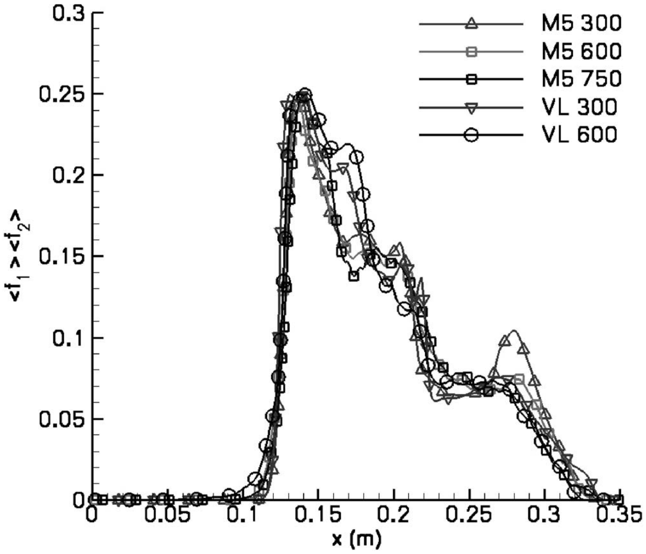

Fig. 6 Comparison of $\langle f_1\rangle\langle f_2\rangle$ at 4 ms

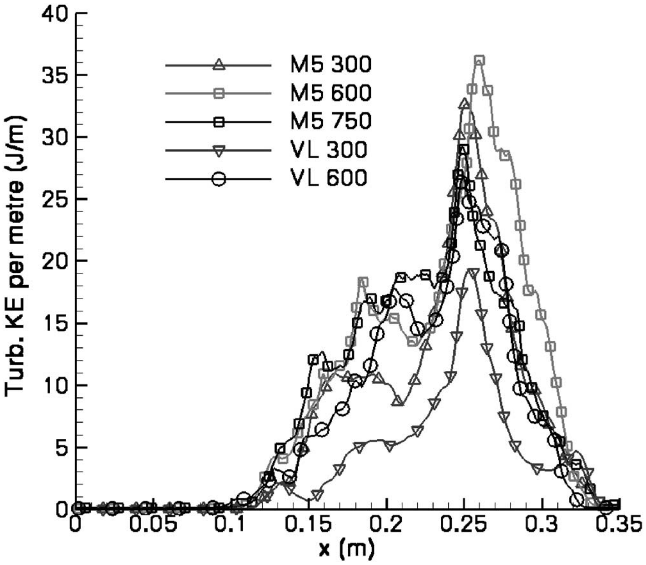

Fig. 8 Comparison of turbulent kinetic energy per meter at 4 ms

$$\mathrm{KE} = \frac{1}{2}\int \rho K dy dz \tag{91}$$

$$K = (u - \tilde{u})^2 + v^2 + (w - \tilde{w})^2 \tag{92}$$

where the tilde quantities are Favre mass-weighted mean velocities in the homogeneous direction

$$\tilde{u} = \frac{\overline{\rho u}}{\bar{\rho}} \qquad \tilde{w} = \frac{\overline{\rho w}}{\bar{\rho}} \tag{93}$$

and $(\bar{\cdot})$ indicates a line averaged quantity in the periodic y direction. This is plotted in Fig. 8 for t=4 ms. There are two peaks in the line averaged kinetic energy corresponding to the location of the mushroom-shaped perturbation and the large primary vortex. There is a fairly large difference in resolved kinetic energy primarily due to the difference in grid scale. However, the fifth-order method gives higher peak plane averaged turbulent kinetic energy at a mesh resolution of $300\times 80\times 160$ than the second-order method at $600\times 160\times 320$. This indicates that the fifth-order method is far superior in terms of resolutions, especially considering that the fifth-order method is only 18% slower in terms of total run time. The location of maximum kinetic energy is at x =0.26 m, and matches to within 5 mm for all grid resolutions.

Finally, the evolution of total resolved turbulent kinetic energy (TKE) as a function of time is shown in Fig. 9. The initially small perturbations on the gas interfaces grow with time due to the combined action of Richtmyer–Meshkov and Kelvin–Helmholtz instabilities. This means that the kinetic energy increase begins earlier in the schemes, which resolve the smaller perturbations, as is illustrated in Fig. 9. As the turbulent perturbations become larger, then kinetic energy is resolved on the coarser grids. However, the injection of energy is in the form of an impulse as the incident shock and reshock pass through the mixing zone. Once the shock has left the domain, the TKE in the smallest scales resolved on the finest grid at fifth-order accuracy begins to dissipate. This does not occur using the other methods or grid sizes as they do not resolve these small vortices. Indeed, at the coarsest

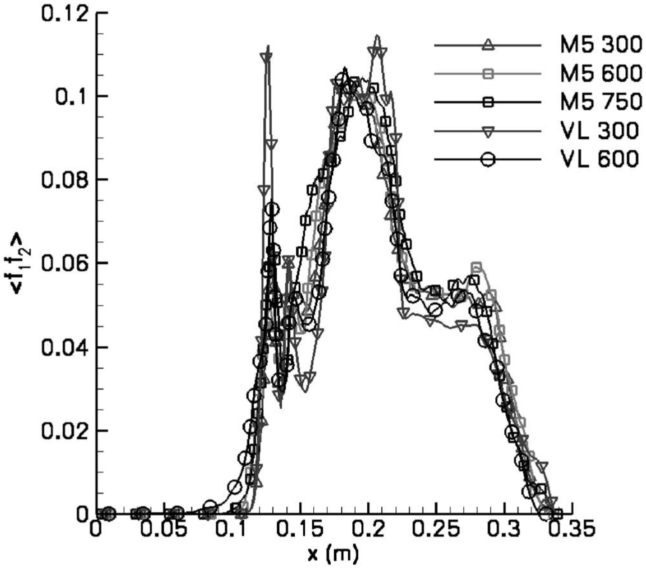

Fig. 7 Comparison of $\langle f_1 f_2\rangle$ at 4 ms

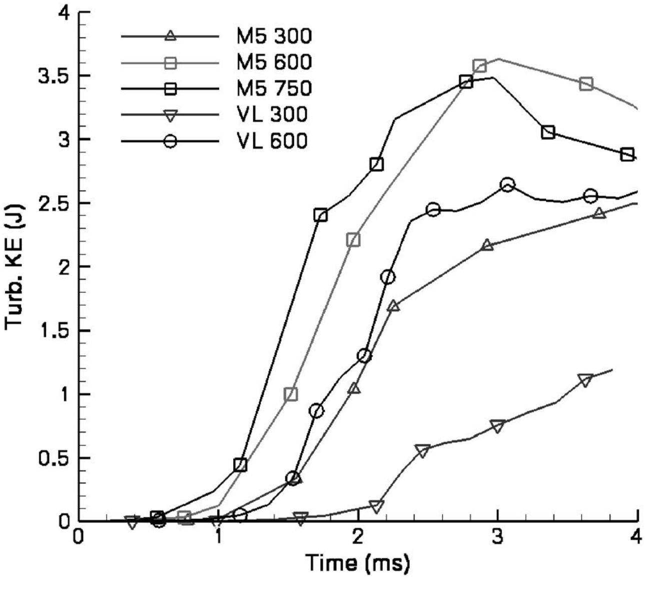

Fig. 9 Comparison of total resolved turbulent kinetic energy variation with time, where time is measured from the passage of the shock through the first interface

Downloaded 03 Jun 2010 to 171.66.16.156. Redistribution subject to ASME license or copyright; see http://www.asme.org/terms/Terms_Use.cfm

resolution with the second-order method, the TKE continues to grow up to the end of the simulation. An important point to note is that the variation and magnitude of the resolved TKE using the fifth-order limiter at the coarse resolution agree very well with that captured by the second-order method on a grid twice the size in each direction. It should be noted that these results are also in excellent agreement with results presented using a semi-Lagrangian code in Ref. [10].

4 Conclusions

This paper has presented a new characteristics-based approximate Riemann solver for the fully coupled solution of the Euler equations plus two additional multicomponent equations. This has been implemented in a finite volume Godunov method in conjunction with both second-order and fifth-order MUSCL-based limiting.

The two limiting methods have been used to simulate a complex three-dimensional compressible shock tube mixing experiment using air and SF_6 on a coarse and fine grid. There is an excellent match in qualitative comparison with experimental results, including the location and magnitude of the main flow features. The shock positions are captured accurately without oscillation demonstrating the effectiveness of the multicomponent model and the new characteristic-based approximate Riemann solver. In comparing the two limiting methods, it is demonstrated that the fifth-order methods provide superior resolution of small scale perturbations in relation to the second-order method; however it is also more sensitive to approximations in the initial conditions. Typically, the fifth-order method obtains almost the same results as the second-order method at half the grid resolution in each direction. This includes key parameters such as resolved turbulent kinetic energy and averaged mixing parameters. As the total computational time is only 20% greater for the fifth-order method, it is clearly more effective computationally. It is a strong indication that with the current maximum allowable grid sizes, it is more important to invert the finite volume filter to a higher order of accuracy than have a truncation error proportional to Δx^2.

Future work is focused on the behavior of the dissipation of kinetic energy in finite volume schemes at low Mach, with emphasis on improving the resolution of the growth of small instabilities in simulations of compressible transitional flows.

Acknowledgment

The authors would like to acknowledge financial support through an EPSRC-AWE PhD CASE award and an EPSRC-MoD (Dstl, AWE) research grant (EP/C515153 and JGS 971). They would also like to acknowledge stimulating discussions with David Youngs, Robin Williams, Anthony Weatherhead at AWE, and Evgeniy Shapiro at Cranfield University.

The computations for this paper were carried out on the Cranfield-Cambridge High Performance Computing Facility.

References

[1] Holder, D., and Barton, C., 2004, "Shock Tube Richtmyer–Meshkov Experiments: Inverse Chevron and Half Height," *Proceedings of the Ninth IWPCTM*.
[2] Meshkov, E., 1969, "Instability of the Interface of Two Gases Accelerated by a Shock Wave," Fluid Dyn., **43**(5), pp. 101–104.
[3] Richtmyer, R., 1960, "Taylor Instability in Shock Acceleration of Compressible Fluids," Commun. Pure Appl. Math., **13**, pp. 297–319.
[4] Sagaut, P., 2001, *Large Eddy Simulation for Incompressible Flows*, Springer, New York.
[5] Lesieur, M., and Metais, O., 1996, "New Trends in Large-Eddy Simulations of Turbulence," Annu. Rev. Fluid Mech., **28**, pp. 45–82.
[6] Pope, S., 2000, *Turbulent Flows*, Cambridge University Press, Cambridge.
[7] Drikakis, D., 2003, "Advances in Turbulent Flow Computations Using High-Resolution Methods," Prog. Aerosp. Sci., **39**, pp. 405–424.
[8] Youngs, D., 1994, "Numerical Simulation of Mixing by Rayleigh–Taylor and Richtmyer–Meshkov Instabilities," Laser Part. Beams, **12**, pp. 725–750.
[9] Youngs, D., 1991, "Three-Dimensional Numerical Simulation of Turbulent Mixing by Rayleigh–Taylor Instability," Phys. Fluids A, **3**(5), pp. 1312–1320.
[10] Thornber, B., Drikakis, D., and Youngs, D., 2007, "Large-Eddy Simulation of Multi-Component Compressible Turbulent Flows Using High Resolution Methods," Comput. Fluids, doi: 10.1016/j.compfluid.2007.04.009
[11] Grinstein, F., and Fureby, C., 2002, "Recent Progress on Miles for High Reynolds Number Flows," ASME Trans. J. Fluids Eng., **848**, pp. 848–861.
[12] Hahn, M., and Drikakis, D., 2005, "Large Eddy Simulation of Compressible Turbulence Using High-Resolution Method," Int. J. Numer. Methods Fluids, **49**, pp. 971–977.
[13] Margolin, L., Smolarkiewicz, P., and Sorbjan, Z., 1999, "Large-Eddy Simulations of Convective Boundary Layers Using Nonoscillatory Differencing," Physica D, **133**, pp. 390–397.
[14] Porter, D., Woodward, P., and Pouquet, A., 1998, "Inertial Range Structures in Decaying Compressible Turbulent Flows," Phys. Fluids, **10**(1), pp. 237–245.
[15] Fureby, C., and Grinstein, F., 2002, "Large Eddy Simulation of High-Reynolds-Number Free and Wall-Bounded Flows," J. Comput. Phys., **181**, pp. 68–97.
[16] Margolin, L., Rider, W., and Grinstein, F., 2006, "Modeling Turbulent Flow With Implicit Les," J. Turbul., **7**(15), pp. 1–27.
[17] Wang, S., Anderson, M., Oakley, J., Corradini, R., and Bonazza, M. L., 2004, "A Thermodynamically Consistent and Fully Conservative Treatment of Contact Discontinuities for Compressible Multi-Component Flows," J. Comput. Phys., **195**, pp. 528–559.
[18] Godunov, S., 1959, "A Finite-Difference Method for the Computation of Discontinuous Solutions of the Equations of Fluid Dynamics," Mat. Sb., **47**, pp. 271–295.
[19] Spiteri, R., and Ruuth, S., 2002, "A Class of Optimal High-Order Strong-Stability Preserving Time Discretization Methods," SIAM J. Sci. Comput. (USA), **40**(2), pp. 469–491.
[20] Drikakis, D., and Rider, W., 2004, *High-Resolution Methods for Incompressible and Low-Speed Flows*, Springer, New York.
[21] Eberle, A., 1987, "Characteristic Flux Averaging Approach to the Solution of Euler's Equations," Tech. rep., VKI Lecture Series.
[22] Drikakis, D., and Tsangaris, S., 1991, "An Implicit Characteristic-Flux-Averaging Method for the Euler Equations for Real Gases," Int. J. Numer. Methods Fluids, **12**, pp. 711–726.
[23] Courant, R., and Hilbert, D., 1968, *Methoden der mathematischen Physik*, Springer, New York.
[24] van Leer, B., 1977, "Towards the Ultimate Conservative Difference Scheme. IV. A New Approach to Numerical Convection," J. Comput. Phys., **23**, pp. 276–299.
[25] Kim, K., and Kim, C., 2005, "Accurate, Efficient and Monotonic Numerical Methods for Multi-Dimensional Compressible Flows Part II: Multi-Dimensional Limiting Process," J. Comput. Phys., **208**, pp. 570–615.
[26] Toro, E., 1997, *Riemann Solvers and Numerical Methods for Fluid Dynamics*, Springer-Verlag, Berlin.
[27] Thornber, B., Mosedale, A., and Drikakis, D., 2007, "On the Implicit Large Eddy Simulation of Homogeneous Decaying Turbulence," J. Comput. Phys., **226**, pp. 1902–1929.
[28] Bates, K., Nikiforakis, N., and Holder, D., 2007, "Richtmyer–Meshkov Instability Induced by the Interaction of a Shock Wave With a Block of SF_6," Phys. Fluids, **19**, p. 036101.
[29] Shi, J., Zhang, Y.-T., and Shu, C.-W., 2003, "Resolution of High Order Weno Schemes for Complicated Flow Structures," J. Comput. Phys., **186**, pp. 690–696.
[30] Latini, M., Schilling, O., and Don, W., 2007, "Effects of Weno Flux Reconstruction Order and Spatial Resolutoin on Reshocked Two-Dimensional Richtmyer-Meshkov Instability," J. Comput. Phys., **221**, pp. 805–836.

Downloaded 03 Jun 2010 to 171.66.16.156. Redistribution subject to ASME license or copyright; see http://www.asme.org/terms/Terms_Use.cfm

ILES and LES of Complex Engineering Turbulent Flows

C. Fureby
Division of Weapons and Protection,
The Swedish Defense Research Agency-FOI,
Tumba, Stockholm SE 147 25, Sweden;
Department of Shipping and Marine Technology,
Chalmers University of Technology,
SE 412 96 Göteborg, Sweden

The present study concerns the application of large eddy simulation (LES) and implicit LES (ILES) to engineering flow problems. Such applications are often very complicated, involving both complex geometries and complex physics, such as turbulence, chemical reactions, phase changes, and compressibility. The aim of the study is to illustrate what problems occur when attempting to perform such engineering flow calculations using LES and ILES, and put these in relation to the issues originally motivating the calculations. The issues of subgrid modeling are discussed with particular emphasis on the complex physics that needs to be incorporated into the LES models. Results from representative calculations, involving incompressible flows around complex geometries, aerodynamic noise, compressible flows, combustion, and cavitation, are presented, discussed, and compared with experimental data whenever possible. [DOI: 10.1115/1.2801370]

Introduction and Background

A grand challenge for computational fluid dynamics (CFD) is the prediction of turbulent flows. In practice, such flows often include additional physics such as compressibility, phase changes, and chemical reactions. Applications include incompressible flows around different vehicles and in confined spaces, compressible flows around air- and spacecrafts, and reacting flows in engines. For such flows, it is not likely that we will ever have a deterministic and predictive framework based on CFD due to the inherent difficulty in modeling and validating all relevant processes and acquiring all the necessary boundary condition data. On the other hand, such applications are representative of fundamental problems for which whole-domain scalable laboratory studies are extremely difficult and for which it is crucial to develop predictability, as well as to establish effective approaches to postprocessing the large simulation database.

The modeling challenge is to develop models that, although not explicitly incorporating all scales, give accurate and reliable predictions for at least the large energy-containing scales. This requires the governing Navier–Stokes equations (NSEs) to be truncated in a way that the energy spectra is consistent with the $|\mathbf{k}|^{-5/3}$ law, with a smooth transition at the high-wave-number cutoff end. The models must be designed as to minimize the contamination of the resolved part of the energy spectrum and to modify the dissipation rate in regions where viscous effects are important. For flows of engineering interest, the Reynolds (Re) number is often high, placing the cutoff wave number in the lower part of the inertial subrange. This, together with the complication of walls and other physical processes, raises the demands for the modeling, incorporating also anisotropic features and multiphysics processes and considerations.

The computational challenge is to solve the model equations accurately, typically requiring a large number of time steps and grid cells. For flows in and around complex geometries, finite volume methods are technically superior to finite difference or element methods since they are based on the integral formulation of the equations and are therefore conservative by construction. However, for unstructured grids, efficient algorithms of higher spatial order than 2 are arduous to implement, and unless we follow that route we cannot expect to be able to discriminate fully between the leading order truncation error and the subgrid model. Alternatively, we may design the numerical algorithm, using the modified equations approach, to use the leading order truncation error as an implicit (or built-in) subgrid model. A further challenge is to design the computational grids to deal *sufficiently* accurately with the *relevant* flow features, such as those associated with geometrical details and with elements of relative motion.

Despite the steady advance in computing power and computational technology, attempts at direct numerical simulation (DNS) of the NSE have been limited to simple geometries and low Re [1]. The most widespread alternative to DNS is Reynolds averaged Navier–Stokes (RANS) models [2] based on a statistical treatment of the fluctuations about a stationary or slowly varying flow and turbulence models for the mean influence of the fluctuations on the mean flow [3]. The limitations of RANS were soon realized, and during the 1980s the concept of large eddy simulation (LES) was introduced [4–7]. In LES, all scales larger than the grid are resolved using a space-time accurate scheme, and only the effects of the small, unresolved eddy scales are to be modeled. The direct computation of the large energy-containing eddies (being geometry and flow dependent) gives LES more generality than RANS, but at a higher computational cost. For wall-bounded flows, however, LES ideally requires a progressively finer grid as the wall is approached (hereafter wall-resolved LES), rendering this approach too costly for practical flow problems [8]. In an attempt to develop less expensive but still accurate models, wall-modeled LES [9], in which a near-wall subgrid model, usually based on an assumed log law [10], or detached eddy simulations (DESs) [11], in which the boundary layer (populated with attached eddies) is modeled using steady-state RANS turbulence models, are used.

RANS, DES, LES, and implicit LES (ILES) [12,13] are compared in Fig. 1 for several challenging flows, such as fully developed turbulent channel flow [9,14,15], flow past a round cylinder at $\mathrm{Re}=3900$ and 140,000 [16–19], and flow around a surface mounted 3D hill at $\mathrm{Re}=130{,}000$ [20,21]. Here, OEEVM denotes the one equation eddy viscosity model, MM the mixed model, and WM the wall model. In summary, we find that the wall-modeled LES/ILES is more accurate than RANS and DES and that DES is too sensitive to the inflow conditions for the turbulent subgrid viscosity—with higher values resulting in RANS-like results and lower values resulting in LES-like results. In addition, we find that the influence of the LES subgrid model is rather small [19], whereas the importance of the turbulence model in RANS can be significant [19]. When other processes are involved or when the unsteadiness of the flow is deemed important, LES and ILES are necessary to avoid excessive and complicated tailor-made model-

---

Contributed by the Fluids Engineering Division of ASME for publication in the Journal of Fluids Engineering. Manuscript received February 8, 2007; final manuscript received June 1, 2007. Review conducted by Fernando Grinstein.

Copyright © 2007 by ASME

Downloaded 03 Jun 2010 to 171.66.16.156. Redistribution subject to ASME license or copyright; see http://www.asme.org/terms/Terms_Use.cfm

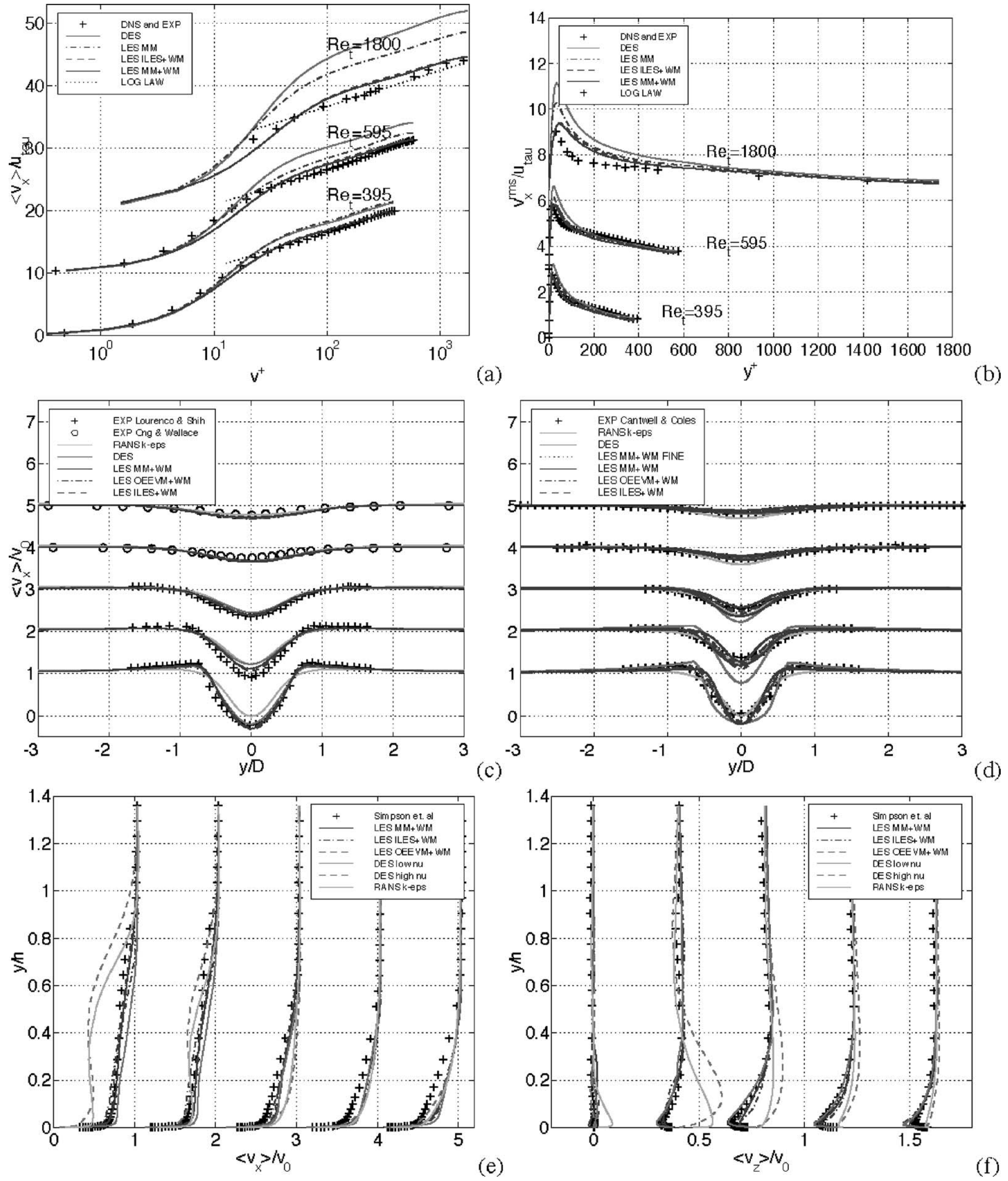

Fig. 1 Comparison between RANS, DES, and LES predictions for the flows past ((*a*) and (*b*)) fully developed turbulent channel flow, ((*b*) and (*c*)) circular cylinders at Re=3900 (left) and Re=140,000 (right), and ((*e*) and (*f*)) the flow over a surface mounted bump at Re=130,000

ing of the physically complicated coupling processes [22], usually resulting in rather poor predictions, for example, [23], and not often with very high case sensitivity.

The goal of this work is to discuss the use of LES and ILES for engineering flows, involving geometrical and physical complexity—the latter in terms of additional physics, such as compressibility and chemical kinetics. To the largest extent possible, we compare with reference data. The aim is to show that realistic engineering flow problems, in several areas of interest, can be examined using wall-modeled LES and ILES, resulting in improved predictions as compared to RANS and DES, in comparison with reference data, with manageable run times.

Incompressible Turbulent Flows

Incompressible flows, i.e., flows without appreciable density variations, are common in engineering problems and include low-speed aerodynamics and hydrodynamics. To illustrate the issues of complex geometry flows, we consider the flow past a submarine in model scale. Besides the conventional ship hydrodynamic design parameters, such as viscous and pressure drag, critical issues in submarine hydrodynamics include the unsteady flow over the stern and the rotating propeller, the flow noise from the propeller and appendage generated vortices and wakes, and the hull wake. This means that we need also to include the propeller in the simulations, which is a grand challenge for unsteady RANS, and a formidable challenge for LES and DES.

We here consider the DARPA AFF8 Suboff configuration [24–26] (Fig. 2) which consists of hull, sail, and stern appendages, with an overall length of $L=4.36$ m and a diameter of $D=0.51$ m. The sail is located on the cylindrical hull at the top dead center, having its leading edge at $x=0.92$ m and its trailing edge at $x=1.29$ m. A cap of elliptical cross section is attached to the sail at a height of $h=0.46$ m, and the stern appendages consist of four NACA 0020 profiles, defined with the trailing edge at $x=4.00$ m. Experimental data are provided by the David Taylor model basin at a Re number of $\mathrm{Re}=12\times10^6$. The computational domain con-

Downloaded 03 Jun 2010 to 171.66.16.156. Redistribution subject to ASME license or copyright; see http://www.asme.org/terms/Terms_Use.cfm

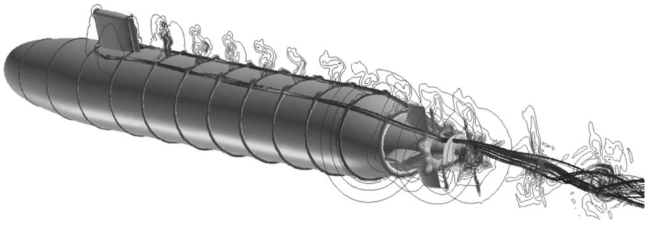

Fig. 2 Submarine hydrodynamics. Schematic of the DARPA AFF8 Suboff hull geometry, [24–26] and the instantaneous flow field for a self-propelled submarine model.

sists of the submarine hull mounted in a large cylinder, and the domain extends one hull length upstream and two hull lengths downstream of the model, being $4L$ in overall length and consists of about 7×10^6 cells. For the hull, an O-O topology is used, while for the sail and stern appendages C-O topologies are used, and care is taken to ensure that the grid is suitable for the subgrid wall model [10] employed. About ten cells are within the boundary layer on the parallel midsection of the hull, resulting in $y^+\approx15$. Conventional inflow and outflow conditions [22] are used together with far-field conditions at the outer boundary, whereas no-slip conditions are used on the hull.

The computational model consist of the incompressible NSE for a linear viscous fluid, and following Ref. [27], the finite volume discretization of the low-pass filtered incompressible NSE and/or the raw incompressible NSE results in the modified equations,

$$\partial_t(\bar{\mathbf{v}}) + \nabla(\bar{\mathbf{v}}\otimes\bar{\mathbf{v}}) = -\nabla\bar{p} + \nabla\cdot\bar{\mathbf{S}} + \boldsymbol{\tau} + \mathbf{m}^{v} \qquad \nabla\cdot\bar{\mathbf{v}} = 0 \tag{1}$$

where $\mathbf{v}$ is the velocity, p the pressure, $\mathbf{S}=2\nu\mathbf{D}$ the viscous stress tensor, ν the molecular viscosity, $\mathbf{m}^{v}=\overline{\nabla(\mathbf{v}\otimes\mathbf{v})}-\nabla(\bar{\mathbf{v}}\otimes\bar{\mathbf{v}})=\overline{\nabla(\mathbf{v}\otimes\mathbf{v})}-\nabla(\overline{\mathbf{v}\otimes\mathbf{v}})+\nabla\cdot\mathbf{B}$ the unresolved transport term, $\mathbf{B}=\overline{\mathbf{v}\otimes\mathbf{v}}-\bar{\mathbf{v}}\otimes\bar{\mathbf{v}}$ the subgrid stress tensor, and $\mathbf{t}$ the truncation error of the numerical algorithm. The unresolved transport term is usually simplified such that only the subgrid force vector $\nabla\cdot\mathbf{B}$ is kept. The subgrid stress tensor is commonly modeled using an explicit subgrid model such as

- the subgrid viscosity model (VM), $\mathbf{B}=-2\nu_k\bar{\mathbf{D}}$ [6]
- the MM, $\mathbf{B}=\overline{\bar{\mathbf{v}}\otimes\bar{\mathbf{v}}}-\bar{\bar{\mathbf{v}}}\otimes\bar{\bar{\mathbf{v}}}-2\nu_k\bar{\mathbf{D}}$ [6]

In contrast to *explict* LES, where high-order central schemes are used to discretize both the convective and diffusive terms, such that $\boldsymbol{\tau}=\boldsymbol{\tau}_{\mathrm{CD}}$, *implicit* LES is based on high-order nonoscillatory schemes for the convective terms, such that $\boldsymbol{\tau}=\boldsymbol{\tau}_{\mathrm{CD}}+\boldsymbol{\tau}_{\mathrm{ND}_{\mathrm{O}}}$, where $\boldsymbol{\tau}_{\mathrm{ND}}$ is related to the flux limiter Ψ and the upwind-biased part of the higher-order nonoscillatory scheme. Comparing modified equations, Chap. 4 in Ref. [13] from LES and ILES implies that $\boldsymbol{\tau}_{\mathrm{ND}}$ can be viewed as an implicit subgrid model with $\mathbf{B}=\mathbf{C}(\nabla\bar{\mathbf{v}})^T+(\nabla\bar{\mathbf{v}})\mathbf{C}^T$ [12,13,27], where $\mathbf{C}=\chi(\bar{\mathbf{v}}\otimes\mathbf{d})$ is the equivalent tensor valued subgrid viscosity with $\chi=\frac{1}{2}(1-\Psi)(\beta^{-}-\beta^{+})$ and $\beta^{\pm}=\frac{1}{2}(\mathrm{sgn}(\bar{\mathbf{v}})\pm1)$.

For VM and MM, we use the OEEVM [28], with coefficients evaluated under the assumption of an infinite inertial subrange. For ILES, we use the flux corrected transport (FCT) algorithm [22]. The discretized equations are combined to form a Poisson equation for the pressure. The scalar equations are solved sequentially, with iteration over the coupling terms, employing a PISO-type procedure. To emulate the propeller, an actuator-disk model is used, in which a source term is added to the momentum equation in the region of the propeller that accelerates the flow resulting in a time-varying thrust and a time-varying and rotating slipstream. This body force field is evaluated using a lifting-line technique [29] based on Goldstein's kappa theory [30] to account for the number of blades.

The main flow features are shown in Fig. 2. The flow past the forebody is dominated by the stagnation point and the favorable pressure gradient on the foreshoulder that slowly develop into a fully turbulent boundary layer. The flow over the midbody is dominated by the horseshoe vortex, originating from the roll-up of the boundary layer just ahead of the sail, and by the sail-wake. The horseshoe vortex continues along the sail, generating additional vortices toward the trailing edge of the sail that interact with the hull-boundary layer and the horseshoe vortex, resulting in an unsteady wake behind the sail. As the horseshoe vortex is transported further aft, it loses its coherence and flattens toward the hull. During this process, it interacts with the hull-boundary layer, developing a complex near-wall flow with embedded vortices approaching the tapered stern. Such complex flow pattern on the sail side of the hull creates transport of momentum across the hull, which affects the boundary layer velocity and shear stress distribution. The sail-tip vortex pair persists far downstream but does not interact with other vortices and passes well above the propeller. The flow over the sail cap is dominated by the flow turning and the development of the sail-tip vortex pair at the junction between the sail and sail cap. Toward the stern, vortex sheets forms along the rudders and counter-rotating tip vortices and horseshoe vortices are formed on each of the rudders. These become embedded in the deep boundary layer that is affected by the tapering of the hull and the adverse pressure gradient. Redistribution of Reynolds stresses are also found to take place in the stern due to the cross flow, caused by the unsteady sail wake and horseshoe vortex. As can be observed in Fig. 3, the presence of the propeller affects the flow over the stern. This is mainly caused by the pressure distribution due to the propeller-induced suction. Only just upstream of the propeller, we note the influence of the

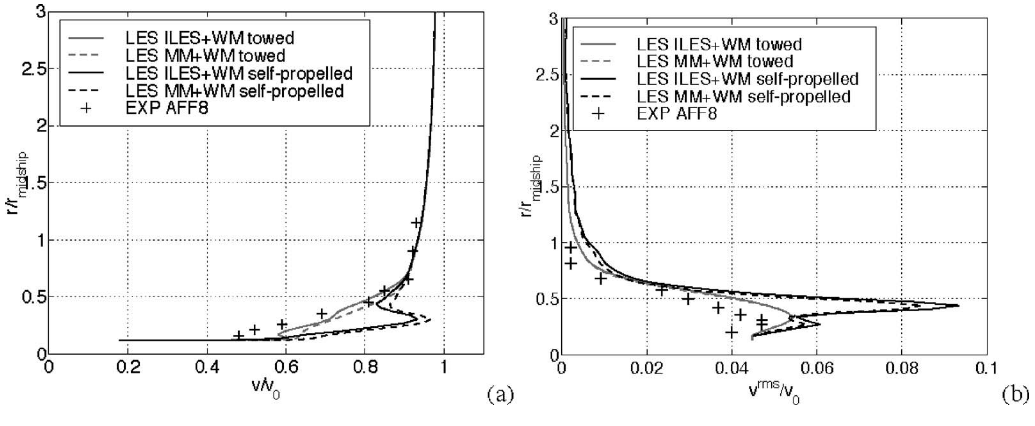

Fig. 3 Submarine hydrodynamics. Comparison of predicted and measured (*a*) time and azimuthally averaged velocity and (*b*) rms-velocity fluctuations at $x/L=0.978$.

Downloaded 03 Jun 2010 to 171.66.16.156. Redistribution subject to ASME license or copyright; see http://www.asme.org/terms/Terms_Use.cfm

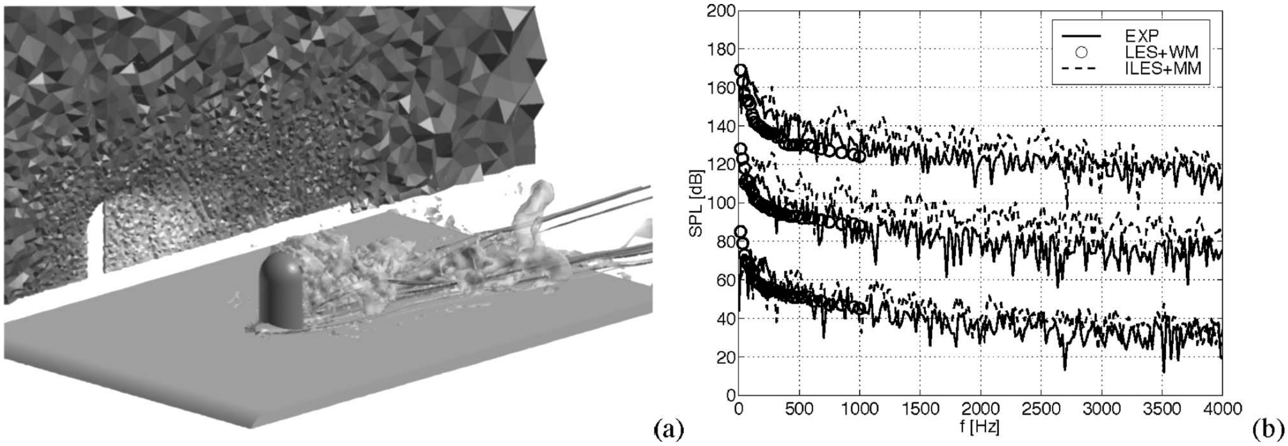

Fig. 4 Aerodynamic noise. (*a*) Perspective view of the flow around the wing mirror, including the grid and (*b*) comparisons of sound pressure levels at discrete points around the wing mirror from the coarse grid. Note that the spectra are shifted 40 dB in the vertical direction to facilitate comparison.

tangential and radial velocity distributions caused by the rotating propeller. Downstream of the propeller, the flow is different and primarily swirl dominated.

In Fig. 3(*a*), we compare the time and azimuthally averaged streamwise velocity $\langle\bar{v}_1\rangle_\varphi$ between LES and experimental data for the towed and self-propelled hulls, at $x/L=0.978$. A good agreement between LES predictions and data is obtained, whereas further away from the hull, $\langle\bar{v}_1\rangle_\varphi$ approaches v_0. In the self-propelled case, the slipstream is clearly visible, revealing that the propeller entrains fluid mainly from the hull-boundary layer, which affects the levels of fluctuations in the boundary layer. Similarly, Fig. 3(*b*) presents a comparison of the mean streamwise rms-velocity fluctuations $\langle\bar{v}_1^{\text{rms}}\rangle_\varphi$. Again, the influence of the explicit or implicit subgrid model is comparatively small. As compared to the towed hull case, the self-propelled hull case produces a bimodal rms-velocity fluctuation profile, with the outer peak associated with the radius of the propeller and the inner peak value associated with the peak in the mean velocity profile, associated with the hull-boundary layer flow.

Aerodynamic Noise

Flow noise has become a significant contributor to the interior noise level in cars and high-speed trains at high cruising speeds due to the developments in mechanical noise reduction. Aspiration noise is reduced through modern sealing techniques, whereas aerodynamic noise, generated by the high-Re-number turbulent external flow, remains a problem to be solved by experimental and computational modeling. The noise characteristics are found to be sensitive to design details, such as door handles, slits, A pillars, wing mirrors, etc., since such details usually create additional flow unsteadiness. This is computationally challenging since the simulations need to include not only the complete, often rather complicated geometry, but also the unsteady effects, which are responsible for the pressure fluctuations recognized as noise. More precisely, flow noise consists of sequence of compressions and rarefactions, traveling with the speed of sound c of the fluid. A characteristic property of these waves is that they permit transport of energy without net transport of material and that the compressible NSE is required to describe flow noise.

If the compressible NSE is used as a model for aerodynamic noise, this requires a resolution of the small density variations of longitudinal waves associated with the propagating sound. This puts severe requirements on numerics, grids, and boundary conditions. High frequency, long time resolution is thus needed, resulting in very expensive computations. Alternative methods include perturbation techniques [31], which reduce the computational time by solving separately the incompressible and acoustic parts. Methods based on acoustic analogies [32], such as the Ffowkcs–Williams–Hawkings (FWH) approach [33], allow the modeling problem to be decomposed into two parts: source prediction and propagation. Kirchhoff's theory [34] also leads to a two-stage method, but here sound sources must be distributed on a virtual surface around the object beyond which nonlinear effects are negligible. An advantage of this method with respect to the previous one is that only surface integrals need to be evaluated, whereas the FWH model involves both surface and volume integrals. For the reasons mentioned, most flow noise problems are solved using the FWH equation together with the incompressible NSE. Here, ILES and LES are used to predict the aerodynamic sources, so that the full model reads

$$\partial_t(\bar{\mathbf{v}}) + \nabla(\bar{\mathbf{v}} \otimes \bar{\mathbf{v}}) = -\nabla\bar{p} + \nabla\cdot\bar{\mathbf{S}} + \boldsymbol{\tau} + \mathbf{m}^v \qquad \nabla\cdot\bar{\mathbf{v}} = 0$$

$$p'(\mathbf{x},t) = \frac{1}{4\pi}\partial_t^2\int_V\left[(\rho'\mathbf{v}_i \otimes \mathbf{v}_i - p_i\mathbf{I})\cdot\frac{(\mathbf{x}-\mathbf{x}')\otimes(\mathbf{x}-\mathbf{x}')}{|\mathbf{x}|^3}\right]dV'$$

$$-\frac{1}{4\pi c}\partial_t\int_{\partial V}\left[(p_i - c^2\rho')\frac{(\mathbf{x}-\mathbf{x}')\cdot\mathbf{n}}{|\mathbf{x}|^2}\right]dS' \qquad (2)$$

where $\mathbf{n}$ is the outward pointing unit normal vector to the surface S, and brackets denotes evaluation at the retarded time. The volume integral, i.e., the so-called quadrupole term, is usually negligible in comparison to the surface integral, i.e., the so-called dipole term, for low Ma-number flows. The derivation of this model can be found in Ref. [32].

To illustrate the problem of predicting flow noise we consider the flow around a wing mirror and the resulting flow noise at $\text{Re}\approx 7\times 10^5$. Höld et al. [35] and Siegert et al. [36] reported experimental measurements of the acoustic fields around a wing mirror on a plate in an aeroacoustic wind tunnel. The wing mirror is composed of a half cylinder 0.20 m in diameter and length topped by a quarter of a sphere with the same diameter. It is mounted on a flat plate 1.60 m wide, 2.40 m long, and 0.05 m thick. The wing mirror is mounted 0.90 m downstream of the elliptically shaped leading edge. The computational model replicates the experimental geometry with the far-field boundaries placed 1.00 m to the sides and above the plate. The lower computational domain coincides with the symmetry plane of the plate. Conventional open inflow/outflow boundary conditions are used, whereas on the wing mirror and the plate, no-slip conditions are used. Two computational grids of about 1.5×10^6 and 3.0×10^6 tetrahedral cells are used.

Downloaded 03 Jun 2010 to 171.66.16.156. Redistribution subject to ASME license or copyright; see http://www.asme.org/terms/Terms_Use.cfm

Figure 4(*a*) shows a perspective view of the flow around the wing mirror, from which it is clear that it creates a large complex wake with eddy structures spanning a range of scales. The flow accelerates to ~95 m/s over the mirror apex, and the separation region extends over a distance about twice the mirror height. A horseshoe vortex system is found to form at the upstream junction between the plate and the wing mirror and to extend along the wing mirror and further along the plate, whereafter it rapidly loses coherence and gradually disappears. The near wake behind the wing mirror hinges on an arch-shaped vortical structure that is observed only in the time-averaged results. This arch-shaped vortical structure is found to meander from side to side, and is most likely not complete at any instant. Furthermore, we notice a quasiperiodic vortex shedding at the vertical edges of the cylindrical part of the mirror resulting in two regions of high rms fluctuations about one diameter downstream of the mirror. Similarly, the vortical structures shed at the top of the mirror impact some two diameters downstream of the mirror. In Fig. 4(*b*), we show comparisons of the sound pressure levels at three points around the wing mirror. The results from the FWH acoustic model, using the LES and the ILES data, are found to match the experimental measurements well [36]. However, the predicted spectra are more jagged than the experimental spectra, a feature observed by other authors, but not understood. One reason may be that the experimental data are filtered whereas the simulation data are not. It seems that the ILES model somewhat overpredicts the sound pressure level in comparison to the data, whereas the LES model results in a very good overall agreement. Moreover, the influence of spatial resolution appears limited when compared on the 1.5×10^6 and 3×10^6 grids.

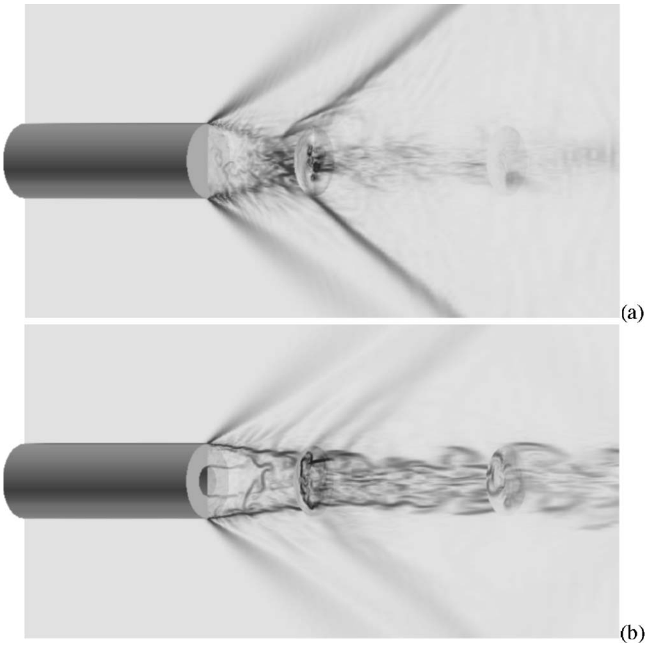

Fig. 5 Supersonic base flow. Perspective view showing emulated schlieren images from the (*a*) zero bleed case (*I*=0) and (*b*) the strongest bleed case (*I*=0.0226) from ILES.

Compressible Turbulent Flows

In contrast to incompressible flows, compressible flows involve density changes and are important in aerodynamics and turbomachinery applications. To demonstrate the challenges of compressible turbulent flows, we focus on the flow around a generic projectile and particularly on its afterbody. Behind the projectile, the pressure is lower than its ambient value, causing base drag [37]. Early attempts to predict afterbody flows are reviewed in Ref. [38]. However, solving the NSE offers the ability to better predict the details of the flow and to take out the assumptions of the simpler methods. Both early and more recent RANS calculations [38,39] fail to predict these flows, and improved models are required. This has been investigated using LES [40] and DES [41,42], and a comparison with experimental data [40] has shown a superior agreement compared to RANS, e.g., Ref. [39]. In addition, we focus on the means for reducing the base drag by injecting fluid into the near wake, thereby expanding the recirculation region by pushing the stagnation point further downstream (Fig. 5(*a*)). Experimental data for this situation, with different bleed rates, are available in Herrin and Dutton [43] and Mathur and Dutton, which provides excellent validation data.

The fluid dynamic model used consists of the compressible NSE, describing conservation of mass, momentum, and energy of a Newtonian fluid obeying Fourier's law of thermal conduction and the ideal gas law. A finite volume discretization of the low-pass filtered compressible NSE and/or the raw compressible NSE results in the modified equations,

$$\partial_t(\bar{\rho}) + \nabla\cdot(\bar{\rho}\,\tilde{\mathbf{v}}) = \tau^{\rho} - m^{\rho}$$

$$\partial_t(\bar{\rho}\,\tilde{\mathbf{v}}) + \nabla\cdot(\bar{\rho}\,\tilde{\mathbf{v}}\otimes\tilde{\mathbf{v}}) = -\nabla\bar{p} + \nabla\cdot\bar{\mathbf{S}} + \boldsymbol{\tau}^{v} - \mathbf{m}^{v}$$

$$\partial_t(\bar{\rho}\tilde{E}) + \nabla\cdot(\bar{\rho}\,\tilde{\mathbf{v}}\tilde{E}) = -\nabla\cdot((\bar{p}\mathbf{I}+\bar{\mathbf{S}})\tilde{\mathbf{v}}+\bar{\mathbf{h}}) + \tau^{E} - m^{E} \tag{3}$$

where ρ is the density, E the total energy, h the heat flux vector, τ^k the truncation error associated with the numerical algorithm, with $k=\{\rho,\mathbf{v},E\}$, and

$$m^{\rho} = \overline{\nabla\cdot(\rho\mathbf{v})} - \nabla\cdot(\bar{\rho}\,\tilde{\mathbf{v}}) = \overline{\nabla\cdot(\rho\mathbf{v})} - \nabla\cdot(\overline{\rho\mathbf{v}})$$

$$\begin{aligned}\mathbf{m}^{v} &= \overline{\nabla\cdot(\rho\mathbf{v}\otimes\mathbf{v}+p\mathbf{I}-\mathbf{S})} - \nabla\cdot(\bar{\rho}\,\tilde{\mathbf{v}}\otimes\tilde{\mathbf{v}}+\bar{p}\mathbf{I}-\bar{\mathbf{S}})\\ &= \overline{\nabla\cdot(\rho\mathbf{v}\otimes\mathbf{v}+p\mathbf{I}-\mathbf{S})} - \nabla\cdot(\overline{\rho\mathbf{v}\otimes\mathbf{v}+p\mathbf{I}-\mathbf{S}}) + \nabla\cdot\mathbf{B}\end{aligned}$$

$$\begin{aligned}m^{E} &= \overline{\nabla\cdot(\rho E\mathbf{v}+p\mathbf{v}+\mathbf{S}\mathbf{v}+\mathbf{h})} - \nabla\cdot(\bar{\rho}\tilde{E}\,\tilde{\mathbf{v}}+\bar{p}\,\tilde{\mathbf{v}}+\bar{\mathbf{S}}\tilde{\mathbf{v}}+\bar{\mathbf{h}})\\ &= \overline{\nabla\cdot(\rho E\mathbf{v}+p\mathbf{v}+\mathbf{S}\mathbf{v}+\mathbf{h})} - \nabla\cdot(\overline{\rho E\mathbf{v}+p\mathbf{v}+\mathbf{S}\mathbf{v}+\mathbf{h}}) + \nabla\cdot\mathbf{b}\end{aligned} \tag{4}$$

where $\mathbf{B}=\bar{\rho}(\overline{\mathbf{v}\otimes\mathbf{v}}-\tilde{\mathbf{v}}\otimes\tilde{\mathbf{v}})+(\bar{p}-\tilde{p})\mathbf{I}+(\tilde{\mathbf{S}}-\bar{\mathbf{S}})$ and $\mathbf{b}=\bar{\rho}(\overline{\mathbf{v}E}-\tilde{\mathbf{v}}\tilde{E})+\tilde{\mathbf{S}}\tilde{v}-\overline{\mathbf{S}v}+\overline{p\mathbf{v}}-\tilde{p}\tilde{\mathbf{v}}+\tilde{\mathbf{h}}-\bar{\mathbf{h}}$. Evidently, the subgrid stress tensor and flux vector in the compressible case include more physics than for the incompressible case. Explicit closure models are typically borrowed from the incompressible case and corrected for the variable density. This may be acceptable for some supersonic flows, but not for hypersonic flows that have received recent attention. Here, we have chosen to use an explicit LES model with $\mathbf{B}=\bar{\rho}(\overline{\tilde{\mathbf{v}}\otimes\tilde{\mathbf{v}}}-\bar{\tilde{\mathbf{v}}}\otimes\bar{\tilde{\mathbf{v}}})-2\mu_k\tilde{\mathbf{D}}$ and $\mathbf{b}=\bar{\rho}(\overline{\tilde{\mathbf{v}}\tilde{E}}-\bar{\tilde{\mathbf{v}}}\bar{\tilde{E}})-2\mu_k/\mathrm{Pr}_T\nabla\tilde{E}$ [45] and an ILES model with $\mathbf{B}=\bar{\rho}(\mathbf{C}(\nabla\tilde{\mathbf{v}})^T+(\nabla\bar{\tilde{\mathbf{v}}})\mathbf{C}^T)$ and $\mathbf{b}=\bar{\rho}\mathbf{C}\nabla\tilde{E}$, where $\mathbf{C}=\chi(\tilde{\mathbf{v}}\otimes\mathbf{d})$ is the tensor valued subgrid viscosity with $\chi=\frac{1}{2}(1-\Psi)(\beta^{-}-\beta^{+})$ and $\beta^{\pm}=\frac{1}{2}(\mathrm{sgn}(\bar{\mathbf{v}})\pm1)$ (see Chap. 4 in Ref. [13]).

The spatial discretization is performed using an unstructured second-order accurate finite volume method using polyhedral control volumes for the decomposition of the computational domain and a cell-centered, colocated variable arrangement. For the explicit LES, we use central differencing for both the convective and diffusive terms, whereas for the ILES, we use either the classical van Leer [46] or FCT algorithms [47]. These two schemes give rise to different limiters Ψ and hence to different subgrid models. Finally, the time integration used employs the two-stage total variational diminishing Runge–Kutta scheme of Gottlieb and Shu [48].

The experiments of Herrin and Dutton [43] and Mathur and Dutton [44], are performed at Ma=2.46 for an afterbody with a diameter of $D=63.5$ mm and a bleed orifice of $d=25.4$ mm. The ambient velocity, pressure, and temperature are $v_{\infty}=576$ m/s, $p_{\infty}=515$ kPa, and $T_{\infty}=294$ K for the zero bleed case and $v_{\infty}=576$ m/s, $p_{\infty}=471$ kPa, and $T_{\infty}=300$ K for the bleed cases that

Downloaded 03 Jun 2010 to 171.66.16.156. Redistribution subject to ASME license or copyright; see http://www.asme.org/terms/Terms_Use.cfm

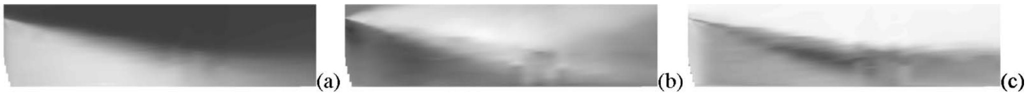

Measurement data I=0, [43-44]

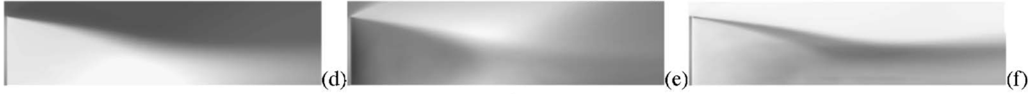

ILES data I=0

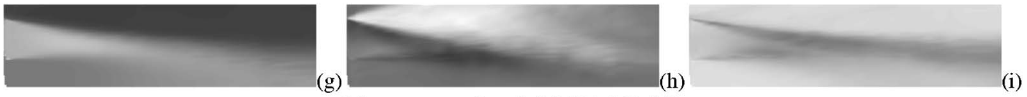

Measurement data I=0.0226, [43-44]

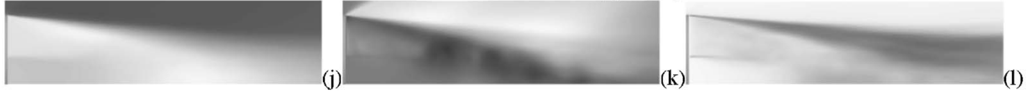

ILES data I=0.0226

Fig. 6 Supersonic base flow. (*a*)–(*f*) show measurement data (top row) and ILES results (bottom row) at $I=0$, respectively. (*g*)–(*i*) show measurement data (top row) and ILES results (bottom row) at $I=0.0226$, respectively. First column shows $\langle v_x \rangle$, second $\langle v_r \rangle$, and third *k*.

are characterized by the injection parameter $I=\rho_j v_j d^2/\rho_\infty v_\infty D^2$, where v_{j_j} and ρ_j are the bleed velocity and density. The computational domain consists of a cylinder with an outer radius of $3D$, extending $4D$ upstream of and $6D$ downstream of the base plane. Two grids with 2×10^6 and 4×10^6 cells, respectively, have been used. Supersonic and subsonic inflow conditions are used at the upstream boundary and for the bleed jet, respectively. Freeflow conditions are imposed at the downstream boundary and in the radial direction, and no-slip adiabatic boundary conditions are imposed on the afterbody.

In Fig. 5, we show numerical schlieren images at the centerplane and at an axial plane $2D$ downstream of the base from two cases with $I=0$ and $I=0.0226$. Irrespective of the value of I, the flows are unsteady and fully 3D. At the base corners, the expansion fans are clearly visible, followed by the near-wake recirculation bubble, the recompression waves, and the trailing wake. At low bleed rates, the flow is reversed virtually out to the corners, whereas at higher bleed rates, the flow only becomes reversed in the annular region around the bleed jet and downstream of the bleed jet. The outer shear layer forms along the body and develops toward reattachment, whereupon it forms the far wake. The inner shear layer occurs only in the bleed cases—its strength dependent on I. The pressure gradient and shear stress gradients in the outer shear layer decrease as the outer shear layer matures as turbulent mixing entrains ambient fluid into the wake. Base bleed widens the wake, increases the mixing, and reduces the shear stresses, but by directing the bleed into the recirculation region, downstream mixing is delayed. For $I=0$, the vorticity is dominated by rings (in the outer shear layer) developing into axial vortices in the region of mean reattachment showing signs of shedding. For $I>0$, the outer vortex rings are supplemented by inner rings developing within the bleed jet shear layer. In the reattachment region, large coherent structures are found in the LES and in the data. Virtually no differences are found between the LES and the ILES, suggesting that the intrinsic differences between these models do not significantly influence the dynamics of the large (resolved) coherent structures.

The influence of the bleed rate is presented in Fig. 6, where contours of the time-averaged axial velocity $\langle \tilde{v} \rangle_x$, radial velocity $\langle \tilde{v} \rangle_r$, and axial rms-velocity fluctuations $\tilde{v}_x^{\mathrm{rms}}$ at the center plane for $I=0$ and 0.0226 are shown. The main features of the flow, the turning of the flow over the base corner expansion, the primary recirculation region (PRR) (relevant for small values of I), the bleed jet, and the secondary recirculation region (SRR) between the bleed jet and the outer shear layer (relevant for large values of I), are clearly visible. Irrespective of I, the $\langle \tilde{v} \rangle_r$ component is considerably smaller than the $\langle \tilde{v} \rangle_x$ component, emphasizing the anisotropy of the flow. The freestream flow angles downstream of the base corner are consistent with data for each case [43,44] and a Prandtl–Meyer turning angle based on the estimated base pressure ratio and the freestream Ma number of 2.46. With increasing bleed flow, the size and strength of the PRR (bounded in the axial direction by the forward and rear stagnation points, respectively) decrease until it finally disappears at $I\approx 0.0226$, as the bleed flow penetrates the outer shear layer reattachment region. In addition, the forward stagnation point is displaced progressively downstream of the base plane, and the radial extent of the forward portion of the PRR decreases. With increasing bleed, the SRR near the base annulus becomes more evident. Much of the reverse flow in the PRR is oriented parallel to the axis of symmetry, which is in contrast to the $I=0$ case, in which the recirculating flow is directed toward the point of separation. The predicted axial and radial velocity distributions are in good agreement with data [43,44], for both LES and ILES, although only ILES results are presented in Fig. 6. The distribution of $\langle \tilde{v} \rangle_x$ in the free shear layer downstream of the base appears to be separated in an inner region and an outer region, of which the former appears to diverge more rapidly toward the centerline. The inner region finally overtakes the outer region and consumes most of the total shear layer width. As the outer flow approaches the axis of symmetry, the magnitude of the radial component $\langle \tilde{v} \rangle_r$ continues to increase due to the axisymmetric effect. The value of I clearly affects the strength of the recompression waves: For $I=0$ a strong recompression is found in the predictions, while at higher values of I this weakens to finally expire at $I=0.0226$. Comparing the predicted and measured $\mathbf{v}$ distributions shows that the simulation models can also predict the second-order statistical moments with reasonable accuracy and that the influence of the bleed jet on $\tilde{v}_x^{\mathrm{rms}}$ is significant.

Chemically Reacting Flows

Combustion is a ubiquitous process where the chemical energy can be used in a controlled fashion in chemical propulsion systems, such as in air-breathing engines (turbojets, ramjets, scramjets, and pulse detonation engines), solid fuel rocket motors, conventional integrated circuit (IC) engines, and gas turbines, as well as in furnaces, afterburners, launch systems, and, in particular, weapon systems. Combustion also occurs in an uncontrolled fashion, such as in explosions and fires, where the released chemical energy may typically cause damage to humans, constructions, and society. Almost all combustion of practical interest takes place in the presence of turbulence, and although our understanding of

Downloaded 03 Jun 2010 to 171.66.16.156. Redistribution subject to ASME license or copyright; see http://www.asme.org/terms/Terms_Use.cfm

turbulent combustion is continuously improving, there can be little doubt that this still represents a serious bottleneck when trying to simultaneously maximize efficiency and minimize emissions without causing structural damage.

The current development of combustion systems is based primarily on empirical data and simple design models that will not be adequate for multivariate optimization of fuel, emissions and signatures, or if new concepts are to be examined. Alternatives involve the use of advanced diagnostics and state-of-the-art computations. Detailed experiments are very expensive and complicated; however, recent advances in high-resolution nonintrusive diagnostics, together with fast and reliable data reduction algorithms, have enabled detailed studies of laboratory devices and efficient data collection from field measurements [49]. The rapid advance on supercomputing and massively parallel processing has brought forth computational capabilities large enough to handle reacting flows [50]. Computational combustion has paved new routes to perform numerical simulations to guide experimental design and to aid in parametric studies, enabling the variation of parameters, and to examine issues that cannot be studied otherwise.

The equations of chemically reactive flows are the conservation and balance equations of mass, momentum, and energy, describing the convective motion of the fluid, the diffusive transport processes, and the chemical reactions. A finite volume discretization of the low-pass filtered and/or unfiltered reactive NSE results in the modified equations,

$$\partial_t(\bar{\rho}) + \nabla\cdot(\bar{\rho}\,\tilde{\mathbf{v}}) = \tau^{\rho} - m^{\rho}$$

$$\partial_t(\bar{\rho}\tilde{Y}_i) + \nabla\cdot(\bar{\rho}\,\tilde{\mathbf{v}}\tilde{Y}_i) = \nabla\cdot\bar{\mathbf{j}}_i + \overline{w_i} + \tau^{Y_i} - m^{Y_i}$$

$$\partial_t(\bar{\rho}\,\tilde{\mathbf{v}}) + \nabla\cdot(\bar{\rho}\,\tilde{\mathbf{v}}\otimes\tilde{\mathbf{v}}) = -\nabla\bar{p} + \nabla\cdot\bar{\mathbf{S}} + \boldsymbol{\tau}^{v} - \mathbf{m}^{v}$$

$$\partial_t(\bar{\rho}\tilde{E}) + \nabla\cdot(\bar{\rho}\tilde{\mathbf{v}}\tilde{E}) = -\nabla\cdot((\bar{p}\mathbf{I} + \bar{\mathbf{S}})\tilde{\mathbf{v}} + \bar{\mathbf{h}}) + \tau^{E} - m^{E} \tag{5}$$

where Y_i is the mass fraction, $\dot{w}_i = M_i P_{ij}\dot{w}_j$ the reaction rate, and M_i the molar mass of species i, and $\dot{w}_j$ the rate of reaction of reaction j, s the thermal radiation term, τ^k the truncation error associated with the numerical algorithm, with $k = \{\rho, Y_i, \mathbf{v}, E\}$, and

$$m^{\rho} = \overline{\nabla\cdot(\rho\mathbf{v})} - \nabla\cdot(\bar{\rho}\,\tilde{\mathbf{v}}) = \overline{\nabla\cdot(\rho\mathbf{v})} - \nabla\cdot(\overline{\rho\mathbf{v}})$$

$$\begin{aligned} m^{Y_i} &= \overline{\nabla\cdot(\rho\mathbf{v}Y_i - \mathbf{j}_i)} - \nabla\cdot(\bar{\rho}\,\tilde{\mathbf{v}}\tilde{Y}_i - \bar{\mathbf{j}}_i) = \overline{\nabla\cdot(\rho\mathbf{v}Y_i - \mathbf{j}_i)} \\ &\quad - \nabla\cdot\overline{(\rho\mathbf{v}Y_i - \mathbf{j}_i)} + \nabla\cdot\mathbf{b}_i \end{aligned}$$

$$\begin{aligned} \mathbf{m}^{v} &= \overline{\nabla\cdot(\rho\mathbf{v}\otimes\mathbf{v} + p\mathbf{I} - \mathbf{S})} - \nabla\cdot(\bar{\rho}\tilde{\mathbf{v}}\otimes\tilde{\mathbf{v}} + \bar{p}\mathbf{I} - \bar{\mathbf{S}}) \\ &= \overline{\nabla\cdot(\rho\mathbf{v}\otimes\mathbf{v} + p\mathbf{I} - \mathbf{S})} - \nabla\cdot(\overline{\rho\mathbf{v}\otimes\mathbf{v} + p\mathbf{I} - \mathbf{S}}) + \nabla\cdot\mathbf{B} \end{aligned}$$

$$\begin{aligned} m^{E} &= \overline{\nabla\cdot(\rho E\mathbf{v} + p\mathbf{v} + \mathbf{S}\mathbf{v} + \mathbf{h})} - \nabla\cdot(\bar{\rho}\tilde{E}\,\tilde{\mathbf{v}} + \bar{p}\,\tilde{\mathbf{v}} + \bar{\mathbf{S}}\tilde{\mathbf{v}} + \bar{\mathbf{h}}) \\ &= \overline{\nabla\cdot(\rho E\mathbf{v} + p\mathbf{v} + \mathbf{S}\mathbf{v} + \mathbf{h})} - \nabla\cdot(\overline{\rho E\mathbf{v} + p\mathbf{v} + \mathbf{S}\mathbf{v} + \mathbf{h}}) + \nabla\cdot\mathbf{b} \end{aligned} \tag{6}$$

where $\mathbf{B} = \bar{\rho}(\overline{\mathbf{v}\otimes\mathbf{v}} - \tilde{\mathbf{v}}\otimes\tilde{\mathbf{v}}) + (\bar{p} - \tilde{p})\mathbf{I} + \tilde{\mathbf{S}} - \bar{\mathbf{S}}$, $\mathbf{b} = \bar{\rho}(\overline{\mathbf{v}E} - \tilde{\mathbf{v}}\tilde{E}) + \tilde{\mathbf{S}}\tilde{v} - \overline{\mathbf{S}\mathbf{v}} + \overline{p\mathbf{v}} - \tilde{p}\,\tilde{\mathbf{v}} + \tilde{\mathbf{h}} - \bar{\mathbf{h}}$, and $\mathbf{b}_i = \bar{\rho}(\overline{\mathbf{v}Y_i} - \tilde{\mathbf{v}}\tilde{Y}_i) + \tilde{\mathbf{j}}_i - \bar{\mathbf{j}}_i$. In addition, the reaction rates $\dot{w}_i$ and the constitutive equations (p, $\mathbf{S}$, $\mathbf{h}$, and $\mathbf{j}_i$) are usually highly nonlinear functions of the dependent variables. For the fluid dynamic part, closure models are typically borrowed from the incompressible case and corrected for the variable density, whereas for the chemistry part, and the reaction rates in particular, other approaches are necessary. First, the number of chemical reaction has to be limited, and reduced mechanisms will be used instead of detailed mechanisms [51], which diminish the ability to predict minor species, which in turn affects the accuracy of the reaction rates. Second, the nonlinearity of the reaction rates makes the handling of the filtered reaction rates difficult [52], but may be decomposed as

$$\begin{aligned} \bar{w}_i &= \tilde{w}'_i + [\bar{w}_i - \tilde{w}'_i] \\ &= \tilde{w}'_i(1 + [\bar{w}_i - \tilde{w}'_i]/\tilde{w}'_i) = \tilde{w}'_i(1 + w_i^{\mathrm{sgs}}/\tilde{w}'_i) \\ &= \tilde{w}'_i(1 + \kappa) \end{aligned} \tag{7}$$

where $\bar{w}_i = \overline{\dot{w}_i(\rho, Y_i, T)}$, $\tilde{w}_i = \tilde{w}'_i(\bar{\rho}, \tilde{Y}_i, \tilde{T})$ and $\kappa = \dot{w}_i'^{\mathrm{sgs}}/\tilde{w}'_i$ is the segregation factor. Instead of following this route, other models, such as flamelet models, linear-eddy models, and probability density function models [53], are often used. Here, we will compare predictions from two finite-rate chemistry models, both employing the same two-step reaction mechanism [54], associated with the ILES and the conventional LES approaches, respectively, to emphasize differences, similarities between LES and ILES, and the robustness of the LES concept.

In the ILES model, the thermodynamic model consists of the equation of state for an ideal gas mixture and the equation of state for the enthalpy of the mixture. Diffusive transport properties, i.e., species diffusion (modeled by a Fickian scheme), mixture viscosity (modeled by Sutherland's law), and thermal conduction (modeled similarly) are included, while thermal diffusion is neglected. In ILES, the "raw" reactive NSE are solved, and in the spirit of this, the decomposition (Eq. (7)) of the reaction rate $\bar{w}_i$ should therefore become $\bar{w}_i \approx \tilde{w}'_i = \tilde{w}'_i(\bar{\rho}, \tilde{Y}_i, \tilde{T})$, with $\kappa = 0$, *neglecting* all subgrid contributions and consequently relying on a quasilaminar combustion description. The time integration is performed by a predictor-corrector method; viscous and diffusive terms are handled using central differencing, whereas convective terms are represented by a FCT scheme [47]. As discussed, the implicit (or built-in) subgrid models for the species, momentum, and energy equations become $\mathbf{b}_i = \bar{\rho}\mathbf{C}(\nabla\tilde{Y}_i)$, $\mathbf{B} = \bar{\rho}(\mathbf{C}(\nabla\tilde{\mathbf{v}})^T + (\nabla\tilde{\bar{\mathbf{v}}})\mathbf{C}^T)$, and $\mathbf{b} = \bar{\rho}\mathbf{C}\nabla\tilde{E}$, respectively, in which $\mathbf{C} = \chi(\tilde{\mathbf{v}}\otimes\mathbf{d})$, $\chi = \frac{1}{2}(1 - \Psi)(\beta^- - \beta^+)$, and $\beta^{\pm} = \frac{1}{2}(\mathrm{sgn}(\bar{\mathbf{v}}) \pm 1)$. It should be emphasized that in contrast to the transport terms that are implicitly modeled by the leading order truncation error [13], the subgrid reaction rates are not included at all for reasons of consistency.

In the LES model, the thermodynamic model consists of the equation of state for an ideal gas mixture and the equation of state for the enthalpy of the mixture. Diffusive transport properties, i.e., species diffusion (described by a Fickian scheme), mixture viscosity (modeled by Sutherland's law), and thermal conduction (modeled similarly) are included, while thermal diffusion is neglected. In LES, the filtered NSE are solved, and in the spirit of this, the segregation factor k in the decomposition Eq. (7) should be modeled, using consistent information from the subgrid stress and flux models used. Here, we have chosen to use the MM, $\mathbf{b}_i = \bar{\rho}(\overline{\tilde{\mathbf{v}}\tilde{Y}_i} - \bar{\tilde{\mathbf{v}}}\bar{\tilde{Y}}_i) - 2\mu_k/\mathrm{Sc}_i\nabla\tilde{Y}_i$, $\mathbf{B} = \bar{\rho}(\overline{\tilde{\mathbf{v}}\otimes\tilde{\mathbf{v}}} - \bar{\tilde{\mathbf{v}}}\otimes\bar{\tilde{\mathbf{v}}}) - 2\mu_k\tilde{\mathbf{D}}$, and $\mathbf{b} = \bar{\rho}(\overline{\tilde{\mathbf{v}}\tilde{E}} - \bar{\tilde{\mathbf{v}}}\bar{\tilde{E}}) - 2\mu_k/\mathrm{Pr}_T\nabla\tilde{E}$, where the subgrid viscosity $\mu_k = \bar{\rho}c_k\Delta k^{1/2}$, where k is obtained from the OEEVM [6]. For modeling the reaction rate, we here use the partially stirred reactor (PaSR) model [55] to estimate the segregation factor. This is a model for the sequential processes of micromixing and chemical reactions, assumed to be highly intermittent, i.e., concentrated in isolated regions, and occupying only a small fraction of the fluid volume. Hence, each LES cell can be viewed as partially stirred reactor containing the reactive fine structures (perfectly stirred reactors), exchanging mass and energy with its surroundings. The factor $1 + \kappa$ is then viewed as the reacting volume fraction, which may be estimated as the ratio between the chemical reaction time τ_c and the reactor conversion time, i.e. the sum of the micromixing time t_m and the chemical reaction time, such that $1 + \kappa = \tau_c/(\tau_c + \tau_m)$. Here, the chemical reaction time is estimated from the laminar flame speed at the laminar flame thickness such that $\tau_c = \delta_L^0/S_u^0 \approx D/(S_u^0)^2$, whereas the mixing time, ranging from the subgrid time $\tau_k = \Delta/(\varepsilon^{1/3}\Delta^{5/3})$ to the Kolmogorov time $\tau_K = (\nu/\varepsilon)^{1/2}$, is modeled as the geometrical mean of the two, i.e., $\tau_m = \sqrt{\tau_k\tau_K} = \nu^{1/4}\Delta^{-1/4}k^{-5/8}$, to incorporate both scales.

The LES and ILES finite-rate chemistry models are here

Downloaded 03 Jun 2010 to 171.66.16.156. Redistribution subject to ASME license or copyright; see http://www.asme.org/terms/Terms_Use.cfm

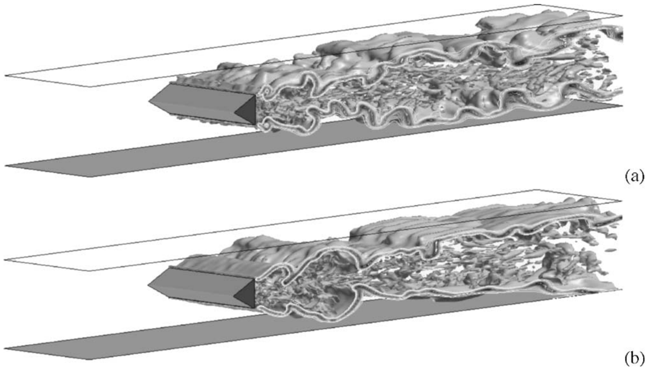

Fig. 7 Combustion. Instantaneous perspective views of the flame and the vorticity in terms of an isosurface of the temperature *T*, contours of the CO mass fraction, and an isosurface of the second invariant of the velocity gradient tensor from (*a*) the finite-rate chemistry PaSR LES and (*b*) the finite-rate chemistry ILES.

gauged using the VOLVO validation rig [56,57] which involves a rectilinear combustor of length $L=25h$, height $3h$, and width $6h$, in which a triangular flame holder, with height $h=0.04$ m is located at $x/h=7.95$. Optical access is provided by quartz windows at the sides of the combustor, whereas the upper and lower walls are water cooled. The computational domain employs about 2×10^6 grid points being periodic in the spanwise direction, with a width of $3h$. At the inlet, Dirichlet conditions are used for all variables besides p for which zero Neumann conditions are used, and at the outlet, wave-transmissive conditions are used. For all walls, no-slip conditions are used. The validation rig was operated under a variety of conditions, and here we focus on a premixed case, using C_3H_8 as fuel, with $v_{\text{in}}=17$ m/s, $T_{\text{in}}=298$ K, and an equivalence ratio of $\phi=0.62$.

According to Fig. 7, the flame anchors behind the flame holder due to the recirculation of hot products in the wake, and spanwise, or $\tilde{\omega}_3$ vortices are shed off the upper and lower edges of the flame holder forming an array of $\tilde{\omega}_3$ vortices. Compared to nonreacting flows, in which they shed alternately from the upper and lower edges of the prism, they here shed simultaneously due to rapid combustion at the vortex cores. This symmetric shedding and roll-up results in longitudinal vortices $\tilde{\omega}_{12}$ stretched between previous spanwise vortices on either side of the combustor. As for the nonreacting case [58], these vortices develop together with undulations of a recently shed $\tilde{\omega}_3$ vortex in regions of high strain to develop a complex unsteady vortex structure that interacts with the flame. The shear layers are responsible for the large-scale mixing taking place between cold reactants and hot products, forming a composition in which combustion can occur. As the flame develops, it propagates normal to itself, causing negatively curved wrinkles to contract and positively curved wrinkles to expand, causing pockets of reactants to tear away from the reactants. As the flame oscillates, it interacts with the pressure, increasing the pressure fluctuations, which, in turn, affects the flame by further perturbing it until instabilities may have developed. The temperature dependent viscosity has a stabilizing effect on the flow, which is apparent from the width of the longitudinal wake vortices as compared to those in the nonreacting case. By analyzing the transverse velocity signal at the centerline just downstream of the flame holder, we notice that the shedding (at ~105 Hz) observed experimentally [57] and computationally [58] in the nonreacting cases is virtually canceled in the nonreacting case; however, in the shear layers, shedding occurs at ~140 Hz, which is consistent with the data [59].

Figure 8 presents a comparison of the time-averaged axial velocity $\langle\tilde{v}_x\rangle$, temperature, $\langle\tilde{T}\rangle$, and CO mass fraction $\langle\tilde{Y}_{\text{CO}}\rangle$ at three locations between the finite-rate chemistry ILES and the finite-rate chemistry PaSR LES. For $\langle\tilde{v}_x\rangle$, we find that both LES models generally result in an adequate agreement with the measurement data. At $x/h=8.7$, the measurement data show a flattened velocity profile that is not well captured by any of the models. This is, however, due to the fact that the experimental and computational averagings are performed differently; in the experiments a Favré averaging is performed, whereas in the LES a conventional averaging is performed. In the recovery region and further downstream (at $x/h=11.5$ and 16.5), the agreement is satisfactory, but with a tendency for the ILES finite-rate chemistry model to predict a somewhat too long recirculation region and also to overpredict $\langle\tilde{v}_x\rangle$ in the core of the combustor ax $x/h=16.5$. For $\langle\tilde{T}\rangle$, there are two sets of measurements: coherent anti-Stokes Raman spectroscopy (CARS) and gas analysis [58], which give slightly different profiles at $x/h=11.5$ and 16.5. It is generally believed that the CARS data are more accurate than the gas analysis data since the samples continue to react after being extracted from the combustor, and therefore we primarily compare with the CARS data. It seems that the finite-rate chemistry PaSR LES results in a somewhat more narrow temperature distribution than the ILES finite-rate chemistry model, which also agrees better with the CARS data at $x/h=16.5$. The peak temperature is well captured by both models, indicating that also NO_x emissions would be reasonably well predicted. For $\langle\tilde{Y}_{\text{CO}}\rangle$, somewhat improved predictions are offered by the PaSR LES, but although the shape can be predicted, both LESs underpredict $\langle\tilde{Y}_{\text{CO}}\rangle$ as compared to the measurement data. Considering the complexity of the laboratory rig, with inflow and outflow components not modeled, the agreement between PaSR LES and ILES and the data is satisfactory.

Concluding Remarks

In the absence of an accepted universal theory of turbulence, the development of improved computational fluid dynamics (CFD) models for engineering applications is unavoidably pragmatic and is based on the use of empirical information. When complex physics is involved, as often is the case for engineering applications, this issue becomes increasingly important since often the turbulence affects the rates of production of noise, chemical species, etc. The alternatives to LES or ILES are DES or RANS, where the latter has many well-known deficiencies and limitations. Regarding DES, sufficient information is not yet available for making proper decisions. In this study, we have compared conventional LES and ILES for incompressible turbulent flows, compressible flows, aerodynamic noise, and combustion. Typically, this involves modeling also quantities other than the subgrid stress tensor or flux vectors, such as reaction rates or noise sources. The modeling of these quantities has here been performed in a manner consistent with LES or ILES. For LES, we here use either the OEEVM or the MM subgrid models since they represent two conceptually different subgrid models and have previously shown a good agreement with reference data. For ILES, the subgrid model is of generalized eddy viscosity type, the intrinsic details of which are dependent on the flux limiter used in the flux reconstruction step of the high-resolution nonoscillatory schemes typically used in ILES. For combustion, we here use a finite-rate chemistry LES model with a PaSR closure model for LES and no modeling for ILES. The models are formulated in a finite volume setting and are presented in terms of the modified equations, involving not only the unresolved transport terms (for LES) but also the commutation error and the leading order truncation error terms. All computations presented in this paper are based on the FOAM or OPENFOAM library [60], using different high-level codes and numerical methods, depending on the case studied. Moreover, LES is expensive due primarily to the time averaging needed to obtain statistical moments of the dependent variables. To obtain converged first-order statistical moments, at least five flowthrough times needs to be computed, and to obtain converged second-order statistics, a further five to ten flowthrough

Downloaded 03 Jun 2010 to 171.66.16.156. Redistribution subject to ASME license or copyright; see http://www.asme.org/terms/Terms_Use.cfm

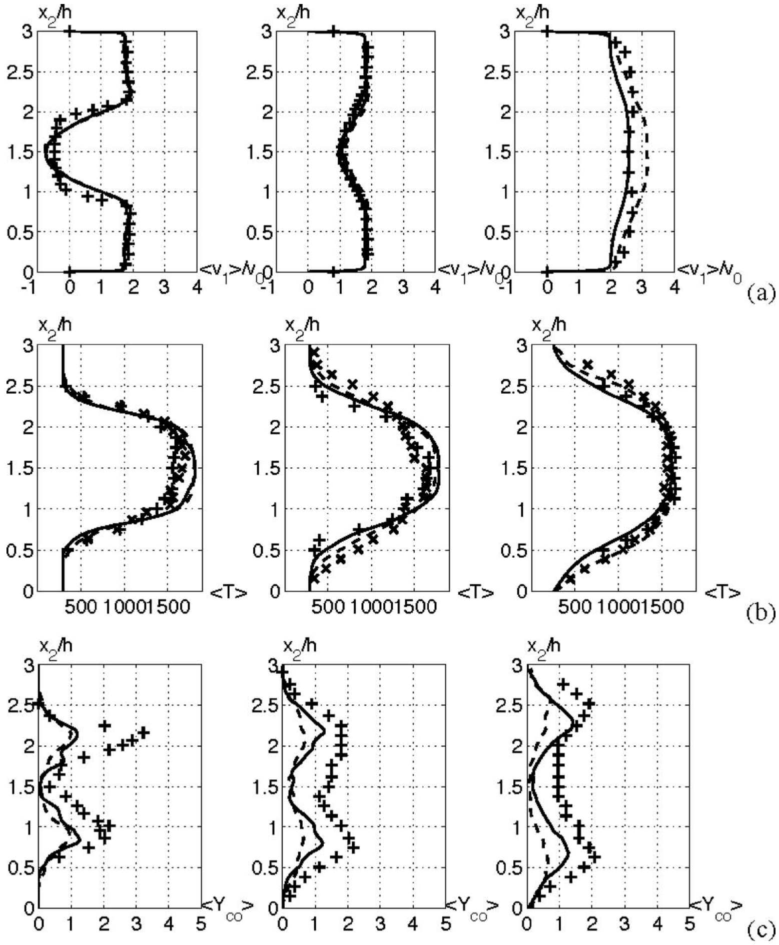

Fig. 8 Combustion. Time-averaged (*a*) axial velocity and (*b*) temperature for the VOLVO validation rig case using the finite-rate chemistry ILES (---) and the finite-rate chemistry PsSR LES (—) models. Experimental data are denoted by symbols (+) for LDV and CARS and (×) for gas analysis.

times are needed. For example, for the submarine case (with $\sim 7 \times 10^6$ grid points), we needed some 400,000 time steps, translating into about 50,000 CPU h of computation. In addition, some 10,000 CPU h are required to advance the simulation from the initial state to a fully developed turbulent flow from which the time averaging can be started. Both ILES and LES typically give good results when compared with experimental data, underlining the robustness of the LES approach. The comparison is usually made with experimental data for which no uncertainty information is available. Further challenges for LES and ILES include constructing a common appropriate mathematical and physical framework for its analysis and development and concepts for building more physics into the overall scheme to improve the global performance of the model.

Acknowledgment

The author whishes to express his appreciation to N. Alin, R. Bensow, M. Berglund, C. Dutton, C. Duwig, F. Grinstein, M. Liefendahl, O. Parmhed, T. Persson, and U. Svennberg for providing experimental and computational data and for many good discussions. The author also acknowledges the financial support from the Swedish Armed Forces.

References

[1] Pope, S. B., 2000, *Turbulent Flows*, Cambridge University Press, Cambridge, England.
[2] Launder, B. E., and Spalding, D. B., 1972, *Mathematical Models of Turbulence*, Academic, New York.
[3] Wilcox, D. C., 1993, *Turbulence Modeling for CFD*, DCW Industries, La Cañada, CA.
[4] Ferziger, J. H., and Leslie, D. C., 1979, "Large Eddy Simulation—A Predictive Approach to Turbulent Flow Computation," AIAA Paper No. 79-1441.
[5] Boris, J. P., Grinstein, F. F., Oran, E. S., and Kolbe, R. L., 1992, "New Insights Into Large Eddy Simulation," Fluid Dyn. Res., **10**, pp. 199–228.
[6] Sagaut, P., 2001, *Large Eddy Simulation for Incompressible Flows*, Springer, New York.
[7] Boris, J. P., 1992, "On Large Eddy Simulations Using Subgrid Turbulence Models," in *Wither Turbulence? Turbulence at the Crossroads*, J. L. Lumly, ed., Lecture Notes in Physics, Vol. 357, Springer-Verlag, Berlin, p. 344.
[8] Bagget, J. S., 1998, "On the Feasibility of Merging LES With RANS for the Near Wall Region of Attached Turbulent Flows," Annual Research Briefs, Center of Turbulence Research, p. 51.
[9] Fureby, C., 2007, "On LES and DES of Wall Bounded Flows," Ercoftac Bulletin, No. 17.
[10] Fureby, C., Alin, N., Wikström, N., Menon, S., Persson, L., and Svanstedt, N., 2004, "Large Eddy Simulations of High Re-Number Wall Bounded Flows," AIAA J., **42**, pp. 457–468.
[11] Nikitin, N. V., Nicoud, F., Wasistho, B., Squires, K. D., and Spalart, P. R., 2000, "An Approach to Wall Modelling in Large Eddy Simulation," Phys. Fluids, **12**, pp. 1629–1632.
[12] Grinstein, F. F., and Fureby, C., 2004, "From Homogeneous Turbulent Flows to Pollutant Dispersion in Urban Areas: Recent Progress in Monotonically Integrated LES," Comput. Sci. Eng., **6**(2), pp. 36–49.
[13] Grinstein, F. F., Margolin, L., and Rider, B., 2007, *Implicit Large Eddy Simulation: Computing Turbulent Fluid Dynamics*, Cambridge University Press, in press.
[14] Moser, R. D., Kim, J., and Mansour, N. N., 1999, "Direct Numerical Simulation of Turbulent Channel Flow up to Re=590," Phys. Fluids, **11**, pp. 943–946.
[15] Wei, T., and Willmarth, W. W., 1989, "Reynolds Number Effects on the Struc-

Downloaded 03 Jun 2010 to 171.66.16.156. Redistribution subject to ASME license or copyright; see http://www.asme.org/terms/Terms_Use.cfm

ture of a Turbulent Channel Flow," J. Fluid Mech., **204**, pp. 57–95.

[16] Lourenco, L. M., and Shih, C., 1993, "Characteristics of the Plane Turbulent Near Wake of a Circular Cylinder, A Particle Image Velocimetry Study." Data taken from Ma, X., Karamanos, G. S., and Karniadakis, G. E., 2000, "Dynamics and Low-Dimensionality of a Turbulent Near Wake," J. Fluid Mech., **410**, pp. 29–65.

[17] Ong, J., and Wallace, L., 1996, "The Velocity Field of the Turbulent Very Near Wake of a Circular Cylinder," Exp. Fluids, **20**, pp. 441–453.

[18] Cantwell, B., and Coles, D., 1983, "An Experimental Study of Entrainment and Transport in the Turbulent Near Wake of a Circular Cylinder," J. Fluid Mech., **136**, pp. 321–374.

[19] Persson, T., Fureby, C., and Bensow, R., 2005, "Large Eddy Simulation and Deatched Eddy Simulation of Turbulent Flow Around a Circular Cylinder," Chalmers Report No. 05:98.

[20] Byun, G., and Simpson, R. L., 2005, "Structure of Three-dimensional Separated Flow on a Axisymmetric Bump," AIAA Report No. 05-0113.

[21] Persson, T. M., Liefevendahl, M., Bensow, R., and Fureby, C., 2005, "Numerical Investigation of the Flow Over an Axisymmetric Hill Using LES, DES and RANS," J. Turbul., **7**, pp. 1–17.

[22] Oran, S. S., and Boris, J. P., 2000, *Numerical Simulation of Reactive Flow*, Cambridge University Press, Cambridge, England.

[23] Chomiak, J., and Nisbeth, J., 1995, "Modeling Variable Density Effects in Turbulent Flames—Some Basic Considerations," Combust. Flame, **102**, pp. 371–386.

[24] Groves, N. C., Huang, T. T., and Chang, M. S., 1989, "Geometric Characteristics of DARPA SUBOFF Models," Report No. DTRC/SHD-1298-01.

[25] Huang, T. T., Liu, H.-L., Groves, N. C., Forlini, T. J., Blanton, J., and Gowing, S., 1992, "Measurements of Flows Over an Axisymmetric Body With Various Appendages (DARPA SUBOFF Experiments)," *Proceedings of the 19th Symposium on Naval Hydrodynamics*, Seoul, Korea.

[26] Persson, T., Bensow, R., Fureby, C., Alin, N., and Svennberg, U., 2004, "Large Eddy Simulation of the Viscous Flow Around Submarine Hulls," *Proceedings of the 25th Symposium on Naval Hydrodynamics*, St. John's, Canada, p. 261.

[27] Grinstein, F. F., and Fureby, C., 2002, "Recent Progress on MILES for High Re Flows," ASME J. Fluids Eng., **124**, pp. 848–861.

[28] Schumann, U., 1975, "Subgrid Scale Model for Finite Difference Simulation of Turbulent Flows in Plane Channels and Annuli," J. Comput. Phys., **18**, pp. 376–404.

[29] Goldstein, R. J., 1996, *Fluid Mechanics Measurements*, Taylor & Francis, Washington, D.C.

[30] Li, D. Q., 1994, "Investigation of Propeller Rudder Interaction by Numerical Methods," Ph.D. thesis, Chalmers University of Technology, Sweden.

[31] Hardin, J. C., and Pope, D. S., 1994, "An Acoustic/Viscous Splitting Technique for Computational Aeroacoustics," Theor. Comput. Fluid Dyn., **6**, pp. 323–340.

[32] Lighthill, M. J., 1952, "On Sound Generated Aerodynamically: I General Theory," Proc. R. Soc. London, Ser. A, **211**, pp. 564–587.

[33] Ffowkcs-Williams, J. E., and Hawkings, D. L., 1969, "Sound Generation by Turbulence and Surfaces in Arbitrary Motion," Philos. Trans. R. Soc. London, Ser. A, **264**(1151), pp. 321–342.

[34] Lyrintzis, A. S., 1994, "Review: The Use of Kirchhoff's Method in Computational Aeroacoustics," ASME J. Fluids Eng., **116**, pp. 665–676.

[35] Höld, R., Brenneis, A., Eberle, A., Schwarz, V., and Siegert, R., 1999, "Numerical Simulation of Aeroacoustic Sound Generated by Generic Bodies Placed on a Plate: Part 1—Prediction of Aerodynamic Sources," AIAA Paper No. 99-1896.

[36] Siegert, R., Schwarz, V., and Reichenberger, J., 1999, "Numerical Simulation of Aeroacoustic Sound Generated by Generic Bodies Placed on a Plate: Part 1—Prediction of Radiated Sound Pressure," AIAA Paper No. 99-1895.

[37] Delery, J., and Lacau, R. G., 1987, "Prediction of Base Flows," AGARD Report No. 654.

[38] Putnam, L. E., and Bissinger, N. C., 1985, "Results of AGARD Assessment of Prediction Capabilities for Nozzle Afterbody Flows," AIAA Paper No. 85-1464.

[39] Sahu, J., 1994, "Numerical Computations of Supersonic Base Flow With Special Emphasis on Turbulence Modelling," AIAA J., **32**, pp. 1547–1549.

[40] Fureby, C., Nilsson, Y., and Andersson, K., 1999, "Large Eddy Simulation of Supersonic Base Flow," AIAA Paper No. 99-0537.

[41] Forsythe, J. R., Hoffmann, K. A., and Squires, K. D., 2002, "Detatched-Eddy Simulation with Compressibility Corrections Applied to a Supersonic Axisymmetric Base Flow," AIAA Paper No. 02-0586.

[42] Simon, F., Deck, P., Guillen, P., and Cayzac, R., 2006, "Numerical Simulations of Projectile Baseflow," AIAA Paper No. 06-1116.

[43] Herrin, J. L., and Dutton, C. J., 1994, "Supersonic Base Flow Experiments in the Near Wake of A Cylindrical Afterbody," AIAA J., **32**, pp. 77–83.

[44] Mathur, T., and Dutton, J. C., 1996, "Base-Bleed Experiments With a Cylindrical Afterbody in Supersonic Flow," J. Spacecr. Rockets, **33**, pp. 30–37.

[45] Bardina, J., Ferziger, J. H., and Reynolds, W. C., 1980, "Improved Subgrid Scale Models for Large Eddy Simulations," AIAA Paper No. 80-1357.

[46] van Leer, B., 1979, "Towards the Ultimate Conservative Differencing Scheme V: A Second Order Sequel to Gudonovs Method," J. Comput. Phys., **32**, pp. 101–136.

[47] Boris, J. P., and Book, D. L., 1973, "Flux-Corrected Transport I. SHASTA, A Fluid Transport Algorithm That Works," J. Comput. Phys., **11**, pp. 38–69.

[48] Gottlieb, S., and Shu, C.-W., 1998, "Total Variational Diminishing Runge-Kutta Schemes," Math. Comput., **67**, pp. 73–85.

[49] Kohse-Höinghaus, K., Barlow, R. S., Aldén, M., and Wolfrum, J., 2005, "Combustion at the Focus: Laser Diagnostics and Control," Proc. Combust. Inst., **30**, pp. 89–123.

[50] Vervish, L., Domingo, P., and Hauguel, R., 2003, "Turbulent Combustion in the Light of Direct and Large Eddy Simulation," *Turbulent Shear Flow Phenomena*, Sendai, Japan, Vol. 3.

[51] Mantel, T., Egolfopoulos, F., and Bowman, C. T., 1996, "A New Methodology to Determine Kinetic Parameters for One- and Two-Step Chemical Models," Stanford CTR Summer Program.

[52] Libby, P. A., and Williams, F. A., 1980, "Fundamental Aspects," in *Turbulent Reactive Flows*, P. A. Libby and F. A. Williams, eds., Springer-Verlag, Berlin, p. 1.

[53] Poinsot, T., and Veynante, D., 2001, *Theoretical and Numerical Combustion*, Edwards, Ann Arbor.

[54] Westbrook, C., and Dryer, F., 1981, "Simplified Reaction Mechanisms for the Oxidation of Hydrocarbon Fuels in Flames," Combust. Sci. Technol., **27**, pp. 31–43.

[55] Fureby, C., 2006, "A Comparison of Flamelet Models for Premixed Turbulent Combustion," AIAA Paper No. 06-0155.

[56] Sjunneson, A., Olovsson, S., and Sjöblom, B., 1991, "Validation Rig—A Tool for Flame Studies," Presented at the *ISABE conference*, Nottingham, UK.

[57] Sjunnesson, A., Henriksson, P., and Löfström, C., 1992, "CARS Measurements and Visualization of Reacting Flows in a Bluff Body Stabilized Flame," AIAA Paper No. 92-3650.

[58] Fureby, C., 2000, "Large Eddy Simulation of Combustion Instabilities in a Jet-Engine Afterburner Model," Combust. Sci. Technol., **161**, pp. 213–243.

[59] Sanquer, S., Bruel, P., and Deshaies, B., 1998, "Some Specific Characteristics of Turbulence in the Reactive Wakes of Bluff Bodies," AIAA J., **36**, pp. 994–1001.

[60] Weller, H. G., Tabor, G., Jasak, H., and Fureby, C., 1997, "A Tensorial Approach to CFD Using Object Oriented Techniques," Comput. Phys., **12**, pp. 620–631 (see also www.http.OpenFoam.com).

Downloaded 03 Jun 2010 to 171.66.16.156. Redistribution subject to ASME license or copyright; see http://www.asme.org/terms/Terms_Use.cfm

Gopal Patnaik
e-mail: patnaik@lcp.nrl.navy.mil

Jay P. Boris
e-mail: boris@lcp.nrl.navy.mil

Theodore R. Young
e-mail: young@lcp.nrl.navy.mil

Laboratory for Computational Physics
and Fluid Dynamics,
Naval Research Laboratory,
Washington, DC 20375

Fernando F. Grinstein
Applied Physics Division,
MS-B259,
Los Alamos National Laboratory,
Los Alamos, NM 87545
e-mail: fgrinstein@lanl.gov

Large Scale Urban Contaminant Transport Simulations With Miles

Airborne contaminant transport in cities presents challenging new requirements for computational fluid dynamics. The unsteady flow involves very complex geometry and insufficiently characterized boundary conditions, and yet the challenging and timely nature of the overall problem demands that the turbulence be included efficiently with an absolute minimum of extra memory and computing time requirements. This paper describes the monotone integrated large eddy simulation methodology used in NRL's FAST3D-CT (CT is contaminant transport) simulation model for urban CT and focuses on critical validation issues that need to be addressed to achieve practical predictability. Progress in validation studies benchmarking with flow data from wind-tunnel urban model simulations and actual urban field studies are reported. Despite inherent physical uncertainties and current model tradeoffs, it is clearly possible to achieve some degree of reliable prediction. [DOI: 10.1115/1.2801368]

Keywords: urban CFD, MILES, LES, urban aerodynamics

1 Introduction

Predicting urban airflow accompanied by contaminant transport presents new, extremely challenging modeling requirements [1]. Reducing health risks from the accidental or deliberate release of chemical, biological, or radiological (CBR) agents and pollutants from industrial leaks, spills, and fires motivates this work. Configurations with very complex geometries and unsteady buoyant flow physics are involved, so the widely varying temporal and spatial scales exhaust current modeling capacities. Crucial technical issues include turbulent fluid transport and boundary-condition modeling, and postprocessing of the simulation results for practical use by responders to actual emergencies.

Relevant fluid dynamic processes to be simulated include complex building vortex shedding, flows in recirculation zones, and approximating the dynamic subgrid-scale (SGS) turbulent and stochastic backscatter. The model must also incorporate a consistent stratified urban boundary layer with realistic wind fluctuations, solar heating including shadows from buildings and trees, aerodynamic drag, and heat losses due to the presence of trees, surface heat variations, and turbulent heat transport. Because of the short time spans and large air volumes involved, modeling a pollutant as well mixed globally is typically not appropriate. It is important to capture the effects of unsteady, buoyant flow on the evolving pollutant concentration distributions. In typical urban scenarios, both particulate and gaseous contaminants behave similarly insofar as transport and dispersion are concerned, so that the contaminant spread can usually be simulated effectively based on appropriate pollutant tracers with suitable sources and sinks. In some cases, the full details of multigroup particle distributions are required. In such cases, additional physics includes the deposition, resuspension, and evaporation of contaminants. Despite inherent physical uncertainties and current model tradeoffs, this paper will show that it is possible to achieve some degree of reliable prediction of contaminant transport within urban areas.

1.1 Established Approach: Gaussian Plume Models. Contaminant plume prediction technology currently in use is based on Gaussian similarity solutions (“puffs”). This class of extended Lagrangian approximations is only appropriate for large scales and flat terrains. Separated flow and vortex shedding from buildings, cliffs, or mountains are absent. Diffusion is used in plume/puff models to mimic the effects of turbulent dispersion caused by the complex building geometry and by wind gusts of comparable and larger size. Detailed comparisons [2,3] using actual “common use” puff/plume models show a range of results depending on how much of the 3D urban boundary layer information from the detailed simulation is incorporated in the Gaussian model.

1.2 Urban Aerodynamics Approach. Since fluid dynamic convection is the most important physical process involved in CBR transport and dispersion, the greatest care and effort should be invested in its modeling. The advantages of the computational fluid dynamics (CFD) approach and large eddy simulation (LES) representation include the ability to quantify complex geometry effects, to predict dynamic nonlinear processes faithfully, and to treat turbulent problems reliably in regimes where experiments, and therefore model validations, are impossible or impractical.

1.2.1 Standard Computational Fluid Dynamics Simulations. Solving for the motion and dispersion of airborne contaminants in the downtown area of a city is a problem for time-dependent aerodynamic CFD methods. Thus, computing urban aerodynamics accurately is a time-intensive, high-performance computing problem. However, using this technology for the emergency assessment of industrial spills, transportation accidents, or terrorist attacks (biological or chemical) requires very tight time constraints that suggest simple approximations, which unfortunately produce inaccurate results. The unavoidable tradeoffs demand choosing between fast (but inaccurate) and much slower (but highly accurate) models.

1.2.2 Large Eddy Simulation Approach for Contaminant Transport. Direct numerical simulation (DNS) is prohibitively expensive for most practical flows at moderate-to-high Reynolds number, and especially so for urban contaminant transport (CT) studies. On the other end of the CFD spectrum are the standard industrial methods such as the Reynolds-averaged Navier-Stokes (RANS) approach, e.g., involving k-ε models, and other first- and second-order closure methods, which simulate the mean flow and approximately model the effects of turbulent scales [4,5]. These are generally unacceptable for urban CT modeling because they are unable to capture unsteady plume dynamics. LES constitutes

---

Contributed by the Fluids Engineering Division of ASME for publication in the Journal of Fluids Engineering. Manuscript received February 13, 2007; final manuscript received April 27, 2007. Review conducted by Dimitris Drikakis.

Copyright © 2007 by ASME

Downloaded 03 Jun 2010 to 171.66.16.156. Redistribution subject to ASME license or copyright; see http://www.asme.org/terms/Terms_Use.cfm

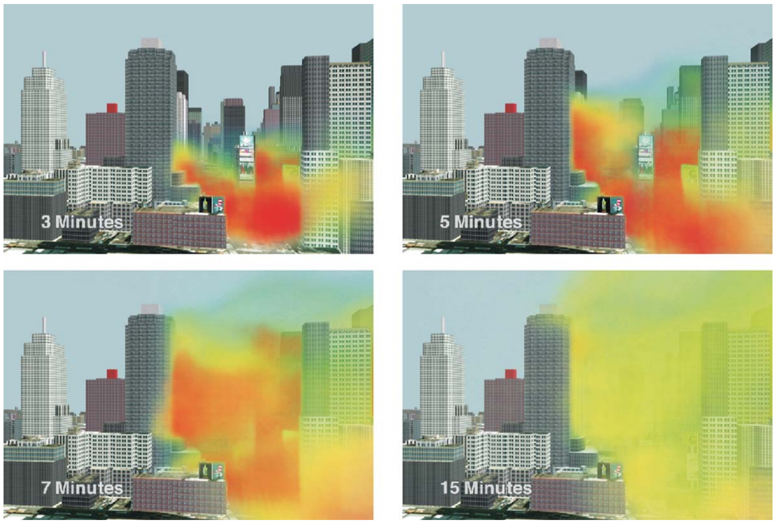

Fig. 1 Contaminant dispersion from an instantaneous release in Times Square, New York City as predicted by the FAST3D-CT MILES model. Concentrations shown at 3 min, 5 min, 7 min, and 15 min after release.

an effective intermediate approach between DNS and RANS methods [6]. LES is capable of simulating key flow features that cannot be handled with RANS or Gaussian plume methods such as significant flow unsteadiness and localized vortex shedding, and provides higher accuracy than the industrial methods but at an increased cost. The main assumptions of LES are (i) that transport is largely governed by large-scale unsteady convective features that can be resolved, (ii) that the less-demanding accounting of the small-scale flow features can be undertaken by using suitable SGS models. Given its potential for computational efficiency, the monotone integrated LES (MILES) approach (see Ref. [7] for a recent review) is ideally suited to CFD-based urban-scale plume simulations, an application where RANS methods are inadequate and classical LES methods are too expensive.

1.2.3 Monotone Integrated Large Eddy Simulation for Urban-Scale Simulations. The three-dimensional FAST3D-CT MILES model [8–10] is based on a scalable, low dissipation, fourth-order phase-accurate FCT convection algorithm [11,12], implementing direction-split convection, second-order predictor-corrector temporal integration, and time step splitting techniques. The particular FCT used in FAST3D-CT is documented in Boris et al. [13]. In the urban CT simulation model [8], the relevant system of equations for the problem under consideration involves the time-dependent buoyant flow equations for mass and momentum conservation,

$$\partial_t(\rho) + \mathrm{div}(\mathbf{v}\rho) = 0$$

$$\partial_t(\rho\mathbf{v}) + \mathrm{div}(\rho\mathbf{v}\otimes\mathbf{v}) = \mathrm{div}(\mathbf{S}) - \mathrm{grad}(P) + \mathbf{f}$$

$$\mathbf{f}_x = \mathbf{f}_y = 0 \quad \mathbf{f}_z = \rho g(1 - T/T_o)$$

$$\partial_t(\Theta) + \mathbf{v}\,\mathrm{grad}(\Theta) = 0$$

$$\partial_t(\eta_i) + \mathbf{v}\,\mathrm{grad}(\eta_i) = 0, i = 1, \ldots$$

where Θ is the potential temperature and (η_i) are pollutant concentration tracers modeling different contaminants and/or release scenarios. The flow equations must be supplemented with an equation of state, appropriate inflow, outflow, and wall boundary-condition models. In the present work, the unfiltered unsteady equations are solved with an ideal-gas equation of state,

$$P = R\rho T$$

The potential temperature Θ is related to the fluid temperature T through

$$\Theta = T(1000/P)^{(R/C_p)}$$

where P is the pressure in millibars [14]. The potential temperature has the convenient property of being conserved during vertical movements of a gas parcel, provided heat is not added or removed during such excursions; in this way, the said parcel can be identified or labeled by its potential temperature. The model uses rough-wall-boundary-condition models for the surface stress and the heat transfer from the walls, and convective conditions at outflow boundaries. Inflow boundary-condition model implementation issues are extensively discussed further below in this paper. The simulation code is designed to run efficiently on a wide range of shared-memory platforms (e.g., SGI Altix, IBM Power4). Computational grids involving between 15×10^6 and 50×10^6 evenly spaced cells were typically used in the presently discussed simulations.

Other required physical models include the ability to emulate multiphase flows, seasonally adjusted drag, and heat transfer effects due to trees, solar heating effects, and stochastic turbulent backscatter. A recent detailed description of the physics submodels can be found elsewhere [15]. Incorporating specific models for these processes in simulation codes is always a challenge but can be accomplished with reasonable fidelity. The primary difficulty is the effective calibration and validation of these physical models since much of the input needed from experimental measurements of these processes is typically insufficient or even nonexistent. Even though the individual models can all be validated separately, the larger problem of validating the overall simulation code has to be tackled as well.

A practical example of urban-scale MILES illustrating the inherently difficult flow simulation issues is given in Fig. 1, showing contaminant dispersion in Times Square, New York City. The figure demonstrates the typical complex unsteady vertical mixing patterns caused by building vortex and recirculation patterns, and predicts endangered regions associated with this particular release scenario. In particular, the figure depicts the so-called *fountain* effect occurring behind three tall buildings. The fountain effect is the systematic migration of contaminant from ground level up the downwind side of tall buildings followed by continuous ejection

Downloaded 03 Jun 2010 to 171.66.16.156. Redistribution subject to ASME license or copyright; see http://www.asme.org/terms/Terms_Use.cfm

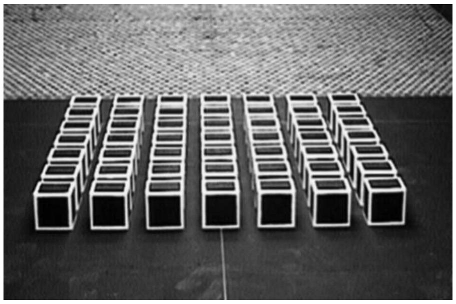

Fig. 2 USEPA Meteorological Wind Tunnel: 3D Array of Buildings (courtesy of Michael Brown, LANL). Previous reported studies used the USEPA wind-tunnel data to test flow simulation models but did not address their effects on CT.

into the air flowing over the tops of these buildings. It is thought to be driven by arch vortices [16] lying behind the buildings and has been observed in field experiments in Los Angeles [17] and reported in wind-tunnel studies (e.g., see Fig. 9 in Ref. [18]). Such inherently unsteady phenomena *cannot be captured by the commonly used puff/plume models* and are crucially important because they involve contaminant being transported downwind much faster than might be otherwise expected.

2 Urban Simulation Model Validation

Establishing the credibility of the solutions is one of the stumbling blocks of urban CFD simulations. The goal of validating a numerical model is to build a basis of confidence in its use and to establish likely bounds on the error that a user may expect in situations where the correct answers are not known. Validation with experiments requires well-characterized data sets with information content suitable to initiate and evaluate unsteady simulation models as well as the cruder steady-state models. Unfortunately, current full-scale field studies do not provide all this information: the data acquired are typically too sparse to fully characterize the flow conditions; the number of trials is limited; and trials cannot be repeated under the same conditions. Two possible validation approaches addressed here are to (1) compare urban flow simulations with carefully controlled laboratory-scale wind-tunnel experiments and (2) carry out detailed comparisons with actual urban field experimental databases as available.

2.1 Benchmarking With Wind-Tunnel Urban Model Data. Comparisons with laboratory measurements of flow and contaminant over a simple urban model were made to evaluate and validate the ability of FAST3D-CT to model contaminant transport. Brown et al. [19] measured velocity distributions and tracer concentrations associated with the flow over an array of cubes in the USEPA wind-tunnel facility (Fig. 2) under controlled conditions. The experiments were conducted in an open-return wind tunnel, with a working test section of length of 18.3 m, width of 3.7 m, and height of approximately 2.1 m. The wind-tunnel experiment simulated a neutrally stratified atmospheric boundary layer (ABL) flow over an array of buildings. The array consisted of 7×11 cubes ($0.15 \times 0.15 \times 0.15\ \mathrm{m}^2$) with one cube-height spacing between cubes. The reference velocity at one cube height is 3 m/s. These data sets provide high quality, spatially dense (but not time-resolved) data. In addition to velocity data, the measured volume fraction data of a C_2H_6 tracer released continuously at the centerline just behind the first cube was also reported. The laboratory profiles used as basic reference for the FAST3D-CT model benchmarking purposes were measured in the vertical symmetry plane of the building array.

One such study [20] of these data used the HIGRAD code, which is used to predict the evolution of atmospheric phenomena. HIGRAD is second order in time and space and uses a Smagorinsky-type or one-equation turbulent kinetic energy based subgrid closure. Advection is done with the multidimensional positive definite advection transport algorithm (MPDATA) scheme. These simulations reproduce the mean longitudinal velocity, including the recirculation patterns in the canyons behind the blocks. The turbulent kinetic energy is modeled well, except for some underprediction in the canyons. Another study [4] modeled the USEPA wind-tunnel experiment on the cube array using a RANS STREAM code. The Kato–Launder model was also used as an alternative to the standard Jones and Launder model. The agreement between the predicted mean velocity profiles and the experimental data is generally very good, with the greatest discrepancy occurring in the recirculation zone immediately downstream of the leeward face of the array. This study indicates that a RANS model is sufficient to predict the *mean flow* features.

Table 1 Runs performed with the FAST3D-CT MILES model. Runs 2 and 3 are omitted for brevity.

Run	Cube array?	Inflow fluctuations?
R1	Yes	Yes
R4	No	Yes
R5	Yes	No

Table 1 summarizes the various runs performed with the FAST3D-CT MILES model. Base line simulations were carried out on a $371 \times 350 \times 60$ mostly uniform grid (R1), with 1 cm resolution (corresponding to 15 cells per cube height). It is important to note here that the resolution would be considered fairly coarse if simulations of flow over a single (surface-mounted) cube are performed. On the other hand, this resolution is representative of what we can afford to resolve practically in urban simulations relative to typical building dimensions.

The inflow velocity consisted of a mean profile and superimposed fluctuations prescribed at $y=-0.5$ m (the front of the first cube is located at $y=0.0$, see Fig. 3). Including some finite-level fluctuation component at the inflow turns out to be crucial, as will be shown further below. The FAST3D-CT deterministic model of wind fluctuations [15] (see also Sec. 3) was included as part of the inflow boundary conditions (at $y=-0.5$ m). The strength of the model velocity fluctuations was calibrated to match the experimentally observed rms values at $y=-0.225$ m. An agreement was achieved visually by adjusting the amplitude, spatial wavelength, and temporal frequency of the imposed wind fluctuations in the

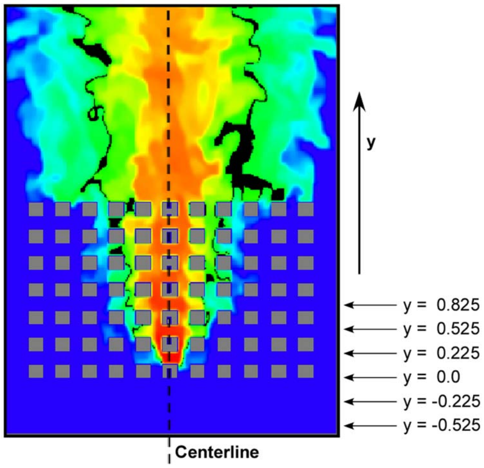

Fig. 3 Instantaneous distributions of the tracer concentration at the 2 cm height plane. Release occurred at a location behind the first cube in the vicinity of the centerline plane. Flow direction is from bottom to top.

Downloaded 03 Jun 2010 to 171.66.16.156. Redistribution subject to ASME license or copyright; see http://www.asme.org/terms/Terms_Use.cfm

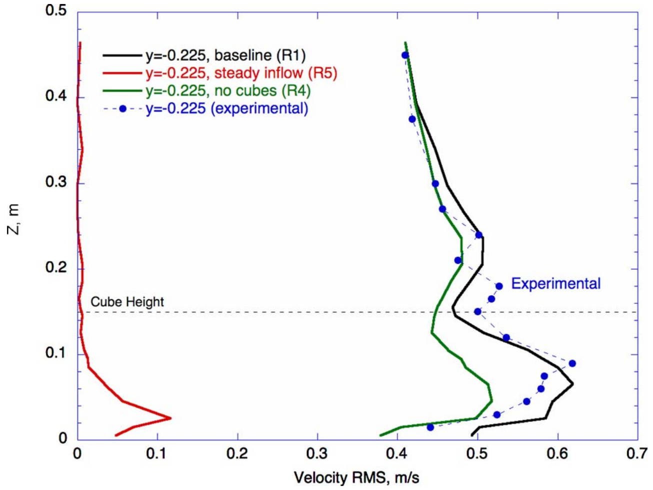

Fig. 4 Average rms streamwise velocity fluctuation profiles upstream of the first cube at the matching location (*y*=−0.225). Note that the cubes enhance fluctuation levels upstream.

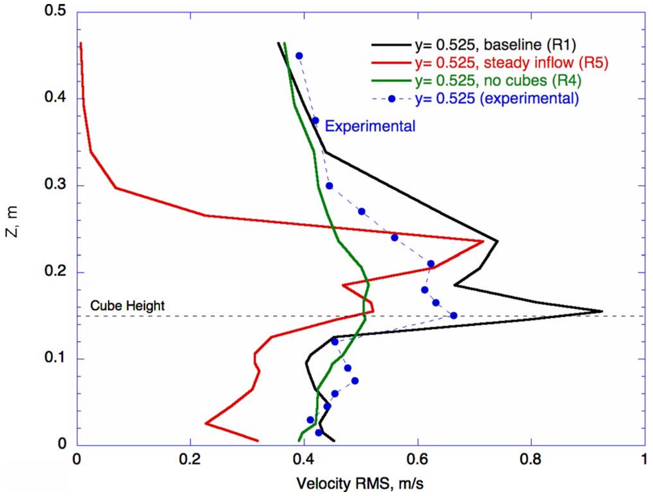

Fig. 6 Average rms streamwise velocity fluctuations in the canyon between the second and the third cube (second canyon). Absence of inflow fluctuations causes a significant underprediction of fluctuation levels.

unsteady-wind model in FAST3D-CT. This approach provided a practical approximation to the turbulent inflow boundary-condition specification problem (consistent with the available laboratory data). However, the actual fluctuation modeling and calibration are inherently difficult, given that there is no unique way to prescribe such fluctuations based on the available mean and standard deviation of the velocity components. In particular, it is well known that a simple inflow velocity model based on white noise perturbations is not adequate to emulate large-scale unsteadiness [21].

Typical instantaneous distributions of a simulated tracer concentration are visualized in a horizontal plane at the 2 cm height, as shown in Fig. 4. The simulated tracer modeled the continuous release in the laboratory experiments at a location behind the first cube on the centerline. The comparisons with experimental results shown in Figs. 4–8 are located in a vertical plane along the centerline. Figure 4 focuses on the rms streamwise velocity profiles at the $y=-0.225$ m location (selected as the location for matching with the experiments). By comparison with a case run with steady inflow conditions (no superimposed fluctuations, R5), the figure clearly shows that the imposed unsteady velocity components account for a large fraction of the velocity fluctuation upstream of the cube array location. Also shown is a curve for velocity rms for flow without the cube arrangement (R4) with exactly the same time-dependent inflow boundary conditions as in the simulations with the cube array present (R1). Interestingly, there is feedback from the cube array that adds to the prescribed velocity fluctuations, even at a reasonable distance upstream of the first cube.

Figure 5 shows profiles of the mean (time-averaged) streamwise velocity in the second canyon between cube rows. The mean velocity shows that the simulation model is able to capture the recirculation zone that is formed. In the experiments, the reverse velocity is highest at the first measurement location above the floor. This detail is not well captured by the simulations, especially in the first canyon (not shown). In the canyon between the second and the third cube (second canyon), the simulations show a better agreement with the experimental results. In this canyon, the flow is strongly conditioned by the effects of the two rows of cubes upstream, and the relative influence of the assumed structure of the inflow velocity fluctuations is diminished both in the experiments and in the simulations. Thus, the agreement is better.

Figure 6 compares rms streamwise velocity fluctuation profiles

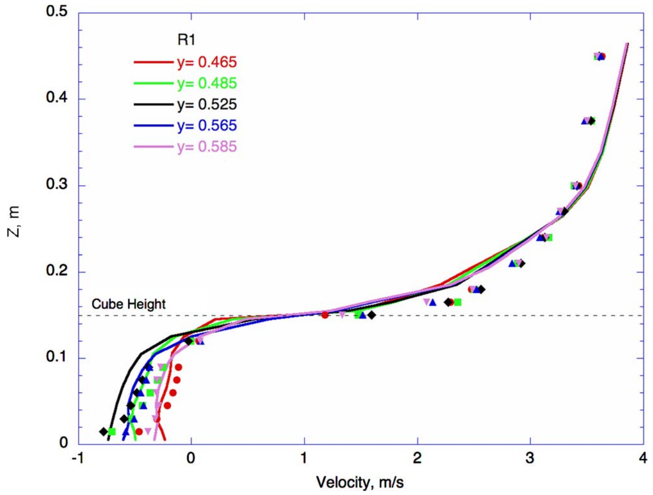

Fig. 5 Average velocity in the canyon between the second and the third cube (second canyon). Symbols are experimental results at the corresponding profile location.

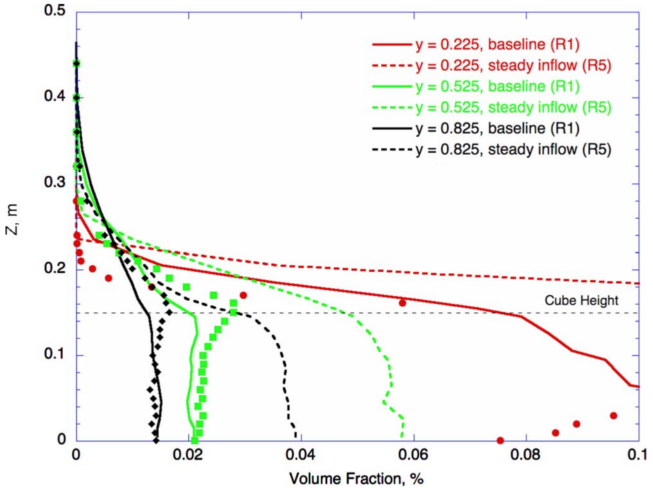

Fig. 7 Average concentration profiles are shown at selected stations located in the first three canyons. Corresponding experimental results are shown by symbols.

Downloaded 03 Jun 2010 to 171.66.16.156. Redistribution subject to ASME license or copyright; see http://www.asme.org/terms/Terms_Use.cfm

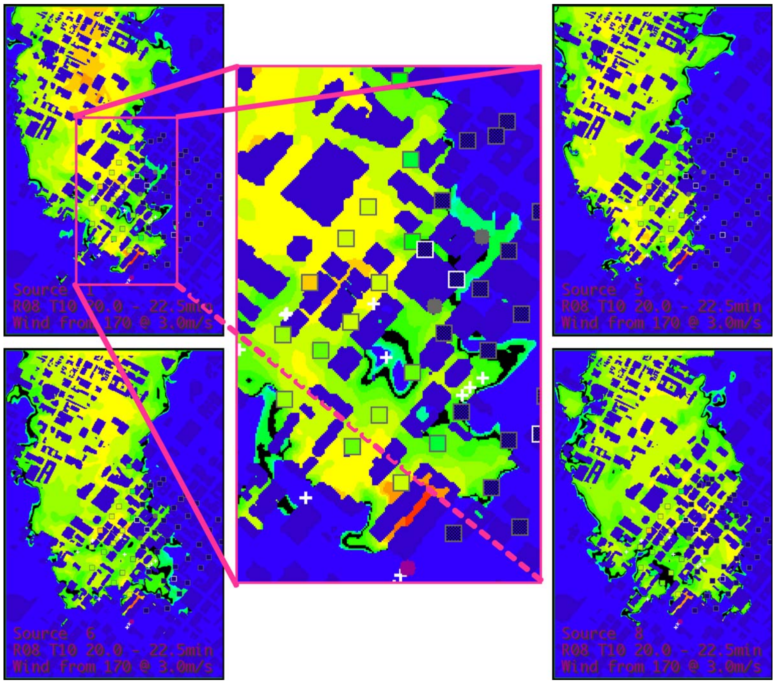

Fig. 8 Four of the eight FAST3D-CT realizations of a single event with different actual release times are compared with Los Angeles experimental sampler data

in the second canyon. Corresponding profiles from the runs carried out with the steady inflow conditions (R5) and without the cube arrangements (R4) are also shown for reference. The comparison shows the influence of the unsteady inflow on the velocity fluctuations in the canyon between the second and third row of cubes. It is apparent that fluctuations are largely due to the cube array up to about 1.5 cube heights.

A comparison of the average tracer concentration profiles from simulations and experiments is shown in Fig. 7 at selected stations located in the first three canyons. In all cases, the agreement is within a factor of 2, with the agreement somewhat worse in the first canyon—perhaps reflecting questions in resolving the precise details of the release there. The agreement gets better as we move downstream. This may also occur because the mean velocity and fluctuations agree better as we move downstream. In the simulations, the contaminant is found to rise somewhat higher in the boundary layer due to higher velocity fluctuations above one cube height in the numerical simulations (Fig. 6).

The crucial need for a finite level of inflow fluctuations in the simulations is very clearly indicated in Fig. 7. Disagreements with the laboratory data are significantly larger when steady inflow conditions (R5) are used. Unsteady fluctuations help condition the flow to enable it to resemble the experimental conditions more quickly downstream. Although the unsteady inflow specifications are important, they are not the main controlling factor once the geometry of the buildings (blocks) have had sufficient chance to influence the flow.

To summarize, we have found a very good agreement between the simulations and the laboratory data with respect to the mean velocities and a fair agreement with respect to the rms velocities and the tracer concentrations. While the agreement could presumably be improved with better calibration of the unsteady component of the prescribed inflow conditions, this calibration is very difficult since it must be based on laboratory (or field) databases, which typically provide single-point statistics, insufficient to characterize the unsteady structure of the flow. However, a particularly valuable insight is that despite these inherent difficulties in calibrating the inflow boundary conditions, the fluid dynamics within the cube arrangement (i.e., beyond the first canyon) seems to be partially insulated by the flow events in the boundary rows and thus appears to be less dependent on the exact details of the inflow conditions. The results indicate that a reasonable agreement can be achieved with benchmark laboratory data, with current MILES CT models using resolutions achievable in actual larger urban contexts. Indeed, for cities, we find also that a few city blocks of buildings strongly control the flow and the resulting contaminant even when the boundary flow is steady.

2.2 Los Angeles Simulations: Validation With Actual Urban Field Data. This section discusses the validation of FAST3D-CT, using full-scale field trial data for acute (short duration) releases in urban settings. Rappolt [17] conducted a series of short duration SF_6 releases in downtown Los Angeles, California. The SF_6 was released continuously for 5 min in each trial. Fifty synchronized samplers each took twelve 2.5 min duration samples for a total experimental trial duration of 30 min. The region instrumented was about 1 km^2, as shown by the square sampler locations in the panels of Fig. 8. Summary results from one of these field trials are presented in a shortened form.

FAST3D-CT was run for the same conditions as field trial 8 (as closely as could be determined). Moderate wind fluctuations were specified, and the sun angle was set to correspond to mid morning. Eight independent realizations of the experimental release were computed, all taken from the same fluctuating wind distribution. These realizations correspond to releases 5 min apart in a continuously computed flow field. 5 min was established as an adequate decorrelation time for the computational experiments.

Cross sections of the contaminant concentration for four of the eight realizations are shown in Fig. 8 for the tenth sampling interval, 22.5 to 25.0 min. This interval begins 25 min after the SF_6 release commenced. The differences from one realization to another are substantial, as evidenced by comparing the four outer panels. Obtaining equivalent multiple realizations of the experimental plumes is not realistically possible at city scale, so there is no direct experimental yardstick for comparing a measured to a computed concentration. This is an acknowledged drawback to

Downloaded 03 Jun 2010 to 171.66.16.156. Redistribution subject to ASME license or copyright; see http://www.asme.org/terms/Terms_Use.cfm

Table 2 Congruency counts

Wind 170 deg at 3 m/s	±20%	0.5 to 2×	0.2 to 5×	0.1 to 10×	Counts
Field trial versus simulations (average)	14.5%	39.5%	73.8%	88.4%	1147
One realization versus simulations (average)	19.5%	53.6%	84.4%	90.0%	1496

field trials. How close two different solutions actually are depends on the natural variability to be expected in the measured contaminant distribution.

By computing multiple realizations, however, we can measure the expected concentration variance computationally, and this provides a quantitative yardstick—as long as background conditions, including the wind fluctuations, are well characterized. When impressed wind gusts were turned off completely in the simulations, only a small reduction in the overall computed concentration variability was observed because building vortex shedding still provides turbulence and the boundary layer is unstable from solar heating. In each of the four realizations shown in Fig. 8, the set of 50 experimental sampler values (squares) is shown for comparison, colored with the same concentration scale as used for the FAST3D-CT simulations. The blow-up of one realization in the center of the figure shows this comparison of the experimental and simulated values more clearly.

Several of the accepted techniques for comparing a simulation with a single experimental realization [22–24] were applied to these data. Scatter plots on a log-log scale were constructed for the experimental measurements plotted versus the ensemble of simulated measurements. The main result is that when one simulated realization is plotted against all the others, as if it were the experiment, the scatter plots are very similar to those showing the experimental data against all the realizations. Congruency counts are also used to compare model results with a single field trial. For the eight computational realizations of a base line simulation (wind from 170 deg at 3 m/s), the percentages of simulation data points within 20% of the experimental values within a factor of 2, 5, and 10 were computed. Table 2 summarizes these results for the field trial and for one computational realization compared to the full set of simulated realizations.

About 160 of the possible 600 field trial values were above the experimental threshold of 20 ppt (parts per trillion). The total number of counts is about eight times this number because there were eight realizations. It is seen that almost 90% of all observations (center row of Table 2) were within a factor of 10, almost 75% within a factor of 5, but barely 40% were within a factor of 2. Only about 15% of the number pairs were within 20% of each other. Is this a good or a bad agreement? Exactly the same congruency count test was performed by comparing the numerical realizations with the ensemble comprised of the set of the remaining seven realizations. In this case, we know that each of the realizations is coming from the same distribution, so the lack of perfect agreement must be attributed to the natural variability from one realization to another. It cannot be the result of any error in the solutions or systematic differences between distributions. A typical result is also given in the bottom row of Table 2. Less than 20% of the number pairs are within 20% of each other, a little over 50% with a factor of 2, less than 85% with a factor of 5, and about 90% within a factor of 10.

We conclude that the field trial-to-simulation congruency comparison is nearly the same as the simulation-to-simulation comparison. This means that there is no reason to expect that any method could give closer congruency between simulation and experiment, given the differences from one simulated realization to another. Therefore, to gain a more quantitative way to look at this comparison, we began to study the distributions of the simulated values in the ensemble of realizations.

Figure 9 shows the distributions of simulated values at the location of Sampler 25 for 6 of the 12 sampling intervals (2.5 min in duration) beginning with the SF_6 release and continuing for half an hour. Sampler 25 was chosen because it had measured concentrations above the threshold for all 12 sampling intervals. The horizontal concentration scale is logarithmic in each small figure, as used in other validation studies because of the wide range of meaningful concentration values. Representative concentration values are collected at the experimental sampling sites in the simulation and at nearby points to build up the relatively continuous distributions shown. The distribution of concentration values collected this way is reasonably Gaussian in each time interval after a few minutes have elapsed. Therefore, the mean and stan-

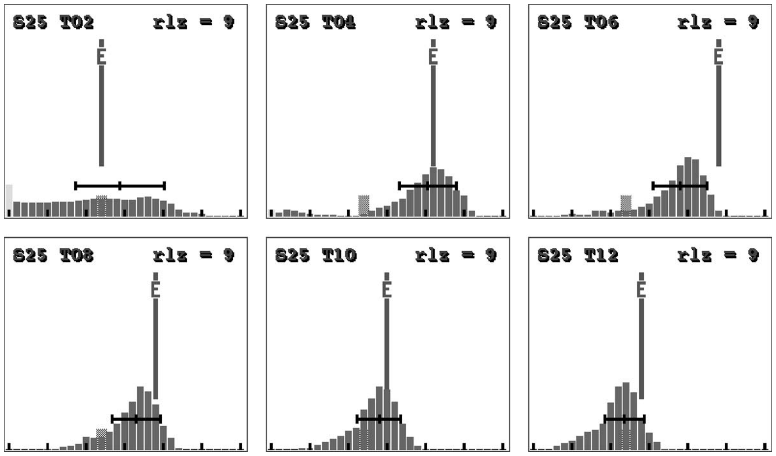

Fig. 9 Ensemble concentration distribution functions from six FAST3D-CT simulated realizations at the location of Sampler 25 in run LA 8. The vertical lines denoted with "E" indicate the experimental measurement and the short crosshatched bar is the threshold value of 20 ppt used for this comparison.

Downloaded 03 Jun 2010 to 171.66.16.156. Redistribution subject to ASME license or copyright; see http://www.asme.org/terms/Terms_Use.cfm

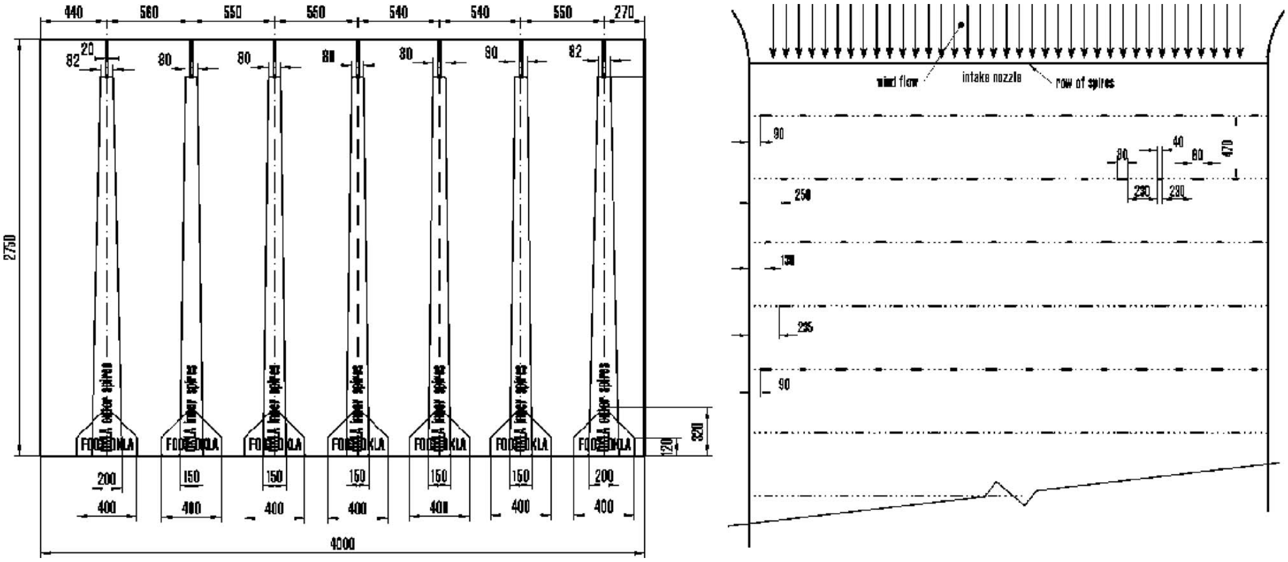

Fig. 10 Geometry of spires and surface roughness elements used to generate the turbulent urban boundary layer in the University of Hamburg Wind Tunnel. (Figure courtesy of B. Leitl, U. Hamburg.)

dard deviations of the concentrations are also meaningful. This standard deviation approximates the concentration variance needed to compare simulated and experimental values quantitatively.

The center of the black bar in each small figure is at the mean value, and the bar extends one standard deviation on either side of the mean for each local distribution. This particular statistical comparison shows that the experimental data taken by Sampler 25 has a 50% chance of having been drawn from the simulated distributions because the chi-square (χ^2) value is about 13 for 12 degrees of freedom [25]. This particular agreement is not very good because the sampler was very close to the source and thus was above the threshold for all 12 sampling intervals.

Most of the other samplers that were above the threshold for a few of the sampling intervals showed much better agreement using the χ^2 test. When all samplers and time intervals were taken into account, there were 159 degrees of freedom in the experiment, and the base line simulation ensemble showed a 98% agreement probability with field trial 8. This means that this level of agreement can be obtained by chances less than 1 in 50. This analysis approach allows us to derive quantitative (probabilistic) results regarding the validity of the FAST3D-CT simulations.

Furthermore, this quantitative analysis permits parameter variations and system sensitivity studies. It was found that the quality of agreement depends at most weakly on the meteorological wind fluctuations assumed because the buildings generate most of the turbulence from vortex shedding. The inflow wind direction and speed were also varied from the nominal base line run at 170 deg at 3 m/s for trail 8. Changing the wind 10 deg in one direction or increasing the speed by 1 m/s gave unacceptably poor results (37% and 2% probability of agreement, respectively). However, changing the wind 10 deg in the other direction or reducing the speed to 2 m/s gaves results in a somewhat better agreement with the field data than the base line simulations (99.7% and 99.9% probability of agreement, respectively). By way of contrast, using only the congruency count test to conduct these sensitivity studies, it could not be determined with any confidence that some case other than the base line simulation conditions might actually be a better fit to the overall experiment.

In closing, we summarize the Los Angeles field trial validation studies to date. The multirealization FAST3D-CT simulations with a 6 m resolution seem to be virtually indistinguishable from the Los Angeles field trial data. Naturally, occurring variations between realizations can be quite large due to building vortex shedding, even when inflow wind gusts are absent, but multirealization CFD simulations provide a way to approximate the missing concentration variability data for a scientifically quantitative comparison of data sets. The χ^2-probability approach also gives a sensitive way to approximate unknown parameters as well as to validate time-dependent CFD models.

3 Atmospheric Boundary Layer Specification

Detailed simulation of unsteady flow and transport phenomena is also very sensitive to the precise unsteady features of the prescribed turbulent upstream flow conditions. The ABL characterization upstream of the finite urban computational domain directly affects the boundary-condition prescription required in the simulations. Numerical sensitivity studies performed by the authors (e.g., Sec. 2.1) show that wind fluctuation specifics are major factors in determining urban contaminant dispersion. The important length scales (tens of meters to kilometers) and time scales (seconds to minutes) in wind gusts can be resolved easily by CFD models that accurately resolve the buildings. Since they can be resolved, the gusts *must not* be averaged out.

A deterministic model for an evolving realization of upstream flow fluctuations is included in FAST3D-CT dependent on input parameters used to approximate particular atmospheric conditions being simulated [15]. Three types of motion can be superimposed at several different wavelengths to construct this function. A shearing motion transverse to the average wind direction, typical of meanders, is impressed with a sinusoidal structure. Superimposed on this are horizontal pancake vortices at several scales to represent a type of flow possible in stratified fluids. The third motion is due to longitudinal vortices with finite vertical and horizontal extent to represent wind-induced hairpin vortices found in typical boundary layers. The vertical dependence of these resolved-scale fluctuations is a superposition of two functions, one for the unobstructed flow and one to provide additional fluctuations due to buildings upstream of the domain. When the simulated flow field is allowed to evolve over 0.5–1.0 km of actual city geometry, initial inconsistencies and uncertainties are replaced by a more self-consistent flow. However, flow data from laboratory experiments and field trials are typically inadequate and/or insufficient to fully characterize the ABL conditions necessary to specify the inflow boundary models used in the simulation model. Typical

Downloaded 03 Jun 2010 to 171.66.16.156. Redistribution subject to ASME license or copyright; see http://www.asme.org/terms/Terms_Use.cfm

difficulties that arise when attempting to model in detail important modes of laboratory turbulent inflow conditions are demonstrated in Sec. 2.1.

Our more recent approach to address this problem involves joint studies with ongoing experiments at the University of Hamburg wind tunnel (UHWT), taking advantage of their extensive experience with the development of a scale model of Oklahoma City for the Joint Urban 2003 Field Experiment [26]. Detailed CFD simulations of upstream conditions in the UHWT seek to provide more accurate and representative inflow conditions. The UHWT experiments use a vertical cross-stream row of thin triangular shaped spires followed by approximately 10 m of roughness elements attached to the lower floor downstream from the spires and upwind of the experimental area (Fig. 10). The spires induce the large turbulent structures in the flow representative of gross (actually observed) ABL field conditions, while the roughness elements induce smaller scale turbulence drag at the lower surface typical of an urban environment.

The CFD code employed for this task, FAST3D [27], is particularly well suited to model a complex geometry of the upwind inlet area of the wind tunnel. The geometry of the spires and roughness elements in the wind-tunnel inlet were accurately modeled in FAST3D to generate the simulated turbulent urban boundary layer data. We modeled three of the inlet spires out of the seven that are actually installed in the wind tunnel, which was needed to capture the important transverse structures. Various configurations of the roughness elements were tried in the numerical simulations. The number, or density, of the elements was the variable. They were imposed at cell boundaries as infinitesimally thin vertical tabs upwind along the lower surface. The tabs effectively blocked the streamwise flow through those cells, creating drag and small-scale turbulence along the floor.

A time history of data from the simulations recorded from a transverse plane just upstream of the urban model corresponding to data gathered in the wind-tunnel campaigns is benchmarked against laboratory wind-tunnel data (e.g., Fig. 11) and can then be used to provide a simulated reconstruction of typical features of a 3D turbulent inflow boundary layer in urban models. The recorded unsteady data can be used directly to calibrate phenomenological models, as described above. Outstanding issues remain unresolved in this area both observationally and computationally; deterministic [28] and other [21] approaches to formulating turbulent inflow boundary conditions for urban simulations are also being investigated.

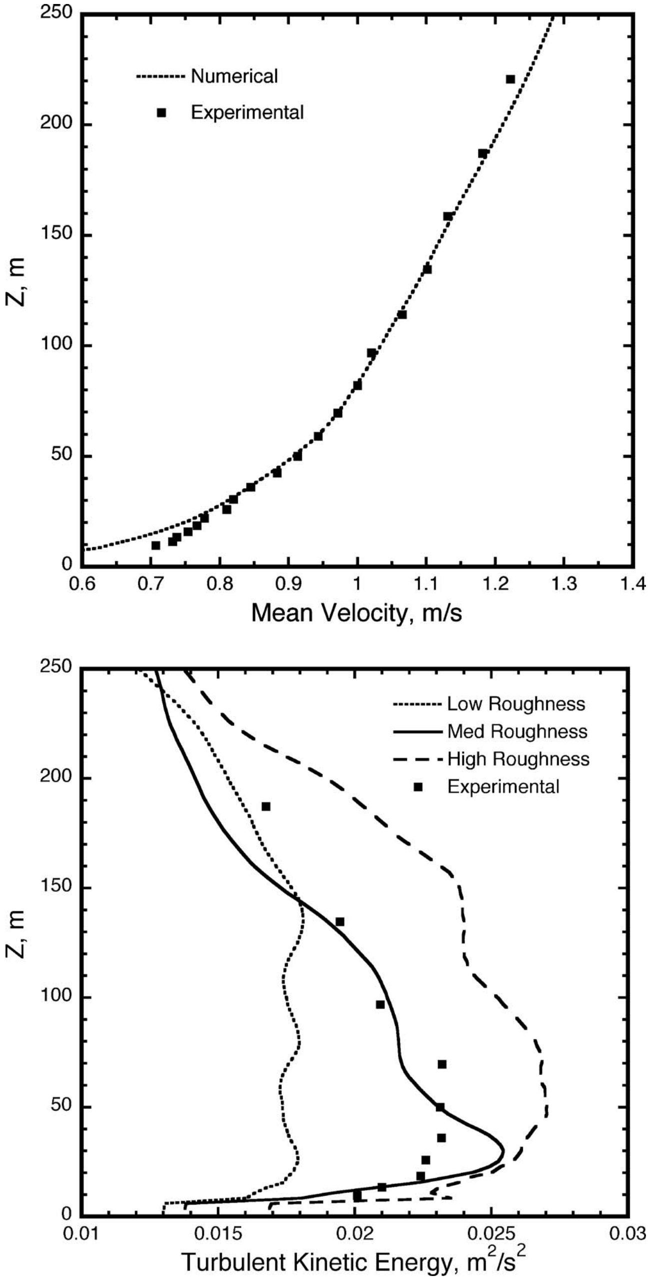

Fig. 11 Comparison of mean velocities (left) and turbulent kinetic energy (right). The figure shows the sensitivity of the TKE to the amount of roughness modeled on the lower surface. The intensity of the TKE increases with the amount of roughness.

4 Conclusions

Physically realistic, time-dependent, urban CT simulations are now possible but still require some resolution compromises due to time and computer limitations. Detailed time-dependent wind field observations at key locations can be processed suitably to provide initial and boundary conditions and, at the least, can be used for global validation. We believe that the building and large-scale fluid dynamics effects that can be captured today govern the turbulent dispersion. We know that the quality of the spatially and time-varying boundary conditions imposed (i.e., the fluctuating winds) requires improvement. Inherent uncertainties in simulation inputs and model parameters beyond the environmental conditions also lead to errors that need to be further quantified by comparison with high quality reference data. A judicious choice of test problems for calibrating models and numerical algorithms is essential, and sensitivity analysis helps to determine the most important processes requiring improvement.

Despite inherent physical uncertainties and current model tradeoffs, it is clearly possible to achieve some degree of reliable prediction. Direct comparisons with field data, e.g., from Los Angeles, provide an intuitively more “believable” validation; however, the sparsity of experimental data makes quantitative validation difficult. Wind-tunnel comparisons allow a more rigorous validation, but typical available data insufficiently characterized the coherent structures that control dispersion.

The FAST3D-CT simulation model can also be used to simulate sensor and system response to postulated threats, to evaluate and optimize new systems, and to conduct sensitivity studies for relevant processes and parameters. Moreover, the simulations constitute a virtual test range for micro- and nanoscale atmospheric fluid dynamics and aerosol physics to interpret and support field experiments and to evaluate, calibrate, and support simpler models. In this context, we note a critical practical dilemma: Although our discussion has demonstrated that realistic unsteady 3D urban-scenario flow simulations are, in principle, currently feasible, they are also very expensive, and first responders and emergency managers coping with contaminant release threats cannot afford to

Downloaded 03 Jun 2010 to 171.66.16.156. Redistribution subject to ASME license or copyright; see http://www.asme.org/terms/Terms_Use.cfm

wait while actual simulations and data postprocessing are performed. An operational solution of this problem carries out unsteady CFD simulations in advance and precomputes compressed databases for specific urban areas incorporating suitable assumed weather and a full set of wind conditions and distributed test sources. The relevant information is summarized as Dispersion Nomograf™ data sets [10] so that it can be readily used through portable devices, with sensors providing current observational information regarding local contaminant concentrations and winds. This new approach is implemented in a system called CT-Analyst® [10].

Acknowledgment

The authors wish to thank Bob Doyle and Julie Pullen for helpful technical discussions and scientific contributions to this effort. They also thank Michael Brown for providing the USEPA Wind-Tunnel Data, as well as for very helpful discussions. The authors are especially grateful to Bernd Leitl for carrying out the experiments and providing the data from the U. Hamburg Wind Tunnel. Aspects of the work presented here were supported by ONR through NRL, MDA, DTRA, and the DoD HPCMPO.

References

[1] Britter, R. E., and Hanna, S. R., 2003, "Flow and Dispersion in Urban Areas," Annu. Rev. Fluid Mech., **35**, pp. 469–496.
[2] Pullen, J., Boris, J. P., Young, T. R., Patnaik, G., and Iselin, J. P., 2005, "A Comparison of Contaminant Plume Statistics From a Gaussian Puff and Urban CFD Model for Two Large Cities," Atmos. Environ., **39**, pp. 1049–1068.
[3] Gaydos, T. M., Nyden, I. J., Patnaik, G., and Obenschain, K. S., 2004, "Survey of Operationally Based Transport and Dispersion Software," *Proceedings of CBIS 2004*, DTRA, Ft. Belvoir, VA.
[4] Lien, F. S., and Yee, E., 2004, "Numerical Modelling of the Turbulent Flow Developing Within and Over a 3-D Building Array, Part 1: A High-Resolution Reynolds-Averaged Navier-Stokes Approach," Boundary-Layer Meteorol., **112**, pp. 427–466.
[5] Hendricks, E., Burrows, D. A., Diehl, S., and Keith, R., 2004, "Dispersion in the Downtown Oklahoma City Domain: Comparisons Between the Joint Urban 2003 Data and the RUSTIC/MESO Models," *Fifth AMS Symposium on the Urban Environment*, AMS, Boston, MA.
[6] Sagaut, P., 2005, *Large Eddy Simulation for Incompressible Flows*, 3rd ed., Springer, New York.
[7] Grinstein, F. F., and Fureby, C., 2004, "From Canonical to Complex Flows: Recent Progress on Monotonically Integrated LES," Comput. Sci. Eng., **6**, pp. 37–49.
[8] Cybyk, B. Z., Boris, J. P., Young, T. R., Lind, C. A., and Landsberg, A. M., 1999, "A Detailed Contaminant Transport Model for Facility Hazard Assessment in Urban Areas," AIAA Paper No. 99–3441.
[9] Cybyk, B. Z., Boris, J. P., Young, T. R., Emery, M. H., and Cheatham, S. A., 2001, "Simulation of Fluid Dynamics Around Complex Urban Geometries," AIAA Paper No. 2001–0803.
[10] Boris, J. P., 2002, "The Threat of Chemical and Biological Terrorism: Preparing a Response," Comput. Sci. Eng., **4**, pp. 22–32.
[11] Boris, J. P., and Book, D. L., 1973, "Flux-Corrected Transport I, SHASTA, A Fluid Transport Algorithm That Works," J. Comput. Phys., **11**, pp. 8–69.
[12] Boris, J. P., and Book, D. L., 1976, "Solution of the Continuity Equation by the Method of Flux-Corrected Transport," Methods Comput. Phys., **16**, pp. 85–129.
[13] Boris, J. P., Landsberg, A. M., Oran, E. S., and Gardner, J. H., 1993, "LCPFCT—A Flux-Corrected Transport Algorithm for Solving Generalized Continuity Equations," U.S. Naval Research Laboratory Memorandum Report No. NRL/MR/6410–93–7192.
[14] Arya, S. P., 1988, *Introduction to Micrometeorology*, Academic, New York.
[15] Patnaik, G., Boris, J. P., Grinstein, F. F., and Iselin, J., 2005, "Large Scale Urban Simulations With FCT," *High-Resolution Schemes for Convection-Dominated Flows: 30 Years of FCT*, D. Kuzmin, R. Lohner, and S. Turek, eds., Springer, New York, pp. 105–130.
[16] Hussein, H. J., and Martinuzzi, R. J., 1996, "Energy Balance for Turbulent Flow Around a Surface Mounted Cube Placed in a Channel," Phys. Fluids, **8**, pp. 764–780.
[17] Rappolt, T. J., 2002, "Measurements of Atmospheric Dispersion in the Los Angeles Urban Environment Summer 2001," Tracer ES&T, Project Report No. 1322.
[18] Brown, M., 2004, "Urban Dispersion—Challenges for Fast Response Modeling," *Fifth AMS Symposium on the Urban Environment*, LANL Report No. LA-UR-04–5129.
[19] Brown, M. J., Reisner, J., Smith, S., and Langley, D., 2001, "High Fidelity Urban Scale Modeling," LANL Report No. LA-UR-01–1422.
[20] Smith, W. S., Brown, M. J., and DeCroix, D., 2002, "Evaluation of CFD Simulations Using Laboratory Data and Urban Field Experiments," *Fourth AMS Symposium on the Urban Environment*, AMS, Boston, MA.
[21] Druault, Ph., Lardeau, S., Bonnet, J. P., Coiffet, C., Delville, J., Lamballais, E., Largeau, J. F., and Perret, L., 2004, "Generation Three-Dimensional Turbulent Inlet Conditions for LES," AIAA J., **42**, pp. 447–456.
[22] Bendat, J. S., and Piersol, A. C., 2000, *Random Data: Analysis and Measurement Procedures*, 3rd ed., Wiley, New York.
[23] Hanna, S. R., Hansen, O. R., and Dharmavaram, S., 2004, "FLACS Air Quality CFD Model Performance Evaluation With Kit Fox, MUST, Prairie Grass, and EMU Observations," Atmos. Environ., **38**, pp. 4675–4687.
[24] Wirsching, P., Paez, T., and Ortiz, K., 2005, *Random Vibrations Theory and Practice*, Wiley, New York.
[25] 1964, *Handbook of Mathematical Functions*, M. Abramowitz and I. A. Stegun, eds., National Bureau of Standards, Washington, DC.
[26] 2001, "Preparation of Meteorological Input Data for Urban Site Studies," Office for Official Publications of the European Communities, Report No. EUR19446.
[27] Landsberg, A. M., Young, T. R., and Boris, J. P., 1994, "An Efficient, Parallel Method for Solving Flows in Complex Three-Dimensional Geometries," AIAA Paper No. 94–0413.
[28] Mayor, S. D., Spalart, P. R., and Tripoli, G. J., 2002, "Application of a Perturbation Recycling Method in the Large-Eddy Simulation of a Mesoscale Convective Internal Boundary Layer," J. Atmos. Sci., **59**, pp. 2385–2395.

Downloaded 03 Jun 2010 to 171.66.16.156. Redistribution subject to ASME license or copyright; see http://www.asme.org/terms/Terms_Use.cfm

Piotr K. Smolarkiewicz
National Center for Atmospheric Research,
Boulder, CO 80307
e-mail: smolar@ucar.edu

Len G. Margolin
Los Alamos National Laboratory,
MS F644, Los Alamos, NM 87545
e-mail: len@lanl.gov

Andrzej A. Wyszogrodzki
National Center for Atmospheric Research,
Boulder, CO 80307
e-mail: andii@ucar.edu

Implicit Large-Eddy Simulation in Meteorology: From Boundary Layers to Climate

The dynamics of the atmosphere and oceans pose a severe challenge to the numerical modeler, due in large part to the broad range of scales of length and time that are encompassed. Modern numerical methods based on nonoscillatory finite volume (NFV) approximations provide a simple and effective means for mitigating this challenge by reproducing the large scale behavior of turbulent flows with no need for explicit subgrid-scale models. In this paper, we describe the remarkable properties of a particular NFV model, multidimensional positive definite advection transport algorithm, and highlight its application to a variety of meteorological and turbulent flows.

[DOI: 10.1115/1.2801678]

Keywords: turbulence, large-eddy simulation, finite-difference methods for fluids, subgrid-scale models

1 Introduction

It is tempting to treat the issues of numerical methods and physics models as distinct. Models are the partial differential equations which with specified initial and boundary conditions, describe the physical processes we consider relevant. Numerical methods are the approximations that we use to solve the model stably and accurately. The introduction of nonoscillatory finite volume (NFV) methods approximately 30 years ago, however, has blurred this distinction. NFV approximations improve the physical realizability of simulations by preserving the monotonicity of solutions, insuring the positivity of fields like density and internal energy and guaranteeing the nonlinear stability of the simulation. More recently, NFV schemes have demonstrated another important property, namely, the ability to reproduce the large scale features of high Reynolds number turbulent flow with no need for any explicit subgrid-scale model. We refer to this property as implicit turbulence modeling. A recent monograph [1] provides an overview of the subject from various perspectives.

The virtues of NFV methods are widely appreciated in the computational fluid dynamics (CFD) community; however, their full potential is not generally realized in meteorology. Although many modern meteorological codes employ some form of nonoscillatory algorithm for the transport of thermodynamic scalars, none of the major global atmospheric or oceanic circulation codes employ NFV methods consistently to solve the entire model. Instead, the principal numerical techniques in use are centered-in-time-and-space (CTS) finite-difference, pseudospectral, or (more recently) semi-Lagrangian schemes. None of these techniques routinely incorporates nonoscillatory approximations and none, in particular, aims at taking advantage of implicit turbulence modeling. We believe this latter property may be an important factor in improving the fidelity of global climate simulations. In this paper, we review our progress in building a fully NFV model for simulating flows in atmospheres and oceans.

The prediction of the Earth's climate and weather is difficult in large part due to the ubiquity of turbulence in the atmosphere and oceans. Geophysical flows evince fluid motions ranging from dissipation scales as small as a fraction of a millimeter to planetary scales of thousands of kilometers. The span in time scales (from a fraction of a second to many years) is equally large. Turbulence in the atmosphere and the oceans is generated by heating and by boundary stresses—just as in engineering flows. However, geophysical flows are further complicated by planetary rotation and density/temperature stratification, which lead to phenomena not commonly found in engineering applications. In particular, rotating stratified fluids can support a variety of inertia-gravity and planetary waves. When the amplitude of such a wave becomes sufficiently large (i.e., comparable to the wavelength), the wave can break, generating a localized burst of turbulence. If one could see the phenomena that occur internally in geophysical flows at any scale, one would be reminded of familiar pictures of white water in a mountain stream or of breaking surf on a beach. The multiphase thermodynamics of the atmosphere and oceans—due to the ubiquity of water substance and salt, respectively—add further complexity of its own.

Because of the enormous range of scales, direct numerical simulation (DNS) of the Earth's weather and climate is far beyond the reach of current computational technology. Consequently, all efforts in numerical simulation must begin with an attempt to truncate the number of degrees of freedom of the atmosphere/ocean system to a magnitude that is tractable on modern computational machines, and to attempt to do so in as physically meaningful a way as possible. One established approach in the numerical study of turbulent atmospheric and oceanic flows is large-eddy simulation (LES). Most often, LES is understood as a numerical integration of coarse-grained (filtered) Navier–Stokes equations, where all scales of motion larger than some multiple of the grid interval ΔX are resolved explicitly, but the effects of finer (unresolved) scales are modeled based on universal properties of fully developed turbulence. The intent of LES is to account for the effects of subgrid-scale (SGS) motions (i.e., below the available resolution of the numerical model) on those resolved on the grid.

The formalism of decomposing flow variables into resolved and unresolved scales of motion by spatial filtering leads straightforwardly to altered equations, modified by the appearance of the divergence of the so-called SGS stress tensor. The elements of the SGS stress tensor are not computable, and their specification in terms of the resolved components of the flow variables forms an explicit SGS model. For example, the Smagorinsky model [2] popular in meteorology postulates a SGS stress tensor proportional to the rate of strain (of the resolved flow) via a local eddy-viscosity coefficient. The eddy coefficient itself is assumed to depend on the magnitude of the local strain rate. Universally valid

---

Contributed by the Fluids Engineering Division of ASME for publication in the JOURNAL OF FLUIDS ENGINEERING. Manuscript received January 18, 2007; final manuscript received July 21, 2007. Review conducted by Fernando Grinstein.

Downloaded 03 Jun 2010 to 171.66.16.156. Redistribution subject to ASME license or copyright; see http://www.asme.org/terms/Terms_Use.cfm

SGS models do not exist as yet, and it is easy to provide examples clearly violating assumptions behind the established LES approach [3]. Furthermore, formal SGS models are not necessarily simple, and when combined with nonorthogonal time-dependent geometries (forming a base for mesh refinement schemes), they become overly complicated and computationally cumbersome. In this context, the implicit modeling of turbulence by means of NFV schemes becomes particularly useful, as it dramatically simplifies the difficult task of simulating complex geophysical flows.

One may argue that the fact that finite-difference advection schemes contain implicit SGS models is by no means a revelation. Consider that any finite-volume advection scheme yields truncation terms in the form of a flux divergence. Thus, when such a scheme is employed to transport momentum, the truncation fluxes effectively define a subgrid-scale stress tensor. However, it remains an open question whether such implicit SGS models can be justified from first principles and whether they are universally useful. Due to the inherent nonlinearity and complexity of nonoscillatory solvers, the details of the leading-order truncation terms may be difficult to derive, although certain commonalities of all NFV schemes can be identified [4]. Successful simulations of turbulent flows that rely only on the dissipative properties of nonoscillatory advection schemes have been reported in a variety of regimes and applications for over ten years. Examples relevant to natural turbulent flows include Ref. [5], where the authors demonstrated that a mesoscale atmospheric code based on the NFV scheme multidimensional positive definite advection transport algorithm (MPDATA) [6,7] accurately reproduced (i.e., in close agreement with field and laboratory data and the existing benchmark computations) the dynamics of the convective planetary boundary layer (PBL), and Ref. [8], where this same numerical model was shown to capture nonstationary inhomogeneous anisotropic turbulence (with both upscale and downscale energy flows) induced by gravity-wave breaking in a deep stratified atmosphere. Complementarily, the implicit LES (ILES) property of MPDATA has been quantified in simulations of the canonical problem of decaying turbulence [4,8–11]. In particular, it has been demonstrated that dissipative properties of MPDATA are consistent with observable properties of dissipation in high Reynolds number flow; i.e., they verify the Kolmogorov "5/3" [10] and "4/5" laws [4].

Although the experimental (numerical) evidence in support of implicit turbulence modeling has been gathered for over a decade, the attempt to establish a theoretical rationale for implicit turbulence modeling has been made only recently. Margolin and Rider [12] have derived a finite-scale (i.e., filtered) version of the pointwise Burgers equation—appropriate for describing the dynamics of finite volumes of (Burgers) fluid. They compared this filtered equation to the MPDATA approximation of the pointwise equation and showed that MPDATA already accounts for the finite-scale effects. Since each computational cell is a finite volume, they rationalized that MPDATA more accurately represents the filtered equations of motion than the pointwise equations. This study has been extended to incompressible Navier–Stokes equations only recently [4].

2 Multidimensional Positive Definite Advection Transport Algorithm

MPDATA was invented in the early 1980s as an inexpensive alternative to flux-limited schemes for evaluating the advection of nonnegative thermodynamic variables (such as liquid water or water vapor) in atmospheric cloud models. Since then, MPDATA has evolved from a simple advection scheme to a general approach for integrating the conservation laws of geophysical fluids from microscales to planetary scales [3]. A comprehensive technical review of MPDATA, including both the underlying concepts and the details of implementation, can be found in Ref. [6]. Recent advancements in an unstructured mesh environment are summarized in Ref. [7]—an introductory article to the (double) special issue of the *International Journal for Numerical Methods in Fluids*, devoted solely to MPDATA methods [13].

In its basic form, MPDATA is sign preserving, fully second-order accurate, and conservative. A variety of options have been documented, which extend MPDATA to full monotonicity preservation, to third-order accuracy, and to fields that do not preserve sign (such as momentum). Unlike most nonoscillatory methods, MPDATA is based directly on the *convexity* of upwind advection—i.e., numerical solutions remain bounded by surrounding local values from the preceding time step, given a uniform advecting flow and adequately limited temporal increment; for nonuniform flow, a weaker condition of sign preservation can be assured—rather than on the idea of flux limiting. In practical terms, the algorithm consists of a series of donor-cell steps; the first step provides a first-order accurate solution, while subsequent steps compensate higher-order truncation errors, derived analytically from modified equation analysis of the upwind scheme. To illustrate, an elementary M-dimensional advection problem $\partial\psi/\partial t+\nabla\cdot(\psi\mathbf{v})=0$, where ψ is a scalar field advected with an arbitrary flow $\mathbf{v}=(v^1,\ldots,v^M)$, yields the MPDATA solution [6] written compactly on a regular grid as

$$\psi_{\mathbf{i}}^{(k)}=\psi_{\mathbf{i}}^{(k-1)}-\sum_{I=1}^{M}\left[F\left(\psi_{\mathbf{i}}^{(k-1)},\psi_{\mathbf{i}+\mathbf{e}_I}^{(k-1)},V_{\mathbf{i}+1/2\mathbf{e}_I}^{I(k)}\right)\right.$$
$$\left.-F\left(\psi_{\mathbf{i}-\mathbf{e}_I}^{(k-1)},\psi_{\mathbf{i}}^{(k-1)},V_{\mathbf{i}-1/2\mathbf{e}_I}^{I(k)}\right)\right] \tag{1}$$

where $\mathbf{i}\equiv(i^1,\ldots,i^M)$ denotes a location on the grid, $\mathbf{e}_I$ is the unit vector in the Ith of M spatial directions, F is the donor-cell flux function that takes the value of either first or second argument depending on the sign of the normalized advective pseudovelocity V^I in the Ith direction, integer and half integer indices correspond to the cell centers and edges, respectively, and $k=1,\ldots,IORD$ numbers MPDATA iterations such that

$$\psi^{(0)}\equiv\psi^{n} \tag{2a}$$

$$\psi^{(IORD)}\equiv\psi^{n+1} \tag{2b}$$

$$V^{I(k+1)}=V^{I}(\mathbf{V}^{(k)},\psi^{(k)},\nabla\psi^{(k)}) \tag{3a}$$

$$V_{\mathbf{i}+1/2\mathbf{e}_I}^{I(1)}\equiv\left.v^{I}\right|_{\mathbf{i}+1/2\mathbf{e}_I}^{n+1/2}\frac{\Delta t}{\Delta X^{I}} \tag{3b}$$

Here, n and $n+1$ denote temporal levels $t^{n+1}=t^{n}+\Delta t$, and ΔX^I denotes spatial grid increment in the Ith direction.

Iterative application of upwinding in MPDATA greatly simplifies the task of designing higher-order schemes without the necessity of knowing details of the resulting truncation error. Since the errors are cast in the form of the advective fluxes—defined as products of the current solution iterate and suitable "diffusive velocities"—the convexity of upwinding warrants their compensation while preserving the sign of the transported field. In consequence, the linear computational stability of the first donor-cell step implies the nonlinear stability of the entire MPDATA advection, a property essential for simulations of turbulent flows. Since the upwind scheme filters high frequencies on the grid and each subsequent step reverses the dissipative error of the preceding step, MPDATA is reminiscent of generalized similarity models, where an estimate of the full unfiltered Navier–Stokes velocity (which enters the SGS stress tensor) is obtained by an approximate inversion of the filtering operation [14]. Another important consequence of this design is the full multidimensionality of MPDATA—i.e., the freedom from spatial splitting errors—which enhances mesh independence and consequently the scheme's suitability for anisotropic flow problems [15].

MPDATA was generalized to a full fluid solver in the early 1990s. In analyzing the truncation error of approximations to the momentum equation, one finds error terms that depend on the interaction of the advection with the forcing terms, including the

Downloaded 03 Jun 2010 to 171.66.16.156. Redistribution subject to ASME license or copyright; see http://www.asme.org/terms/Terms_Use.cfm

pressure gradient. Many implementations of nonoscillatory algorithms treat advection separately from the forcings, leaving this error uncompensated and thereby reducing the order of accuracy of the solution and potentially leading to oscillations and even instability [16]. In MPDATA, this error is compensated by effectively integrating the forcing terms along a flow trajectory rather than at a grid point.

3 Multiscale Geophysical Fluid Model

MPDATA is implemented in the 3D program EULAG for simulating rotating stratified flows in complex time-dependent curvilinear geometries [3,17–19]—the name EULAG alludes to the capability to solve the fluid equations in either an Eulerian (flux form) or a Lagrangian (advective form) framework. The default analytic formulation of EULAG assumes the nonhydrostatic anelastic equations of motion, with options available for compressible/incompressible Boussinesq, and incompressible Euler/Navier–Stokes equations [20]; in either case, an elliptic equation for pressure is solved using a preconditioned nonsymmetric Krylov solver. EULAG is fully parallelized using message passing and runs efficiently on a variety of platforms.

Because of the enormous span of the spatial and temporal scales, and the wave phenomena important in geophysical fluids, explicit integrations of generic compressible equations are impractical (viz., prohibitively expensive) for the majority of applications. In order to account for this broad range of scales while deriving a numerical model still useful with existing computational resources, one has no choice but to invoke analytic or numerical approximations that allow for reasonably large time-step integrations of the governing equations. In effect, meteorological models encompass a variety of approximate (filtered) systems of fluid equations (e.g., hydrostatic, elastic, anelastic, and Boussinesq; cf. Ref. [21]) and engender many split-explicit or semi-implicit methods for their integration [22].

For research studies of all-scale turbulent geophysical fluids, we have so far found the anelastic nonhydrostatic system to be optimal. The anelastic approximation may be thought of as a generalized Boussinesq approximation where the effects of density variations on mass balance and inertia are neglected in the equations of mass continuity and momentum, but are accounted for in the buoyancy forces. The classical, incompressible Boussinesq system is applicable to shallow motions with small material displacement compared to a characteristic vertical scale of the fluid, thereby allowing for a simple uniform reference state. The anelastic approximation extends this concept by accounting for the density/temperature stratification of the static background. Although the anelastic equations were proven accurate for modeling the elements of weather and climate up to the synoptic scale, our recent results [20] document that they can adequately capture a range of planetary flows while requiring relatively minor overhead due to the nonhydrostatic formulation. This adequacy of the anelastic approximation has important practical consequences. Inherent in the anelastic system are (i) the Boussinesq linearization of the pressure gradient forces and the mass fluxes in the momentum and mass continuity equations, respectively, and (ii) the anelasticity per se, equivalent to taking the limit of an infinite speed of sound. Working in concert, these two approximations greatly simplify the design of accurate, flexible, and computationally efficient (viz., implicit with respect to inertia-gravity waves) "all-scale-research" models for meteorological circulations. This is especially important within the class of NFV models, where two-time-level self-adaptive nonlinear numerics lead inevitably to difficult nonlinear elliptic problems for the implicit discretization of fully compressible Euler equations. From the viewpoint of numerical engineering, the anelastic model readily branches into either a compressible/incompressible Boussinesq or an incompressible Euler system [20].

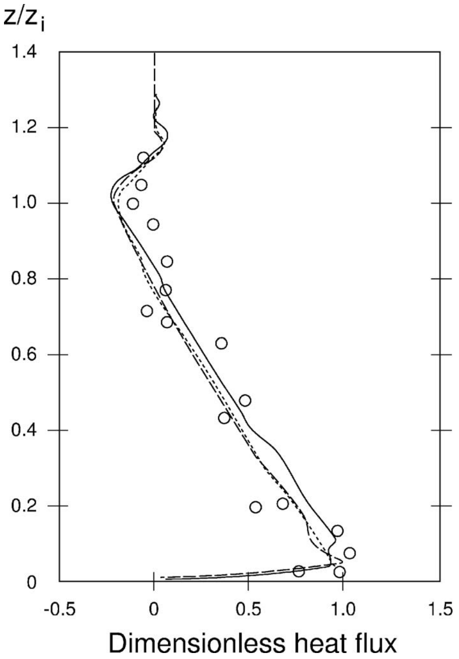

Fig. 1 Turbulence modeling of the convective PBL. ILES (solid line) and LES (long dashes) versus Schmidt–Schumann LES benchmark results (short dashes) and data (circles).

4 Examples of Applications

Our model can be applied to a broad class of problems encompassing simulating atmospheric/oceanic circulations across a wide range of scales [23,24] to biomechanics and solar physics applications [25,26], in either DNS [27], LES [28], or ILES [29] mode. For substantiation, as well as to show the "dissipativity" of MPDATA at work, in the following we discuss two distinct examples ranging from micrometeorology to global climate.

4.1 Boundary Layers. Our first example highlights the results of explicit versus implicit turbulence modeling for a benchmark simulation of the convective PBL using the NFV incompressible Boussinesq version of EULAG, after Margolin et al. [5]. The three curves shown in Fig. 1 represent mean profiles of the normalized resolved heat flux (horizontally averaged product of temperature perturbation and vertical velocity) from three different simulations: The short-dashed curve is from LES benchmark simulations of Schmidt and Schumann [30] using a CTS model; the long-dashed curve is from explicit LES simulations with MPDATA using the Smagorinsky model consistent with Ref. [30]; and the solid curve is for MPDATA with no explicit subgrid-scale model, that is, ILES. Circles represent field and laboratory data superimposed by Schmidt and Schumann. The comparability of all the results with the data is excellent (for other characteristics of the flow, see Ref. [5]). Without the ILES result, one might be tempted to argue that the dissipativity of the employed NFV approach is simply negligibly small. However, the results reveal a more interesting story. A full appreciation of the results in Fig. 1 intertwines with understanding the mechanics of nonoscillatory schemes. NFV schemes are nonlinear (even for linear problems) as they employ coefficients that depend on the transported variables. In other words, these schemes are *self-adaptive* in the course of the simulation. Thus, in contrast to linear CTS methods, different realizations of the same turbulent flow use different numerical approximations of the governing equations of motion. When the explicit SGS model is included (LES), the resolved flow is sufficiently smooth, and the entire machinery assuring nonoscillatory properties of the numerics is effectively turned off (there is no need to limit/adjust linear components of the scheme). In the

Downloaded 03 Jun 2010 to 171.66.16.156. Redistribution subject to ASME license or copyright; see http://www.asme.org/terms/Terms_Use.cfm

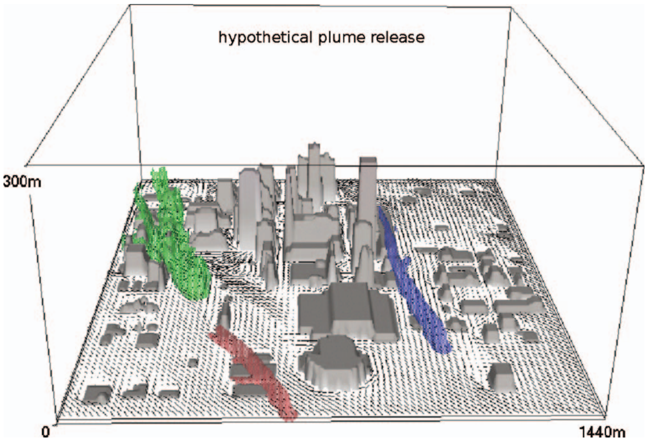

Fig. 2 EULAG LES of a hypothetical flow and contaminant dispersion in downtown of Oklahoma City

absence of an explicit SGS model, the nonoscillatory machinery adapts the numerics "smartly" so as to assure solutions that are apparently as smooth as those generated with physically motivated explicit SGS models. Thus, insofar as the dissipativity per se of the NFV methods is concerned, there is no simple unique quantification since the resulting transport scheme can be effectively either nondissipative or dissipative, depending on the presence or absence, respectively, of an explicit SGS model.

The above-discussed LES/ILES benchmark addresses a classical problem of micrometeorology. Figure 2 highlights an extension of this idealized PBL study to a practical problem of airborne contaminant transport in an urban area. Due to the complexity of the building geometries and the unsteady turbulent nature of the street-level flow, urban PBL flows present a challenge to contemporary LES models. In the simulation highlighted in Fig. 2, buildings are represented by fictitious body forces (in the equations of motion) that attenuate flow to stagnation within $\mathcal{O}(\Delta t)$ time, where Δt denotes the model time step. The technical description of this so-called immersed boundary approach, together with a quantitative discussion of a representative study of urban PBL, can be found in Ref. [31]. For a realistic risk assessment of contaminant releases, EULAG is coupled with a global climatology analysis tool (GCAT) [32]. The coupled system estimates the climatology of street-level conditions and tracks dispersion of hazardous gases and particles from either stationary or moving sources. Figure 2 shows an instantaneous EULAG solution for LES of hypothetical urban PBL flow and contaminant dispersion in the downtown area of the Oklahoma City for late-afternoon ambient conditions. Here, the computational grid $240\times240\times51$ covers a $1.5\times1.5\times0.3$ km^3 urban volume with uniform resolution of $\Delta X=\Delta Y=\Delta Z=6$ m.

The highlighted result exemplifies the importance and merit of explicit SGS models. In the convective PBL benchmark discussed earlier, the predominant source of turbulence is buoyant production in response to intense surface heating, and the results are insensitive to the means of distributing heat in the vicinity of ground [5]. In effect, LES and ILES results compare closely. The selected urban PBL is much more complex, as substantial turbulence is generated near frictional boundaries, and the results (e.g., flow direction and contaminant dispersion) are sensitive to the means of momentum distribution therein (Fig. 3). In general, truncation terms of accurate advective transport schemes vanish in the absence of a flow, in particular, in a no-flow direction. Consequently, in applications where wall effects are essential, an explicit mechanism must be supplied for modeling transport of dependent variables normal to the boundary. Whether such a mechanism is built into the NFV transport scheme or provided separately, it constitutes an explicit SGS model. Here in the LES of urban PBL, we employed a standard prognostic (Smagorinsky-type) turbulence model [5,30]. It is noteworthy that we have attempted abbreviated approaches (Fig. 3) but have so far found no simple solution competitive to an established explicit model. This corroborates the results of PBL simulations past rapidly evolving sand dunes, discussed thoroughly in Ref. [28].

4.2 Planetary Weather and Climate.

The PBL studies address small scale atmospheric dynamics susceptible to incompressible Boussinesq approximation, and are posed on a Cartesian nonrotating domain. The next example—the idealized climate problem of Held and Suarez [33]—represents thermally forced baroclinic instability on the rotating sphere. In a sense, it bears a striking resemblance to LES studies of convective boundary layers, where small differences in model setups can lead to totally different instantaneous flow realizations and where different model designs can lead to quite divergent integral flow characteristics. In other words, these simulated flows are both turbulent and stochastic.

Figure 4 illustrates the overall complexity of the flow. It shows instantaneous vertical cross sections in the equatorial plane and surface plots of the isentropes θ and isolines of zonal velocity u after three years of flow simulated with the anelastic option of EULAG formulation. The results displayed typify the response of an initially stagnant and uniformly stratified fluid to a diabatic forcing that mimics the long-term thermal and frictional forcing in the Earth's atmosphere. Figure 5 contrasts the complexity of the instantaneous flow in Fig. 4, viz. "weather," with the display of the resulting "climate," i.e., zonally averaged three-year means of zonal velocity and potential temperature.

The results of Figs. 4 and 5 exemplify the role of implicit turbulence modeling of geophysical flows. Here, the globe is covered by uniform spherical mesh with $nx\times ny=64\times32$ grid intervals (no grid points at the poles); the $H=32\times10^3$ m deep atmosphere is resolved with $nz=40$ uniform grid intervals; and the time step of integration is $\Delta t=900$ s (see Ref. [20] for further details of the simulation performed). There is no explicit SGS model employed, and it would be unreasonable to expect that any standard turbulence model in the sense of LES could represent the actual turbulence of the Earth's atmosphere at such low grid resolutions. Consider that near the equator, the horizontal extent of the model grid boxes (approximately 600×600 km^2) is comparable to the size of a small European country, where convection, terrain forcing, gravity-wave breaking, etc., are responsible for generating the energy of the subgrid scales but are not accounted for in standard turbulence models.

5 Discussion

Elementary advection schemes (such as classical donor-cell, one-step Lax–Wendroff, or CTS leapfrog; see Ref. [34] for details) yield simple, compact forms for the resulting advective fluxes. Notwithstanding their simplicity, these elementary schemes yield poor solutions that are either overly smooth or are contaminated by spurious oscillations (noise). The "nonoscillatory" property refers to highly accurate yet smooth solutions free of spurious oscillations. It is achieved via essential nonlinearity in the numerical representation of advective fluxes with respect to transported field. The latter complicates advection schemes quite substantially—modern NFV methods yield complex fluxes that often require many equations for their representation. Nevertheless, NFV methods produce superior results with regard to stability and accuracy, and so are worth the extra effort involved.

NFV advection schemes possess enhanced computational stability because the total "energy" (domain integrated square of the transported field) of a sign-preserving solution is uniformly bounded in time. For a sufficiently small time step Δt, advection schemes that are sign-preserving for arbitrary flows (e.g., MPDATA) can always be designed—thus, nonoscillatory schemes exhibit nonlinear as well as linear stabilities. These results hold if

Downloaded 03 Jun 2010 to 171.66.16.156. Redistribution subject to ASME license or copyright; see http://www.asme.org/terms/Terms_Use.cfm

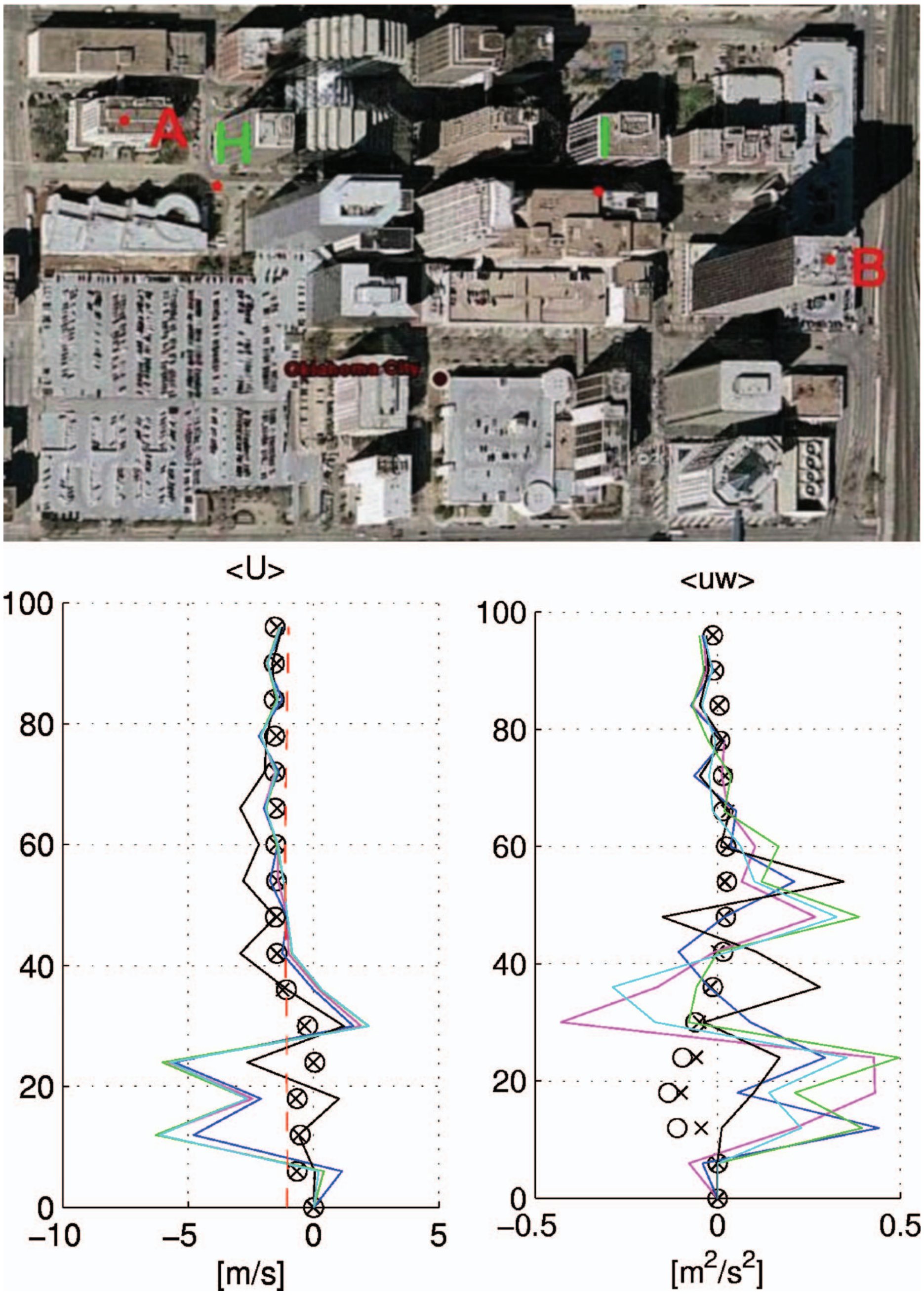

Fig. 3 Time-averaged westerly wind component (lower left) and resolved Reynolds stress (lower right) at a street-canyon location $(x,y)=(474,954)$ m of Fig. 2, indicated by H in the upper panel. Circles and crosses denote results from two alternate LES, whereas thin lines are for alternate ILES runs. All alternate runs explore different means of momentum distribution near frictional boundaries.

the dependent variable field is either of constant or of variable sign. Further, these arguments can be generalized (over a single time step) to a transport equation with forcings and/or sources leading to the conclusion that sign-preserving advection schemes offer the means of controlling nonlinear stability in numerical models.

A numerical property of great importance to turbulence simulations is flow topology—or *realizability*. This means that a quantity ψ must be advected along nonintersecting numerical trajectories. This property is subtle as, superficially, intersecting trajectories may give the impression of turbulent motions. For a flow to be realizable, the magnitudes of local velocity derivatives must be properly bounded, and thus the nonoscillatory property of NFV schemes should improve the fidelity of the simulations. Since such limiting is also effected by filtering small, poorly resolved eddies on the grid—regardless of the formal theoretics underlying LES—SGS models act quite similarly as the limiters of nonoscillatory schemes.

Many nonoscillatory schemes are available nowadays, and no one can make claims for them all. In general, however, nonoscillatory advection schemes are dissipative. In practice, this means that (i) they contain both even and odd order derivatives in their Taylor series expansion (in contrast to CTS schemes such as the leapfrog method) and (ii) they tend to dissipate (rather than con-

Downloaded 03 Jun 2010 to 171.66.16.156. Redistribution subject to ASME license or copyright; see http://www.asme.org/terms/Terms_Use.cfm

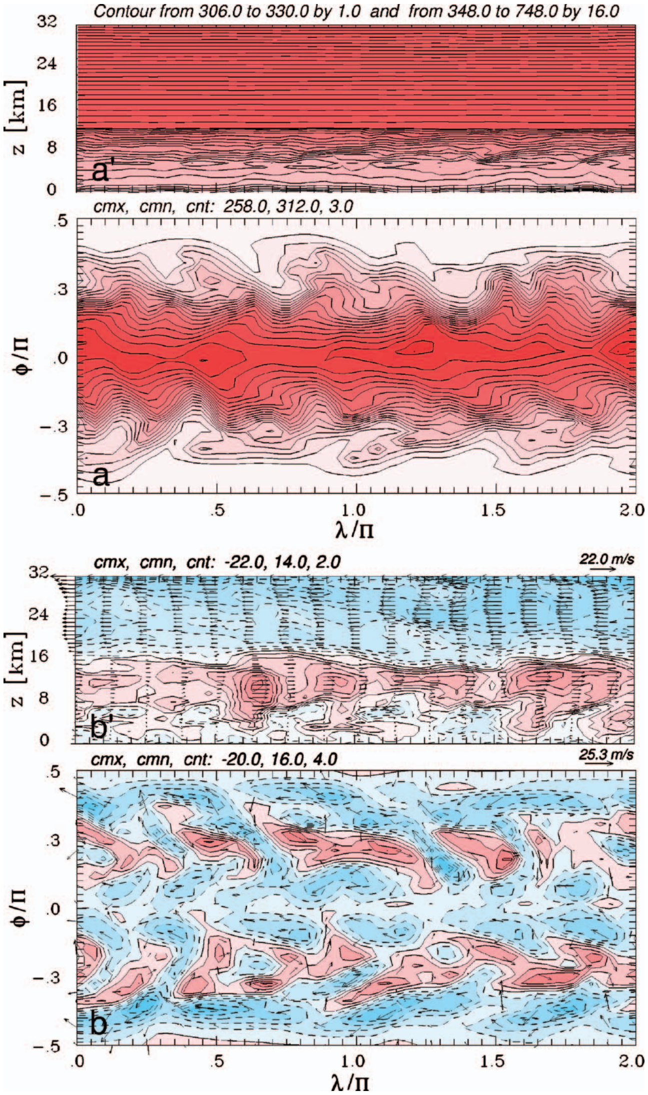

Fig. 4 Instantaneous solutions of the idealized climate problem after three years of simulation. Plates *a′* and *a* show isentropes in the vertical equatorial plane and at the surface, respectively. Plates *b′* and *b* display the zonal velocity contours with imposed flow vectors, respectively, in the equatorial plane and at the surface. Contour extrema and intervals are shown in the upper left corner of each plate (in plate *a′*, we used a variable contour to capture θ variability in the troposphere). Negative values are dashed. Maximum vector lengths are shown in the upper right corner of plates *b′* and *b*.

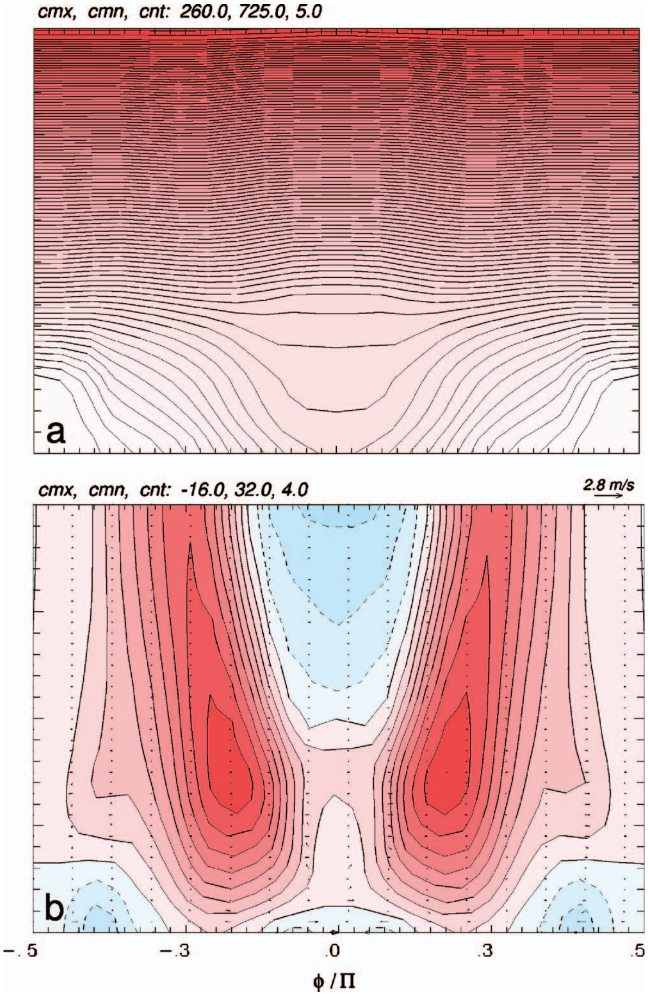

Fig. 5 The zonally averaged three-year means of potential temperature (plate *a*) and zonal velocity (plate *b*) for the simulation highlighted in Fig. 4. Contouring convention is similar to that used in Fig. 4.

serve) the quadratic energy integrals—thus conforming with the second law of thermodynamics [4]—of the transported variable (in contrast to CTS schemes such as Arakawa-type methods [35]). By no means does dissipativity imply low accuracy—although statements in this spirit appear occasionally in the literature. Nonoscillatory algorithms are available for a number of existing advection schemes that take into account flow variability and multidimensionality, and typically offer uniformly second-order accurate solutions for arbitrary flows. These algorithms are particularly attractive for implicit turbulence modeling of geophysical fluids.

6 Summary

The overall accuracy of approximation is not the only measure of the quality of a numerical scheme. Modern numerical algorithms based on NFV methods embody physical constraints that enhance the realizability of simulations. In this paper, we have described a particular NFV scheme, MPDATA, among whose properties are the preservation of sign of scalar quantities such as density, water content, etc., the nonlinear stability of the simulation, and the suppression of unphysical oscillations. We also described the relatively recently validated property of implicit turbulence modeling, which enables the representation of high Reynolds number flows without the need for explicit subgrid-scale models.

To give substance to our theoretical framework, we have provided examples of a few diverse calculations of turbulent flows. Comparisons of MPDATA simulations of convective boundary layers with and without subgrid models demonstrate that this NFV scheme is not overly dissipative and imply that the implicit turbulence property is adaptive. Extensions to building-resolving urban flows illustrate the merit of explicit subgrid-scale models for complex strain flows, thus indicating practicality of a hybrid LES/ILES approach.

Global simulations of climate contain broad ranges of scales of time as well as space. Our simulations of an idealized climate further support the utility of NFV models. However, the earth's climate system contains many additional processes beyond fluid dynamics, many of which cannot be resolved on computers of the present nor of the foreseeable future. The construction of appropriate models for these processes and their integration into NFV schemes will continue to be a challenge for many years.

Downloaded 03 Jun 2010 to 171.66.16.156. Redistribution subject to ASME license or copyright; see http://www.asme.org/terms/Terms_Use.cfm

Acknowledgment

Los Alamos National Laboratory is operated by the Los Alamos National Security, LLC for the U.S. Department of Energy NNSA under Contract No. DE-AC52-06NA25396. The National Center for Atmospheric Research is sponsored by the National Science Foundation. This work has been supported in part by the Department of Energy's "Climate Change Prediction Program" research initiative and by the Defense Threat Reduction Agency. Computer time was provided by NSF MRI Grant Nos. CNS-0421498, CNS-0420873, and CNS-0420985, NSF sponsorship of the National Center for Atmospheric Research, the University of Colorado, and a grant from the IBM Shared University Research (SUR) program.

References

[1] *Implicit Large Eddy Simulation: Computing Turbulent Fluid Dynamics*, F. F. Grinstein, L. G. Margolin, and W. Rider, eds., (2007), pp. 552.

[2] Smagorinsky, J., 1993, "Some Historical Remarks on the Use of Nonlinear Viscosities," in *Large Eddy Simulation of Complex Engineering and Geophysical Flows*, B. Galperin and S. A. Orszag, eds., Cambridge University Press, New York, pp. 3–36.

[3] Smolarkiewicz, P. K., and Prusa, J. M., 2002, "Forward-In-Time Differencing for Fluids: Simulation of Geophysical Turbulence," in *Turbulent Flow Computation*, D. Drikakis and B. J. Guertz, eds., Kluwer Academic, Boston, Chap. 8, pp. 279–312.

[4] Margolin, L. G., Rider, W. J., and Grinstein, F. F., 2006, "Modeling Turbulent Flow With Implicit LES," J. Turbul., **7**(15), pp. 1–27.

[5] Margolin, L. G., Smolarkiewicz, P. K., and Sorbjan, Z., 1999, "Large-Eddy Simulations of Convective Boundary Layers Using Nonoscillatory Differencing," Physica D, **133**, pp. 390–397.

[6] Smolarkiewicz, P. K., and Margolin, L. G., 1998, "MPDATA: A Finite-Difference Solver for Geophysical Flows," J. Comput. Phys., **140**, pp. 459–480.

[7] Smolarkiewicz, P. K., 2006, "Multidimensional Positive Definite Advection Transport Algorithm: An Overview," Int. J. Numer. Methods Fluids, **50**, pp. 1123–1144.

[8] Smolarkiewicz, P. K., and Prusa, J. M., 2002, "VLES Modeling of Geophysical Fluids With Nonoscillatory Forward-in-Time Schemes," Int. J. Numer. Methods Fluids, **39**, pp. 799–819.

[9] Margolin, L. G., Smolarkiewicz, P. K., and Wyszogrodzki, A. A., 2002, "Implicit Turbulence Modeling for High Reynolds Number Flows," ASME Trans. J. Fluids Eng., **124**, pp. 862–867.

[10] Domaradzki, J. A., Xiao, Z., and Smolarkiewicz, P. K., 2003, "Effective Eddy Viscosities in Implicit Large Eddy Simulations of Turbulent Flows," Phys. Fluids, **15**, pp. 3890–3893.

[11] Margolin, L. G., Smolarkiewicz, P. K., and Wyszogrodzki, A. A., 2006, "Dissipation in Implicit Turbulence Models: A Computational Study," Trans. ASME, J. Appl. Mech., **73**, pp. 469–4737.

[12] Margolin, L. G., and Rider, W. J., 2002, "A Rationale for Implicit Turbulence Modeling," Int. J. Numer. Methods Fluids, **39**, pp. 799–819.

[13] Szmelter, J., 2006, "MPDATA Methods," Int. J. Numer. Methods Fluids, **50**, pp. 1121–1293.

[14] Domaradzki, J. A., and Adams, N. A., 2002, "Direct Modelling of Subgrid Scales of Turbulence in Large Eddy Simulation," J. Turbul., **3**, pp. 1–19.

[15] Smolarkiewicz, P. K., and Szmelter, J., 2005, "MPDATA: An Edge-Based Unstructured-Grid Formulation," J. Comput. Phys., **206**, pp. 624–649.

[16] Smolarkiewicz, P. K., and Margolin, L. G., 1993, "On Forward-in-Time Differencing for Fluids: Extension to a Curvilinear Framework," Mon. Weather Rev., **121**, pp. 1847–1859.

[17] Prusa, J. M., and Smolarkiewicz, P. K., 2003, "An All-Scale Anelastic Model for Geophysical Flows: Dynamic Grid Deformations," J. Comput. Phys., **190**, pp. 601–622.

[18] Wedi, N. P., and Smolarkiewicz, P. K., 2004, "Extending Gal-Chen and Somerville Terrain-Following Coordinate Transformation on Time Dependent Curvilinear Boundaries," J. Comput. Phys., **193**, pp. 1–20.

[19] Smolarkiewicz, P. K., and Prusa, J. M., 2005, "Towards Mesh Adaptivity for Geophysical Turbulence," Int. J. Numer. Methods Fluids, **47**, pp. 1369–1374.

[20] Smolarkiewicz, P. K., Margolin, L. G., and Wyszogrodzki, A. A., 2001, "A Class of Nonhydrostatic Global Models," J. Atmos. Sci., **58**, pp. 349–364.

[21] Davis, T., Staniforth, A., Wood, N., and Thuburn, J., 2003, "Validity of Anelastic and Other Equation Sets as Inferred from Normal-Mode Analysis," Q. J. R. Meteorol. Soc., **129**, pp. 2761–2775.

[22] Durran, D. R., 1999, *Numerical Methods for Wave Equations in Geophysical Fluid Dynamics*, Springer-Verlag, New York.

[23] Smolarkiewicz, P. K., and Margolin, L. G., 2007, "Studies in Geophysics," in *Implicit Large Eddy Simulation: Computing Turbulent Fluid Dynamics*, F. F. Grinstein, L. Margolin, and W. Rider, eds., pp. 413–438.

[24] Warn-Varnas, A., Hawkins, J., Smolarkiewicz, P. K., Chin-Bing, S. A., King, D., and Hallock, Z., 2007, "Solitary Wave Effects North of Strait of Messina," Ocean Model., **18**, pp. 97–121.

[25] Cotter, C. S., Smolarkiewicz, P. K., and Szczyrba, I. N., 2002, "A Viscoelastic Model for Brain Injuries," Int. J. Numer. Methods Fluids, **40**, pp. 303–311.

[26] Elliott, J. R., and Smolarkiewicz, P. K., 2002, "Eddy Resolving Simulations of Turbulent Solar Convection," Int. J. Numer. Methods Fluids, **39**, pp. 855–864.

[27] Wedi, N. P., and Smolarkiewicz, P. K., 2006, "Direct Numerical Simulation of the Plumb-Mcewan Laboratory Analogue of the QBO," J. Atmos. Sci., **63**, pp. 3226–3252.

[28] Ortiz, P., and Smolarkiewicz, P. K., 2006, "Numerical Simulation of Sand Dune Evolution in Severe Winds," Int. J. Numer. Methods Fluids, **50**, pp. 1229–1246.

[29] Andrejczuk, A., Grabowski, W. W., Malinowski, S. P., and Smolarkiewicz, P. K., 2006, "Numerical Simulation of Cloud-Clear Air Interfacial Mixing: Effects on Cloud Microphysics," J. Atmos. Sci., **63**, pp. 3204–3225.

[30] Schmidt, H., and Schumann, U., 1989, "Coherent Structure of the Convective Boundary Layer Derived from Large-Eddy Simulation," J. Fluid Mech., **200**, pp. 511–562.

[31] Smolarkiewicz, P. K., and Sharman, R., 2004, "Pentagon Shield: Experiments With a Nonoscillatory Forward-In-Time CFD Code (EULAG) to Simulate Flow Around the Pentagon," *18th Annual George Mason University Conference on Atmospheric Transport and Dispersion Modeling*, George Mason University Fairfax, VA, Jul. 13–15 (http://www.rap.ucar.edu/projects/shield/references/gmu04/EuLag_gmu.pdf).

[32] Wyszogrodzki, A. A., Vendenberghe, F., and Warner, T., 2006: "The Use of Coupled Mesoscale and LES Models for Calculating Urban Climatologies of Street Level and Boundary Layer Winds With Risk Assessment Implications," *Tenth Annual George Mason University Conference on Atmospheric Transport and Dispersion Modeling*, George Mason University Fairfax, VA, Aug. 1–3.

[33] Held, I. M., and Suarez, M. J., 1994, "A Proposal for Intercomparison of the Dynamical Cores of Atmospheric General Circulation Models," Bull. Am. Meteorol. Soc., **75**, pp. 1825–1830.

[34] Roache, P. J., 1972, *Computational Fluid Dynamics.*, Hermosa, Albuquerque.

[35] Arakawa, A., 1996, "Computational Design for Long-Term Numerical Integration of the Equations of Fluid Motions: Two-Dimensional Incompressible Flow," J. Comput. Phys., **1**, pp. 119–143.

Downloaded 03 Jun 2010 to 171.66.16.156. Redistribution subject to ASME license or copyright; see http://www.asme.org/terms/Terms_Use.cfm

Prediction of Leading-Edge Sheet Cavitation Inception on Hydrofoils at Low to Moderate Reynolds Number Flows

Zvi Rusak

Wallace J. Morris II

Yoav Peles

Department of Mechanical, Aerospace,
and Nuclear Engineering,
Rensselaer Polytechnic Institute,
Troy, NY 12180-3590

The inception of leading-edge sheet cavitation on two-dimensional smooth thin hydrofoils at low to moderately high Reynolds number flows is investigated by an asymptotic approach and numerical simulations. The asymptotic theory is based on the work of Rusak (1994, "Subsonic Flow Around Leading Edge of a Thin Aerofoil With a Parabolic Nose," Eur. J. Appl. Mech., **5***, pp. 283–311) and demonstrates that the flow about a thin hydrofoil can be described in terms of an outer region, around most of the hydrofoil chord, and an inner region, around the nose, which asymptotically match each other. The flow in the outer region is dominated by the classical thin hydrofoil theory. Scaled (magnified) coordinates and a modified (smaller) Reynolds number (Re_M) are used to correctly account for the nonlinear behavior and extreme velocity changes in the inner region, where both the near-stagnation and high suction areas occur. It results in a model (simplified) problem of a uniform flow past a semi-infinite smooth parabola with a far-field circulation governed by a parameter $\tilde{A}$ that is related to the hydrofoil's angle of attack, nose radius of curvature, and camber. The model parabola problem consists of a viscous flow that is solved numerically for various values of $\tilde{A}$ and Re_M to determine the minimum pressure coefficient and the cavitation number for the inception of leading-edge cavitation as function of the hydrofoil's geometry, flow Reynolds number, and fluid thermodynamic properties. The predictions according to this approach show good agreement with results from available experimental data. This simplified approach provides a universal criterion to determine the onset of leading-edge (sheet) cavitation on hydrofoils with a parabolic nose in terms of the similarity parameters $\tilde{A}$ and Re_M and the effect of hydrofoil's thickness ratio, nose radius of curvature, camber, and flow Reynolds number on the onset.* [DOI: 10.1115/1.2801350]

1 Introduction

The inception of cavitation on hydrofoils is a basic phenomenon in hydrodynamics, which refers to the appearance of vapor phase when liquid flows around a hydrofoil. For thin hydrofoils at moderate angles of attack, the first occurrence of cavitation is closely related to the minimum pressure near the leading edge and a laminar separation bubble [1–5]. Under these conditions, the inception of cavitation marks the establishment of a relatively large separated flow of vapor on the upper surface near the leading edge, commonly referred as sheet cavitation. Other forms of cavitation, such as bubble cavitation at hydrofoil's midchord, are not associated with the leading-edge flow dynamics. Once sheet cavitation is developed, the pressure on the upper surface of the hydrofoil is higher than the noncavitating flow. This in turn limits the hydrofoil's maximal lift, increases drag, changes the pitching moment, and can significantly affect the operation envelope of ship and submarine propellers. It may also be responsible for propellers' noise and vibrations as well as efficiency drop and material erosion. The typical design objective is to delay cavitation to higher angles of attack in order to widen the performance of propeller blades.

Over the past 50 years, cavitation over hydrofoils has been extensively investigated experimentally [1–9], numerically [10–14], as well as analytically [15,16], most often for high Reynolds number flows. Due to the importance of cavitation inception conditions, considerable amount of the published data on cavitation has been devoted to this topic. Although cavitation inception is well known to depend on various effects, such as surface roughness [6,17–20], cavitation nuclei [9,21–25], and transport of noncondensable gases, of particular importance within the study of sheet cavitation inception is the minimum pressure coefficient $Cp_{\min}$. Note that any attempt to correlate and measure inception is resolved through the use of $Cp_{\min}$.

Various studies [5–8] provided the cavitation inception index on assorted hydrofoils at various angles of attack. It is well documented [5,6,26,27] that for leading-edge (sheet) cavitation on a given hydrofoil at a fixed angle of attack, the cavitation inception index σ_i tends to increase with the flow Reynolds number. Furthermore, the presence of a long separation region can significantly reduce the magnitude of the mean minimum pressure coefficient on foils and cause an abrupt increase in cavitation inception index at some critical Reynolds numbers [3,6,28–30]. Increasing the angle of attack up to the stall (long separation bubble) angle at a fixed Reynolds number also causes the increase of σ_i. In addition, changing the geometry of thin hydrofoils by increasing the thickness ratio and/or the nose radius of curvature at a given flow Reynolds number increases the cavitation inception angle, thereby increasing the hydrofoil's maximum lift coefficient.

Recent results obtained in the High Speed Cavitation Tunnel in EPFL by Guennoun [31] have shown that the onset and detachment of a vapor cavity is highly influenced by the boundary-layer development and the flow unsteadiness as well as the surface roughness in the vicinity of the leading edge. It has been shown that cavities may be completely suppressed for a particular combination of hydrofoil oscillation frequency and flow parameters.

Contributed by the Fluids Engineering Division of ASME for publication in the JOURNAL OF FLUIDS ENGINEERING. Manuscript received May 16, 2006; final manuscript received June 27, 2007. Review conducted by Joseph Katz.

Copyright © 2007 by ASME

Downloaded 03 Jun 2010 to 171.66.16.156. Redistribution subject to ASME license or copyright; see http://www.asme.org/terms/Terms_Use.cfm

The measurements of pressure near leading edge show that liquid upstream to the main cavity detachment withstands a negative pressure without any vaporization. This important result outlines the complexity of leading-edge cavitation detachment and the need to perform further basic investigations to better understand this phenomenon.

The existing body of scientific knowledge on cavitation enables the design of a hydrofoil, which can meet numerous engineering tasks. Computation fluid dynamic (CFD) methods coupled with experimental verification provide invaluable engineering tools to predict cavitation inception. It is a common practice in the design of hydrofoils to perform extensive CFD simulations of several selected hydrofoils over a large range of operating conditions, and subsequently experimentally test selected configurations. Despite being a well practice process, it suffers from some major drawbacks. The large number of CFD runs required to fully elucidate the hydrodynamic performance envelope is frequently a time consuming and costly process. Means to reduce the computational effort required in the design of hydrofoils is therefore of great interest to the hydrodynamic community.

The current analysis provides a universal scientific prediction of the conditions leading to the complicated physical phenomenon of sheet cavitation inception, based on fundamental theory of the fluid flow equations. The mathematical analysis relates for the first time the leading-edge cavitation inception index to the flow Reynolds number, angle of incidence, and hydrofoil camber and shape. Comparison with available experimental data demonstrates the validity of the analysis. This formula can be employed as a quick and invaluable measure to provide a *first-order* design optimization with a minimal computational effort. The results from such a reduced-order analysis can then offer focus for conducting an in-depth study of specific designs using CFD solvers and experiments.

The present analysis is based on the asymptotic theory developed by Rusak [32] and demonstrates that the flow around a thin, smooth hydrofoil can be described in terms of an outer region, around most of the hydrofoil chord, and an inner region, around the nose, which asymptotically match each other. Scaled (magnified) coordinates and a modified (smaller) Reynolds number (Re_M) are used to correctly account for the nonlinear behavior of the flow in the inner region, where both the near-stagnation and high suction areas occur. The matching results in a reduced-order model parabola (nose) problem with a far-field circulation dictated by the linearized outer solution. The inner region viscous flow around a smooth parabola is solved numerically using the Reynolds-averaged Navier–Stokes equations where the Spalart–Allmaras viscous turbulence model is used to account for the effect of turbulence on laminar leading-edge bubble separation and its reattachment due to turbulence. The minimum pressure coefficient $Cp_{\min}$ and the inception of cavitation index $\sigma_i \approx -Cp_{\min}$ are determined as function of angle of attack, hydrofoil geometry, and flow Reynolds number. The results of the parabola problem can be readily used for any thin hydrofoil to predict sheet cavitation without any need for additional CFD analysis. The predictions from the parabola solution are used for several hydrofoils and show good agreement with results from available experimental data. The present reduced-order approach provides a universal criterion for the onset of leading-edge (sheet) cavitation on thin hydrofoils and an analysis method that can be used to predict this phenomenon on other thin hydrofoils using its respective nose geometry. The present approach is limited to thin hydrofoils with thickness ratios less than about 12%. For larger values of thickness ratios, flow separation starts from the trailing edge and cannot be described by the present theory.

We point out here the interesting work of Darrozes [33], who was the first to use the method of matched asymptotic expansions to study the nose flow of a uniform stream around a thin foil at high Reynolds number flows and when the boundary-layer thickness is smaller than the nose radius of curvature. He formulated an outer inviscid flow solution that is based on the classical linearized airfoil theory and an inner flow solution in the vicinity of the foil leading edge and matched between these solutions. The boundary-layer solution in the inner region is found from a parabolic equation, which accounted for the foil small thickness. It was shown that in tangential flow around, the foil leading edge is independent of the transverse speed normal to the foil.

Darrozes [33] approach, however, was not extended to predict the onset of leading-edge cavitation on hydrofoils. No numerical results of $Cp_{\min}$ as function of flow Reynolds number or hydrofoil's angle of attack and camber were given to compare the asymptotic theory predictions with experimental data or with modern numerical computations using the Navier–Stokes viscous flow equations, as is done in the present paper. Also, the flow boundary layer was treated by a reduced-order parabolic approach, whereas in the present work, the high Reynolds number viscos flow around the nose is solved numerically using the Reynolds-averaged Navier–Stokes equations and the boundary layer is resolved as an integral part of the inner region solution. The present approach also includes a turbulence model in the numerical solution in the inner flow region to represent the important effects of turbulence on the boundary-layer laminar separation and its immediate reattachment due to turbulence to form a short separation bubble at moderately high Reynolds numbers (Tani [34]), which were not included in the boundary-layer approach of Darrozes [33]. Boundary-layer reattachment has effects on the flow upstream of the laminar separation bubble [34]. Therefore, it plays an important role in determining the minimum pressure coefficient $Cp_{\min}$ and the inception of leading-edge cavitation index, specifically at moderately high Reynolds number flows and at high angles of attack, before the occurrence of stall [4]. This effect cannot be determined by the parabolic boundary-layer approach, which allows information to propagate only downstream.

2 Theoretical Study

To investigate the onset of cavitation on thin hydrofoils, a multiscale matched asymptotic analysis for a moderately high Reynolds number ($\mathrm{Re} \gg 1$) flow of an incompressible liquid around a thin hydrofoil at low to moderate angles of attack was developed. The smooth hydrofoil geometry is given by $y = \delta c F_{u,l}(x/c)$ for $0 \leqslant x \leqslant c$, where c is the chord, the upper and lower surface shape functions $F_{u,l}(x/c)$ are described by $F_{u,l}(x/c) = C_a(x/c) - Ax/c \pm t(x/c)$ with $0 < \delta \ll 1$ and $A = \alpha/\delta$. Here, $C_a(x/c)$ is the camber-line function, $t(x/c)$ is the thickness function, and the hydrofoil nose is parabolic, with a radius of curvature R_c. The hydrofoil is placed in a uniform freestream flow with speed U_∞ and pressure p_∞. The fluid density (ρ), temperature (T), and viscosity (μ) are assumed constant. Asymptotic expansions of the velocity components and pressure are constructed in an outer region around most of the hydrofoil and in an inner region near the nose, in terms of the hydrofoil small thickness ratio δ. The analysis extends the work of Rusak [32] on the inviscid flow around a thin hydrofoil.

2.1 Outer Expansion. In the outer expansion, reference parameters c, U_∞, and ρU_∞^2 are used to scale the axial and vertical distances, velocity components, and pressure, respectively. The steady-state dimensionless equations governing the flow are

$$\nabla \cdot \mathbf{V} = 0$$

$$\mathbf{V} \cdot \nabla \mathbf{V} + \nabla p = \frac{1}{\mathrm{Re}} \nabla \cdot [2(\nabla \mathbf{V} + (\nabla \mathbf{V})^T)] \qquad (1)$$

Here, $\mathbf{V}$ is the dimensionless velocity vector, p is the dimensionless pressure perturbation due to velocity measured from the base constant static pressure of the liquid, and $\mathrm{Re} = \rho U_\infty c/\mu$ is the flow Reynolds number. Typically, $\mathrm{Re} \gg 1$ and the effect of viscosity is localized to very thin boundary layers and plays only a secondary (or even smaller) role in determining the pressure distribution

Downloaded 03 Jun 2010 to 171.66.16.156. Redistribution subject to ASME license or copyright; see http://www.asme.org/terms/Terms_Use.cfm

along most of the hydrofoil. Except for the very thin boundary layers near the hydrofoil surfaces and the hydrofoil's nose region, the flow in the outer region, around most of the hydrofoil, is dominated by the inviscid version of Eq. (1),

$$\begin{aligned} \nabla \cdot \mathbf{V} &= 0 \\ \mathbf{V} \cdot \nabla \mathbf{V} + \nabla p &= 0 \end{aligned} \tag{2}$$

Actually, since the upstream flow is uniform, the flow is also irrotational and potential. Then, $\mathbf{V}=\nabla\Phi$, where $\Phi(x,y;\delta)$ is the velocity potential where $\nabla^2\Phi=0$. The solution of the Laplace equation with the no penetration condition along the hydrofoil surfaces and the upstream uniform flow conditions at the far field provides the far-field conditions for the boundary layers. Specifically, the velocity and pressure distributions along the hydrofoil surfaces from this inviscid solution are also the velocity and pressure distributions at the edge of the boundary layers and the pressure is the hydrofoil's surface pressure.

Moreover, since typically the hydrofoil's thickness ratio is small ($0<\delta \ll 1$), it can be shown (see Rusak [32]) that the solution of $\nabla^2\Phi=0$ in the outer region (around most of the hydrofoil except for the nose region) is dominated in this case by the classical, incompressible flow, linear airfoil theory, i.e., $\Phi(x,y;\delta) = Ux+\delta\phi_1(x,y)+O(\delta^2)$. Then, the pressure coefficient along most of the hydrofoil's upper (u) and lower (l) surfaces (in the range $\delta < x/c < 1$) may be approximated in the leading-order terms by $Cp_{u,l}=-2\delta\phi_{1x}+O(\delta^2)$. Rusak [32] shows that

$$\begin{aligned} Cp_{u,l}(x/c) = -2\delta\Bigg\{ & h(1+2\cos\theta) \\ & + 2\sum_{k=2}^{\infty} A_{2k-1}\left(\frac{\sin((2k-1)\theta)-\sin\theta}{\sin\theta}\right) \\ & + 2\sum_{k=2}^{\infty} A_{2k}\left(\frac{\sin(2k\theta)-\sin(2\theta)}{\sin\theta}\right) + (-1)^m A \\ & \times\left[w_0\frac{1+\cos\theta}{\sin\theta} - \sum_{n=1}^{\infty}(-1)^n w_n\sin(n\theta)\right]\Bigg\} + O(\delta^2) \end{aligned} \tag{3}$$

Here, $x/c=(1-\cos\theta)/2$, $0\leqslant\theta\leqslant\pi$, $h=R_c/(2\delta^2 c)$ is the airfoil's nose parameter, $A_n=2n/\pi\int_0^\pi t(x/c)\sin n\theta d\theta$, $w_0=1-(1/\pi A)\int_0^\pi C_a'(x/c)d\theta$, and $w_n=2n/\pi A\int_0^\pi C_a'(x/c)\cos n\theta d\theta$. Also, $m=1$ for the hydrofoil's upper surface and $m=0$ for the lower surface. Note that the linear theory solution (3) exhibits a singular behavior as x/c approaches the leading edge, i.e., $Cp_{u,l}(x/c) \sim (-1)^m 2\alpha w_0\sqrt{c/x}$ as x/c approaches zero. Also note that according to the thin hydrofoil theory, the hydrofoil's lift coefficient is $C_l=2\pi(\alpha-\alpha_{0l})$ where the zero lift angle is given by $\alpha_{0l}=\delta(\bar{w}_0-\bar{w}_1/2)$ and $\bar{w}_0=1/\pi\int_0^\pi C_a'(x/c)d\theta$, $\bar{w}_1=2/\pi\int_0^\pi C_a'(x/c)\cos\theta d\theta$.

2.2 Inner Expansion. In the inner region around the hydrofoil's nose ($0\leqslant x/c<R_c/c$), scaled coordinates and flow parameters are used to correctly describe the local nonlinear behavior of the flow, which includes the extreme velocity changes due to the near-stagnation and suction areas around the nose. There, the nose radius of curvature $R_c=2\delta^2h^2c$ is used to scale the axial and vertical coordinates, $x^*=x/R_c$ and $y^*=y/R_c$. The scaling parameters U_∞ and ρU_∞^2 are used for the velocity components and pressure, respectively. The problem in the nose region becomes in the leading order the flow of an incompressible, viscous stream described by the dimensionless equations:

$$\begin{aligned} \nabla^* \cdot \mathbf{V}^* &= 0 \\ \mathbf{V}^* \cdot \nabla^* \mathbf{V}^* + \nabla^* p^* &= \frac{1}{\mathrm{Re}_M}\nabla^* \cdot [2(\nabla^*\mathbf{V}^* + (\nabla^*\mathbf{V}^*)^T)] \end{aligned} \tag{4}$$

Equation (4) shows that the inner flow problem is characterized by a modified Reynolds number $\mathrm{Re}_M=\mathrm{Re}R_c/c$, which is much smaller than Re. In this way, the local viscous effects around the hydrofoil nose are correctly accounted for. Moreover, in the inner region, to the leading orders the hydrofoil is described by a canonic smooth parabola $y^*=\pm\sqrt{2x^*}$. Along the parabola upper and lower surfaces, the no-penetration and no-slip conditions are satisfied. Also, in the far field of the inner region viscous effects decay and the velocity vector is described by a velocity potential, $\mathbf{V}^*=\delta^2\nabla\Phi+O(\delta^3)$, where

$$\Phi \approx x^* + \sqrt{2r^*}\sin\frac{\theta^*}{2} + (Aw_0/h)\sqrt{2r^*}\cos\frac{\theta^*}{2} + O(\log r^*, \theta^*) \tag{5}$$

Here, $r^*=\sqrt{x^{*2}+y^{*2}}$, $\theta^*=\arctan(y^*/x^*)$. For more details of this expansion, see Rusak [32]. Equation (5) shows that the far-field flow is near uniform with speed U_∞ (of the flow around the hydrofoil), pressure p_∞, and temperature T and with higher-order correction terms that relate to a symmetric flow due to the symmetric nose curvature and an asymmetric circulatory flow with the circulation parameter $\tilde{A}=Aw_0/h$. Equations (4) and (5) show that in the inner region, the flow is governed by the modified Reynolds number Re_M and the circulation parameter $\tilde{A}$. Note that the circulation parameter is given by $\tilde{A}=(\alpha-\delta\bar{w}_0)/\delta h=(\alpha-\alpha_{0l}-\delta\bar{w}_1/2)/\sqrt{R_c/2c}$. Here the relationship $\delta h=\sqrt{R_c/2c}$ is used.

In the present work, the relationship between the minimum pressure coefficient $Cp_{\min}$ and the circulation parameter $\tilde{A}$ at various values of Re_M (i.e., $Cp_{\min}(\tilde{A},\mathrm{Re}_M)$) is sought. In the subsequent section, this relationship is established from the numerical solution of the parabola model problem given by Eqs. (4) and (5). The matching between the inner and outer expansions (Sec. 2.3) shows that this relationship closely represents $Cp_{\min}$ of the hydrofoil.

To relate the minimum pressure coefficient to the condition leading to onset of cavitation, it is useful to present the cavitation number (σ):

$$\sigma = \frac{p_\infty - p_v(T)}{1/2\rho U_\infty^2} \tag{6}$$

Here, $p_v(T)$ is the saturation pressure at temperature T. The cavitation index at inception σ_i is related to the minimum pressure coefficient according to Refs. [6, 18, and 19]

$$\sigma_i = -Cp_{\min} + K_1\frac{p'}{1/2\rho U_\infty^2} - \frac{T'}{1/2\rho U_\infty^2} + \frac{\beta C_g}{1/2\rho U_\infty^2} \tag{7}$$

where K_1 is the pressure fluctuations constant, β is Henry's law constant, C_g is the concentration of dissolved gas, and T' the tensile strength. The second, third, and fourth terms on the right hand side of Eq. (7) incorporate the effects of unsteadiness due to pressure fluctuations p' [18–20], bubble dynamics governed by surface tension T' [35], and influence of dissolved gases in the liquid [36], respectively. For the steady flow of liquid free from noncondensable gases that also cannot withstand any tension (e.g., cavitation occurs instantaneously when the liquid locally reaches the saturation pressure) over a smooth hydrofoil, the classical theory of cavitation inception can be employed such that $\sigma_i \approx -Cp_{\min}$. In this sense, the present results are ideal but universal and may provide a reasonable prediction of the inception of cavitation for a wide range of applications where the effects of the pressure fluctuations, surface tension, and dissolved gas are small.

The inner viscous flow model parabola problem is solved numerically. The solution results in the velocity field around the parabola and the distribution of the pressure coefficient

Downloaded 03 Jun 2010 to 171.66.16.156. Redistribution subject to ASME license or copyright; see http://www.asme.org/terms/Terms_Use.cfm

$Cp^*(x^*,\tilde{A},\mathrm{Re}_M)$ along the parabola surfaces. Both are strongly affected by Re_M, specifically when the Reynolds number is relatively low. The solutions are used to determine $Cp_{\min}(\tilde{A},\mathrm{Re}_M)$ and thereby the value of σ_i as function of the angle of attack α and Reynolds number Re. It should also be noted that for most relevant applications, Re_M is sufficiently large ($\mathrm{Re}_M > 300$) such that thin velocity boundary layers, with thickness much smaller than the parabola radius of curvature, form along the parabola surfaces, even when x^* increases above 10. The flow around the parabola and outside these boundary layers is approximately inviscid and potential. Therefore, we focus on this case and following Rusak [32], the pressure coefficient $Cp^*(x^*,\tilde{A},\mathrm{Re}_M)$ along the parabola surfaces decays like $(-1)^m A w_0 \sqrt{2/x^*}/h$ as x^* increases (where $m=1$ for the upper surface and $m=0$ for the lower surface).

2.3 Matching. For a complete analysis, an asymptotic matching between the inner and outer solutions for the pressure distribution in an overlap region between the two regions ($R_c < x/c < \delta$) is also established. It is found that the two expansions have a common part of the pressure distribution along the hydrofoil surface, which is approximated by

$$Cp_{cp}(x/c;\delta,\alpha) = (-1)^m 2\alpha w_0 \sqrt{c/x} \qquad (8)$$

Note that the common part given by Eq. (8) coincides with the singular behavior of $Cp_{u,l}$ as x approaches zero and with the decay of Cp^* as x^* increases. The asymptotic matching results also in a uniformly valid asymptotic composite solution of the pressure distribution along the entire hydrofoil chord that can be approximated by

$$\begin{aligned} Cp(x/c;\delta,\alpha,\mathrm{Re}) = {} & Cp^*(x^*,\tilde{A},\mathrm{Re}_M) + [Cp_{u,l}(x/c,A) \\ & - Cp_{cp}(x/c,\delta,\alpha)]V^* \end{aligned} \qquad (9)$$

Here, $V^* = \sqrt{1-Cp^*}$. It represents the nondimensional velocity at the edge of the boundary layers that form in the inner region along the parabola surfaces. The formula (9) shows that the pressure distribution along the hydrofoil is composed of a nonlinear combination of the linear theory solution and the nose solution. As the leading edge of the hydrofoil is approached (x tends to zero and $0 < x/c < R_c/c$), the common part pressure Cp_{cp} cancels the nose singularity of the outer linear pressure coefficient solution both on the upper and lower surfaces of the hydrofoil. Also, in this region, V^* is small and tends to zero near the stagnation point. Therefore, the dominant term in the leading-edge region is the parabola pressure coefficient Cp^*, which is strongly affected the modified Reynolds number. As x is increased beyond the leading-edge region, $\delta < x/c < 1$, the parabola velocity V^* tends to 1, and the common part pressure Cp_{cp} cancels the parabola pressure Cp^*. Therefore, the dominant term in the outer region is the classical incompressible linear foil theory solution $Cp_{u,l}$. In the intermediate region, $R_c/c < x/c < \delta$, the pressure changes uniformly from Cp^* to $Cp_{u,l\ l}$.

3 Numerical Solution of the Model Parabola Problem

The inner viscous flow model problem is solved numerically using the commercial code FLUENT for the solution of the Reynolds-averaged Navier–Stokes equations. The Spalart–Allmaras viscous turbulence model is used with a turbulent viscosity ratio of 10. We conducted convergence studies of the numerical solutions with mesh refinement (see details in Kim et al. [37] and Morris [38]) and meshes that provide fully converged results were used in the present work.

The computed pressure coefficient distributions along the parabola upper surface for various values of $\tilde{A}$ are shown in Figs. 1(*a*) and 1(*b*) for the representative cases where $\mathrm{Re}_M=720$ and 7200. It can be seen that as $\tilde{A}$ increases the minimum suction point (where $Cp_{\min}$ occurs) shifts upstream along the upper surface. Only when $\tilde{A} > 0.5$ the point of maximum suction appears at the nose region and it shifts upstream toward the leading edge and the suction deepens, up to the certain state where $\tilde{A} > \tilde{A}_s$ and separation and stall develop on the parabola. Note that $\tilde{A}_s=2.2$ when $\mathrm{Re}_M=720$ and $\tilde{A}_s=2.9$ when $\mathrm{Re}_M=7200$. At these conditions, the position of the minimum pressure point is within a distance of 1 R_c or less from the leading edge, which is well within the inner region and thereby supports the present theoretical approach.

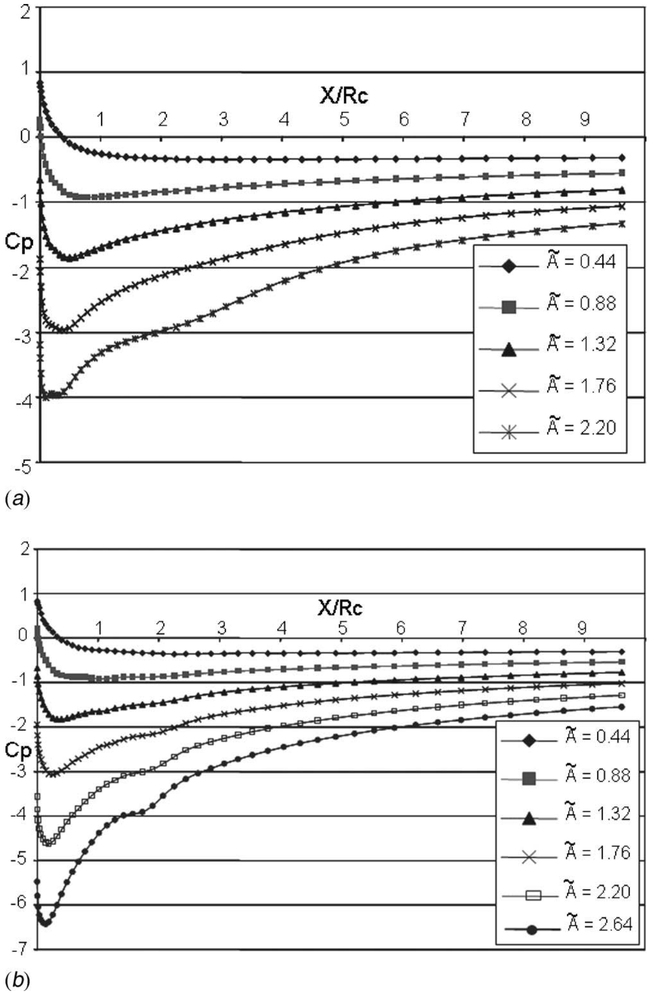

Fig. 1 (*a*) The distribution of the pressure coefficient along the parabola upper surface at various values of $\tilde{A}$. Here, Re_M=720. (*b*) The distribution of the pressure coefficient along the parabola upper surface at various values of $\tilde{A}$. Here, Re_M=7200.

Figure 2 presents the change of $\sigma_i = -Cp_{\min}$ with the circulation parameter $\tilde{A}$ at various values of Re_M. It can be seen that σ_i increases with $\tilde{A}$ for all Re_M at low $\tilde{A}$. Note that σ_i weakly depends on the Reynolds number before the occurrence of stall, i.e., when $\tilde{A} < \tilde{A}_s(\mathrm{Re}_M)$ where the stall circulation parameter may be given by $\tilde{A}_s(\mathrm{Re}_M) = 0.29\ln(\mathrm{Re}_M) + 0.31$ (see Morris [38]). However, when $\tilde{A} \geq \tilde{A}_s(\mathrm{Re}_M)$ flow separation and stall occur and then σ_i strongly depends on Reynolds number.

Figure 3 presents the above results in the range $0.4 < \tilde{A} < 1.45$ where the flow is attached for all Reynolds numbers. Also shown in this figure is the empirical linear relationship $\sigma_i = 17(\alpha - 2) = 17\tilde{A}\sqrt{R_c/2c} - 0.6$ of Kjeldsen et al. [8] for the inception of cavitation (the dot-dashed line) in the range 3 deg $< \alpha <$ 8 deg. We used here $\mathrm{R}_c/c = 0.0248$ of the NACA0015 tested in the experiments, α is in radians and a 2 deg bias is subtracted from α in accordance with the reported experimental bias in measuring α.

Downloaded 03 Jun 2010 to 171.66.16.156. Redistribution subject to ASME license or copyright; see http://www.asme.org/terms/Terms_Use.cfm

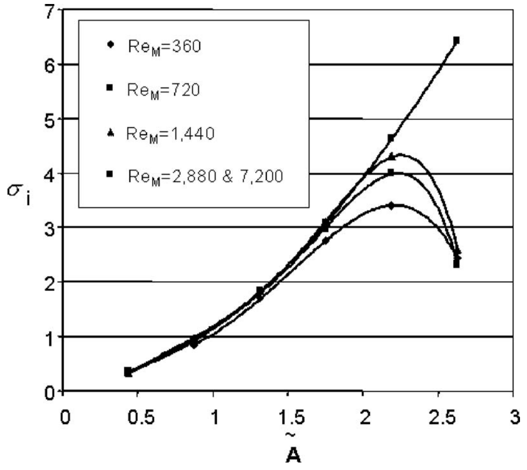

Fig. 2 σ_i **as function of** $\tilde{A}$ **for various values of** Re_M

The present theoretical predictions show a good agreement with the empirical predictions of Kjeldsen et al. [8] for the whole range.

The variation of $\sigma_i = -Cp_{\min}$ with Re_M at various fixed values of $\tilde{A}$ is shown in Fig. 4. It can be seen that σ_i increases with the modified Reynolds number for all $\tilde{A}$ and tends to a nearly constant value when Re is sufficiently high. Also note that when $\tilde{A}$ is sufficiently high, $\tilde{A}=2.7$, there is a clear jump in the values of σ_i with the increase of Re_M around $Re_M=2750$. The flow is fully separated (stall) and $\sigma_i = -Cp_{\min}$ is relatively low (~ 1.7) when $Re_M < 2750$. On the other hand, the flow is fully attached and $\sigma_i = -Cp_{\min}$ is high (~ 7.6) when $Re_M > 2750$. The case of $\tilde{A}=2.7$ describes the transition from a state with a long separation bubble to a state with a short separation bubble as Re_M (or the oncoming speed of the flow) increases, which has been previously shown to significantly effect the conditions leading to cavitation inception in a manner similar to the current results [3,6,28–30].

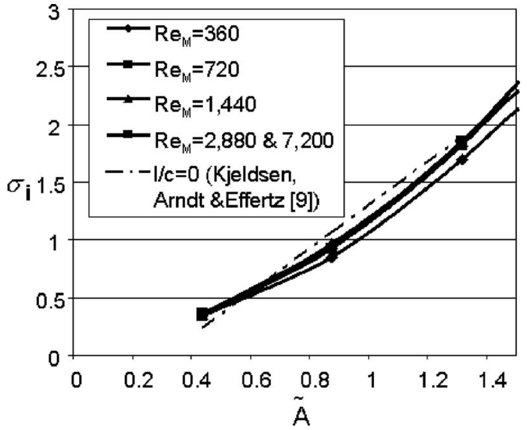

Fig. 3 σ_i **as function of** $\tilde{A}$ **for various values of** Re_M **for the range of attached flow** $0.4 < \tilde{A} < 1.45$**. Experimental data from Kjeldsen et al. [8].**

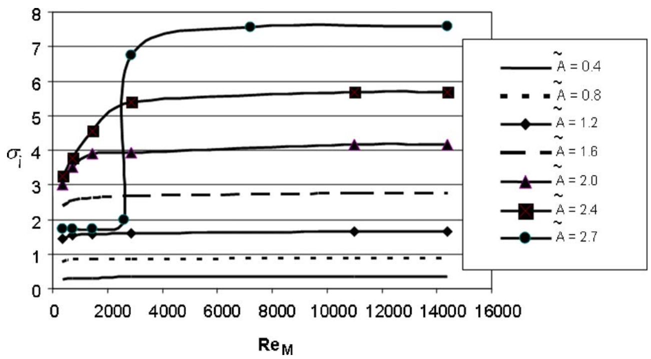

Fig. 4 σ_i **as function of** Re_M **for various values of** $\tilde{A}$

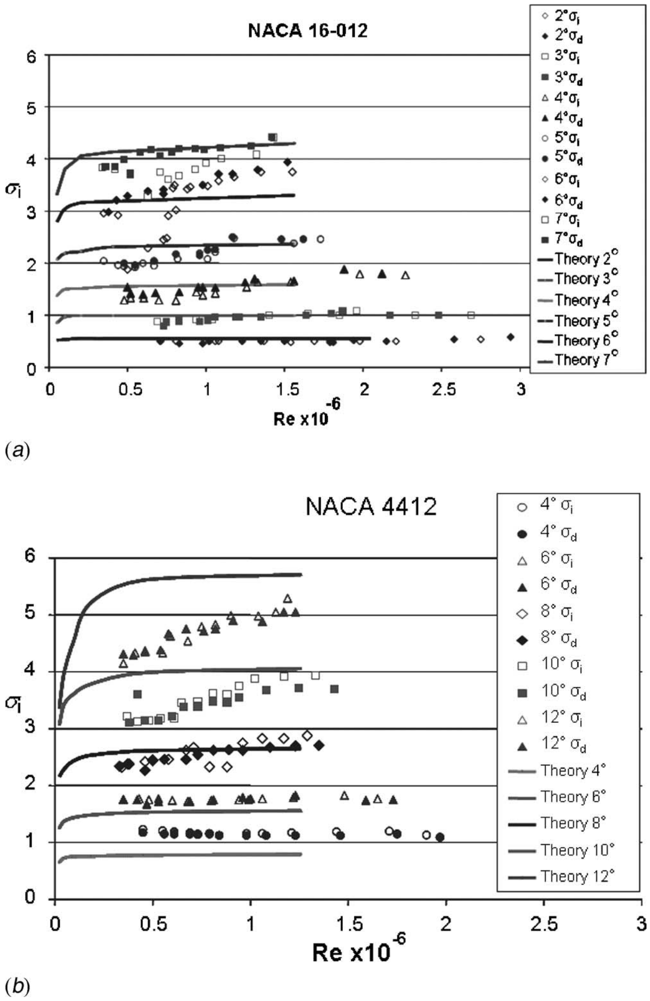

Fig. 5 (*a*) σ_i **as function of Re for a NACA 16-012 at various fixed values of angle of attack** α**. Experimental results from Van der Meulen [5]. (*b*)** σ_i **as function of Re for a NACA 4412 at various fixed values of angle of attack** α**. Experimental results from Van der Meulen [5].**

The results of Fig. 4 are now used to predict the onset of leading-edge (sheet) cavitation over two classical airfoils, the NACA 16-012 and 4412, as function of Re at various fixed angles of attack. Note that for the symmetric NACA 16-012 foil $R_c/c = 0.00703$ and $\delta w_0 = 0$ and for the cambered NACA 4412 foil $R_c/c = 0.0158$ and $\delta w_0 = 0.006$. The theoretical predictions are compared with the available experimental data of van der Meulen [5], see Figs. 5(*a*) and 5(*b*). Both figures present a relatively good agreement (usually within 10%) between the theoretical predictions of the onset of cavitation according to the model parabola problem and the measured results, specifically with the desinent cavitation number σ_d. The average difference between the predictions and the data for the NACA 16-012 is about 5% and that for the NACA 4412 is about 10%. The theory overpredicts the results for NACA4412 at the higher angles of attack with about 15%. These differences may be attributed to limitations of the theoret-

Downloaded 03 Jun 2010 to 171.66.16.156. Redistribution subject to ASME license or copyright; see http://www.asme.org/terms/Terms_Use.cfm

ical model problem and measurement errors in the experiments. The model parabola problem is limited to the prediction of the onset of leading-edge cavitation at the first 3% of the foil's chord. It does not account for the effects of hydrofoil local geometry changes beyond the nose region, of surface roughness, of unsteady pressure fluctuations, of water surface tension, and of dissolved gases in the liquid. Therefore, as expected and documented in earlier studies [8] $(-Cp_{\min})$ in most cases is higher than σ_i and essentially provides an upper limit to the value of σ_i. On the other hand, the experimental data may include uncertainties due to the detection of the onset of cavitation and errors in measuring the far-field pressure and speed to determine σ_i or σ_d. Secondary effects in the experiments may be related to the foil surface roughness, the effect of the water tunnel walls, the foil end effects, and the hysteresis in the appearance of the cavitation bubble. Note that the experiments of van der Meulen [5] did not report any attempt to correct the reported results due to the above uncertainties and errors and, therefore, the differences between the theoretical predictions and the data are satisfactory. The results in Figs. 5(*a*) and 5(*b*) support the conclusion that Figs. 2 and 4 provide a universal criterion for the onset of leading-edge sheet cavitation on hydrofoils.

4 Summary and Discussion

The inception of leading-edge sheet cavitation on two-dimensional smooth thin hydrofoils at low to moderate Reynolds number flows can be investigated by an asymptotic approach and numerical simulations. Scaled (magnified) coordinates and a modified (smaller) Reynolds number (Re_M) are used to correctly account for the nonlinear behavior and extreme velocity changes in the hydrofoil nose region, where both the near-stagnation and high suction areas occur. A reduced-order model parabola problem is formulated where the far-field circulation is governed by a parameter $\tilde{A}$ that is related to the hydrofoil's angle of attack, nose radius of curvature, and camber. The numerical solution of the model parabola problem for various values of $\tilde{A}$ and Re_M results in the minimum pressure coefficient $Cp_{\min}$ and the cavitation number $\sigma_i = -Cp_{\min}$ for the inception of leading-edge cavitation as function of the hydrofoil's geometry, flow Reynolds number, and fluid thermodynamic properties. The predictions according to this approach show good agreement with results from available experimental data.

Figures 2 and 4 provide a universal criterion to determine the onset of leading-edge sheet cavitation on hydrofoils with a parabolic nose in terms of the similarity parameters $\tilde{A}$ and Re_M. The figures help to analyze the effects of the hydrofoil's thickness ratio, nose radius of curvature, camber, and flow Reynolds number on this phenomenon. For example, it can be seen that by increasing the nose radius of curvature for a fixed chord (by using a different hydrofoil) it is possible to maintain the same σ_i by increasing the angle of attack and decreasing the Reynolds number (oncoming flow velocity or hydrofoil's chord) so that $\tilde{A}$ and Re_M remain the same. Alternatively, for a given hydrofoil, a lower angle of attack is needed while increasing the oncoming flow velocity or increasing the chord to maintain a certain σ_i.

Finally, it should be noted that when the Reynolds number is sufficiently high it can be shown that $\sigma_i = -Cp_{\min} = \tilde{A}^2$ before the occurrence of stall. Then, using the relationship $\tilde{A} = (\alpha - \delta\bar{w}_0)/\delta h = (\alpha - \alpha_{0l} - \delta\bar{w}_1/2)/\sqrt{R_c/2c}$, the condition for the inception of sheet cavitation is

$$\sigma_i = \frac{(\alpha - \delta\bar{w}_0)^2}{R_c/2c} \tag{10}$$

or the angle of attack and lift coefficient at cavitation onset are

$$\alpha_i = \sqrt{\frac{R_c}{2c}\sigma_i} + \alpha_{0l} + \delta\frac{\bar{w}_1}{2} = \sqrt{\frac{R_c}{2c}\sigma_i} + \delta\bar{w}_0 \tag{11a}$$

$$C_{l,i} = 2\pi(\alpha_c - \alpha_{0l}) = 2\pi\sqrt{\frac{R_c}{2c}\sigma_i} + \pi\delta\bar{w}_1 \tag{11b}$$

It can be seen from Eq. (10) that the inception of sheet cavitation occurs at a higher value of the cavitation number when the angle of attack of a given hydrofoil is increased or when the nose radius of curvature of hydrofoil's thickness ratio is decreased at a fixed angle of attack. Moreover, since usually $\delta\bar{w}_0 > 0$ for cambered foils, it can be seen that the cavitation number σ_i decreases with the increase of camber. Moreover, Eqs. (11*a*) and (11*b*) show that for a given σ_i and when there is no camber ($\delta\bar{w}_0 = \delta\bar{w}_1 = 0$), the cavitation inception angle and the related lift coefficient increase with the square root of the cavitation number and with the square root of the nose radius of curvature. Note, however, that these results are limited to thin hydrofoils with thickness ratios less than 12%.

Nomenclature

A = scaled angle of attack, $=\alpha/\delta$
A_n = pressure coefficient solution's coefficients
$\tilde{A}$ = circulation parameter
c = airfoil's chord
C_a = airfoil's camber function
C_g = the concentration of dissolved gas
C_l = airfoil's lift coefficient
Cp = pressure coefficient
F = airfoil's shape function
h = airfoil's nose parameter, $=R_c/(2\delta^2 c)$
K_1 = the pressure fluctuations constant
p = pressure
p_v = saturation pressure
p' = pressure fluctuations
r = distance from origin
R_c = airfoil's nose radius of curvature
Re = Reynolds number
Re_M = modified Reynolds number
t = airfoil's thickness function
T = temperature
T' = the tensile strength
U_∞ = uniform flow speed
V = speed
$\mathbf{V}$ = velocity vector
w_n = integral of camber function
x = axial coordinate
y = vertical coordinate
α = airfoil's angle of attack
β = Henry's law constant
δ = airfoil's thickness ratio
Φ = velocity potential
σ = cavitation number
σ_i = cavitation inception index
μ = viscosity
ρ = density
θ = transformation variable or angle of point with respect to x axis
ξ = integration parameter

Indices

cp = common part
i = cavitation inception
min = minimum pressure point
m,n = indices
u,l = along airfoil's upper and lower surfaces, respectively
s = stall
∞ = property of upstream flow
$'$ = differentiation
$*$ = inner solution
$0l$ = zero lift

Downloaded 03 Jun 2010 to 171.66.16.156. Redistribution subject to ASME license or copyright; see http://www.asme.org/terms/Terms_Use.cfm

References

[1] Arakeri, V. H., and Acosta, A. J., 1973, “Viscous Effects in the Inception of Cavitation on Axisymmetric Bodies,” ASME J. Fluids Eng., **95**(4), pp. 519–527.

[2] Arakeri, V. H., 1975, “Viscous Effects on the Position of Cavitation Separation from Smooth Bodies,” J. Fluid Mech., **68**, pp. 779–799.

[3] Arakeri, V. H., Carroll, J. A., and Holl, J. W., 1981, “A Note on the Effect of Short and Long Laminar Separation Bubbles on Desinent Cavitation,” ASME J. Fluids Eng., **103**(1), pp. 28–32.

[4] Van der Meulen, J. H. J., 1978, “A Holographic Study of the Influence of Boundary Layer and Surface Characteristics on Inception and Developed Cavitation on Axisymmetric Bodies,” *Proceedings of 12th Symposium on Naval Hydrodynamics*, Washington, DC, pp. 443–451.

[5] Van der Meulen, J. H. J., 1980, “Boundary Layer and Cavitation Studies of NACA 16–012 and NACA 4412 Hydrofoils,” *Proceedings of 13th Symposium on Naval Hydrodynamics*, Tokyo, Japan, pp. 195–219.

[6] Billet, M. L., and Holl, J. W., 1981, “Scale Effects on Various Types of Limited Cavitation,” ASME J. Fluids Eng., **103**(3), pp. 405–414.

[7] Franc, J. P., and Michel, J. M., 1985, “Attached Cavitation and the Boundary Layer: Experimental Investigation and Numerical Treatment,” J. Fluid Mech., **154**, pp. 63–90.

[8] Kjeldsen, M., Arndt, R. E. A., and Effertz M., 2000, “Spectral Characteristics of Sheet/Cloud Cavitation,” ASME J. Fluids Eng., **122**(3), pp. 481–487.

[9] Shen, Y. T., and Dimotakis, P. E., 1989, “Viscous and Nuclei Effects on Hydrodynamic Loadings and Cavitation of a NACA 66 (MOD) Foil Section,” ASME J. Fluids Eng., **111**, pp. 306–316.

[10] Kinnas, S. A., and Mazel, C. H., 1993, “Numerical Versus Experimental Cavitation Tunnel (A Supercavitating Hydrofoil Experiment),” ASME J. Fluids Eng., **115**(4), pp. 760–765.

[11] Yamaguchi, H., and Kato, H., 1983, “On Application of Nonlinear Cavity Flow Theory to Thick Foil Sections,” *Second International Conference on Cavitation*, Edinburgh, Scotland, pp. 167–174.

[12] Lemonnier, H., and Rowe, A., 1988, “Another Approach in Modeling Cavitating Flows,” J. Fluid Mech., **195**, pp. 557–580.

[13] Pellone, C., and Rowe, A., 1988, “Effect of Separation on Partial Cavitation,” J. Fluid Mech., **110**(2), pp. 182–189.

[14] Berntsen, G. S., Kjeldsen, M., and Arndt, R. E. A., 2001, “Numerical Modeling of Sheet and Tip Vortex Cavitation With Fluent 5,” *Fourth International Symposium on Cavitation*, Pasadena, CA.

[15] Wu, T. Y. T., 1972, “Cavity and Wake Flows,” Annu. Rev. Fluid Mech., **4**, pp. 243–284.

[16] Furuya, O., 1980, “Non-Linear Theory for Partially Cavitating Cascade Flows,” *Tenth International Symposium Hydraulic Machinery and Equipment Associated With Energy Systems in the New Decade of the 1980s*, Tokyo, Japan, pp. 221–241.

[17] Holl, J. W., 1969, “Limited Cavitation,” *Symposium on Cavitation State of Knowledge*, Evanston, IL, pp. 26–63.

[18] Arndt, R. E. A., 1995, “Vortex Cavitation,” *Fluid Vortices*, S. Green, ed., Kluwer, Dordrecht, Chap. 17.

[19] Arndt, R. E. A., 1981, “Cavitation in Fluid Machinery and Hydraulic Structures,” Annu. Rev. Fluid Mech., **13**, pp. 273–328.

[20] Arndt, R. E. A., Holl, J. W., Bohn, J. C., and Bechtel, W. T., 1979, “Influence of Surface Irregularities on Cavitation Performance,” J. Ship Res., **23**(3), pp. 157–170.

[21] Holl, J. W., and Wislicenus, G. F., 1961, “Scale Effects on Cavitation,” ASME J. Basic Eng., **83**, pp. 385–398.

[22] Holl, J. W., 1970, “Nuclei and Cavitation,” ASME J. Basic Eng., **92**, pp. 681–688.

[23] Meyer, R. S., Billet, M. L., and Holl, J. W., 1992, “Freestream Nuclei and Traveling-Bubble Cavitation,” ASME J. Fluids Eng., **114**(4), pp. 672–679.

[24] Liu, Z., and Brennen, C. E., 1998, “Cavitation Nuclei Population and Event Rates,” ASME J. Fluids Eng., **120**, pp. 728–737.

[25] Gowing, S., and Shen, Y., 2001, “Nuclei Effects on Tip Vortex Cavitation Scaling,” *Fourth International Symposlum on Cavitation*, Pasadena, CA.

[26] McCormick, B. W., 1962, “On Cavitation Produced by a Vortex Trailing From a Lifting Surface,” ASME J. Basic Eng., **84**, pp. 369–379.

[27] Arndt, R. E. A., Arakeri, V. H., and Higuchi, H., 1991, “Some Observations of Tip-Vortex Cavitation,” J. Fluid Mech., **229**, pp. 269–289.

[28] Huang, T. T., and Peterson, F. B., 1976, “Influence of Viscous Effects on Model/Full-Scale Cavitation Scaling,” J. Ship Res., **20**(4), pp. 215–223.

[29] Arakeri, V. H., 1976, “A Note on the Transition Observation on an Axisymmetric Body and Some Related Fluctuating Wall Pressure Measuerments,” ASME J. Fluids Eng., **97**, pp. 82–86.

[30] Robertson, J. M., McGinley, J. H., and Holl, J. W., 1957, “On Several Laws of Cavitation Scaling,” La Houille Blanche, **4**, pp. 540–547.

[31] Guennoun, F. M., 2006, “Physical Study of a Leading Edge Cavity Dettachment,” Ph.D. thesis, Ecole Polytechnic Federale de Lausanne, Switzerland.

[32] Rusak, Z., 1994, “Subsonic Flow Around the Leading Edge of a Thin Aerofoil With a Parabolic Nose,” Eur. J. Appl. Math., **5**, pp. 283–311.

[33] Darrozés, J. S., 1977, “Comportement Singulier des écoulements à Grand Nombre de Reynolds au Voisinage du Bord d’attaque d’Une Aile Mince,” *Singular Perturbations and Boundary Layer Theory*, Lecture Notes in Mathematics No. 594, Springer-Verlag, New York, pp. 77–107.

[34] Tani, I., 1964 “Low Speed Flows Involving Bubble Separations,” Prog. Aeronaut. Sci., **5**, pp. 70–103.

[35] Keller, A. P., 1984, “Scale Effects at Beginning Cavitation Applied to Submerged Bodies,” *International Symposyum on Cavitation Inception, FED-16, The Winter Annual Meeting of the ASME*, New Orleans, LA, pp. 43–47.

[36] Holl, J. W., 1960, “An Effect of Air Content on the Occurrence of Cavitation,” ASME J. Basic Eng., **82**, pp. 941–946.

[37] Kim, J.-M., Rusak, Z., and Koratkar, N., 2003, “Small-Scale Airfoil Aerodynamic Efficiency Improvement by Surface Temperature and Heat Transfer,” AIAA J., **11**, pp. 2105–2113.

[38] Morris, W. J., II, 2005, “On the Prediction of Stall Onset for Airfoils at Moderately High Reynolds Number Flows,” M.S. thesis, Rensselaer Polytechnic Institute, Troy.

Downloaded 03 Jun 2010 to 171.66.16.156. Redistribution subject to ASME license or copyright; see http://www.asme.org/terms/Terms_Use.cfm

Flow Past a Sphere With Surface Blowing and Suction

Prosenjit Bagchi
Department of Mechanical and Aerospace
Engineering,
Rutgers, The State University of New Jersey,
98 Brett Road,
Piscataway, NJ 08854
e-mail: pbagchi@jove.rutgers.edu

The effect of uniform surface blowing and suction on the wake dynamics and the drag and lift forces on a sphere is studied using a high-resolution direct numerical simulation technique. The sphere Reynolds number Re, based on its diameter and the freestream velocity, is in the range 1–300. The onset of recirculation in the sphere wake occurs at higher Re, and the transition to nonaxisymmetry and unsteadiness occurs at lower Re in the presence of blowing. The size of the recirculation region increases with blowing, but it nearly disappears in the case of suction. Wake oscillation also increases in the presence of blowing. The drag coefficient in the presence of blowing is reduced compared to that in uniform flow, in the range $10<\mathrm{Re}<250$, *whereas it is increased in the presence of suction. The reduction in the wake pressure minimum associated with the enhanced vortical structures is the primary cause for drag reduction in the case of blowing. In the case of suction, it is the increased surface vorticity associated with the reduction of the boundary layer that results into increased drag. The fluctuations in the instantaneous lift and drag coefficients are significant for blowing, and they result from the asymmetric movement of the wake pressure minimum associated with the shedding process.*
[DOI: 10.1115/1.2801361]

1 Introduction

Accurate prediction of forces acting on particles moving through a fluid is important in many engineering and environmental applications. Equally important is the detailed understanding of the dynamics of the wake of the individual particle, which can strongly affect its trajectory [1]. Uniform flow past a rigid sphere has been studied extensively over the past decades using experimental, numerical, and analytical approaches [2–11]. The flow characteristics are parametrized in terms of the sphere Reynolds number (Re), which is based on the sphere diameter and the relative velocity between the sphere and the undisturbed ambient flow. These studies revealed primarily four distinct regimes of the sphere wake: axisymmetric unseparated flow for $\mathrm{Re}<20$, steady axisymmetric wake with separation for $20<\mathrm{Re}<210$, steady nonaxisymmetric flow for $210<\mathrm{Re}<270$, and unsteady vortex shedding for $\mathrm{Re}>270$.

The force on the sphere at low Re is given by the well-known Stokes drag. At small but finite Re, the Stokes drag is corrected by the Oseen term [12]. At higher Re, empirical correlations such as those by Schiller and Neumann [13] are available for the drag on the sphere [12]. At moderate Reynolds numbers (i.e., $1<\mathrm{Re}<500$ [6]), the problem is further complicated due to the appearance of the recirculation region, nonaxisymmetry, and vortex shedding in the sphere wake. One needs full 3D simulation in this range as the forces on the sphere are often dependent on the wake dynamics. In addition, the freestream flow could be inhomogeneous, unsteady, or turbulent, and hence could alter the drag and lift forces [14–28].

In many engineering applications, mass injection (blowing) or suction occurs on the surface of the sphere. Examples are evaporation and condensation of droplets in the presence of an oncoming freestream flow. Niazmand and Renksizbulut [29,30] numerically studied the effect of nonuniform surface blowing on a sphere rotating about an axis normal to the freestream flow in the range of $10\leq\mathrm{Re}\leq300$. Niazmand and Renksizbulut [31] also considered the combined effect of particle spin (i.e., rotation about an axis parallel to the freestream flow) and surface blowing. They observed that the transition to unsteady vortex shedding under the combined effect of particle rotation/spin and surface blowing occurs at a Reynolds number as low as 200. However, from their simulations, it was not clear whether the early onset of vortex shedding is due to the effect of rotation/spin or surface blowing. Bagchi and Balachandar [21] and Kurose and Komori [18] performed numerical simulation of a rotating sphere in linear shear flows. Kim and Choi [32] simulated flow past a spinning sphere in the similar range of Re. These simulations did not predict any early transition to three-dimensional or unsteady regime. Thus, the effect of surface blowing/suction alone appears to be poorly understood and is the subject of the present study.

The objective of this study is to characterize the effect of surface blowing and suction on the wake dynamics and the drag and lift forces on the sphere. The blowing or suction is considered to be uniform over the sphere surface, and the sphere Reynolds number is in the range $1\leq\mathrm{Re}\leq300$. We employ a direct numerical simulation (DNS) technique to solve fully 3D Navier–Stokes equation using a pseudospectral collocation method. In the next section, the numerical method is briefly outlined, followed by the presentation of the results.

2 Simulation Technique

The problem formulation and the numerical methodology are the same as that described in Refs. [20,33]. We consider a sphere of diameter d located at the origin of a reference frame (X,Y,Z), and subject to an oncoming uniform flow U_∞ directed toward the positive X. The flow is assumed to be incompressible, isothermal, and with constant physical properties. Using the sphere diameter as a characteristic length scale, U_∞ as the velocity scale, and d/U_∞ as the time scale, the governing equations in the dimensionless form can be written as

$$\nabla\cdot\mathbf{u}=0 \tag{1}$$

$$\frac{\partial\mathbf{u}}{\partial t}+\mathbf{u}\cdot\nabla\mathbf{u}=-\nabla p+\frac{1}{\mathrm{Re}}\nabla^2\mathbf{u} \tag{2}$$

where $\mathrm{Re}=dU_\infty/\nu$ is the sphere Reynolds number. The computational domain is a spherical region concentric with the sphere, and has a diameter $40d$. The governing equations are written in the spherical coordinate system (r,θ,ϕ). The spatial discretization of the equations is done using a pseudospectral scheme. In the radial direction (r), a Chebyshev expansion is used, and in the azimuthal

---

Contributed by the Fluids Engineering Division of ASME for publication in the Journal of Fluids Engineering. Manuscript received December 16, 2006; final manuscript received June 30, 2007. Review conducted by Malcolm J. Andrews.

Copyright © 2007 by ASME

Downloaded 03 Jun 2010 to 171.66.16.156. Redistribution subject to ASME license or copyright; see http://www.asme.org/terms/Terms_Use.cfm

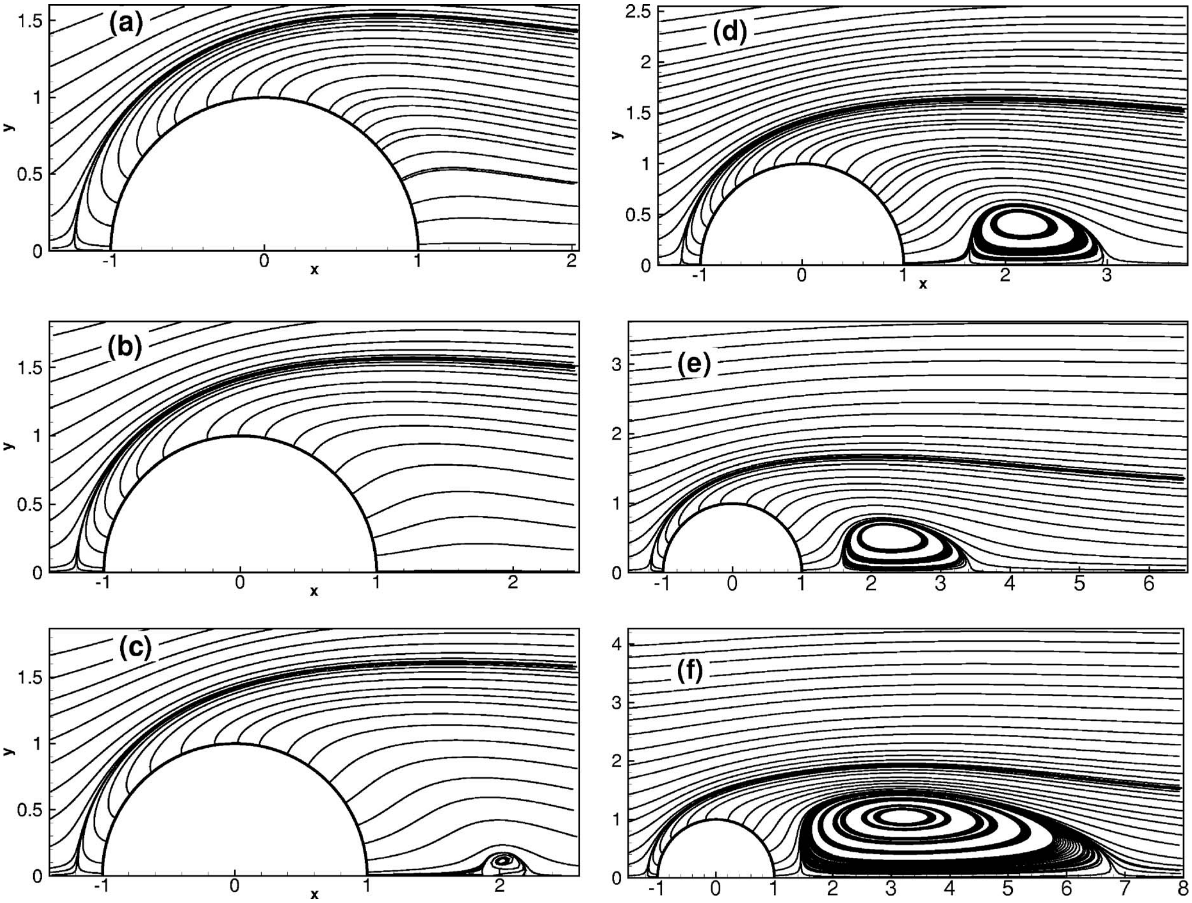

Fig. 1 Streamlines in the presence of surface blowing at $B=0.2$. (*a*)–(*f*) are for Re=10, 26, 38, 45, 50, and 100, respectively.

(ϕ) direction, a Fourier expansion is used. In the tangential (θ) direction, a sine or cosine expansion is used, which satisfies the "pole parity" condition in the spherical coordinates [9]. The grid points are clustered near the surface of the sphere, and in the wake region, using appropriate mapping functions to resolve the boundary layer and the wake structure. A typical grid used in the simulation consists of 121, 80, and 32 points in the radial, tangential, and azimuthal directions, respectively. The accuracy of the numerical method and the adequacy of the resolution used in the simulation have been tested in numerous flows, such as uniform freestream flow, linear shear flow, axisymmetric and planar straining flow, and turbulent freestream flow. These validations are presented in Refs. [33,20–25] and are not repeated here. Similar resolution check is also done in the present case of surface blowing. In the context of the spectral method used here, the decay of the velocity spectra with respect to the azimuthal wave numbers and Chebyshev coefficients provides a measure of the sufficiency of the resolution. A decay of at least seven orders of magnitude is ensured at every point in the entire computational domain [20–25,33]. The effect of the computational domain size has also been addressed in these references and found to be minimal.

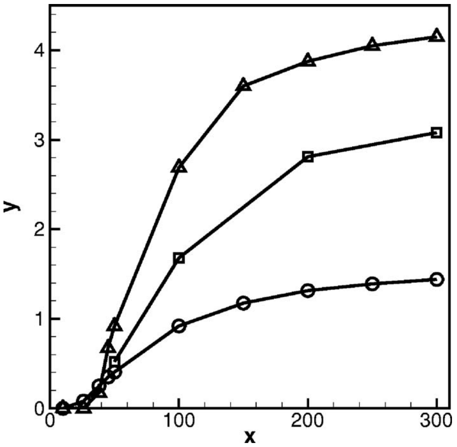

Fig. 2 Dimensionless length L_e/d of the recirculation region: (—○—) $B=0$, (—□—) $B=0.1$, and (—△—) $B=0.2$

A two-step time-split method is used to advance the flow field. In the first step, an advection-diffusion equation is solved to predict the velocity. Here, the nonlinear terms are treated explicitly using second-order accurate Adams–Bashforth scheme, and the viscous terms are treated semi-implicitly using Crank–Nicolson scheme. The velocity is not divergence-free at the end of the advection-diffusion step. The Poisson equation is then solved to obtain pressure at the next time level. Using the new pressure, the velocity is corrected to make it divergence-free. In order to reduce computation, the Poisson equation is Fourier transformed in the ϕ direction yielding a set of 2D decoupled partial differential equations (PDEs), which is directly inverted to obtain pressure.

At the inflow, the Dirichlet boundary condition specifying the undisturbed uniform flow U_∞ is used. At the outflow, a nonreflecting boundary condition by Mittal and Balachandar [34] is used. On the surface of the sphere, the slip condition and the blowing/suction/zero mass flow condition are implemented as

Downloaded 03 Jun 2010 to 171.66.16.156. Redistribution subject to ASME license or copyright; see http://www.asme.org/terms/Terms_Use.cfm

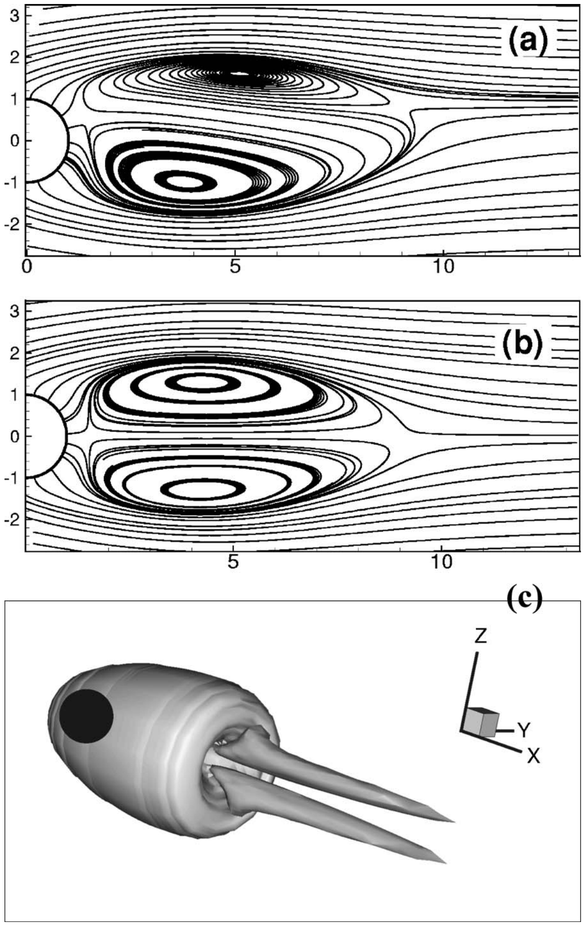

Fig. 3 Streamlines for Re=150, $B=0.2$: (*a*) *x-y* plane, (*b*) *x-z* plane, and (*c*) 3D vortex topology

$$u_r = B \quad u_\theta = 0 \quad u_\phi = 0 \tag{3}$$

where $B=B^*/U_\infty$ is dimensionless, and B^* is the dimensional blowing/suction velocity. For uniform flow without suction/blowing, $B=0$. The positive values of B indicate surface blowing, while the negative values indicate suction.

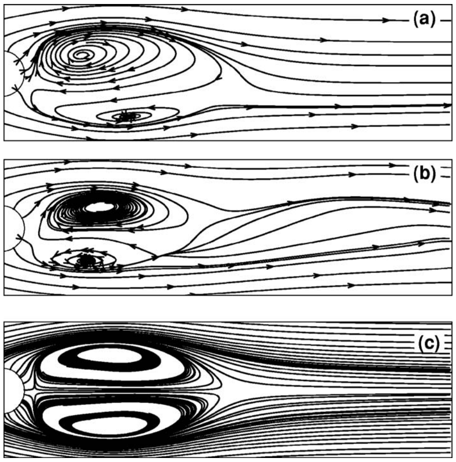

Fig. 4 ((*a*) and (*b*)) Streamlines at Re=200, $B=0.2$ in the *x-y* plane for two time instants. (*c*) Streamlines in the *x-z* plane.

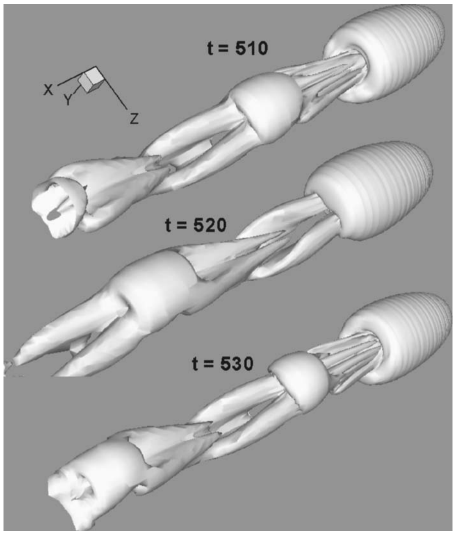

Fig. 5 3D vortex topology for Re=200, $B=0.1$

The mean quantities of interest are the drag and lift forces acting on the sphere, which are obtained by integrating the normal and tangential stresses on the surface as

$$\mathbf{F}(t) = \int_S [-p\mathbf{e}_r + \tau_{r\theta}\mathbf{e}_\theta + \tau_{r\phi}\mathbf{e}_\phi] dS \tag{4}$$

The nondimensional force coefficient is defined as

$$\mathbf{C_F} = \frac{\mathbf{F}}{(1/2)\rho U_\infty^2 \pi (d/2)^2} \tag{5}$$

The component of $\mathbf{C_F}$ along X is the drag coefficient C_D, and the normal component is the lift coefficient C_L. Quantitative comparison of the present methodology with the previous experimental and numerical results has been done in the aforementioned references and is not repeated here. In brief, the present numerical method shows excellent agreement with the previously established results for flow past a rigid sphere in the range $1 \leqslant \mathrm{Re} \leqslant 600$ in terms of the drag and lift coefficients, separation angle, separation length, Strouhal number of vortex shedding, and the structure of the wake.

3 Results and Discussion

3.1 Wake Structure. Numerical simulations are performed for Reynolds numbers ranging from 1 to 300, and blowing parameter B from -0.2 to 0.2. Following the literature of wake control (e.g., Ref. [35]), we can also define a suction coefficient Q_B/Q, where $Q_B = \pi d^2 B^*$ is the blowing/suction volume flow rate, and $Q = \pi d^2 U_\infty/4$ is a reference flow rate. This yields suction coefficient $Q_B/Q = 4B$. The range of values of B considered here is similar to those considered in previous studies, e.g., by Gogos et al. [36] and Jog et al. [37]. In practice, the specific values, however, depend on the specific fuel and ambient combination (see, e.g., Ref. [38]). Also, in practice, the blowing/suction may not be uniform as assumed here (see, e.g., Refs. [29,30]).

3.1.1 Surface Blowing. The streamline patterns in the presence of blowing are shown in Fig. 1 for Re up to 100. These plots can be compared with the previously known results for the uniform flow for which the flow remains axisymmetric until $\mathrm{Re} \approx 210$. The flow at finite Re also shows a fore-aft asymmetry about $\theta = \pi/2$. At Re=26, a recirculation region appears in the wake of the sphere. As Re increases further, the recirculation region grows in size.

When surface blowing is introduced, several changes in the streamline patterns can be observed in Fig. 1. First, the streamlines representing the oncoming uniform flow are strongly diverted away from the sphere. There are streamlines originating from the surface of the sphere due to blowing. The front stagna-

Downloaded 03 Jun 2010 to 171.66.16.156. Redistribution subject to ASME license or copyright; see http://www.asme.org/terms/Terms_Use.cfm

tion point is observed to lift off the surface and moves upstream, whereas the rear stagnation point is absent. At Re=10, the fore-aft asymmetry about $x=0$ line is strongly enhanced compared to the uniform flow case. The recirculation region no longer emerges at Re=26. The first appearance of the recirculation region occurs at Re≈38 (Fig. 1(*c*)). This Reynolds number is nearly independent of the range of values (0.05–0.2) of B considered here. The delay in the onset of recirculation is due to the acceleration of the fluid close to the surface of the sphere caused by blowing. One of the most striking features of the recirculation in the presence of surface blowing is that it is not attached to the sphere. The upstream end of the recirculation region appears at a downstream distance of about one radius from the rear of the sphere.

As Re increases beyond 38, the recirculation region grows very rapidly in the presence of blowing. Above Re≈45, the size of the recirculation region in the presence of blowing is larger than that in uniform flow. At Re=100, the length of the recirculation region in the presence of blowing is nearly twice that in a uniform flow. The dimensionless length L_e/d of the recirculation region is plotted in Fig. 2 as a function of Re and B. The higher the blowing parameter B, the larger the recirculation region for a given Re. At Re=300, L_e is nearly four times higher for $B=0.2$ than for $B=0$. At any Re, the recirculation region in the presence of blowing is not attached to the sphere, rather it is shifted downstream.

Numerical experiments suggest that the flow in the presence of surface blowing remains steady and axisymmetric up to Re=100 for the range of $B \leq 0.2$ considered here. The bifurcation to nonaxisymmetry occurs at a much lower Reynolds number in the presence of surface blowing than that for the uniform flow. However, the transition to nonaxisymmetry strongly depends on B. As an example, the next higher Re considered in our simulation is 150, for which the flow at $B=0.1$ is steady and axisymmetric. However, as B is increased to 0.2, the flow at Re=150 becomes nonaxisymmetric, as shown in Fig. 3. The streamline plots in figure resemble those observed for uniform flow at 210<Re<270, for which a plane of symmetry exists. As seen in Fig. 3, the planar symmetry of the wake exists even in the presence of blowing. The 3D vortex topology in the sphere wake, using the isocontours of the swirling strength, for the above case is presented in Fig. 3(*c*), which shows a double-threaded structure. In the case of a uniform flow, the double-threaded wake appears for 210<Re<270. Results suggest that first transition to three dimensionality could occur at a Reynolds number as low as 150 in the presence of blowing.

Next, we consider Re=200 for which the flow is known to be axisymmetric and steady in the absence of blowing. When surface blowing is introduced at $B=0.05$, the wake becomes nonaxisymmetric and steady, and forms a double-threaded structure as discussed above. At Re=200 and $B \geq 0.1$, the wake becomes both nonaxisymmetric and unsteady with vortex shedding. Streamlines at two time instants are shown in Fig. 4 for Re=200 and $B=0.2$. Interestingly, the planar symmetry in the wake is still maintained. The spiraling motion of the fluid particle in the lower and upper halves of the recirculation region is evident in the figure, similar to that known to occur in uniform flow in the range 270<Re<300. At one instant in the vortex shedding cycle, the fluid in the bottom half in the near-wake region spirals inward. Once it reaches the focus, it moves out of plane in the azimuthal direction and reaches the focus of the upper half. It then spirals outward and eventually moves downstream. In the latter half of the shedding cycle, the spiraling motion of the fluid is reversed. The reversal of the spiraling motion is associated with the orientation of the shed vortices.

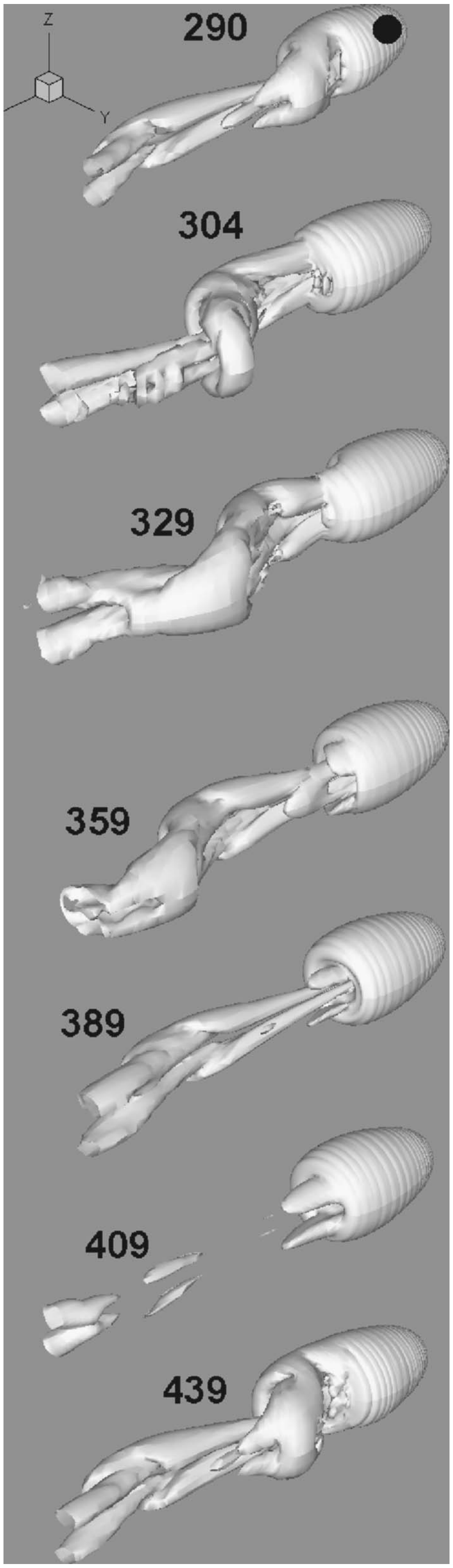

Fig. 6 3D vortex topology for Re=200, $B=0.2$ at various time instants

The 3D wake topology at Re=200 for $B=0.1$ and 0.2 is shown in Figs. 5 and 6, respectively. At $B=0.1$, the vortices are shed at regular interval. The structure of the shed vortices resembles a hairpinlike structure. One shedding cycle consists of shedding of two hairpin vortices oriented in opposite directions. In the first panel of Fig. 5, a hairpin vortex has just formed with its head directed toward the negative y axis. In the second panel, the same vortex is seen convecting downstream, while a new vortex with head directed toward the positive y axis is formed. The third panel shows the formation of another new hairpin vortex with its head directed toward the negative y axis. The vortical structures at Re=200 and $B=0.2$ shown in Fig. 6 suggest a loss of organized

Downloaded 03 Jun 2010 to 171.66.16.156. Redistribution subject to ASME license or copyright; see http://www.asme.org/terms/Terms_Use.cfm

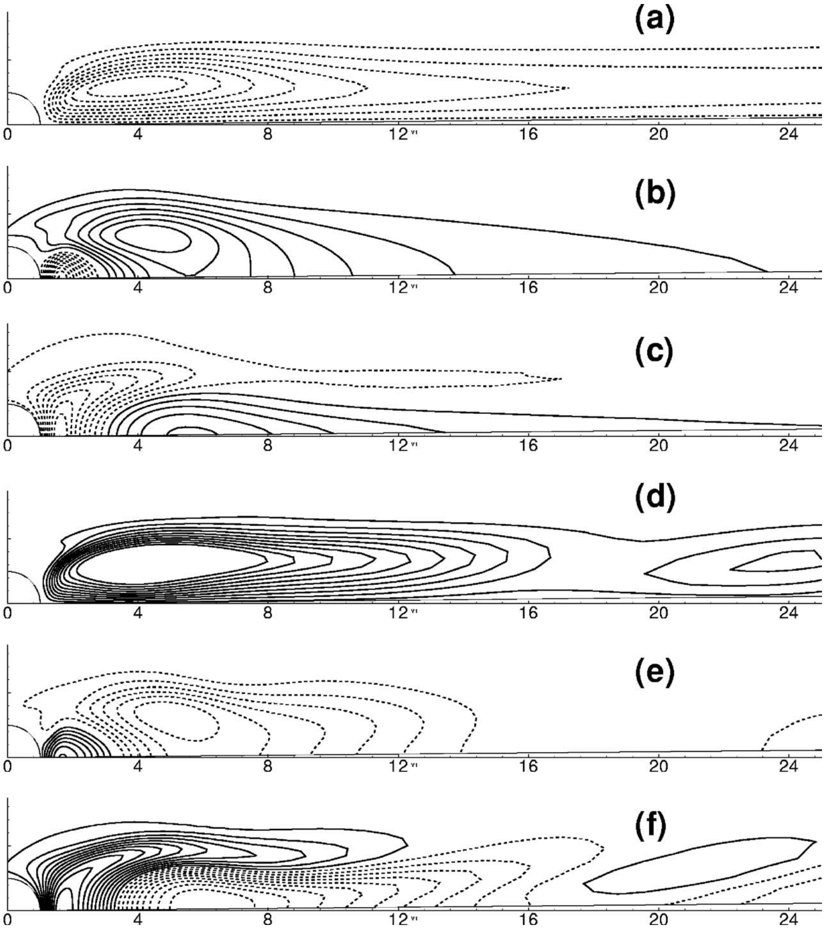

Fig. 7 Eigenfunctions corresponding to $K_{\phi}=1$ mode in the presence of surface blowing at $B=0.2$. (*a*)–(*c*) Imply streamwise, tangential, and azimuthal velocities, respectively, for Re=150. (*d*)–(*f*) Same for Re=200.

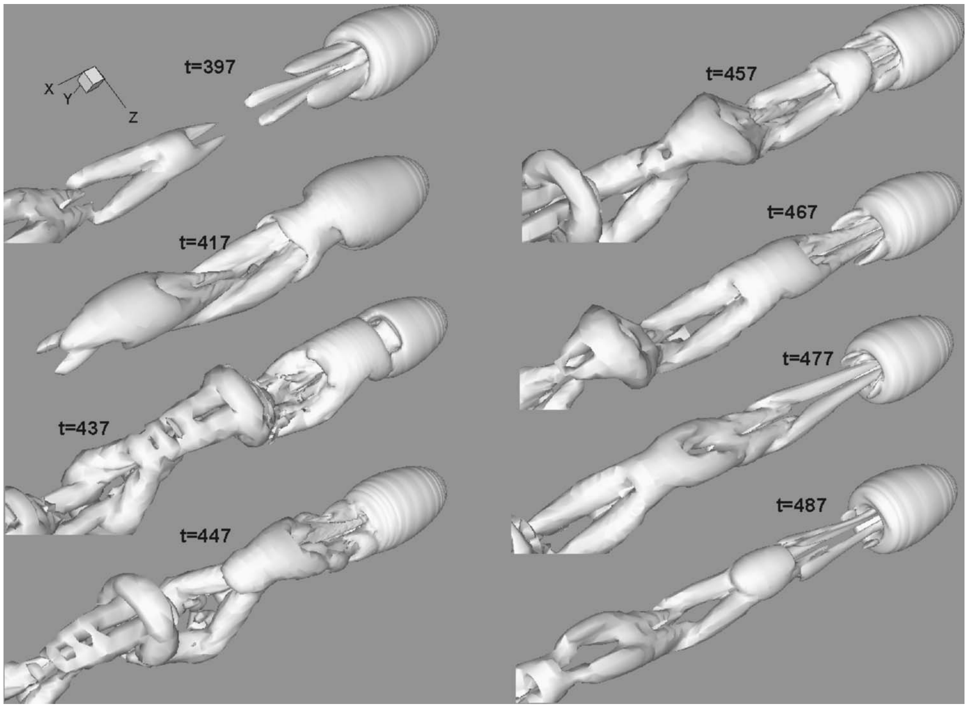

Fig. 8 3D vortex topology at Re=250, $B=0.1$

Downloaded 03 Jun 2010 to 171.66.16.156. Redistribution subject to ASME license or copyright; see http://www.asme.org/terms/Terms_Use.cfm

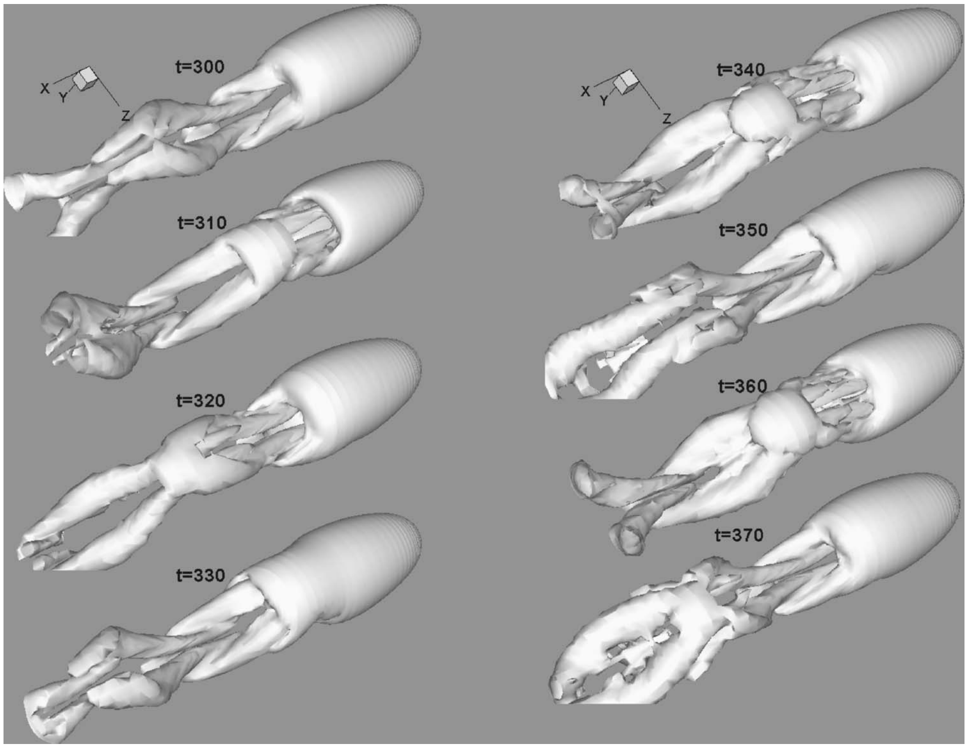

Fig. 9 3D vortex topology at Re=250, $B=0.2$

structures in the wake. At $t=304$, a toroidal ring is also seen. Once the toroidal ring convects downstream, hairpinlike vortices are shed until $t\approx 389$. Beyond this time, the vortices gradually weaken, and at around $t=409$, no coherent structure can be observed. This temporary pause in the shedding process is followed by reemergence of a toroidal ring at $t=439$, similar to the one observed at $t=290$, and the entire process is repeated.

The 3D nature of the flow can be considered as perturbation to the axisymmetric base flow, and can be expressed in terms of the Fourier modes in the azimuthal direction as $e^{iK_\phi \phi}$, where K_ϕ is the wave number. In the case of uniform flow, it is known that $K_\phi=1$ mode is the most unstable mode [5]. In the presence of blowing, we observe that the same $K_\phi=1$ mode is the most unstable one. In Fig. 7, we plot the contours of the eigenfunctions corresponding to this mode in the presence of surface blowing at Re=150, $B=0.2$ and Re=200, $B=0.2$. The eigenfunctions are similar in nature to those observed in uniform flow.

The flow structure at Re=250 is considered next. When surface blowing is introduced, the wake at this Re becomes unsteady. The 3D wake topology over a selected time window is shown in Figs. 8 and 9 for $B=0.1$ and 0.2, respectively. Hairpin shaped vortices are shed from the stationary toroidal vortex attached to the rear of the sphere, and advect downstream. The size of the vortices increases with increase in B. For Re=250, $B=0.1$, the shedding process consists of generation and advection of ringlike structures and hairpin vortices, and a temporary absence of coherent structures. The shedding process at Re=250, $B=0.2$ shows the presence of larger vortical structures with less resemblance to hairpin vortices.

The 3D topology at Re=300 and at $B=0.1$ and 0.2 was also examined but not shown for brevity. At $B=0.1$, vortices increase in size, and the hairpin structures are distorted. At $B=0.2$, the toroidal vortex and one hairpin vortex nearly occupy the entire computational domain.

The steady/unsteady nature of the wake for all values of Re and B as considered here is summarized in Table 1. The onset of recirculation in the presence of surface blowing is delayed to higher Reynolds number, which is independent of B. The first and second transitions to 3D and unsteady wake occur much earlier in the presence of blowing. The critical Reynolds numbers for these transitions are dependent on B. The higher the value of B, the lower the critical Reynolds number. The critical values of B for two transitions are as follows: $B=0.13$ at Re=150 for steady axisymmetric to steady 3D; $B=0.03$ and 0.07 at Re=200 for steady

Table 1 Sphere wake in blowing/suction. US: unseparated axisymmetric wake; SA: steady axisymmetric recirculation; SNA: steady nonaxisymmetric recirculation; UNS: unsteady wake (vortex shedding).

Re	$B=0$	$B=0.05$	$B=0.1$	$B=0.2$	$B=-0.05$	$B=-0.1$	$B=-0.2$
10	US	US	US	US	US	US	US
26	SA	US	US	US	US	US	US
36	SA	US	US	US	US	US	US
40	SA	SA	SA	SA	US	US	US
100	SA	SA	SA	SA	US	US	US
150	SA	SA	SA	SNA	US	US	US
200	SA	SNA	UNS	UNS	US	US	US
250	SNA	UNS	UNS	UNS	US	US	US
300	UNS	UNS	UNS	UNS	SNA	US	US

Downloaded 03 Jun 2010 to 171.66.16.156. Redistribution subject to ASME license or copyright; see http://www.asme.org/terms/Terms_Use.cfm

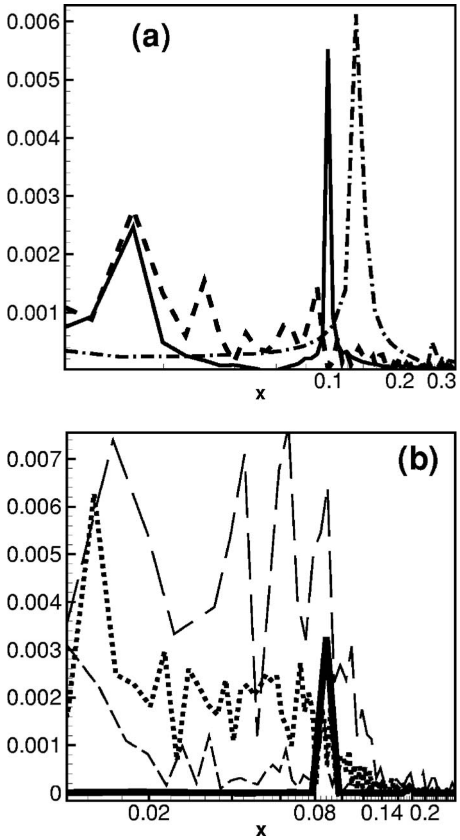

Fig. 10 Spectra of wake velocity fluctuations showing frequency content (St): (*a*) Re=300; (–·–) *B*=0; (—) *B*=0.1; (------) *B*=0.2; (*b*) thick line Re=200, *B*=0.1; (··· ···) Re=200, *B*=0.2; (— —) Re=250, *B*=0.1; (– – –) Re=250, *B*=0.2

axisymmetric to steady 3D, and for steady 3D to unsteady 3D, respectively; and $B=0.02$ at Re=250 for steady 3D to unsteady 3D. One could attempt to relate the onset of vortex shedding at lower Re to the increase in local absolute instability of the near wake in the presence of blowing. The near wake of a bluff body is governed by absolute instability, and the far wake is governed by convective instability (see, e.g., Refs. [39,40]). The increased size of the recirculation region in the presence of blowing is likely to increase the region of absolute instability. This is different from the flow past a cylinder, where blowing and suction both tend to reduce absolute instability and hence suppress vortex shedding. Here, we do not pursue the analysis of wake instability along this line, and leave it for future study.

The wake velocity traces are Fourier transformed to obtain the frequency spectra, from which the vortex shedding frequency is obtained (Fig. 10). In dimensionless form, the shedding frequency is given by the Strouhal number $\mathrm{St}=fd/U$. At Re=300 without surface blowing, the numerical result predicts St=0.133, which agrees well with previous experimental and numerical studies [4,7,8]. When surface blowing is introduced, the dominant shedding frequency at Re=200 and 300 at $B=0.1$ is St=0.09±0.01. At Re=300 and $B=0.1$ and 0.2, a lower frequency of 0.01 is also observed. For all other cases (Re=250, $B=0.1$ and 0.2; Re=200, $B=0.2$), several low *St* modes contain significant energy. We note that the planar symmetry of the wake is maintained for all 3D and unsteady cases for the range of B considered here.

It has been well known in the literature of particle-laden flows that the presence of the particles (or droplets) can modulate the nature of the fluid phase [41,42]. The wake oscillations and vortex shedding add energy to the fluid phase increasing the level of turbulence. In order to explore the background flow modulation, we compute the root-mean-square (rms) of the cross-stream velocity fluctuations surrounding the sphere. Results for Re=300 at $B=0$, 0.1, and 0.2 are shown in Fig. 11. For $B=0$, the rms decreases rapidly downstream. When surface blowing is present, the

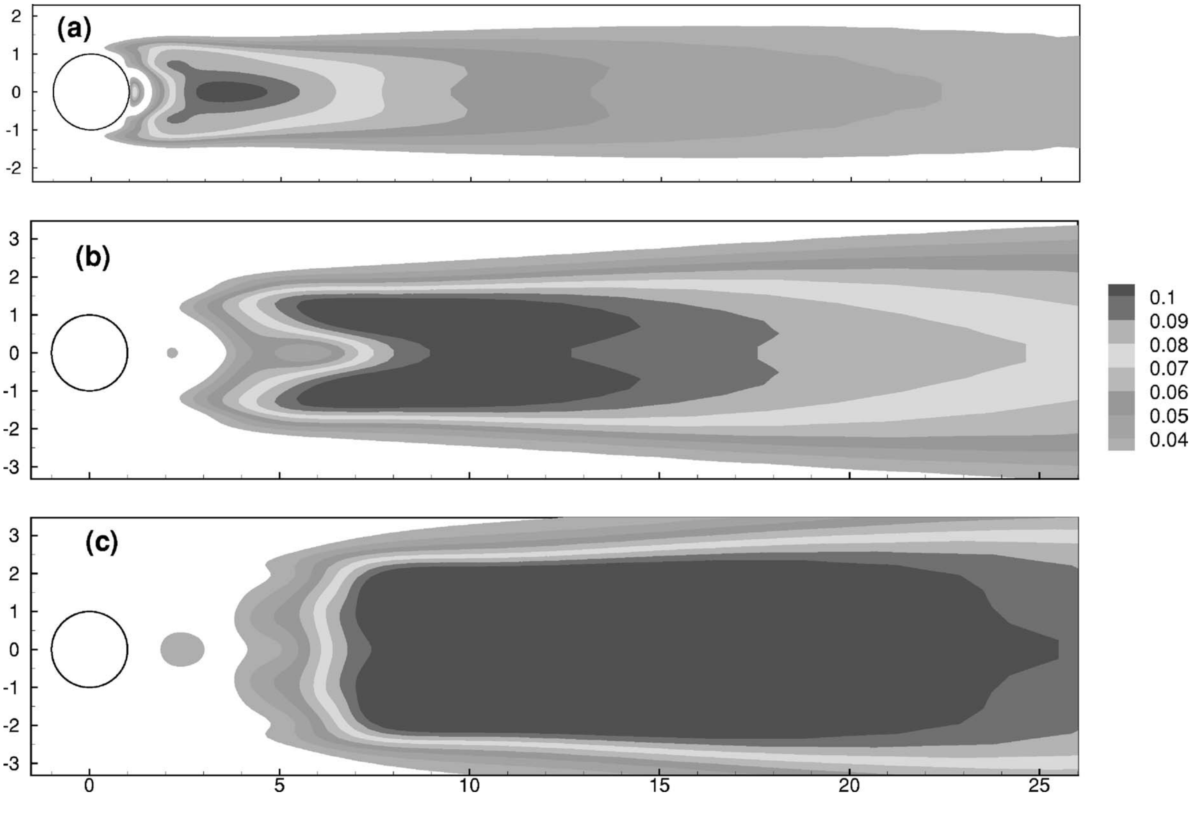

Fig. 11 Contours showing the rms of cross-stream velocity fluctuation at Re=300: (*a*) *B*=0, (*b*) *B*=0.1, and (*c*) *B* =0.2

Downloaded 03 Jun 2010 to 171.66.16.156. Redistribution subject to ASME license or copyright; see http://www.asme.org/terms/Terms_Use.cfm

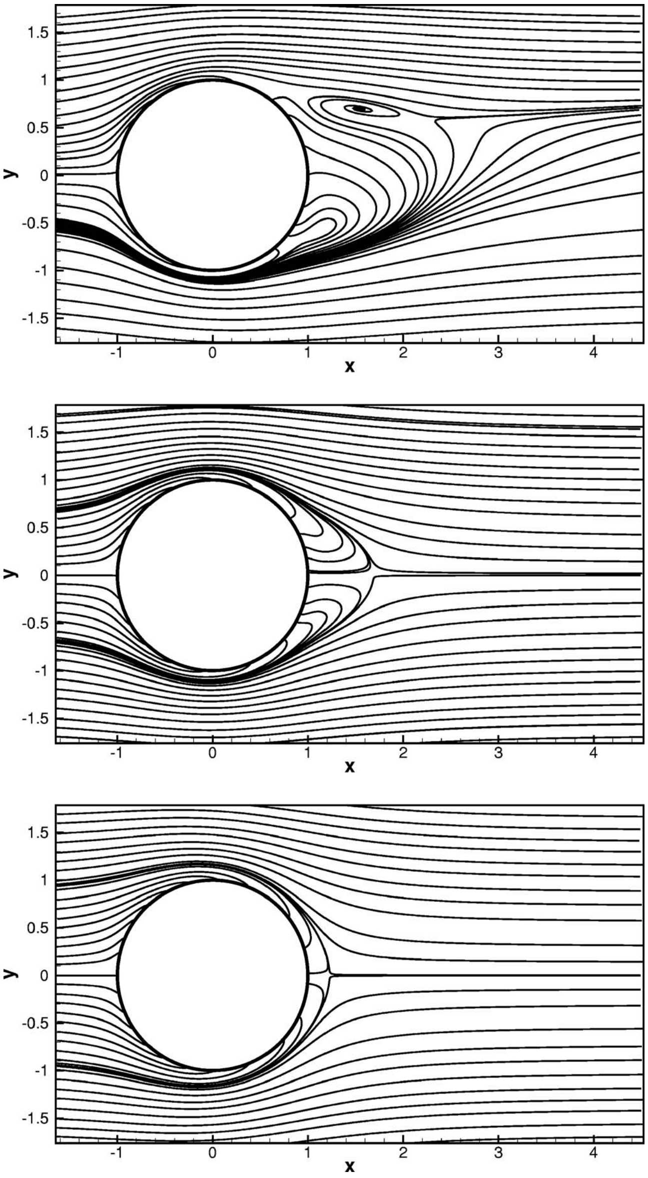

Fig. 12 Effect of suction on the sphere wake. The top three figures are the streamline plots at Re=300 and for B=−0.05, −0.1, and −0.2, respectively.

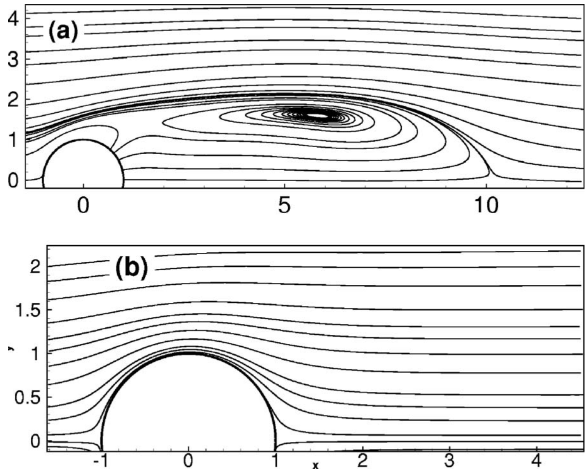

Fig. 13 Streamlines based on perturbation field at Re=300; (*a*) B=0.2 and (*b*) B=−0.2

contour representing the higher rms (0.1, in the figure) extends over a much larger region, implying the strong influence of the sphere wake on the background flow in the presence of blowing. The result implies that fluctuations in the wake are much stronger in the presence of blowing than those without blowing. It is also interesting to note that the region of influence moves further away from the sphere as B increases. The results clearly establish that in the presence of surface blowing in a dilute suspension of particles, the level of turbulence in the background flow significantly increases compared to that without blowing.

We have also examined azimuthal vorticity for all cases (not shown for brevity). When blowing is introduced, the vorticity contours are spread further away from the surface and elongated downstream. The contours are less closely spaced compared to those without blowing. The maximum magnitude is also significantly reduced in the presence of blowing due to reduction of the velocity gradient near the surface of the sphere. The maximum magnitude of vorticity at Re=250 is as follows: 14.5, 6.5, and 3.5 at B=0, 0.1, and 0.2, respectively. In the absence of blowing, the maximum vorticity occurs at the surface of the sphere and it increases as Re increases, due to the thinning of the boundary layer over the sphere. Interestingly, when surface blowing is present, the location of the maximum vorticity is slightly above the surface. Our simulations also suggest that in the presence of blowing, the magnitude of the maximum vorticity is independent of Re and is a function of B only.

3.1.2 Suction. Simulations are performed in the range $10 < \mathrm{Re} < 300$ and for B=−0.05, −0.1, and −0.2. The presence of the suction prevents the onset of recirculation. It also prevents the transition to 3D and the unsteady vortex shedding. As a representative case, Fig. 12 shows the streamlines for Re=300 at B=−0.05, −0.1, and −0.2. The flow remains axisymmetric without any recirculation even at Re=300 and for B=−0.1 and −0.2. However, for Re=300 and B=−0.05, the flow appears to be nonaxisymmetric, though a well-developed recirculation region is not

Table 2 Mean drag coefficient C_D for various values of Re and B. Values in bracket for $B>0$ are control efficiency defined as the ratio of the amount of drag decrease to the drag at B=0.

Re	B=0	B=0.1	B=0.2	B=−0.1	B=−0.2
1	27.57		26.91 (2.39%)		
10	4.3		3.7 (13.95%)		
26	2.3		1.82 (20.87%)		
50	1.57		1.19 (24.20%)		
100	1.09	0.91 (16.51%)	0.84 (22.94%)	1.42	1.93
150	0.87	0.75 (13.79%)	0.70 (19.54%)		
200	0.77	0.67 (12.99%)	0.68 (11.69%)		
250	0.69	0.65 (5.80%)	0.67 (2.90%)		
300	0.66	0.62 (6.06%)	0.67 (−1.51%)	1.00	1.65

Downloaded 03 Jun 2010 to 171.66.16.156. Redistribution subject to ASME license or copyright; see http://www.asme.org/terms/Terms_Use.cfm

Table 3 Mean viscous (C_{VD}) and pressure drag (C_{PD}) coefficients

	$B=0$		$B=0.2$		$B=-0.2$	
Re	C_{PD}	C_{VD}	C_{PD}	C_{VD}	C_{PD}	C_{VD}
1	9.02	18.55	8.97	17.96		
10	1.50	2.79	1.51	2.20		
26	0.88	1.42	0.95	0.87		
50	0.64	0.93	0.77	0.42		
100	0.49	0.60	0.67	0.17	0.30	1.62
150	0.45	0.44	0.62	0.10		
200	0.41	0.36	0.64	0.07		
250	0.39	0.30	0.61	0.06		
300	0.38	0.27	0.62	0.05	0.10	1.55

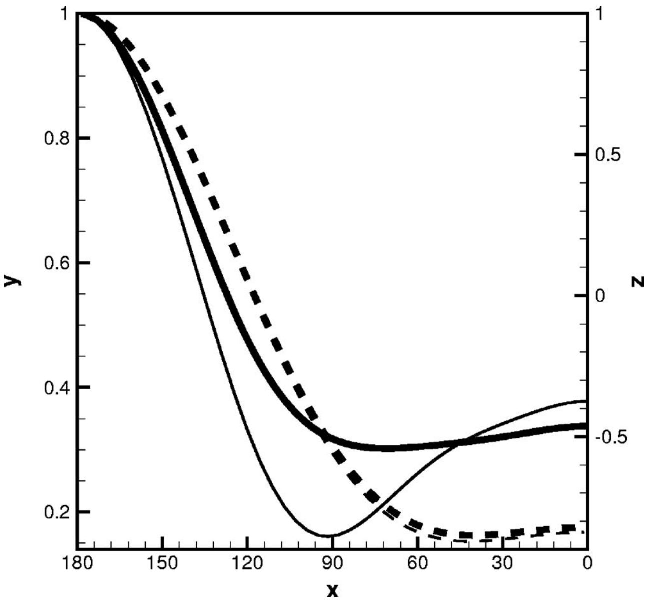

Fig. 14 Surface pressure coefficient. Thin lines are for $B=0$; thick lines are for $B=0.2$. Line symbols are as follows: (-----) Re=1, (—) Re=100. The right axis is for Re=1, and the left axis is for Re=100.

observed. The azimuthal vorticity contours are now strongly clustered close to the surface (not shown for brevity). The magnitude of the surface vorticity is significantly higher than that in a uniform flow indicating a strong velocity gradient in the wall-normal direction.

We have also examined the perturbation flow field by subtracting the potential flow for a blowing/suction (which corresponds to a source/sink) from the total flow (Fig. 13). The perturbation flow, similar to the total flow, also shows increased wake size in the presence of blowing, and absence of recirculation in the case of suction.

3.2 Drag and Lift Forces

3.2.1 Surface Blowing. The mean (time-averaged) drag coefficients are given in Table 2. In the presence of blowing, the drag coefficient is reduced compared to that without blowing. The reduction in C_D is due to the reduction in the velocity gradient near the sphere surface and the thickening of the boundary layer. The effect of surface blowing is stronger in the range $26<\mathrm{Re}<150$, where up to 25% reduction in C_D is observed at $B=0.2$. As Re approaches lower (e.g., Re=1) or higher values (e.g., Re=300), the reduction in C_D is less pronounced.

The total drag can be decomposed into pressure and viscous drag (Eqs. (4) and (5)). In dimensionless form, these are denoted by C_{PD} and C_{VD}, respectively. The values of C_{PD} and C_{VD} are shown in Table 3. For $\mathrm{Re}<10$, the pressure drag coefficients with or without blowing do not show much difference. This is consistent with the analytical work of Dukowicz [43] who derived the expression of the drag coefficient for a sphere in the presence of surface blowing or suction in the limit of low Reynolds number ($\mathrm{Re}\ll 1$). Dukowicz [43] showed that in this limit, the decrease in the drag coefficient in surface blowing is caused by the changes in the viscous drag due to the reduction of the velocity gradient (and vorticity) near the surface of the sphere. However, after the recirculation region develops at Re=38 in the presence of blowing, the pressure drag is higher than that without blowing. This is more evident in Fig. 14, where we plot the dimensionless pressure along the surface of the sphere for two axisymmetric cases. We see that at Re=1, the surface pressures nearly coincide for $B=0$ and $B=0.2$ cases. For Re=100, the surface pressures in the rear half of the sphere are significantly different for $B=0$ and $B=0.2$ resulting in higher values of C_{PD} for $B>0$. Thus, the following picture arises: At low Re, the change in C_{PD} in the presence of blowing is negligible. The decrease in total drag is then caused by the de-

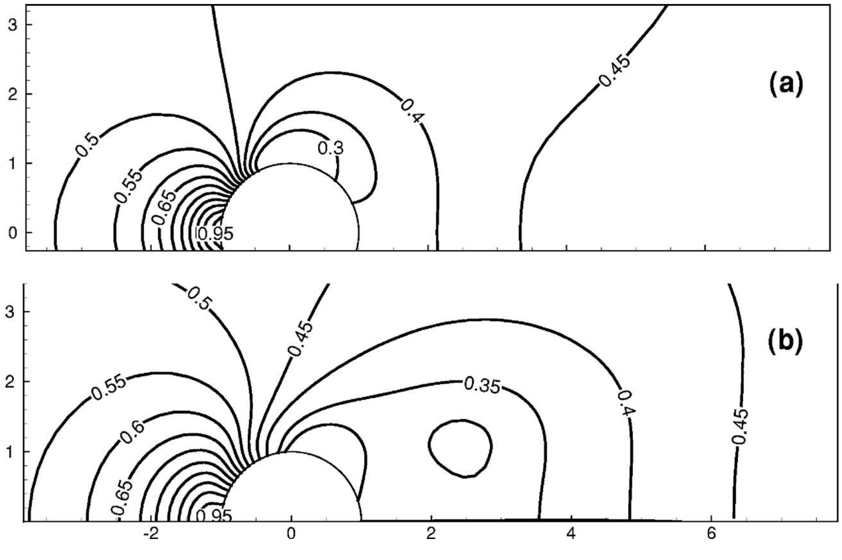

Fig. 15 Pressure contours for (*a*) Re=100, *B*=0 and (*b*) Re=100, *B*=0.2

Downloaded 03 Jun 2010 to 171.66.16.156. Redistribution subject to ASME license or copyright; see http://www.asme.org/terms/Terms_Use.cfm

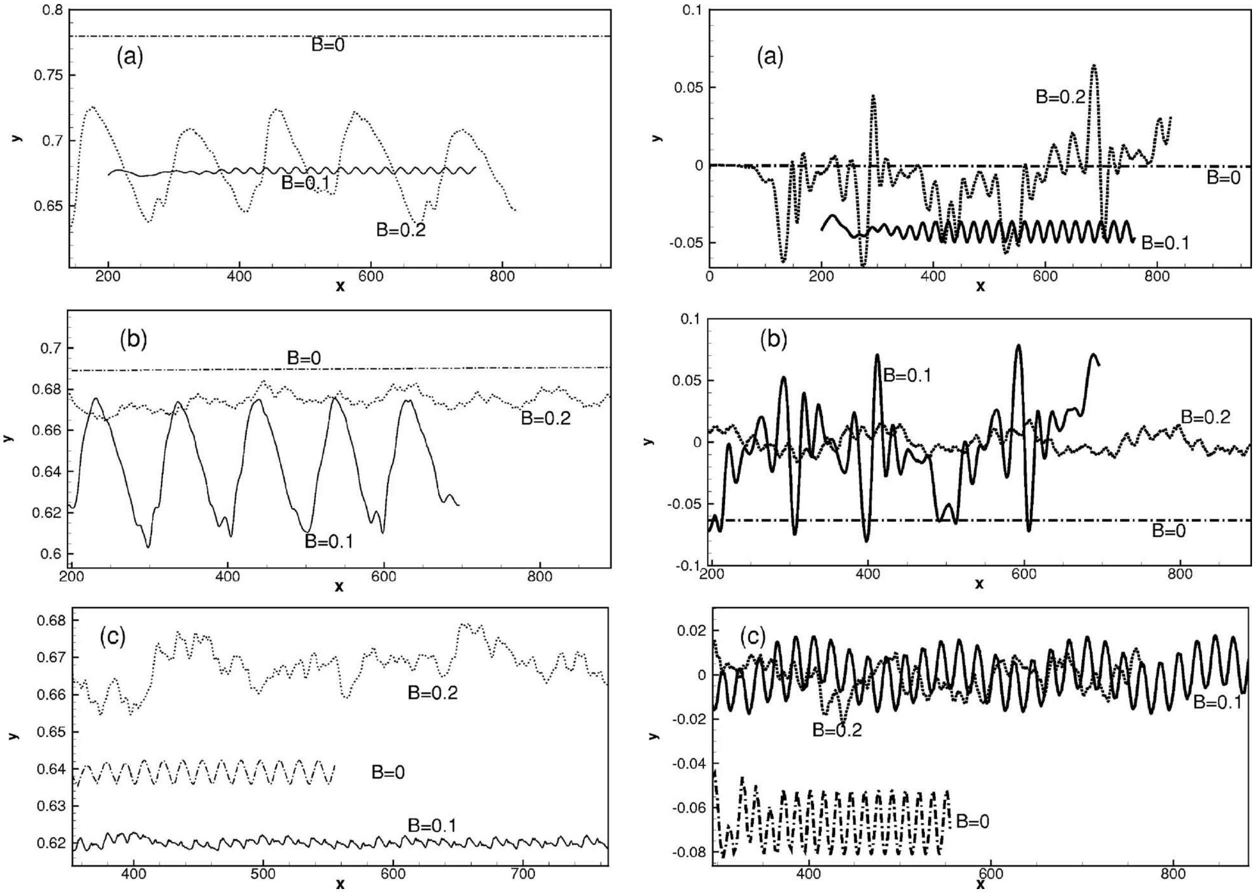

Fig. 16 Instantaneous drag and lift for (*a*) Re=200, (*b*) Re=250, and (*c*) Re=300: (–·–·–) *B*=0; (—) *B*=0.1; (··· ··· ···) *B* =0.2

crease in viscous drag. As Re increases, the viscous drag continues to decrease, but the pressure drag increases after the flow separation occurs. In the range of $26<\mathrm{Re}<200$, the decrease in viscous drag predominates over the increase in pressure drag, and hence the total drag decreases. For $\mathrm{Re}>250$, the increase in pressure drag nearly balances the decrease in viscous drag, and the net decrease in the total drag is not significant.

As a further illustration of the coupling between the wake structure and the drag force on the sphere, we consider the contours of the pressure in the near-wake region, which are shown in Fig. 15 for Re=100 at $B=0$ and $B=0.2$ for which the flow remains axisymmetric. For $B=0$, the pressure minimum occurs on the sphere surface in the equatorial region. For $B=0.2$, additional pressure minima also occur away from the sphere between $x=2$ and 2.5. The downstream pressure minimal approximately corresponds to the center of the toroidal vortex in the sphere wake. It has been shown in Ref. [7] that the swirling motion in a vortex generates regions of pressure minimal. Results presented above on the wake topology suggest that the increased size of the recirculation vortex in the presence of surface blowing generates a larger region of pressure deficiency. As a result, a larger pressure differential across the sphere and an increase in the pressure drag are observed.

The temporal behavior of the drag coefficient C_D is shown in Fig. 16. As an illustrative example, we analyze the case at Re =200. At $B=0.1$, time-dependent oscillations in C_D are seen due to the onset of vortex shedding. The peaks and valleys in C_D correspond to the shedding of the hairpin vortices when their heads are directed toward the negative and positive y axis, respectively. At $B=0.2$, remarkably different behavior characterized by large amplitude but low frequency oscillations is observed. A comparison of Fig. 16 with the sequence of the vortical structures given in Fig. 6 reveals that the large amplitude low frequency oscillations in C_D correspond to the shedding of the ringlike structures, which occurs over a longer time period. The valleys in C_D correspond to the temporary weakening of the shedding process (corresponding to $t=409$ in Fig. 6), and the peaks correspond to the generation of the first hairpin vortex after the ring vortex moves downstream ($t=329$ in Fig. 6).

When the flow is nonaxisymmetric (steady or unsteady), a lift force is also generated. The vortex shedding process for a sphere is biased to one side. Thus, the mean lift coefficient for a sphere is nonzero, unlike that for a cylinder. The mean lift coefficients are shown in Table 4. Here, only $\mathrm{Re}\geqslant 150$ is considered since below this Re, the flow remains steady and axisymmetric. The magnitude of C_L is much smaller than that of C_D. In the presence of surface blowing, the instantaneous lift coefficients show more chaotic behavior than the drag coefficients (Fig. 16). The time-averaged C_L over a long time is expected to be zero. Though the simulations were performed over long time ($t\approx 1000$, in some cases), the time

Table 4 Mean lift coefficients. Only Re⩾150 considered, since the flow is axisymmetric below this Re, and hence C_L=0.

Re	$B=0$	$B=0.1$	$B=0.2$
150	0.0		−0.028
200	0.0	−0.043	−0.02
250	−0.06	−0.01	0.0
300	−0.067	0.0	−0.004

Downloaded 03 Jun 2010 to 171.66.16.156. Redistribution subject to ASME license or copyright; see http://www.asme.org/terms/Terms_Use.cfm

window is not long enough for averaging purpose due to the very low frequency content, as discussed before in Fig. 10. The nonzero mean lift is possibly due to the inadequate time averaging. Due to limitation of computational resource, we have not continued more extended simulations.

Although the mean lift could be zero (or very small), instantaneous lift could be significant. As an illustration of the instantaneous behavior of the lift coefficient, we consider the flow at $\mathrm{Re}=200$ (Fig. 16). For $\mathrm{Re}=200$, $B=0.1$, the lift is phase lagged by the drag by π. Thus, the valleys in the C_L correspond to the shedding of hairpin vortices with their heads aligned in the negative y direction. At these instants, the pressure minimal is located near the bottom half of the sphere resulting in low values of C_L. For $\mathrm{Re}=200$, $B=0.2$, the instantaneous lift shows highly chaotic nature. This is associated with the complex movement of the pressure minimum associated with the shedding of hairpin vortices and the ring vortices. For all cases, the main contribution to the instantaneous lift comes from the pressure contribution, which is at least one order of magnitude higher than the viscous contribution.

3.2.2 Effect of Suction on Drag and Lift Forces. Tables 2 and 3 list the drag coefficients and their pressure and viscous components in title presence of suction. The drag coefficient significantly increases during suction. At low Re (e.g., at $\mathrm{Re}=1$ in the table), the increase in C_D is essentially due to the increase in the viscous component resulting from the increased surface vorticity. The pressure drag at small Re is nearly unchanged in the presence of suction. A similar observation was made earlier for the case of surface blowing. This observation is consistent with the analytical derivation of Dukowicz [43] who showed that in the limit of $\mathrm{Re} \ll 1$, it is only the viscous drag that contributes to the increased C_D in the presence of suction. As Re increases, the viscous drag increases rapidly in the presence of suction, whereas the pressure drag decreases. The pressure drag is significantly lower compared to $B=0$, whereas viscous drag could be nearly an order of magnitude higher compared to $B=0$. Note that the pressure drag is associated with the existence of a pressure minimum in the near-wake vortex. Since no vortex is formed in the presence of suction, the pressure in the wake region is significantly higher compared to that without suction, resulting in a low pressure differential across the sphere and hence a reduced contribution from the pressure.

4 Summary and Conclusions

DNS based on pseudospectral methodology was used to study the wake dynamics and the drag and lift forces on a sphere subject to surface blowing or suction in the range of $1 \leq \mathrm{Re} \leq 300$. The major results from this study are as follows.

(1) The onset of recirculation region in the sphere wake is delayed to higher Re in the presence of surface blowing, but the transitions to 3D and unsteady wake occur at lower Re. The critical Re for transitions are dependent on the blowing velocity.
(2) The recirculation region in the presence of blowing is significantly larger than that without blowing, and is not attached to the sphere.
(3) Suction on the surface prevents the formation of the recirculation, and the transition to three-dimensionality and vortex shedding regimes.
(4) The vortex shedding frequency in the presence of blowing is reduced compared to that without blowing. The presence of surface blowing results in increased oscillations in the wake velocity. By considering the distribution of rms velocity fluctuations, it is argued that the background flow modulation by the sphere in the presence of blowing is significantly stronger than that without blowing.
(5) The drag coefficient in the presence of blowing is reduced, in the range $10 < \mathrm{Re} < 250$, whereas it is increased in the presence of suction. It is shown that at moderate Re ($10 < \mathrm{Re} < 250$), the reduction in the wake pressure minimum associated with the enhanced vortical structures is the primary cause for drag reduction in the case of blowing. In the case of suction, it is the increase in the surface vorticity associated with the thinning of the boundary layer that results into increased drag.
(6) The mean and the instantaneous lift coefficients in the presence of blowing are nonzero, and they result from the asymmetric movement of the wake pressure minimum associated with the biased shedding process. The lift coefficient in the case of suction is zero.

It should be mentioned that the effect of blowing/suction on flow past 2D cylinders has been studied by many investigators [44–46]. These studies have shown that with optimal blowing/suction, the mean drag and the fluctuations in lift and drag can be reduced by suppressing the vortex shedding process. Thus, this result is different from those obtained here for a sphere for which blowing (suction) acts differently to enhance (suppress) vortex shedding. Transition to vortex shedding increases the drag for a cylinder, but not for a sphere [47].

Acknowledgment

We thank the referees for their suggestions to improve the quality of the paper. Computational support at NCSA, Illinois is acknowledged. Thanks are due to Malik Khan for helping with some of the simulations.

References

[1] Mougin, G., and Magnaudet, J., 2002, "Path Instability of a Rising Bubble," Phys. Rev. Lett., **88**, pp. 014502.
[2] Magarvey, R. H., and Bishop, R. L., 1961, "Transition Ranges for Three-Dimensional Wakes," Can. J. Phys., **39**, pp. 1418–1422.
[3] Achenbach, E., 1974, "Vortex Shedding From Spheres," J. Fluid Mech., **62**, pp. 209–221.
[4] Sakamoto, H., and Haniu, H., 1990, "A Study on Vortex Shedding From Spheres in a Uniform Flow," ASME J. Fluids Eng., **112**, pp. 386–392.
[5] Natarajan, R., and Acrivos, A., 1993, "The Instability of the Steady Flow Past Spheres and Disks," J. Fluid Mech., **254**, pp. 323–344.
[6] Wu, J. S., and Faeth, G. M., 1993, "Sphere Wake in Still Surrounding at Intermediate Reynolds Numbers," AIAA J., **31**, pp. 1448–1455.
[7] Johnson, T. A., and Patel, V. C., 1999, "Flow Past a Sphere up to a Reynolds Number of 300," J. Fluid Mech., **378**, pp. 19–70.
[8] Mittal, R., 1999, "A Fourier Chebyshev Spectral Collocation Method for Simulation Flow Past Spheres and Spheroids," Int. J. Numer. Methods Fluids, **30**, pp. 921–937.
[9] Tomboulides, A. G., and Orszag, S. A., 2000, "Numerical Investigation of Transitional and Weak Turbulent Flow Past a Sphere," J. Fluid Mech., **416**, pp. 45–73.
[10] Thompsom, M. C., Leweke, T., and Provansal, M., 2001, "Kinematics and Dynamics of Sphere Wake Transition," J. Fluids Struct., **15**, pp. 575–585.
[11] Schouveiler, L., and Provansal, M., 2002, "Self-Sustained Oscillations in the Wake of a Sphere," Phys. Fluids, **14**, pp. 3846–3854.
[12] Clift, R., Grace, J. R., and Weber, M. E., 1978, *Bubbles, Drops and Particles*, Academic, New York.
[13] Schiller, L., and Neumann, A., 1933, "Uber die Grundlegenden Berechungen bei der Schwer Kraftaufbereitung," Verein Deutscher Ingenieure, **77**, pp. 318–324.
[14] Maxey, M. R., and Riley, J. J., 1983, "Equation of Motion for a Small Sphere in a Nonuniform Flow," Phys. Fluids, **26**, pp. 883–889.
[15] McLaughlin, J. B., 1993, "The Lift on a Small Sphere in Wall-Bounded Linear Shear Flows," J. Fluid Mech., **246**, pp. 249–265.
[16] Dandy, D. S., and Dwyer, H. A., 1990, "A Sphere in Shear Flow at Finite Reynolds Number: Effect of Shear on Particle Lift, Drag and Heat Transfer," J. Fluid Mech., **216**, pp. 381–410.
[17] Magnaudet, J., Rivero, M., and Fabre, J., 1995, "Accelerated Flows Past a Rigid Sphere or a Spherical Bubble. Part 1. Steady Straining Flow," J. Fluid Mech., **284**, pp. 97–135.
[18] Kurose, R., and Komori, S., 1999, "Drag and Lift Forces on a Rotating Sphere in a Linear Shear Flow," J. Fluid Mech., **384**, pp. 183–206.
[19] Mittal, R., 2000, "Response of the Sphere Wake to Freestream Fluctuations," Theor. Comput. Fluid Dyn., **13**, pp. 397–413.
[20] Bagchi, P., and Balachandar, S., 2002, "Steady Planar Straining Flow Past a Rigid Sphere at Moderate Reynolds Number," J. Fluid Mech., **466**, pp. 365–407.
[21] Bagchi, P., and Balachandar, S., 2002, "Effect of Free Rotation on the Motion of a Solid Sphere in Linear Shear Flow at Moderate Re," Phys. Fluids, **14**, pp. 2719–2737.

Downloaded 03 Jun 2010 to 171.66.16.156. Redistribution subject to ASME license or copyright; see http://www.asme.org/terms/Terms_Use.cfm

[22] Bagchi, P., and Balachandar, S., 2002, “Shear Versus Vortex-Induced Lift Force on a Rigid Sphere at Moderate Re,” J. Fluid Mech., **473**, pp. 379–388.
[23] Bagchi, P., and Balachandar, S., 2003, “Inertial and Viscous Forces on a Rigid Sphere in Straining Flows at Moderate Reynolds Numbers,” J. Fluid Mech., **481**, pp. 105–148.
[24] Bagchi, P., and Balachandar, S., 2003, “Effect of Turbulence on the Drag and Lift of a Particle,” Phys. Fluids, **15**, pp. 3496–3513.
[25] Bagchi, P., and Balachandar, S., 2004, “Wake Response of an Isolated Particle Subjected to Isotropic Turbulent Flow,” J. Fluid Mech., **518**, pp. 95–123.
[26] Kim, I., Elghobashi, S., and Sirignano, W. A., 1995, “Unsteady Flow Interactions Between an Advected Cylindrical Vortex Tube and a Spherical Particle,” J. Fluid Mech., **288**, pp. 123–155.
[27] Kim, I., Elghobashi, S., and Sirignano, W. A., 1998, “On the Equation for Spherical-Particle Motion: Effect of Reynolds and Acceleration Numbers,” J. Fluid Mech., **367**, pp. 221–254.
[28] Legendre, D., Merle, A., and Magnaudet, J., 2006, “Wake of a Spherical Bubble or a Solid Sphere Set Fixed in a Turbulent Environment,” Phys. Fluids, **18**, pp. 048102–048106.
[29] Niazmand, H., and Renksizbulut, M., 2003, “Transient Three-Dimensional Heat Transfer From Rotating Spheres With Surface Blowing,” Chem. Eng. Sci., **58**, pp. 3535–3554.
[30] Niazmand, H., and Renksizbulut, M., 2003, “Surface Effects on Transient Three-Dimensional Flows Around Rotating Spheres at Moderate Reynolds Numbers,” Comput. Fluids, **32**, pp. 1405–1433.
[31] Niazmand, H., and Renksizbulut, M., 2005, “Flow Past a Spinning Sphere With Surface Blowing and Heat Transfer,” ASME J. Fluids Eng., **127**, pp. 163–171.
[32] Kim, D., and Choi, H., 2002, “Laminar Flow Past a Sphere Rotating in the Streamwise Direction,” J. Fluid Mech., **461**, pp. 365–386.
[33] Bagchi, P. 2002, “Particle Dynamics in Inhomogeneous Flows at Moderate to High Reynolds Numbers,” Ph.D. thesis, University of Illinois, Urbana-Champaign.
[34] Mittal, R., and Balachandar, S., 1996, “Direct Numerical Simulation of Flow Past Elliptic Cylinders,” J. Comput. Phys., **124**, pp. 351–367.
[35] Delaunay, Y., and Kaiktsis, L., 2001, “Control of Circular Cylinder Wakes Using Base Mass Transpiration,” Phys. Fluids, **13**, pp. 3285–3298.
[36] Gogos, G., Sadhal, S. S., Ayyaswamy, P. S., and Sundararajan, T., 1986, “Thin-Flame Theory for the Combustion of a Moving Liquid Drop: Effects Due to Variable Density,” J. Fluid Mech., **171**, pp. 121–144.
[37] Jog, M. A., Ayyaswamy, P. S., and Cohen, I. M. 1996, “Evaporation and Combustion of a Slowly Moving Liquid Fuel Droplet: Higher-Order Theory,” J. Fluid Mech., **307**, pp. 135–165.
[38] Williams, F. A., 1985, *Combustion Theory*, 2nd ed., Addison-Wesley, New York.
[39] Huerre, P., and Monkewitz, P., 1990, “Local and Global Instabilities in Spatially Developing Flows,” Annu. Rev. Fluid Mech., **22**, pp. 473–537.
[40] Leu, T.-S., and Ho, C.-H., 2000, “Contral of Global Instability in a Non-Parallel Near Wake,” J. Fluid Mech., **404**, pp. 345–378.
[41] Hetsroni, G., 1989, “Particle-Turbulence Interaction,” Int. J. Multiphase Flow, **15**, pp. 735–747.
[42] Gore, R. A., and Crowe, C. T., 1989, “The Effect of Particle Size on Modulating Turbulent Intensity,” Int. J. Multiphase Flow, **15**, pp. 279–296.
[43] Dukowicz, J. K., 1982, “An Exact Solution for the Drag of a Sphere in Low Reynolds Number Flow With Strong Uniform Suction or Blowing,” Phys. Fluids, **25**, pp. 1117–1118.
[44] Li, Z., Navon, I., Hussaini, M. Y., and Le Dimet, F. X., 2003, “Optimal Control of Cylinder Wakes via Suction and Blowing,” Comput. Fluids, **32**, pp. 149–171.
[45] Min, C., and Choi, H., 1999, “Suboptimal Feedback Control of Vortex Shedding at Low Reynolds Numbers,” J. Fluid Mech., **401**, pp. 123–156.
[46] Ling, G. P., and Fang, J. W., 2002, “Numerical Study on the Flow Around a Circular Cylinder With Surface Suction or Blowing Using Vorticity-Velocity Method,” Appl. Math. Mech., **23**, pp. 1089–1096.
[47] Mittal, R., and Balachandar, S., 1995, “Effect of 3-Dimensionality on the Lift and Drag of Nominally 2-Dimensional Cylinders,” Phys. Fluids, **7**, pp. 1841–1865.

Downloaded 03 Jun 2010 to 171.66.16.156. Redistribution subject to ASME license or copyright; see http://www.asme.org/terms/Terms_Use.cfm

A Generalized Neural Network Model of Refrigerant Mass Flow Through Adiabatic Capillary Tubes and Short Tube Orifices

Ling-Xiao Zhao
Institute of Refrigeration and Cryogenics,
Shanghai Jiaotong University,
Shanghai 200240, China

Chun-Lu Zhang[1]
China R&D Center,
Carrier Corporation,
No. 3239 Shen Jiang Road, Pudong,
Shanghai 201206, China
e-mail: chunlu.Zhang@carrier.utc.com

Liang-Liang Shao
Institute of Refrigeration and Cryogenics,
Shanghai Jiaotong University,
Shanghai 200240, China

Liang Yang
China R&D Center,
Carrier Corporation,
No. 3239 Shen Jiang Road, Pudong,
Shanghai 201206, China

Adiabatic capillary tubes and short tube orifices are widely used as expansive devices in refrigeration, residential air conditioners, and heat pumps. In this paper, a generalized neural network has been developed to predict the mass flow rate through adiabatic capillary tubes and short tube orifices. The input/output parameters of the neural network are dimensionless and derived from the homogeneous equilibrium flow model. Three-layer backpropagation (BP) neural network is selected as a universal function approximator. Log sigmoid and pure linear transfer functions are used in the hidden layer and the output layer, respectively. The experimental data of R12, R22, R134a, R404A, R407C, R410A, and R600a from the open literature covering capillary and short tube geometries, subcooled and two-phase inlet conditions, are collected for the BP network training and testing. Compared with experimental data, the overall average and standard deviations of the proposed neural network are 0.75% and 8.27% of the measured mass flow rates, respectively. [DOI: 10.1115/1.2801352]

Keywords: adiabatic capillary tube, short tube orifice, mass flow rate, dimensionless parameter, neural network

1 Introduction

A pressure-reducing device is indispensable in every refrigerating system in order to produce large pressure drop and lower the temperature entering the evaporator, and control mass flow rate according to load demand. Adiabatic capillary tubes and short tube orifices are especially popular expansion device due to their simple, reliable, and inexpensive characteristics. Because of their pressure equalizing characteristics, they allow lower starting torque of the compressor.

Although the adiabatic capillary tube and the short tube orifice have many common features, refrigerant flow through them is quite different. First, their geometry is different. The short tube orifice is typically 10–13 mm length, with the ratio of length-to-diameter (L/D) from 3 to 20, while the adiabatic capillary tube with L/D much larger than 20 is much longer than the short tube [1]. Accordingly, in the short tube orifices, the entrance effect is significant and the entrance pressure loss is very large as well. Rather, in the capillary tubes, the entrance loss is very small and usually out of consideration. Secondly, refrigerant flow through short tube orifices shows obvious hydrodynamic and thermodynamic nonequilibriums, while in adiabatic capillary tubes, equilibrium assumptions are acceptable in engineering applications. Therefore, refrigerant flows through the adiabatic capillary tube and the short tube orifice were always studied separately.

Many theoretical and experimental investigations have been made on adiabatic capillary tubes and short tube orifices [1–36]. Since theoretical two-phase critical flow models are not very easy for engineering applications, many researchers developed empirical or semiempirical correlations of refrigerant flow through capillary and short tubes [15–25,27–35]. To get more generalized correlations, researchers in recent years developed some dimensionless parameter groups based on dimensional analysis [1,19–25,33–35]. Particularly, ASHRAE [1] recommended such correlations for the adiabatic capillary tube and short tube orifice, respectively. Most investigators used the traditional power-law correlations. For the purpose of accuracy and generality improvement, Payne et al. [35] recommended replacing the power-law correlation with the rational polynomial correlation. Lately, Zhang [25] used the literature dimensionless parameter group but the neural network to replace the power-law correlation, which is for capillary tube only and not available for two-phase inlet.

For easy and to avoid numerical discontinuity over the available parameter range, a generalized correlation is supposed to include tube geometry change from short tubes to long (capillary) tubes and inlet state change from liquid to two-phase. The objective of this work is to develop such a generalized correlation. Accordingly, a new group of dimensionless parameters will be derived from the homogeneous equilibrium flow model (HEM) rather than those from the dimensional analysis. A three-layer backpropagation (BP) neural network will be recommended as the universal correlation function.

2 Dimensionless Parameter Group

Instead of the dimensionless parameter groups proposed by other researchers [19–25,33–35], here the authors propose a new dimensionless group based on the HEM. In the HEM, the interphase velocity slip and temperature difference are ignored. It is the simplest theoretical two-phase flow model and has been proved proper for predicting the refrigerant flow through capillary tubes [4,5]. Meanwhile, the HEM was also found to overestimate the mass flow rate through short tube orifices [26]. However, the HEM still reflected an acceptable qualitative trend. Furthermore, the correlation is actually a black-box model including the operating conditions and refrigerant properties. Therefore, even though we use some more complex model as the reference model, we will not get more sensitive inputs to improve the accuracy. Therefore, the HEM is a good base for developing a new generalized mass flow rate correlation for capillary and short tubes.

---

[1] Corresponding author.

Contributed by the Fluids Engineering Division of ASME for publication in the JOURNAL OF FLUIDS ENGINEERING. Manuscript received November 19, 2006; final manuscript received May 29, 2007. Review conducted by Malcolm J. Andrews.

Copyright © 2007 by ASME

Downloaded 03 Jun 2010 to 171.66.16.156. Redistribution subject to ASME license or copyright; see http://www.asme.org/terms/Terms_Use.cfm

In the HEM, the refrigerant flow through an adiabatic capillary tube could be approximated as an isenthalpic progress, namely,

$$h = h_{\rm in} \tag{1}$$

The governing equation of pressure drop is

$$-dp = G^2 dv + \frac{f}{2D} G^2 v dL \tag{2}$$

Here, G is the mass flux, p is the pressure, v is the specific volume, h is the specific enthalpy, f is the friction factor, D is the inner diameter, and L is the length of the capillary tube.

Equation (2) can be written in an integral form

$$p_{\rm in} - p_{\rm out} = G^2 (v_{\rm out} - v_{\rm in}) + \frac{f_m}{2D} G^2 v_m L \tag{3}$$

Then Eq. (3) is reorganized in a dimensionless form

$$\frac{G^2 v_{\rm in}}{p_{\rm in}} = \frac{1-(p_{\rm out}/p_{\rm in})}{(v_{\rm out}/v_{\rm in}) - 1 + (f_m L/2D v_m/v_{\rm in})} \tag{4}$$

Dimensionless parameter group for the generalized correlation can be developed from Eq. (4). The dimensionless mass flux or mass flow rate is

$$\pi_1 = \sqrt{\frac{G^2 v_{\rm in}}{p_{\rm in}}} = \frac{4m}{3.1416 D^2 \sqrt{p_{\rm in}\rho_{\rm in}}} = \frac{1.273m}{D^2 \sqrt{p_{\rm in}\rho_{\rm in}}} \tag{5}$$

The original dimensionless pressure is $p_{\rm out}/p_{\rm in}$, but the outlet pressure is unknown under the critical flow condition. Even for the short tubes, the mass flow rate is generally insensitive to a change in downstream pressure [29]. Therefore, it is replaced by the saturated pressure at the inlet temperature. Namely,

$$\pi_2 = \frac{p_{\rm sat}}{p_{\rm in}} \tag{6}$$

The original dimensionless specific volume is $v_{\rm out}/v_{\rm in}$ or $v_{\rm m}/v_{\rm in}$. They mainly depend on v_f/v_g and the quality. The quality will be considered separately. Hence,

$$\pi_3 = \frac{v_f}{v_g} = \frac{\rho_g}{\rho_f} \tag{7}$$

where the liquid and vapor densities are evaluated at the saturation state using the capillary tube inlet temperature.

The dimensionless geometry is

$$\pi_4 = \frac{L}{D} \tag{8}$$

The effect of viscosity is considered in the friction factor. The friction factor is dimensionless and mainly depends on the Reynolds number that is related to the mass flux. Therefore, π_1 is used to eliminate the mass flux in the Reynolds number.

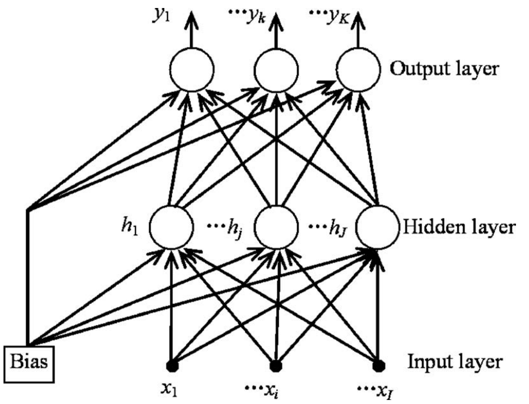

Fig. 1 Architecture of three-layer perceptron network

$$\pi_5 = \frac{\rm Re}{\pi_1} = \frac{GD}{\mu_{\rm in}} \frac{\sqrt{p_{\rm in}\rho_{\rm in}}}{G} = \frac{D\sqrt{p_{\rm in}\rho_{\rm in}}}{\mu_{\rm in}} \tag{9}$$

where, for the two-phase inlet condition, $\mu_{\rm in} = x_{\rm in}\mu_g + (1-x_{\rm in})\mu_f$, $1/\rho_{\rm in} = (x_{\rm in}/\rho_{\rm g}) + [(1-x_{\rm in})/\rho_f]$.

Finally, the inlet quality and the isenthalpic condition can be considered together as follows:

$$\pi_6 = \frac{h_{\rm in} - h_f}{h_g - h_f} \tag{10}$$

where the liquid and vapor enthalpies are evaluated at the saturation state using the capillary tube inlet pressure. For the two-phase inlet condition, π_6 is equal to inlet quality. For the subcooled inlet condition, π_6 is negative.

In addition, the surface tension that contributes to bubble growth or metastable region is not taken into account. For capillary tubes, the reason is that its effect on the mass flow rate is not pronounced [19]. For short tubes, we will tentatively ignore it as well and see if we can get good correlation without it.

All in all, the generalized correlation of mass flow rate through adiabatic capillary tubes and short tube orifices could be described as the following expression:

$$\pi_1 = F(\pi_2, \pi_3, \pi_4, \pi_5, \pi_6) \tag{11}$$

where F is the correlation function. Traditionally, the power-law function is widely used. In this work, we choose the neural network because of its universality.

Table 1 Data sources used for NN training

Fluid	Tube	References	Inlet	N	L (mm)	D (mm)	T_c (°C)	$\theta_{\rm sc}$ (K)	x
R12	C	[2,20]	SC	24	1500–3027	0.66–1.41	23.4–62.3	0.9–13.4	
	S	[29]	SC/TP	58	9.43–25.3	1.1–1.72	21.6–54	0–14.6	0.001–0.065
R22	C	[3,21,22]	SC	97	500–1500	1.0–2.0	23.4–51.1	1.6–13.5	
	S	[30]	SC/TP	105	9.46–25.5	1.34–1.72	12.3–51.5	0–26.1	0.02–0.07
R134a	C	[9,20]	SC	28	2009–3048	0.6–1.05	21.5–59.1	3.4–16.7	
	S	[28,29]	SC/TP	525	9.43–38.4	1.1–1.72	17–85.4	0–26.4	0.01–0.96
R600a	C	[20]	SC	19	2009–2926	0.77–0.77	37.8–68.4	3.3–15.7	
R407C	C	[10,11,21,22]	SC/TP	68	500–1500	1.0–2.0	25.8–50.6	1.4–15.5	0–0.047
	S	[32]	SC/TP	74	1.27–25.4	1.1–1.94	23–51.2	0.03–11.4	0–0.042
R410A	C	[10,11,22]	SC/TP	34	500–1500	1.1–2.0	28.8–43.3	0.9–10	0–0.04
	S	[31]	SC/TP	120	1.27–25.4	1.1–1.94	23–51.2	0.03–11.4	0.004–0.05

Downloaded 03 Jun 2010 to 171.66.16.156. Redistribution subject to ASME license or copyright; see http://www.asme.org/terms/Terms_Use.cfm

Table 2 Training accuracy against neuron number

Neurons in hidden layer	AD (%)	SD (%)
1	1.33	12.08
2	0.67	8.27
3	0.58	7.58
4	0.53	7.41
5	0.47	6.87

Table 3 Gaussian sensitivity analysis

Input parameters with variations	Output AD (%)	Output SD (%)
π_2	0.27	5.88
π_3	0.00	0.24
π_4	0.02	0.74
π_5	0.01	0.48
π_6	0.02	0.84
All π	0.34	6.32

3 Neural Network Modeling

Because of the complex two-phase critical flow mechanism in capillary tubes and short tube orifices, it is really difficult to build a simple correlation to cover such a wide range of parameters. Multiple-layer neural networks (NNs) have been verified to be able to approximate any unknown nonlinear function without prior knowledge of the input data distribution [37,38]. Therefore, a NN could be a good alternative to the traditional power-law or rational polynomial function.

Many different types of NNs have been developed, such as multiple-layer perceptron (MLP) network (also called BP network), radial basis function (RBF) network, and generalized regression neural network (GRNN). After comparing many types of NNs, a three-layer perceptron network is employed in this work. Its structure is shown in Fig. 1. The architecture has one input layer, one hidden layer, and one output layer, whose number of neurons is *I*, *J*, and *K*, respectively. Each neuron in the input layer makes the weighted summation of all the neurons in the hidden layer, and then passes this summation through a transfer function. Next, the neuron in the hidden layer makes the weighted summation of all the neurons in the output layer, and then passes the summation through the transfer function, which is the last output.

The relationship of input layer-hidden layer-output layer in mathematical form is described as follows:

$$h_j = g\left(\sum_{i=1}^{I} u_{ji}x_i + b_{1,j}\right) \quad (j=1,\ldots,J) \tag{12}$$

$$y_k = g\left(\sum_{j=1}^{J} w_{kj}h_j + b_{2,k}\right) \quad (k=1,\ldots,K) \tag{13}$$

where x_i stands for input parameters (π_2, π_3, π_4, π_5, and π_6 in this case), h_j are outputs of the hidden layer, and y_k denotes output parameters (π_1 in this case). u_{ji} is the associated weight connected by the *i*th neuron of the input layer to the *j*th neuron of the hidden layer. $b_{1,j}$ is the bias of the *j*th neuron of the hidden layer. w_{kj} is the associated weight connected by the jth neuron of the hidden layer to the kth neuron of the output layer. $b_{2,k}$ is the bias of the kth neuron of the output layer.

There are three different kinds of transfer functions in common use, named the tangent sigmoid function (Eq. (14)), the log sigmoid function (Eq. (15)), and the pure linear function (Eq. (16)).

$$f(x) = (2/(1+e^{-2x})) - 1 \tag{14}$$

$$f(x) = 1/(1+e^{-x}) \tag{15}$$

$$f(x) = x \tag{16}$$

In order to improve the efficiency of network training, preprocessing and postprocessing are needed. If we choose the tangent or log sigmoid transfer functions, neuron output will range from $(-1,1)$ or $(0, 1)$, and there is no range limit for input. However, if the absolute value of the input is large, all the outputs will be very near the boundary value -1, 0, or 1. Therefore, the network will become insensitive to different inputs. In such a case, it is necessary to scale the inputs to some smaller range, such as $(0, 1)$ or $(-1,1)$. After comparison, we chose the log sigmoid transfer function for the hidden layer and the pure linear transfer function for the output layer.

To train the NN, experimental data from the open literature are collected, as shown in Table 1. The total data sets used for NN training are 1152 including 882 sets of short tube orifice (S) data and 270 sets of capillary tube (C) data. Also, the database can be classified into 850 sets of subcooled (SC) inlet data and 302 sets of two-phase (TP) inlet data. The related refrigerant property calculation is carried out by REFPROP 7.0 [39].

Commercial software MATLAB 7.0 is chosen for NN training. The learning algorithms in MATLAB 7.0 Neural Network Toolbox are tried and finally the Bayesian regularization BP algorithm (TRAINBR) is chosen for NN training.

Table 2 gives the training error versus neuron number in the hidden layer, where the average deviation (AD) and standard deviation (SD) are defined as follows:

$$\mathrm{AD} = \frac{1}{N}\sum_{N}\frac{m_{\mathrm{prediction}} - m_{\mathrm{exp}}}{m_{\mathrm{exp}}} \tag{17}$$

$$\mathrm{SD} = \sqrt{\frac{1}{N-1}\sum_{N}\left(\frac{m_{\mathrm{prediction}} - m_{\mathrm{exp}}}{m_{\mathrm{exp}}} - \mathrm{AD}\right)^2} \tag{18}$$

In theory, more neurons in the hidden layer will lead to higher training accuracy. On the other hand, more neurons in the hidden layer will lead to network complexity and possible overtraining. Therefore, the proper number of neurons in the hidden layer should balance the accuracy and the network complexity. According to Table 2, more than two neurons in the hidden layer make little improvement to accuracy. Thus, two neurons are preferred in the hidden layer.

In order to verify whether the trained NN has good generalization, a Gaussian sensitivity analysis method is recommended [40,41]. This method provides another way to verify the goodness of the trained NN. We choose 115 sets of data and add on 10,000

Table 4 Weights and biases of the trained NN (Eq. (19))

$u_{j,i}(j=1-2,i=1-5)$					$b_{1,j}(j=1-2)$
4.561253	2.962082	$5.265086E-3$	$2.311472E-8$	$-4.940942E-1$	-4.055723
4.611665	-9.139079	$1.359944E-3$	$-1.173672E-8$	-4.939531	-4.644751
$w_{k,j}(k=1,j=1-2)$		b_2			
$-5.832737E-1$	$-2.314420E-1$	$8.852334E-1$			

Downloaded 03 Jun 2010 to 171.66.16.156. Redistribution subject to ASME license or copyright; see http://www.asme.org/terms/Terms_Use.cfm

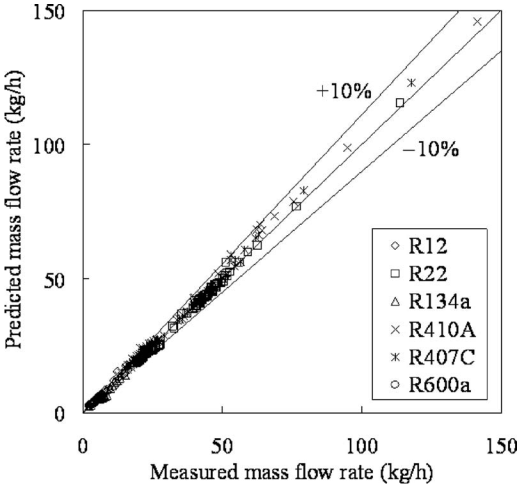

Fig. 2 Comparison of predicted and measured mass flow rates through adiabatic capillary tubes

random input variations using Gaussian error with $\sigma = 5\%$ and zero mean. The corresponding output variations are shown in Table 3. Apparently, the standard sensitivity of the trained NN is good compared to the deviations seen in Table 2 and therefore the network training was successful.

As a result, the trained 5-2-1 NN can be formulated as

$$\pi_1 = \sum_{j=1}^{2} \frac{w_{1,j}}{1 + \exp\left[-\left(\sum_{i=1}^{5} u_{j,i}\pi_{i+1} + b_{1,j}\right)\right]} + b_2 \qquad (19)$$

where the weights and biases are given in Table 4.

4 Results and Analysis

Figures 2 and 3 illustrate the comparison of the NN predicted and measured mass flow rates through adiabatic capillary tubes and short tube orifices, respectively. Figures 4 and 5 demonstrate the comparison of NN predicted and measured mass flow rates under SC and TP inlet conditions, respectively. For any category of data, most points fall into ±20%.

Table 5 lists the deviations and statistical percentages of the data points shown in Figs. 2–5. The overall average and standard deviations are 0.75% and 8.27%, respectively, which is comparable to other published researches. The overall percentages of data within ±10% and ±20% are 81% and 96%, respectively. Therein, the prediction of capillary tube data is a little better than that of short tube data and the result of SC inlet data is somehow better than that of TP inlet data.

There are some additional experimental data from Motta et al. [36] and Kim et al. [34], which are not included in the NN training but used for independent testing. All data are under SC inlet conditions. Figures 6 and 7 show the comparison of NN predicted and measured mass flow rates through capillary and short tubes. In Fig. 6, most data falls into ±20%. Although there are no R404A data included in the NN training, the NN gives good predictions. In Fig. 7, most data are within ±10%. Even though the operating conditions of these data are near the critical point, the prediction using the trained NN is still satisfactory. Therefore, the additional validation demonstrates the trained NN is generalized.

The continuity of NN prediction from the SC inlet conditions to the TP inlet conditions is shown in Fig. 8, where the inlet quality is defined as $(h_{\text{in}} - h_f)/(h_g - h_f)$. By comparison, the corresponding predictions by the ASHRAE correlations [1] are discontinuous at zero inlet quality or subcooling. In fact, the applicability of ASHRAE correlations are $1\text{ K} < \theta_{\text{sc}} < 17\text{ K}$ for SC inlet and $0.03 < x_{\text{in}} < 0.25$ for TP inlet. That indicates both continuity and

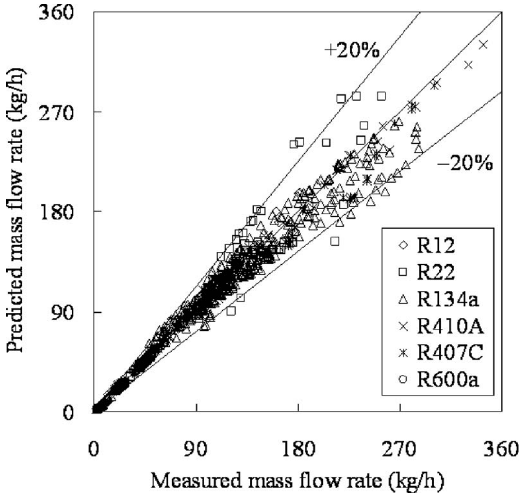

Fig. 4 Comparison of predicted and measured mass flow rates under SC inlet conditions

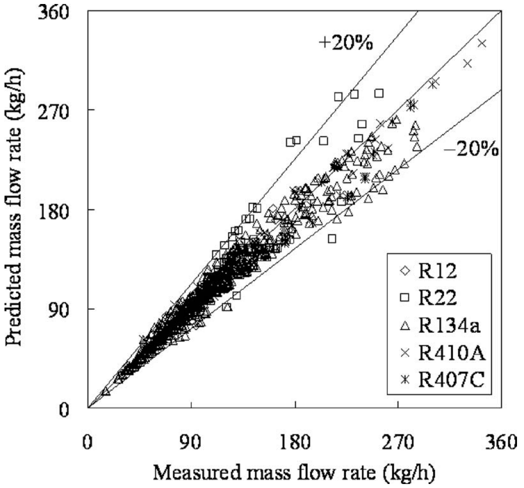

Fig. 3 Comparison of predicted and measured mass flow rates through short tube orifices

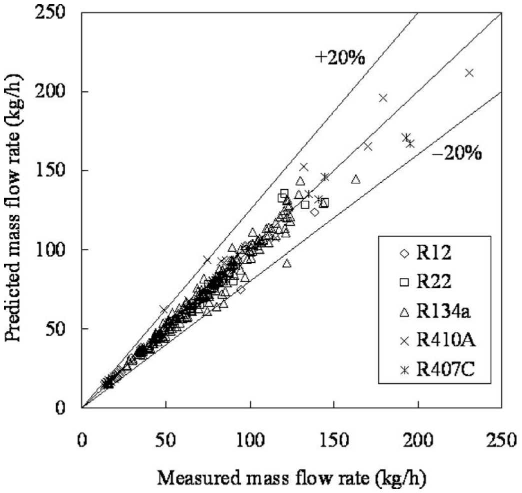

Fig. 5 Comparison of predicted and measured mass flow rates under TP inlet conditions

Downloaded 03 Jun 2010 to 171.66.16.156. Redistribution subject to ASME license or copyright; see http://www.asme.org/terms/Terms_Use.cfm

Table 5 Deviations and statistical percentages

Data	AD (%)	SD (%)	Within ±10%	Within ±20%
Capillary	0.85	7.13	87.4	96.3
Short tube	0.72	8.58	79.3	95.7
Subcooled	0.96	8.83	78.2	95.1
Two phase	0.15	6.36	89.4	98.0
All	0.75	8.27	81.2	95.8

accuracy cannot be guaranteed using these correlations at the lower subcooling or quality. However, the proposed NN will never have such issues.

In Fig. 9, the trained NN predicts the change in mass flow rate with the length-to-diameter ratio L/D under different condensing temperatures. When shown in normal and logarithmic scales of L/D, the mass flow rate change is flat at L/D lower than 20 or higher than 2000. Rather, at $20 < L/D < 2000$, the mass flow rate changes sharply. This is reasonable because the mass flow rate is predominated by the entrance effect when L/D is small and changes slower when the tube is long enough. This correlation will help designers match length and diameter to achieve a desired mass flow. Besides, with increase of the condensing temperature, the mass flow rate goes up as expected. Therefore, the trained NN can well predict the mass flow rate from the short tube orifices to the longer capillary tubes. However, when the L/D is lower than 3–5, flow choking could not be established. In this case, the effects of the exit pressure cannot be ignored and accordingly the present model is not very applicable.

5 Conclusion

In this study, a generalized NN model of refrigerant mass flow rates through adiabatic capillary and short tubes under the SC and TP inlet conditions has been developed. Based on the simple HEM, a new group of dimensionless parameters is proposed as the input and output parameters of the NN. The experimental data from the open literature including R12, R22, R134a, R600a, R404A, R407C, and R410A are used for the NN training and validation. Three-layer BP network containing two neurons in the hidden layer is identified with average and standard training deviations of 0.75% and 8.27%, respectively. The generalized NN model makes good predictions on the new R404A data and the data near the critical point as well. Again, this work shows the NN is a promising approach to generalized correlations in engineering.

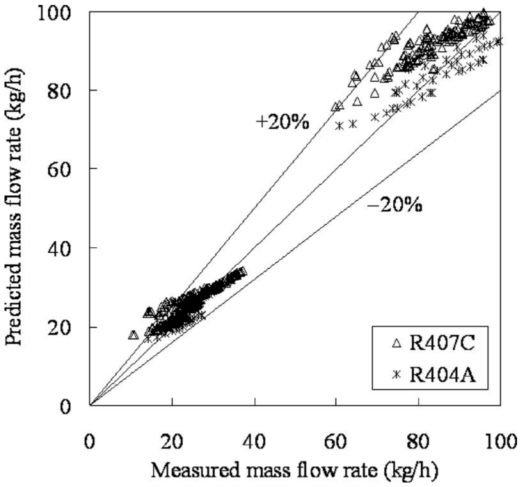

Fig. 6 Comparison of predicted and measured mass flow rates [36] through adiabatic capillary tubes

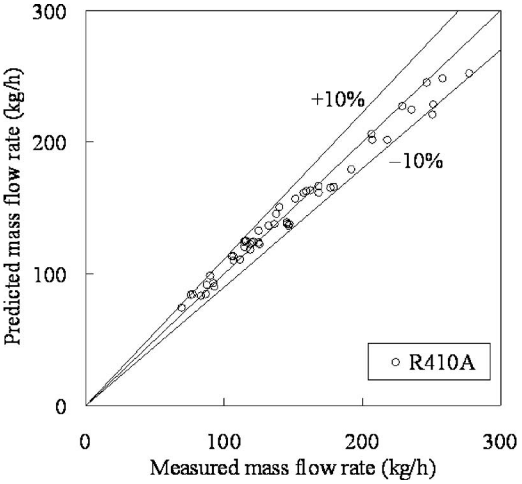

Fig. 7 Comparison of predicted and measured mass flow rates [34] through short tube orifices

Nomenclature

b = bias
D = tube diameter (m)
f = friction factor
G = mass flux (kg m^{-2} s^{-1})
h = specific enthalpy (J kg^{-1})
L = tube length (m)
N = number of data
m = mass flow rate (kg s^{-1})
p = pressure (Pa)
p_{sat} = saturated pressure related to inlet temperature (Pa)
Re = Reynolds number
T = temperature (°C)
u = weighting factors between input and hidden layers
v = specific volume (m^3 kg^{-1})
w = weighting factors between hidden and output layers
x = quality

Greek Symbols

μ = viscosity (N s m^{-2})
π_i = dimensionless parameters
θ_{SC} = subcooling (K)

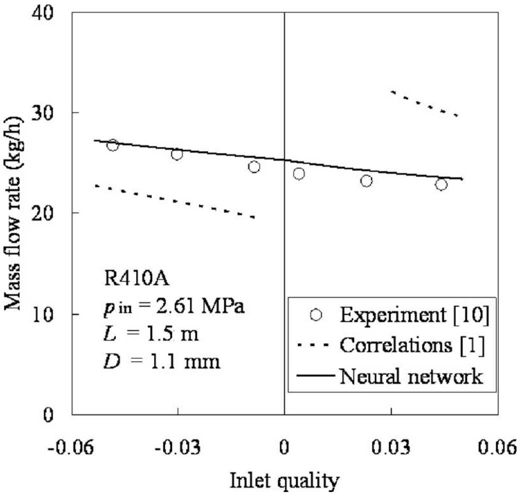

Fig. 8 Mass flow rate change with inlet conditions

Downloaded 03 Jun 2010 to 171.66.16.156. Redistribution subject to ASME license or copyright; see http://www.asme.org/terms/Terms_Use.cfm

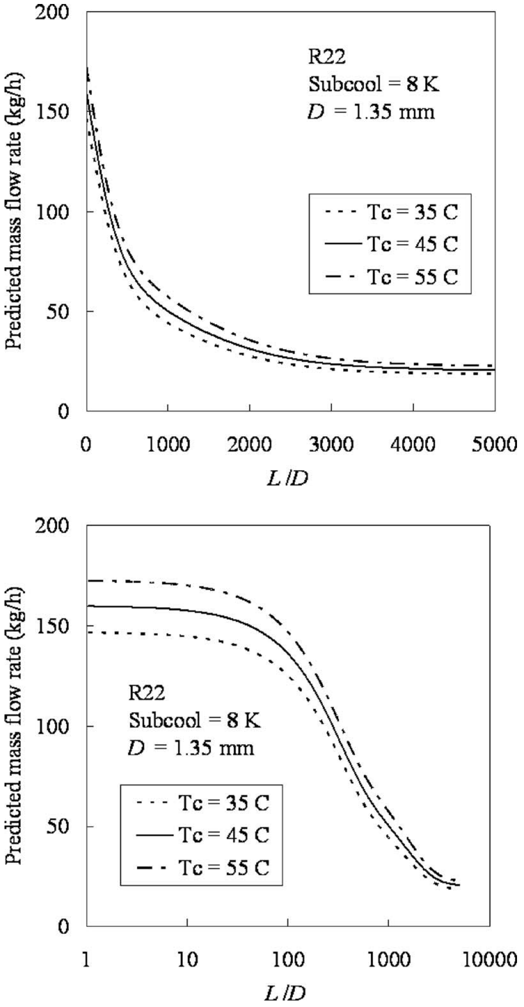

Fig. 9 Mass flow rate change with length-to-diameter ratio

ρ = density (kg m^{-3})

Superscripts and Subscripts

c = condensing
f = saturated liquid
g = saturated vapor
in = inlet
m = mean value
out = outlet

References

[1] ASHRAE, 2002, *ASHRAE Handbook: Refrigeration*, American Society of Heating, Refrigerating and Air-Conditioning Engineers, Inc., Atlanta, Chap. 45.

[2] Li, R. Y., Lin, S., and Chen, Z. H., 1990, "Numerical Modeling of Thermodynamic Non-Equilibrium Flow of Refrigerant Through Capillary Tubes," ASHRAE Trans., **96**(1), pp. 542–549.

[3] Kuehl, S. J., and Goldschmidt, V. W., 1991, "Modeling of Steady Flows of R-22 Through Capillary Tubes," ASHRAE Trans., **97**(1), pp. 139–148.

[4] Escanes, F., Perez-Segarra, C. D., and Oliva, A., 1995, "Numerical Simulation of Capillary-Tube Expansion Devices," Int. J. Refrig., **18**(2), pp. 113–122.

[5] Bittle, R. R., and Pate, M. B., 1996, "A Theoretical Model for Predicting Adiabatic Capillary Tube Performance With Alternative Refrigerants," ASHRAE Trans., **102**(2), pp. 52–64.

[6] Garcia-Valladares, O., Perez-Segarra, C. D., and Oliva, A., 2002, "Numerical Simulation of Capillary Tube Expansion Devices Behavior With Pure and Mixed Refrigerants Considering Metastable Region, Part I: Mathematical Formulation and Numerical Model," Appl. Therm. Eng., **22**(2), pp. 173–182.

[7] Zhang, C. L., and Ding, G. L., 2001, "Modified General Equation for the Design of Capillary Tubes," ASME J. Fluids Eng., **123**(4), pp. 914–919.

[8] Zhang, C. L., and Ding, G. L., 2004, "Approximate Analytic Solutions of Adiabatic Capillary Tube," Int. J. Refrig., **27**(1), pp. 17–24.

[9] Wijaya, H., 1992, "Adiabatic Capillary Tube Test Data for HFC-134a," *The IIR-Purdue Refrigeration Conference*, West Lafayette, IN, Vol. 1, pp. 63–71.

[10] Fiorelli, F. A. S., Huerta, A. A. S., and Silvares, O. M., 2002, "Experimental Analysis of Refrigerant Mixtures Flow Through Adiabatic Capillary Tubes," Exp. Therm. Fluid Sci., **26**, pp. 499–512.

[11] Fiorelli, F. A. S., and Silvares, O. M., 2003, "Refrigerant Mixtures Flow Through Capillary Tubes: A Comparison Between Homogeneous and Separated-Flow Models," HVAC&R Res., **9**(1), pp. 33–53.

[12] Yana Motta, S. F., Parise, J. A. R., and Braga, S. L., 2002, "A Visual Study of R-404A/oil Flow Through Adiabatic Capillary Tubes," Int. J. Refrig., **25**, pp. 586–596.

[13] Fukuta, M., Yanagisawa, T., Arai, T., and Ogi, Y., 2003, "Influences of Miscible and Immiscible Oils on Flow Characteristics Through Capillary Tube, Part I: Experimental Study," Int. J. Refrig., **26**, pp. 823–829.

[14] Garcia-Valladares, O., 2004, "Review of Numerical Simulation of Capillary Tube Using Refrigerant Mixtures," Appl. Therm. Eng., **24**, pp. 949–966.

[15] Bansal, P. K., and Rupasinghe, A. S., 1996, "An Empirical Model for Sizing Capillary Tubes," Int. J. Refrig., **19**(8), pp. 497–505.

[16] Jung, D., Park, C., and Park, B., 1999, "Capillary Tube Selection for HCFC22 Alternatives," Int. J. Refrig., **22**(8), pp. 604–614.

[17] Chen, S. L., Liu, C. H., Cheng, C. S., and Jwo, C. S., 2000, "Simulation of Refrigerants Flowing Through Adiabatic Capillary Tubes," HVAC&R Res., **6**(2), pp. 101–115.

[18] Trisaksri, V., and Wongwises, S., 2003, "Correlations for Sizing Adiabatic Capillary Tubes," Int. J. Energy Res., **27**, pp. 1145–1164.

[19] Bittle, R. R., Wolf, D. A., and Pate, M. B., 1998, "A Generalized Performance Prediction Method for Adiabatic Capillary Tubes," HVAC&R Res., **4**(1), pp. 27–43.

[20] Melo, C., Ferreira, R. T. S., Neto, C. B., Goncalves, J. M., and Mezavila, M. M., 1999, "An Experimental Analysis of Adiabatic Capillary Tubes," Appl. Therm. Eng., **19**(6), pp. 669–684.

[21] Wei, C. Z., Lin, Y. T., Wang, C. C., and Leu, J. S., 1999, "Experimental Study of the Performance of Capillary Tubes for R-407C Refrigerant," ASHRAE Trans., **105**(2), pp. 634–638.

[22] Kim, S. G., Kim, M. S., and Ro, S. T., 2002, "Experimental Investigation of the Performance of R22, R407C and R410A in Several Capillary Tubes for Air-Conditioners," Int. J. Refrig., **25**, pp. 521–531.

[23] Choi, J., Kim, Y., and Kim, H. Y., 2003, "A Generalized Correlation for Refrigerant Mass Flow Rate Through Adiabatic Capillary Tubes," Int. J. Refrig., **26**(7), pp. 881–888.

[24] Choi, J., Kim, J. T., and Chung, J. T., 2004, "An Empirical Correlation and Rating Charts for the Performance of Adiabatic Capillary Tubes with Alternative Refrigerants," Appl. Therm. Eng., **24**(1), pp. 29–41.

[25] Zhang, C. L., 2005, "Generalized Correlation of Refrigerant Mass Flow Rate Through Adiabatic Capillary Tubes Using Artificial Neural Network," Int. J. Refrig., **28**, pp. 506–514.

[26] Yang, L., and Zhang, C. L., "Two-Fluid Model of Refrigerant Two-Phase Flow Through Short Tube Orifices," 2005, Int. J. Refrig., **28**, pp. 419–427.

[27] Aaron, D. A., and Domanski, P. A., 1990, "Experimentation Analysis and Correlation of Refrigerant-22 Flow Through Short Tube Restrictors," ASHRAE Trans., **96**(1), pp. 729–742.

[28] Singh, G. M., Hrnjak, P. S., and Bullard, C. W., 2001, "Flow of Refrigerant 134a Through Short Tubes," HVAC&R Res., **7**(3), pp. 245–262.

[29] Kim, Y., O'Neal, D. L., and Yuan, X. L., 1994, "Two-Phase Flow of HFC-134a and CFC-12 Through Short-Tube Orifices," ASHRAE Trans., **100**(2), pp. 582–591.

[30] Kim, Y., and O'Neal, D. L., 1994, "Two-Phase Flow of R-22 Through Short-Tube Orifices," ASHRAE Trans., **100**(1), pp. 323–334.

[31] Payne, W. V., and O'Neal, D. L., 1999, "Multiphase Flow of Refrigerant 410A Through Short Tube Orifices," ASHRAE Trans., **105**(2), pp. 66–74.

[32] Payne, W. V., and O'Neal, D. L., 1998, "Mass flow characteristic of R407C through short tube orifices," ASHRAE Trans., **104**(1), pp. 197–209.

[33] Choi, J., Chung, J. T., and Kim, Y., 2004, "A Generalization Correlation for Two-Phase Flow of Alternative Refrigerants Through Short Tube Orifices," Int. J. Refrig., **27**, pp. 393–400.

[34] Kim, Y., Payne, V., Choi, J., and Domanski, P., 2005, "Mass Flow Rate of R-410A Through Short Tubes Working Near the Critical Point," Int. J. Refrig., **28**, pp. 547–553.

[35] Payne, V., and O'Neal, D. L., 2004, "A Mass Flow Rate Correlation for Refrigerants and Refrigerant Mixtures Flowing Through Short Tubes," HVAC&R Res., **10**(1), pp. 73–87.

[36] Motta, S. Y., Braga, S. L., and Parise, J. A. R., 2000, "Critical Flow of Refrigerants Through Adiabatic Capillary Tubes: Experimental Study of Zeotropic Mixtures R407C and R404A," ASHRAE Trans., **106**(1), pp. 534–549.

[37] Hornik, K., Stinchcombe, M., and White, H., 1989, "Multilayer Feedforward Networks Are Universal Approximators," Neural Networks, **2**, pp. 359–366.

[38] Hagan, M. T., and Demuth, H. B., 1996, *Neural Network Design*, PWS Publishing Company, Boston, MA.

[39] 2000, REFPROP, Version 7.0, Reference Fluid Thermodynamic and Transport Properties NIST Standard Reference Database, 23, Gaithersburg, MD.

[40] Wang, W. J., Zhao, L. X., and Zhang, C. L., 2006, "Generalized Neural Network Correlation for Flow Boiling Heat Transfer of R22 and Its Alternative Refrigerants Inside Horizontal Smooth Tubes," Int. J. Heat Mass Transfer, **49**(15–16), pp. 2458–2465.

[41] Le Niliot, C., and Lefevre, F., 2004, "A Parameter Estimation Approach to Solve the Inverse Problem of Point Heat Sources Identification," Int. J. Heat Mass Transfer, **47**, pp. 827–841.

Downloaded 03 Jun 2010 to 171.66.16.156. Redistribution subject to ASME license or copyright; see http://www.asme.org/terms/Terms_Use.cfm

Flow Field Characterization at the Onset of Gas Entrainment in a Single Downward Discharge Using Particle Image Velocimetry

R. C. Bowden

I. G. Hassan[1]
e-mail: ibrahimh@alcor.concordia.ca

Department of Mechanical and Industrial Engineering,
Concordia University,
Montreal, QC, H3G 2W1, Canada

The incipience of two-phase flow in discharging branches from a stratified gas-liquid region has major implications in industrial applications where safety is of concern. An experimental investigation of the liquid side flow field at the onset of gas entrainment, in a single downward oriented discharging branch, was presented. Particle image velocimetry was used to measure the liquid side flow field in horizontal and vertical planes. Averaged velocity profiles were presented and demonstrated a highly radial flow. The particle image velocimetry data were validated using continuity and showed that the mass flow rate to be in the range of 10–25% of the expected value. Further, the vortex-free flow field assumption, used previously in the development of analytical and empirical models, was found to be reasonable. [DOI: 10.1115/1.2801356]

Keywords: onset of gas entrainment, two-phase flow visualization, particle image velocimetry

1 Introduction

It is not uncommon that reservoirs serve as fluid storage buffers between various devices, such as pumps and heat exchangers, in pressurized fluid distribution systems. An engineer may, for example, design a reservoir that both receives and supplies the fluid to multiple devices within the system. It may be important for a safe operation that these devices operate with a single-phase fluid. In certain instances, this requirement can be compromised by an unforeseen accident, causing two phases to be present within the reservoir and, potentially, the device. An industrial example where this can occur is the Canada deuterium and uranium (CANDU) nuclear reactor. The CANDU reactor incorporates a fluid distribution system, whereby coolant flows from a large reservoir (known as the header) through a network of pipes (known as feeders) to the reactor fuel channels. A break in the distribution network, or a pump failure, can cause a two-phase environment to occur within the header. This, in turn, can lead to the gas phase entraining into the feeder branches, where liquid flows under normal operation, resulting in a two-phase mixture to flow into the fuel channels. The two-phase flow impacts the designed cooling effectiveness and can lead to an increase in the reactor core temperature. Not too surprisingly, a rise in core temperature poses serious safety concerns. Such potentially catastrophic scenarios are known as loss-of-coolant accidents (LOCAs), and considerable efforts have been made to understand and prevent them.

Zuber [1] found that if the gas-liquid interface was located above the discharging branch inlet, gas would be entrained into the branch at a critical height, which is called the onset of gas entrainment (OGE). The OGE occurred by either the vortex induced or vortex-free mechanism. Several authors investigated experimentally the critical height at the OGE by the vortex-free mechanism in a single, downward oriented discharging branch. The experiments were performed with stratified two-phase flow in the main duct at various operating pressures, discharge branch diameters, and fluids. The authors provided empirical correlations of the critical height as a function of the discharge Froude number from a circular pipe [2–5] and a square duct [6]. The traditional Froude number, which is a ratio of the inertial to gravitational forces, was modified in these studies to include the density ratio of both fluid phases, following Ref. [1]. There was some disagreement between their correlations, particularly where the inflow of the liquid phase near the discharge inlet was concerned. When the inflow was symmetrical near the discharge inlet, these authors agreed that the vortex-free gas entrainment mechanism was dominant, and the critical height correlated well as a function of the Froude number. The coefficients in their correlations did, however, vary slightly.

Several authors experimentally investigated the critical height at the onset of vortex-free gas entrainment in multiple discharges on a flat vertical wall [7–10]. These studies demonstrated the effects of the branch location relative to one another, which could be oriented in the same vertical plane, horizontal plane, or inclined plane. These studies maintained a symmetrical inflow at the discharge inlet by locating the discharge on one end of a large reservoir. The large reservoir was supplied with a controllable source of both air and water, which enabled the liquid height to be well controlled. The discharge diameter that they selected was 6.35 mm, and the reservoir was operated at pressures ranging between 300 kPa and 500 kPa. The critical height was presented as a function of the discharge Froude number, similar to the previous works. Later, Ahmad and Hassan [11] experimentally investigated the critical height at the onset of vortex-free gas entrainment in single, dual, and triple discharge cases with three 6.35 mm diameter orifices located on a curved wall at 0 deg, 45 deg, and 90 deg, down from horizontal. The data were not correlated, but notably the critical height was also presented as a function of the discharge Froude number. They also used a test facility where the test section was mounted at the end of a large reservoir. This ensured a symmetrical inflow and a smooth-stratified two-phase environment with a controllable liquid and gas supply.

Ahmed et al. [12] modeled the onset of vortex-free gas entrainment in a single discharging side branch, located on a flat vertical wall, with symmetrical inflow. Two models were developed, a

---

[1] Corresponding author.

Contributed by the Fluids Engineering Division of ASME for publication in the JOURNAL OF FLUIDS ENGINEERING. Manuscript received July 17, 2006; final manuscript received June 4, 2007. Review conducted by Theodore Heindel. Paper presented at the 2006 ASME Fluids Engineering Division Summer Meeting and Exhibition (FEDSM2006), Miami, FL, July 17–20, 2006.

Copyright © 2007 by ASME

Downloaded 03 Jun 2010 to 171.66.16.156. Redistribution subject to ASME license or copyright; see http://www.asme.org/terms/Terms_Use.cfm

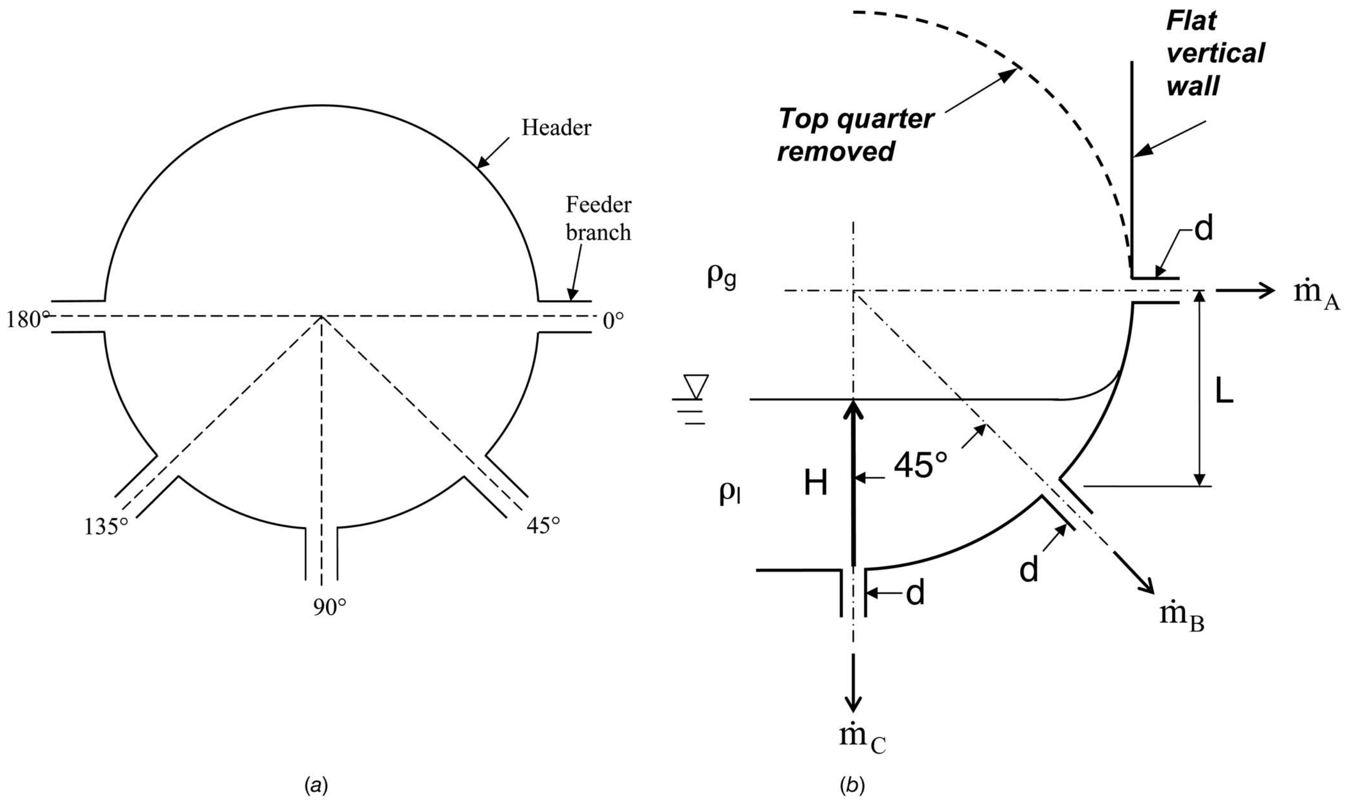

Fig. 1 (*a*) Typical cross section of a CANDU header-feeder and (*b*) test section geometry to model the circular cross section

simplified point-sink model and a more complex finite branch model. They assumed two immiscible fluid phases, gas and liquid, contained in a large reservoir, and the equilibrium of the interface was governed by a balance of inertia and gravity. Surface tension was neglected, and the fluids were said to be inviscid, irrotational, incompressible, and quasisteady. These assumptions caused the problem to be dominated by the modified discharge Froude number, as above. The heavier fluid had a potential flow field, and the lighter fluid was stagnant. The velocity field of the heavier fluid was found in the first model by representing the discharge flow by a three-dimensional point sink. The second model—called the finite branch model—used the three-dimensional continuity equation with the same assumptions and appropriate boundary conditions. The well known Laplace equation resulted when the potential function was used to describe the velocity field. The results demonstrated that the critical height in both models showed reasonable similarity above a discharge Froude number of 10. The finite branch model was found to more appropriately model the physical limits at lower discharge Froude numbers. A relatively good agreement with available experimental data was found.

Found to be lacking from the literature survey was experimental evidence that the vortex-free mechanism was valid when describing the OGE flow field. The previous experimental works described the vortex-free mechanism based on their visual observations but made no attempt to map the flow field nor to discuss the effects of the branch discharge strength on it. The vortex-free assumption was also a main contributor in the development of the analytical model discussed above. The model, which developed the velocity field by assuming a potential flow, can be further validated by experimental evidence of the flow field. Future researchers may find quantitative flow field data useful for semi-empirical modeling. This work experimentally investigated the flow field at the onset of vortex-free gas entrainment, in a single downward oriented discharging branch, using particle image velocimetry (PIV). The liquid side velocity field was investigated, and the effects of varying the discharge strength were explored. A single discharging bottom branch was selected as a starting point to map the two-phase flow field using PIV. This preliminary study was conducted to understand the challenges of adapting PIV to the two-phase experiment. Future studies will include more complex multiple discharge scenarios.

2 Experimental Investigation

2.1 Problem Description. A typical header has a circular cross section and measures approximately 6 m in length and between 0.356 m and 0.406 m in inner diameter, and is closed on both ends. Flow enters the top of the header through a number of orifices (called turrets) and exits through a network of feeder banks. Each feeder bank contains five 50.8 mm diameter orifices located radially at 0 deg, 45 deg, 90 deg, 135 deg, and 180 deg from the horizontal axis, shown in Fig. 1(*a*). Hassan et al. [13] found that a semicircular test section, with three discharging branches, had several experimental advantages and provided reasonable dynamic similarity to a header-feeder bank with five discharges. The semicircular geometry was selected for this study.

The geometry and relevant parameters, with smooth-stratified two-phase conditions, were presented in Fig. 1(*b*). A semicircular cross section, with discharging branches located at 0 deg, 45 deg, and 90 deg from the horizontal axis, referred to as branches *A*, *B*, and *C*, respectively, was used. A model of the semicircular geometry was developed using a dimensional analysis. The dimensional analysis, with up to three simultaneous discharges and a smooth-stratified two-phase regime, neglected viscous and surface tension effects and considered both fluids to be incompressible and irrotational. The following relationship was found:

$$\frac{H_C}{d} = f\left(\mathrm{Fr}_C, \mathrm{Fr}_A, \mathrm{Fr}_B, \frac{L}{d}\right) \tag{1a}$$

The assertion in this analysis was that the critical height H at the onset of vortex-free gas entrainment in branch C showed a depen-

Downloaded 03 Jun 2010 to 171.66.16.156. Redistribution subject to ASME license or copyright; see http://www.asme.org/terms/Terms_Use.cfm

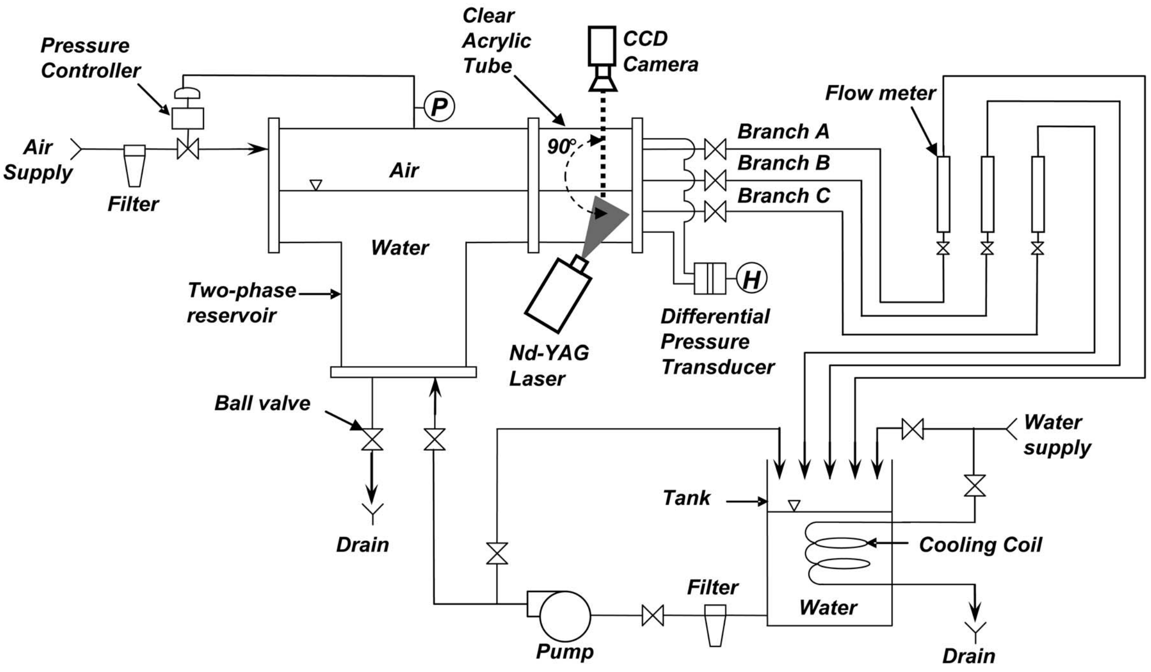

Fig. 2 Simplified schematic of the experimental test facility

dent relationship with the active ($\dot{m} > 0$) branch discharge Froude number Fr, and the separating distance between the branches, L. In this study, only the downward oriented discharge, branch C, was considered active so the two remaining discharges and the separating distance between the branches were not considered. The relationship, with only branch C active and using the same methodology, reduced to

$$\frac{H_C}{d} = f(\mathrm{Fr}_C) \tag{1b}$$

This relationship was also previously demonstrated, for example, by Refs. [2, 7, and 9] for various geometrical configurations. The critical height H_C, measured vertically from the center of the branch C inlet to the gas-liquid interface, was nondimensionalized with the discharge branch diameter d. The Froude number Fr_C for a circular branch of diameter d was found to be

$$\mathrm{Fr}_C = \frac{4\dot{m}_l}{\pi\sqrt{(g d^5 \rho_l \Delta\rho)}} \tag{2}$$

The mass flow rate of the single-phase liquid flowing in branch C prior to the OGE, was defined by $\dot{m}_l$. The acceleration due to gravity was denoted as g. These parameters demonstrate that the physics of the problem were expected to be governed by a ratio of the inertial and gravitational forces. The density ratio of the two fluid phases appeared as $\rho_l \Delta\rho$ when $\dot{m}_l$ was used instead of the average discharge velocity. The difference between the heavier ρ_l and lighter ρ_g fluid densities was defined as $\Delta\rho = \rho_l - \rho_g$. This study used the header-feeder geometry as the prototype for the model; however, it was meant to be relevant, in general, to applications of similar geometry and flow conditions.

2.2 Test Section. Two factors were considered in the design of the test section. The first being that it should model the geometry shown in Fig. 1, and second that measurements of the flow field, using PIV, should be possible. A tradeoff was necessary to allow optical access to the flow field, resulting in the top half of the semicircular wall being replaced with a flat vertical wall. The change in geometry meant that the effect of wall curvature on the flow field would not be observed when the gas-liquid interface was above the branch A centerline. Experiments were, therefore, not performed with the gas-liquid interface above the branch A centerline. The test section was manufactured from a solid piece of cast clear acrylic rod. The quarter-circular surface, with a flat vertical wall, was machined into one end of the acrylic rod. The radius of the quarter-circular surface was 25.4 mm after being scaled down 1:8 from the prototype. Three holes, 6.35 mm in diameter, were drilled 30.4 mm deep into the quarter-circular surface at 0 deg, 45 deg, and 90 deg, and then enlarged to 9.54 mm in diameter for a remaining 90.3 mm depth. After machining the test section, all surfaces were polished using an abrasive technique to enhance surface quality.

2.3 Test Facility and Particle Image Velocimetry System. Recently, an experimental facility was established at Concordia University in Montreal, Canada by Ahmad and Hassan [11]. A simplified schematic of the test facility was presented in Fig. 2. The two-phase reservoir was made from two stainless steel pipes welded together in a T shape; flanges were welded onto the three ends. Two of the flanges were capped with stainless steel covers. On the third flanged end, a clear acrylic tube was fastened and its open end capped with a stainless steel cover. The test section was installed through a hole machined at the center of this cover. The test section was bolted to the cover and an O-ring provided adequate sealing. The test section was shown installed on the stainless steel flange in Fig. 3(*a*). The test section discharges, branches A, B, and C, were controlled by downstream ball valves installed at their outlets. Downstream of the ball valve, each discharge was connected to a flow meter that was regulated with an inline needle valve. Four water flow meters, with overlapping flow rates up to a maximum of 75 l/min, were used. The flow meters were selected to provide different orders of magnitude of the discharge Froude number ($0.001 \leq \mathrm{Fr} \leq 30$). The flow meters were connected together in parallel, by inlet and outlet headers, which allowed easy adjustment of the flow rate within the various ranges.

Regulated air was supplied to the two-phase reservoir by a fisher pressure controller. The discharge air was released to atmosphere downstream of the flow meters. The air pressure in the two-phase reservoir was monitored by a Rosemount liquid crystal display (LCD) pressure transducer with a factory calibrated range of 0–830 kPa. Water was stored in a 208 l tank and supplied to

Downloaded 03 Jun 2010 to 171.66.16.156. Redistribution subject to ASME license or copyright; see http://www.asme.org/terms/Terms_Use.cfm

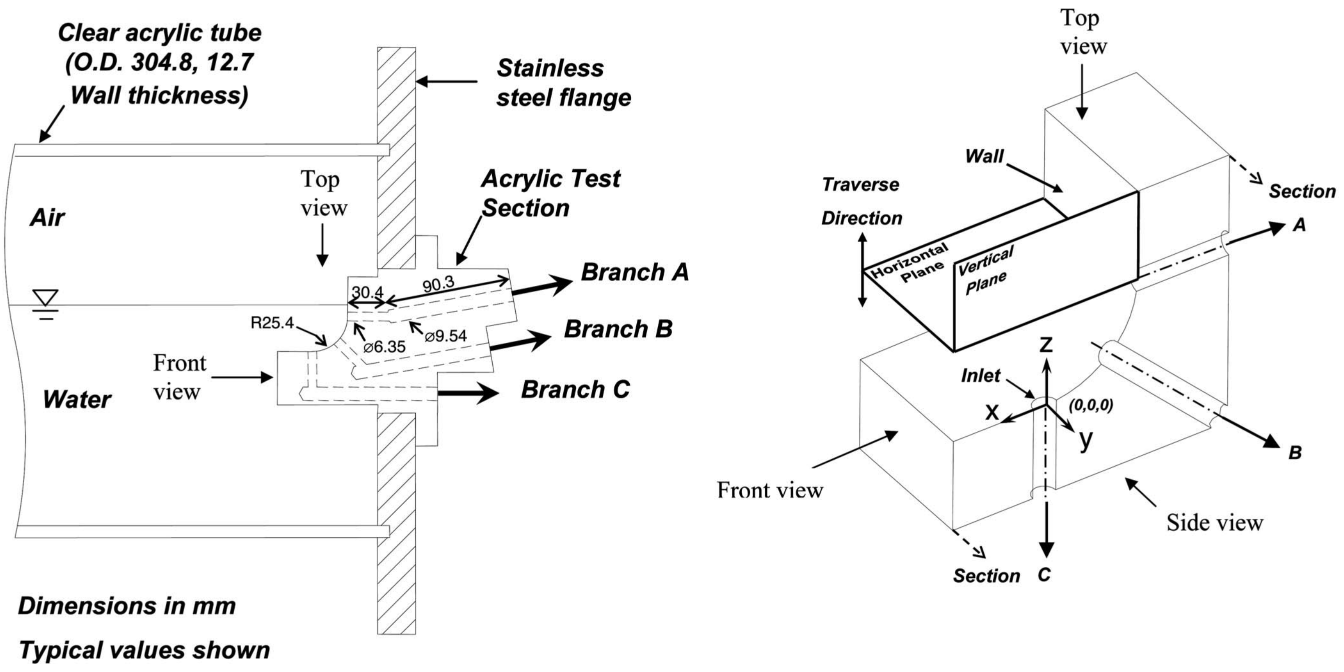

(*a*) (*b*)

Fig. 3 (*a*) Elevation view of the test section installed in the test facility. (*b*) Sectioned view of the test section surface demonstrating the alignment of investigated planes and coordinate system.

the two-phase reservoir by a 2.23 kW (3 hp) eight-stage vertical pump. The discharged water downstream of the flow meters was circulated back to the tank. The water height was measured by a Rosemount LCD differential pressure transducer with a factory calibrated range of 0–255 mm H_2O. Plumbing between the two-phase reservoir and all other devices—which include the pump, pressure regulator, pressure transducer, differential pressure transducer, and flow meters—was established using flexible polyvinyl chloride (PVC) tubing.

The PIV system was commercially available from Dantec Dynamics. The system was arranged for two-dimensional liquid side velocity field measurements. The seeding particles used were polyamide PSP-20 having a mean diameter of 20 μm. A New Wave Research Solo XT 120 Nd:YAG (yttrium aluminum garnet) pulsed laser, capable of 120 mJ/pulse at a 532 nm wavelength and a pulse rate of 15 Hz, was used to illuminate the seeding particles in the liquid flow. A series of lenses in a packaged optics assembly converted the single beam output from the laser head into a light sheet with variable thickness. The particle displacement was captured using a HiSense MkII 12 bit digital output charge coupled device (CCD) camera with a 1344×1024 pixel resolution. In the current setup, a maximum capture rate of 5.67 Hz was found for an image pair. A Nikon objective lens, mounted to the camera, provided focal and illumination adjustments. A National Instruments NI-IMAQ PCI-1426 frame grabber card was used in conjunction with the camera to capture and store the images. A National Instruments NI-DQQ PCI-6601 timer board was used to synchronize the camera imaging with the laser pulses. The large data processing requirements were handled by a Dell Precision Workstation, with two 3.60 GHz processors, 4 Gbytes of random access memory (RAM), and two 250 Gbyte 7200 rpm hard drives. Dantec's FLOW MANAGER software was used to perform the necessary calibration, correlation functions, filtering, and statistical calculations on the images to generate the resolved velocity fields.

2.4 Experimental Procedure. The procedure for recording the critical height at the onset of vortex-free gas entrainment, using air and water as the two fluids, was as follows. Water was first pumped into the two-phase reservoir until the height of the air-water interface was sufficiently above the branch *C* inlet. Typically, this starting liquid height was around 35 mm above the branch *C* inlet. The objective of positioning the air-water interface was to ensure initial single-phase flow when branch *C* was activated. The two-phase reservoir was then pressurized to 206 kPa. The pressurized environment was important to achieve higher discharge Froude numbers. Branch *C*'s valve was opened, thereby activating it, and its discharge flow rate was adjusted to the desired value. The water level in the reservoir was then slowly decreased at a rate of approximately 1 mm/min, until the onset of vortex-free gas entrainment occurred in branch *C*, at which point H_{OGE} was recorded. OGE was said to occur when a gas tube extended from the interface to the discharge branch inlet and gas was steadily entrained into the branch. The OGE was considered steady when the gas tube tip did not oscillate between the discharge inlet and the interface. This criterion was important to distinguish between vortex induced gas entrainment, where gas entrainment was unsteady, and vortex-free gas entrainment, where gas entrainment was relatively stable. The water level was maintained steady by matching the reservoir's inlet flow rate and the discharge's flow rate. The relatively large volume of the reservoir, compared to that of the test section, allowed a smooth-stratified interface to be maintained, even under conditions of gas entrainment.

The procedure for recording the liquid velocity field, at the OGE in the bottom branch *C*, was summarized as follows. The polyamide seeding particles were mixed into the water storage tank. The digital CCD camera was positioned such that the desired field of view was obtained. The laser was pulsed at low intensity to make adjustments to the focal length and light shutter until a reasonable particle resolution was obtained. The field of view was scaled using the known branch diameter. Finding the best particle resolution required several fine adjustments to the focal length, light shutter, the camera and light sheet placement, and seeding

Downloaded 03 Jun 2010 to 171.66.16.156. Redistribution subject to ASME license or copyright; see http://www.asme.org/terms/Terms_Use.cfm

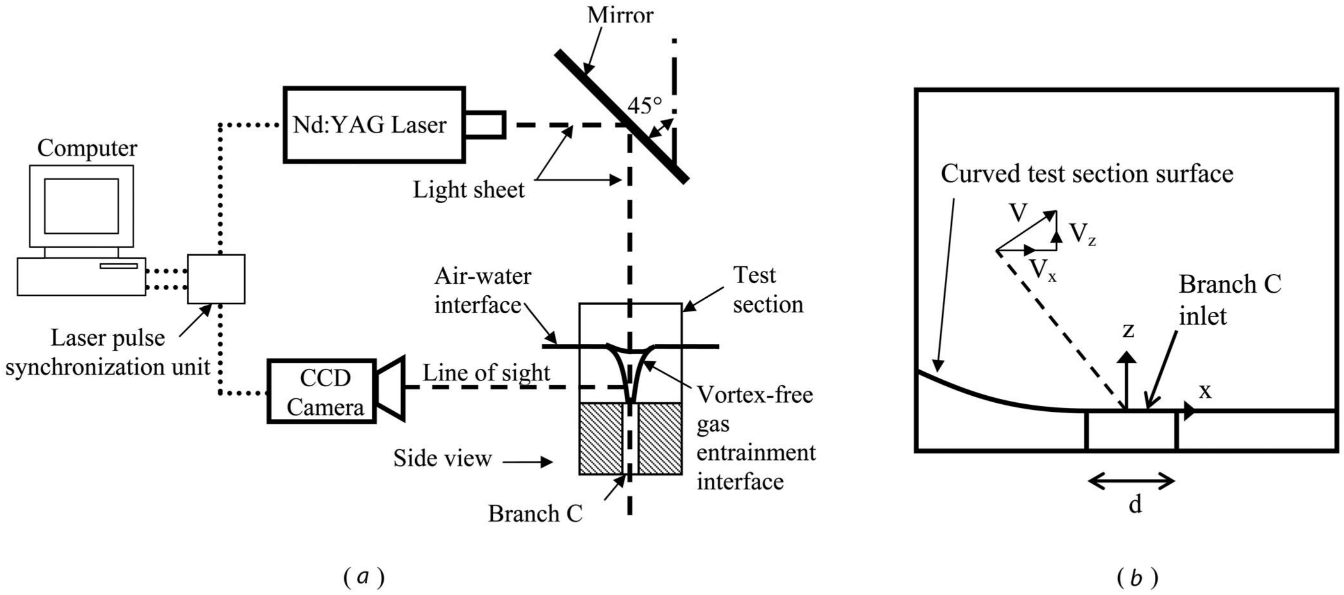

Fig. 4 (*a*) Typical vertical image plane setup using PIV and (*b*) its corresponding image plane and coordinate system

density. The laser intensity was then increased and the light shutter opening was reduced to compensate, and a sample image was recorded. Using FLOW MANAGER's cross-correlation scheme, the necessary timing sequence to capture the flow field was established. The timing sequence was defined as the time interval between the two sequentially recorded images, commonly known as the image pair, required to resolve a single velocity field. If the correlation was poor, then the time interval was adjusted appropriately, and a new sample image was recorded and timing sequence again evaluated. This iterative procedure was repeated until a satisfactory timing sequence was achieved. The condition for satisfactory timing was a particle displacement not exceeding 25% of the interrogation area. This ensured that the image capture rate was sufficient to record the particle displacement within any interrogation area. With a satisfactory timing sequence established, a set of 100 image pairs was then recorded. Using FLOW MANAGER's adaptive correlation scheme, the recorded image pairs were correlated to produce velocity vector fields. A 32×32 pixel interrogation window area and a relative peak validation of 1.2 were used to resolve the velocity vectors. To remove outliers from the velocity field, a moving-average filter, with a 3×3 neighborhood size, was used in the FLOW MANAGER. A temporally averaged velocity field of the 100 image sample size was then obtained using FLOW MANAGER's statistics scheme.

The flow field was divided into four image planes, each of which required a different camera and laser setup. They consisted of three horizontal and a single vertical image planes. The image plane orientations relative to the test section were shown in Fig. 3(*b*). The chosen coordinate system was also shown in the figure; the origin (0,0,0) was placed at the inlet of branch *C*. The negative *x* direction was chosen toward the curved test section surface, and the positive *z* direction was taken upward. A typical vertical plane setup was shown in Fig. 4(*a*). The vertical image plane was chosen to lie along the $y=0$ line and therefore passed through the branch center; the test section was also symmetrical about this line. The orientation and coordinate system relative to the vertical image plane was shown in Fig. 4(*b*). The velocity vector **V** was resolved into components in the *x* and *z* directions as $\mathbf{V}_x$ and $\mathbf{V}_z$, respectively.

A typical horizontal plane setup was shown in Fig. 5(*a*). The three horizontal image planes were achieved by traversing the light sheet in the vertical direction. The three horizontal planes were located just below the air-water interface at approximately $z=H_{\mathrm{OGE}}$, at the midplane at approximately $z=H_{\mathrm{OGE}}/2$, and just above the branch inlet at approximately $z=0$. The orientation and coordinate system relative to the horizontal image plane was shown in Fig. 5(*b*). The velocity vector **V** was resolved into radial and tangential directions relative to the branch center as $\mathbf{V}_r$ and $\mathbf{V}_t$, respectively. The radial velocity $\mathbf{V}_r$ was taken to be positive toward the branch center, and $\mathbf{V}_t$ was positive counterclockwise.

A test matrix of the experimental cases was presented in Table 1. The two fluids used were air and water. The water temperature was maintained constant by a cooling coil installed in the water tank. The air pressure was maintained at 206 kPa, and experiments were performed at room temperature. The discharge Froude number was determined from Eq. (2), knowing the fluid properties and the discharge mass flow rate.

2.5 Technical Challenges. Several technical challenges were met in order to produce results of the two-phase flow field. The majority were due to the various surfaces, such as test section walls and the air-water interface, which were present in the optical path of the camera. The surfaces created refractive distortions and bright reflections from interactions with the laser sheet, both of which caused losses in image quality. The refractive distortions were unavoidable since the test section was installed in the cylindrical cast clear acrylic viewing section to allow optical access to the flow field. However, due to the relatively large radius of curvature of the acrylic viewing section compared to the small field of view, distortions were not as significant as originally anticipated. A mirror was used to reflect the horizontal light sheet downward 90 deg to create a vertical light sheet. However, this was found to cause a loss of light sheet intensity and, consequently, image quality. It was evident that reflections on the various surfaces—which include the air-water interface and test section—significantly distorted the image quality. A masking method was adopted to reduce the reflections where possible. Masking was done by painting solid surfaces black. Painting surfaces black also improved the contrast of the illuminated particles within the field of view.

2.6 Uncertainty. All measurement devices were calibrated by the manufacturer as per component specifications. The maximum uncertainty in the calculation of the Froude number, where water was the working fluid, was found to be ±5%. The instrument uncertainty in measuring P_0 was ±0.83 kPa, and an acceptable

Downloaded 03 Jun 2010 to 171.66.16.156. Redistribution subject to ASME license or copyright; see http://www.asme.org/terms/Terms_Use.cfm

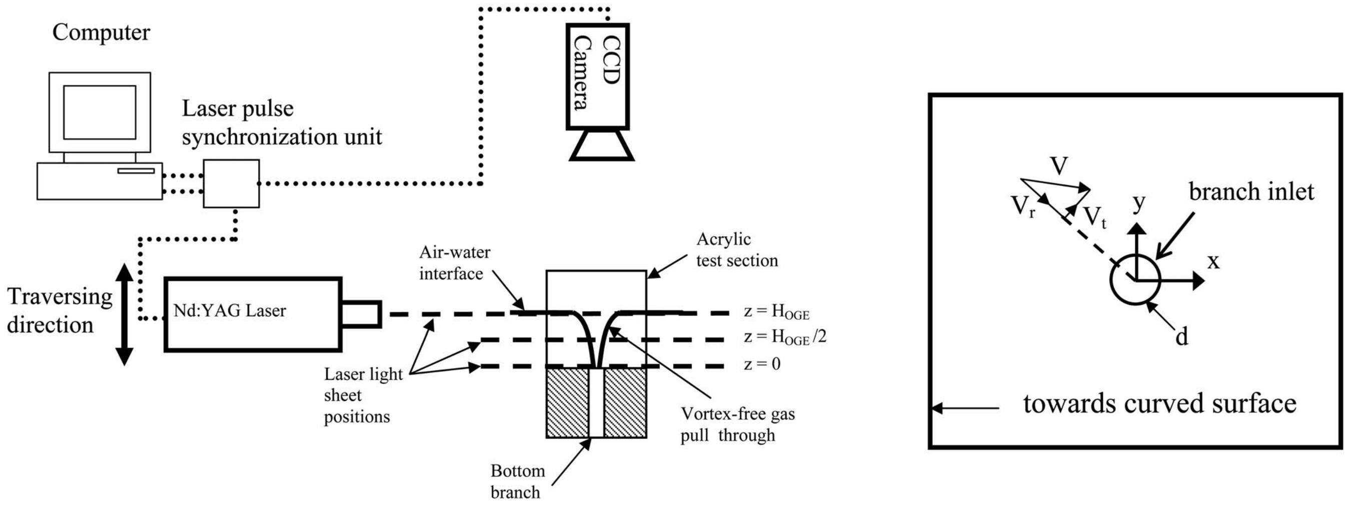

(*a*) (*b*)

Fig. 5 (*a*) Typical horizontal image plane setup using PIV and (*b*) its corresponding image plane and coordinate system

range for this parameter during experimentation was 206±6.8 kPa. The instrument uncertainty in measuring the height of water H in the reservoir was found to be ±0.165 mm H_2O. In Sec. 3.5, a detailed description of the velocity field validation was provided.

3 Results and Discussion

3.1 Critical Height. It was first necessary to determine the critical height at the onset of vortex-free gas entrainment in branch C. Secondly, a validation of the quarter-circular test section was provided through a comparison with Ref. [11]. Results from this validation were shown in Fig. 7; the dimensionless critical height H/d was presented as a function of the Froude number, as defined in Eq. (2). A comparison showed that the present results are in good agreement with Ref. [11]. The objective of this comparison was also to demonstrate any differences in the critical height due to the wall curvature above $H/d=4$, where the curved wall was replaced by a flat wall.

Two Froude numbers were selected to investigate the flow field using PIV. These were Fr=3.47 and 15.84 at $H/d=0.94$ and 1.81, respectively. Based on the selection of these two Froude numbers, the location of the investigation planes could be determined based on the critical height. The horizontal planes, with Fr=3.47, were just below the interface near $z/d=0.94$, at the midplane with $z/d=0.47$, and just above the branch inlet near $z/d=0$. The vertical coordinate z was nondimensionalized with the branch diameter d to be consistent with H/d. Similarly, for Fr=15.84, the horizontal planes were just below the interface at $z/d=1.81$, near the midplane at $z/d=0.905$, and just above the branch inlet near $z/d=0$. This information was also provided in Table 1.

Table 1 OGE test matrix using PIV

Fr_C	Plane orientation	Plane location	Description
3.47	Vertical $(x-z)$	$y/d=0$	Vertical
	Horizontal $(x-y)$	$z/d=0$	Bottom
		$z/d=0.47$	Midplane
		$z/d=0.94$	Interface
15.84	Vertical $(x-z)$	$y/d=0$	Vertical
	Horizontal $(x-y)$	$z/d=0$	Bottom
		$z/d=0.91$	Midplane
		$z/d=1.81$	Interface

3.2 Two-Phase Flow Field Visualization. A sample image of the flow field, at the onset of vortex-free gas entrainment, was presented in Fig. 6(*a*). The image was recorded using the PIV CCD camera during a measurement in a vertical plane. The gas tube extended from the interface into the discharging branch inlet. It was important that the gas tube was steadily entrained, with the liquid height remaining relatively constant, to be considered the vortex-free definition of OGE. The locations of the horizontal light sheet for image planes near the interface, midplane, and branch inlet were also shown in the figure. Examples of light sheet reflections off the various surfaces were also shown in the figure on the air-water interface and test section, and were shown to have caused bright spots in the image, resulting in a loss of image quality. An example of a PIV image captured in a horizontal plane was shown in Fig. 6(*b*). The illuminated particles were more easily visible in the horizontal plane images.

3.3 Two-Phase Liquid Velocity Field. The flow field measurements, at the onset of vortex-free gas entrainment in the bottom branch, were presented in Figs. 8 and 9. The results demonstrated the velocity fields in the water side of the two-phase flow field. The complex flow structure was divided into four two-dimensional planes. The four planes consist of a single vertical plane through the center of the branch and three horizontal planes located just below the interface, just above the branch inlet, and midway between the two planes. Throughout the text, the three horizontal planes were referred to by their vertical coordinate, z. The horizontal plane just below the interface was denoted by $z/d=H_{OGE}/d$, just above the branch inlet as $z/d=0$, and at the midplane as $z/d=H_{OGE}/2d$. The values of z/d were only estimates of the actual location of the horizontal plane due to the thickness of the laser light sheet, which was estimated to be between 2 and 3 mm. The results were presented for a nonsimultaneous measurement of the individual planes; therefore, the out of plane motions between the three horizontal planes were only estimated by the vertical plane results. The horizontal plane velocity fields were described in two separate contour plots, with the vec-

Downloaded 03 Jun 2010 to 171.66.16.156. Redistribution subject to ASME license or copyright; see http://www.asme.org/terms/Terms_Use.cfm

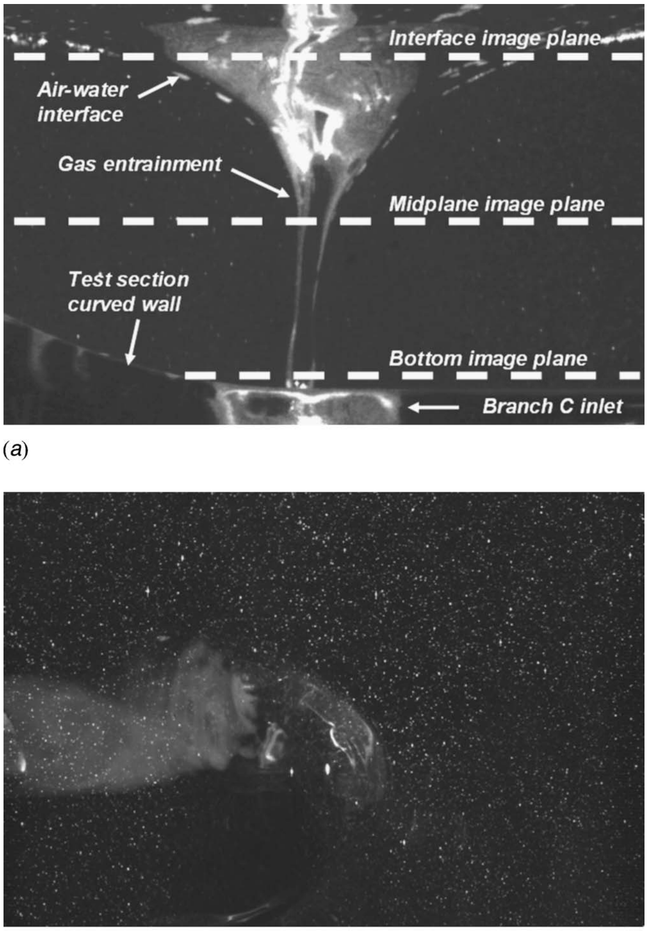

(*a*)

(*b*)

Fig. 6 Gas entrainment in a single discharging bottom branch, PIV image in (*a*) vertical and (*b*) horizontal planes

tor field superimposed on contours of the velocity magnitude. Similarly, the vertical plane vector field was also shown superimposed on contours of the velocity magnitude. The contour plots described the velocity field magnitude in terms of the radial $\mathbf{V}_r$ and tangential $\mathbf{V}_t$ components in the horizontal planes and in terms of the axial $\mathbf{V}_z$ in the vertical plane. Presenting the velocity fields using a cylindrical coordinate system was found to be more conducive to describing the flow. In all the velocity fields presented, both vertical and horizontal planes, the curved test section wall was toward the negative x direction.

The velocity fields obtained in the three horizontal planes, with $z/d=0.94$, $z/d=0.47$, and $z/d=0$, and the vertical plane, with Fr $=3.47$, were presented in Fig. 8. Presented in Fig. 9 were the velocity fields obtained in the three horizontal planes, with $z/d=1.81$, $z/d=0.91$, and $z/d=0$, and the vertical plane, with Fr $=15.84$. Although the flow fields were captured at separate instants in time, due to the relatively stable nature of vortex-free gas entrainment, they yield a fair assessment of what could be expected from simultaneous measurements. Stability refers to the gas phase entraining continuously into the discharging branch, with a smooth gas-liquid interface and negligible variations in liquid height. Comparing the superimposed vector fields in the horizontal planes, it was apparent that the flow field was nearly symmetric about $y=0$. Overall, from the vector field, it seemed that when x was positive, the flow was directed almost completely radially toward the branch center at (0,0). When x was positive, no effects of the curved test section wall were present. However, when x was negative, the presence of the curved wall was shown on the flow field. The flow was required to negotiate the wall by flowing nearly parallel with it and then curling away from it toward the branch center at (0,0). This curling of the flow is nearly symmetrical about $y=0$, with both positive and negative values of tangential velocity on either side of the line. A comparison between the relative magnitudes of the radial and tangential components suggested that the flow field was dominated by the radial component. A higher radial velocity magnitude was found when x was positive, where no wall was present, compared to when x was negative, where the influence of the wall caused a decrease in magnitude. The influence of the wall caused a larger tangential velocity magnitude when x was negative. These features were similar for the three investigated horizontal planes. Interestingly, an increase in the discharge Froude number seemed to impact both the magnitudes of radial and axial velocities; however, minor effects were found on the tangential velocity magnitude. In Fig. 9(*a*), a portion of the data was omitted since it was found to be of poor quality. This was caused by the gas-liquid interface curvature, which resulted in a portion of the flow field being out of the image plane. The vertical plane flow field provided some additional insight into the out of plane motion, not captured in the horizontal planes. It was apparent from Figs. 8(*g*) and 9(*g*) that the axial component of the velocity was higher as the center of the branch was approached. Interestingly, the effect of the curved wall, where x was negative, indicated a slightly higher axial velocity. This implies that the solid wall helped guide the flow from a horizontal to a vertical direction.

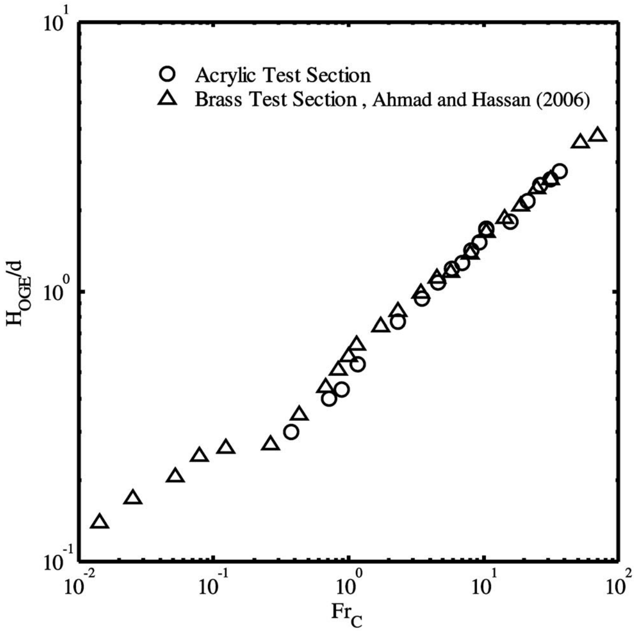

Fig. 7 The critical height at the OGE using the current acrylic test section compared with Ahmad and Hassan [11]

3.4 Averaged Velocity Profiles.

Although the contour plots are useful, a meaningful comparison between them is somewhat difficult to achieve. To aid in the comparison of the velocity fields for the two Froude numbers investigated, the average velocity along the circumference of a circle, centered at $x=0$, $y=0$ with radius r, was calculated for each horizontal vector field. These calculations were performed using a code written in MATLAB. Since the vector fields themselves are placed on a rectangular grid due to the way the CCD camera stores the image, an algorithm was required to search the image for a vector at a given radius. Any returned valid vectors were stored, and a running count of the number of valid vectors at that radius was also stored. The average radial and tangential velocity profiles were determined. Since it was observed from the contour plots that the radial velocity was

Downloaded 03 Jun 2010 to 171.66.16.156. Redistribution subject to ASME license or copyright; see http://www.asme.org/terms/Terms_Use.cfm

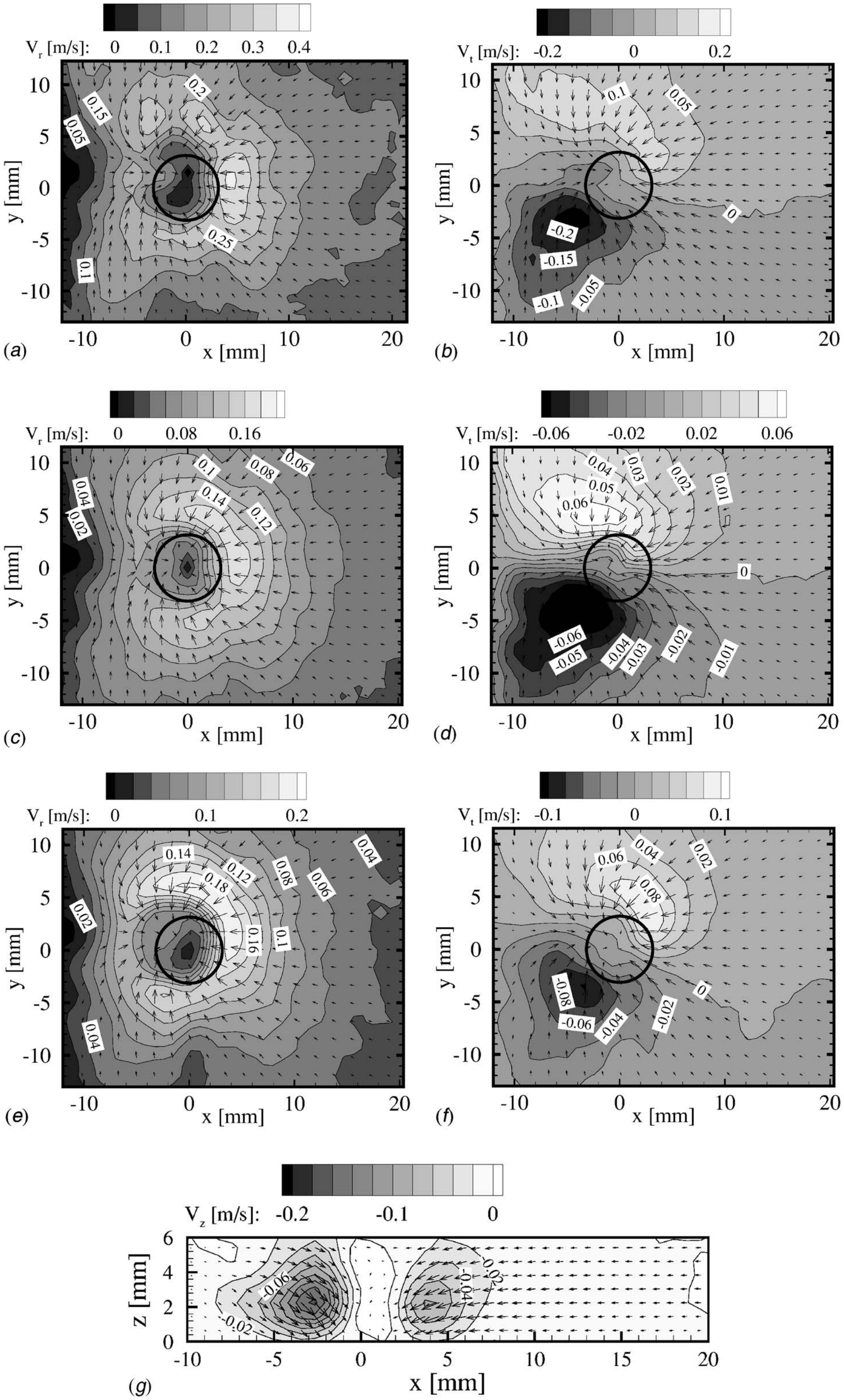

Fig. 8 Velocity field with $Fr_C=3.47$ in horizontal planes at $z/d=0.94$ for (*a*) V_r and (*b*) V_t, at $z/d=0.47$ for (*c*) V_r and (*d*) V_t, and at $z/d=0$ for (*e*) V_r and (*f*) V_t, and a vertical plane at (*g*) $y/d=0$ for V_z

uniquely positive, the average value was determined by adding the valid vectors and dividing by their total number. The tangential velocity was both positive and negative on either side of $y=0$. The summation of these values yielded an average of near 0 m/s at any given r. To address this, the summation of the absolute value of the tangential velocity was used instead in the calculation of the average value. The tangential velocity profiles were therefore representative of the magnitude; however, the direction should be extracted from the vector field. For the vertical plane vector fields, a search algorithm was also used to find the corresponding vertical velocity in each horizontal plane.

The velocity profiles of the Fr=3.47 and 15.84 data sets were

Downloaded 03 Jun 2010 to 171.66.16.156. Redistribution subject to ASME license or copyright; see http://www.asme.org/terms/Terms_Use.cfm

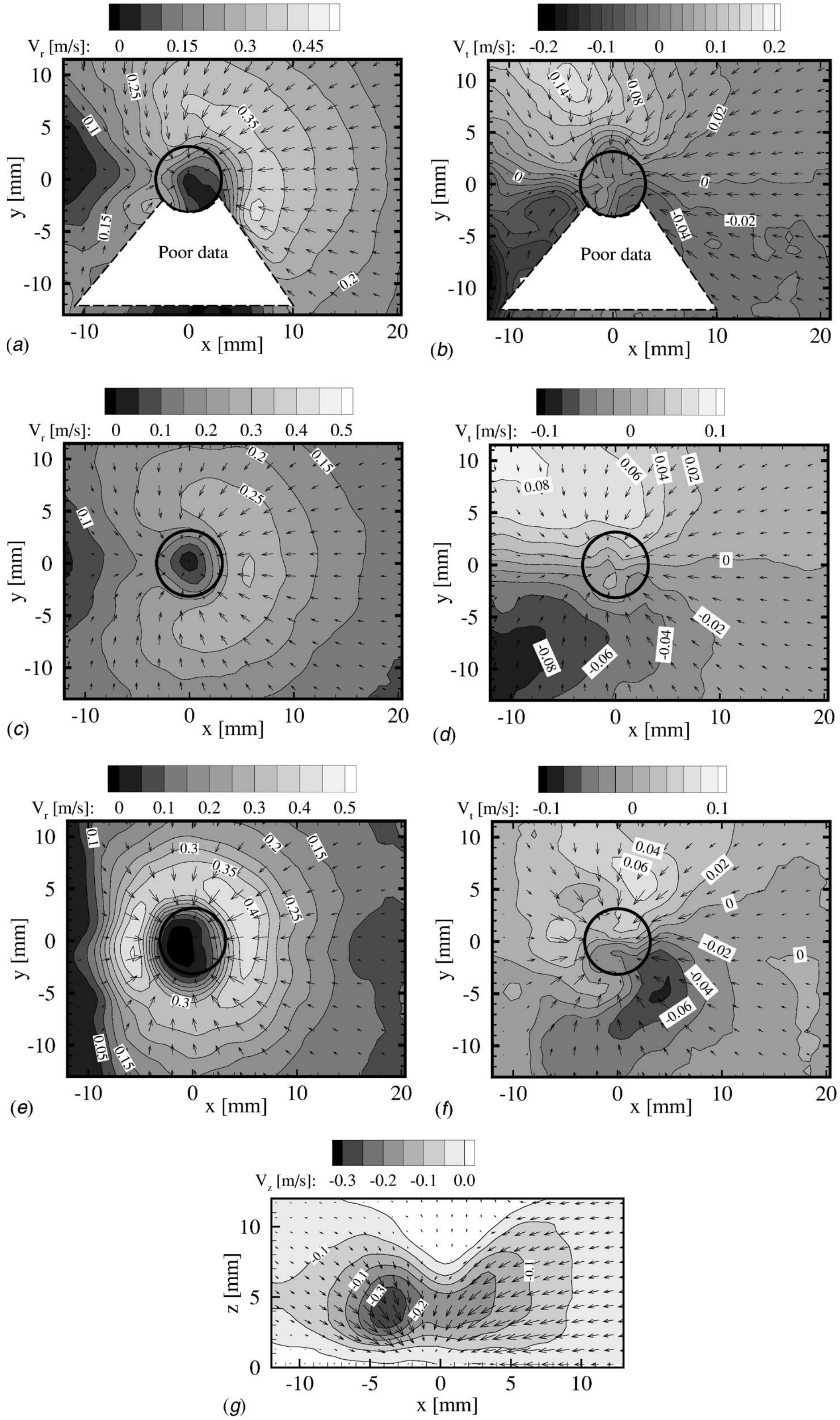

Fig. 9 Velocity field with $Fr_C=15.84$ in horizontal planes at $z/d=1.81$ for (*a*) V_r and (*b*) V_t, at $z/d=0.91$ for (*c*) V_r and (*d*) V_t, and at $z/d=0$ for (*e*) V_r and (*f*) V_t, and a vertical plane at (*g*) $y/d=0$ for V_z

shown in Figs. 10 and 11, respectively. By comparing the two figures, a similarity in the velocity profile trends was found. Comparisons showed that the radial and tangential velocities tended toward 0 m/s as r approached 0 m. As r increased, the velocity increased almost linearly to a peak value near $r=0.006$ m. The branch diameter of 0.00635 m shared a similarity to the peak

Downloaded 03 Jun 2010 to 171.66.16.156. Redistribution subject to ASME license or copyright; see http://www.asme.org/terms/Terms_Use.cfm

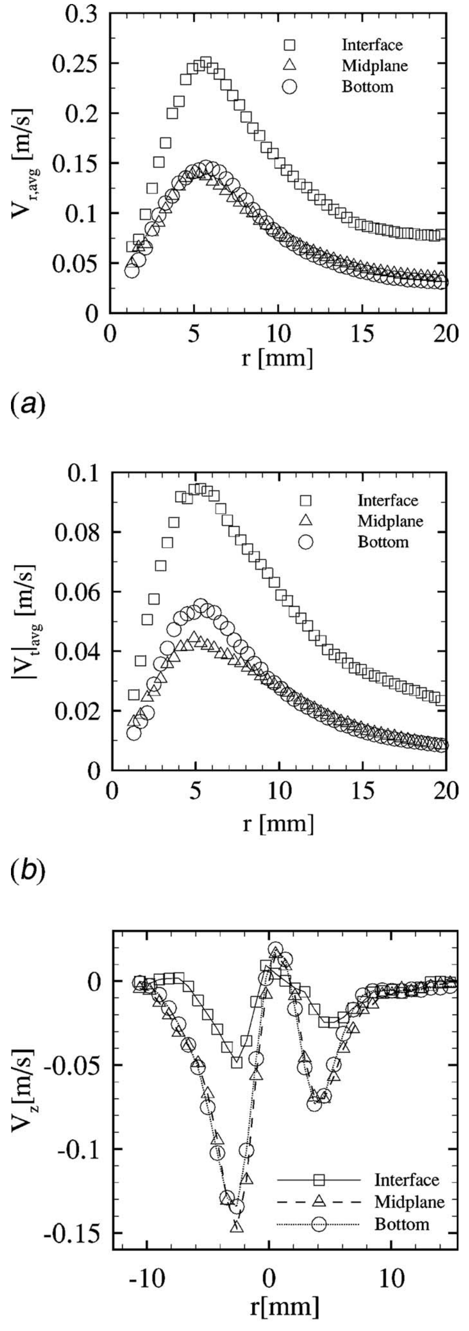

(*a*)

(*b*)

(*c*)

Fig. 10 Average values of (*a*) radial (V_r), (*b*) tangential (V_t) and (*c*) axial (V_z) velocity at three selected horizontal planes with Froude=3.47

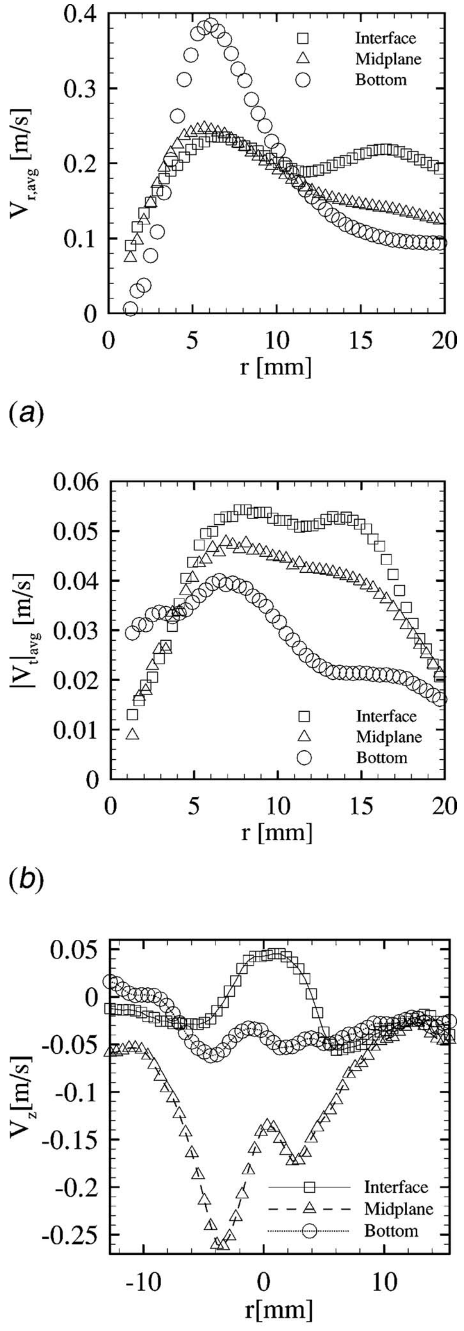

(*a*)

(*b*)

(*c*)

Fig. 11 Average values of (*a*) radial (V_r), (*b*) tangential (V_t) and (*c*) axial (V_z) velocity at three selected horizontal planes with Froude=15.84

value of $r=0.006$ m. It implied that the velocity magnitude reached a peak at a distance from the branch center equal to the branch diameter. As r was increased beyond the peak value, there was a smooth decrease in the velocity that seemed to be inversely proportional to r.

An interesting observation was found comparing the two Froude number results in the location of the highest radial velocity. In the case of Fr=3.47, the radial velocity was clearly highest in the plane near the interface, while with Fr=15.84, the radial velocity was highest in the plane near the branch inlet. One possibility for this observed difference was the size of the gas cone that resulted in a reduction of liquid flow area at the branch inlet. With an increase in critical height, the gas cone profile was stretched thinner at the branch inlet, and at a lower critical height, the profile was wider at the branch inlet. This difference in the gas cone profile caused a reduction in the area that the liquid phase had to flow into the branch. The reduction of flow area at the branch inlet caused an increased liquid flow resistance, which made the liquid closer to the interface to travel faster for mass conservation. Since the critical height at Fr=3.47 was lower than that at Fr=15.84, its gas cone was wider at the inlet, and the plane of highest radial velocity was nearest the interface, which was sensible based on the above assertions.

The tangential velocity profile showed a trend similar to that of the radial velocity; however, the magnitude was between two and

Downloaded 03 Jun 2010 to 171.66.16.156. Redistribution subject to ASME license or copyright; see http://www.asme.org/terms/Terms_Use.cfm

ten times smaller than the radial velocity. The tangential profiles were presented as an average of the absolute value; using the actual velocity resulted in an approximately zero average of tangential velocity at any r. If this was used to find the circulation at any r, it would show a nearly zero result. This had strong implications on the validity of the vortex-free assumption in gas entrainment. A vortex flow would have a higher contribution of tangential velocity, and a nonzero circulation would result. This was not the case here, and it would be reasonable to say that the flow field was vortex-free based on a near zero circulation.

The axial velocity $\mathbf{V}_z$ was also shown in these two figures. Interestingly, it was not uniquely negative—directed toward the branch inlet at (0,0,0)—but did show a significant decrease, and sometimes positive velocity, between $-0.006 < x < 0.006$ m. The reason for this could be due to the gas core extending through the liquid velocity field. The peak in the vertical velocity occurred near the horizontal midplane, and as the distance from the branch was increased in all cases, the velocity tended toward zero.

3.5 Particle Image Velocimetry Data Validation. In order to ensure that the velocity fields presented were reasonable, a validation was required to provide an estimate of their uncertainty. The method used was to perform a mass balance on a control volume to ensure that continuity was satisfied. Since the flow field was seen to be increasingly horizontal, away from the branch center, it was asserted that the horizontal velocity fields could be used with an appropriately sized control volume. A cylindrical control volume was selected, whose base was centered at the branch inlet (0,0,0) and extended laterally in the positive z direction until the air-water interface. The size of the control volume was, therefore, constrained by its radius r. Based on the previous observation, when $r > 0.006$ m, the flow field vertical velocity tended toward zero; the control volume radius should be equal to, or greater than, this value in order for the approach to be meaningful. With the control volume size, orientation, and origin established, the remaining requirement was to find the value of mass flow rate through each of the three control surfaces. The mass flow rate of the control surface located at the branch inlet was known by the measured value from the flow meter. The control surface at the interface was assumed to have no influx of liquid, a reasonable assumption based on the vertical velocity profiles. Last, the mass flow rate through the lateral control surface was found using an averaged value of the radial velocity at the three horizontal planes. The tangential and vertical velocities played no role in the mass flow entering the lateral surface since, by definition, the flow entering a control surface should be perpendicular to it. The averaged velocities, for a particular control volume radius r, in each horizontal plane were then also averaged to find a total average velocity over the entire lateral surface. The mass flow entering the surface was then calculated by multiplying the lateral surface area, average velocity, and density of water. Using this value, a comparison of the mass flow leaving the control volume and the known value measured using the flow meter was done. A code was written using MATLAB to do the calculations for a range of control volume radius. The results were shown in Fig. 12. The results were presented by comparing the Froude number calculated using the mass flow rate from the flow meter, as the expected or true value, and that found entering the lateral surface of the control volume. The Froude number was used instead of the average velocity or flow rate since an estimation of its uncertainty was previously provided. The two investigated values of Froude number were shown in the figure. To demonstrate the effect of the wall on the average value of radial velocity, the results were also calculated using the average velocity on the wall side, when x was uniquely negative, or the no wall side, when x was positive. From these figures, the difference in Froude number tended from −100, with $r=0$, which was expected since the radial velocity was small compared to the vertical component, and increased almost asymptotically with r. With a sufficiently sized control volume, $r > 0.006$ m, the difference in Froude number was seen to be in the range of approximately 10–25%. The near wall difference was always less than the average value, and, conversely, the no wall side was always greater. This demonstrated that the average radial velocity decreased on the wall side when x was negative.

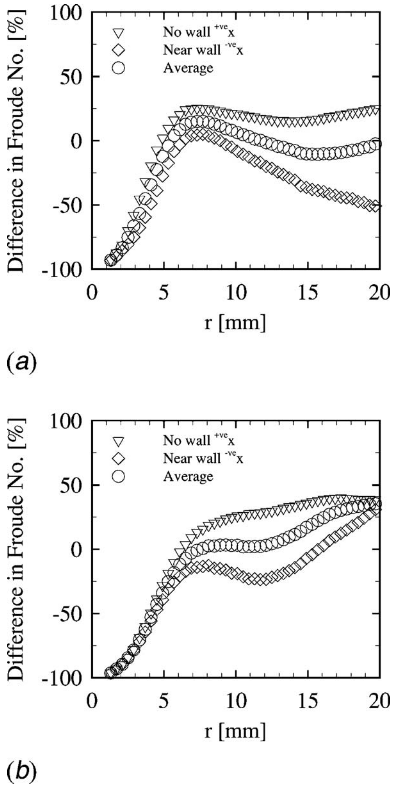

Fig. 12 Validation of PIV data using continuity and cylindrical control volume with (*a*) Fr=3.47 and (*b*) Fr=15.85

3.6 Comments on Using Particle Image Velocimetry in Two-Phase Measurements. To complete the discussion of the complex three-dimensional liquid flow field obtained using PIV, a few improvements can be made to the current experimental setup. First, due to the three-dimensional nature of the flow field, the three-dimensional capabilities of the PIV system should be incorporated. Second, steps should be taken to reduce the light sheet reflections to improve the image quality. Modifications to the experimental facility could also improve the image quality by reducing the effect of the curved acrylic viewing section through refractive index matching. In future studies, it would be useful if more than three horizontal image planes were used to describe the entire flow field. This would greatly improve both the description of the flow field as well as the validation if a similar control volume approach is used. In more complex cases of multiple discharges, the PIV technique will certainly be applicable; however, care should be taken to address the technical issues associated with loss of image quality on gas-liquid interfaces.

4 Conclusion

The experiments performed to record the liquid velocity field, at the OGE due to the vortex-free mechanism in a bottom discharging branch, presented novel information of the flow structure in four discrete planes. The planes studied were a single vertical plane passing through the center of the branch and three horizontal planes at selected liquid heights. The heights selected were just above the branch inlet, just below the branch interface, and the midplane. The results demonstrated that the flow field in the horizontal planes was dominated by the radial component. The assertion that previous researchers made in developing both empirical

Downloaded 03 Jun 2010 to 171.66.16.156. Redistribution subject to ASME license or copyright; see http://www.asme.org/terms/Terms_Use.cfm

and analytical models of a vortex-free flow field was confirmed through the discussion of the tangential velocity component and expected near zero circulation. The results also demonstrated that due to the complex three-dimensional nature of the flow field and the two-dimensional measurement technique, some improvements to the system could be done to address the image quality.

4.1 Future Directions. Effects of multiple discharges on the liquid flow structure using the PIV should be investigated. Simultaneous liquid and gas velocity measurements of the two-phase flow field could be performed and could be explored using PIV. Investigations beyond the onset domain could be pursued to include simultaneous two-phase, quality, and velocity field measurements. An investigation that includes cross-flow and stratified-wavy flow using PIV could demonstrate the effects of jet impingement on the gas-liquid interface, which may arise in certain practical scenarios.

Acknowledgment

The financial support given by the Natural Sciences and Engineering Research Council of Canada (NSERC) and the Canada Foundation for Innovation (CFI) in the undertaking of this research program is greatly appreciated.

References

[1] Zuber, N., 1980, "Problems in Modeling of Small Break LOCA," Nuclear Regulatory Commission, Report No. NUREG-0724.

[2] Reimann, J., and Khan, M., 1984, "Flow Through a Small Break at the Bottom of a Large Pipe With Stratified Flow," Nucl. Sci. Eng., **88**, pp. 297–310.

[3] Smoglie, C., and Reimann, J., 1986, "Two-Phase Flow Through Small Branches in a Horizontal Pipe With Stratified Flow," Int. J. Multiphase Flow, **12**, pp. 609–625.

[4] Schrock, V. E., Revankar, S. T., Mannheimer, R., Wang, C. H., and Jia, D., 1986, "Steam-Water Critical Flow Through Small Pipes From Stratified Upstream Regions," *Proceedings of the Eighth International Heat Transfer Conference*, San Francisco, CA, Vol. 5, pp. 2307–2311.

[5] Micaelli, J. C., and Memponteil, A., 1989, "Two-Phase Flow Behavior in a Tee-Junction: The CATHARE Model," *Proceedings of the Fourth International Topical Meeting on Nuclear Reactor Thermal-Hydraulics*, Karlsruhe, Germany, Vol. 2, pp. 1024–1030.

[6] Yonomoto, T., and Tasaka, K., 1988, "New Theoretical Model for Two-phase Flow Discharged From Stratified Two-Phase Region Through Small Break," J. Nucl. Sci. Technol., **25**, pp. 441–455.

[7] Parrott, S. D., Soliman, H. M., Sims, G. E., and Krishnan, V. S., 1991, "Experiments on the Onset of Gas Pull-Through During Dual Discharge From a Reservoir," Int. J. Multiphase Flow, **17**, pp. 119–129.

[8] Hassan, I. G., Soliman, H. M., Sims, G. E., and Kowalski, J. E., 1996, "Experimental Investigation of the Two-Phase Discharge From a Stratified Region Through Two Side Branches Oriented Horizontally," Exp. Therm. Fluid Sci., **13**, pp. 117–128.

[9] Hassan, I. G., Soliman, H. M., Sims, G. E., and Kowalski, J. E., 1996, "Discharge From a Smooth Stratified Two-Phase Region Through Two Horizontal Side Branches Located in the Same Vertical Plane," Int. J. Multiphase Flow, **22**, pp. 1123–1142.

[10] Maier, M. R., Soliman, H. M., Sims, and G. E., 2001, "Onsets of Entrainment During Dual Discharge From a Stratified Two-Phase Region Through Horizontal Branches With Centerlines Falling in an Inclined Plane: Part 2—Experiments on Gas and Liquid Entrainment," Int. J. Multiphase Flow, **27**, pp. 1029–1049.

[11] Ahmad, T., and Hassan, I., 2006, "Experimental Investigation on the Onset of Gas Entrainment From a Stratified Two-Phase Region Through Multiple Branches Mounted on a Curved Surface," ASME J. Fluids Eng., **128**, pp. 726–733.

[12] Ahmed, M., Hassan, I., and Esmail, N., 2003, "Modeling the Onset of Gas Entrainment Through a Finite-Side Branch," ASME J. Fluids Eng., **125**, pp. 902–909.

[13] Hassan, I. G., Soliman, H. M., Sims, G. E., and Kowalski, J. E., 1997, "Single and Multiple Discharge From a Stratified Two-Phase Region Through Small Branches," Nucl. Eng. Des., **176**, pp. 233–245.

Downloaded 03 Jun 2010 to 171.66.16.156. Redistribution subject to ASME license or copyright; see http://www.asme.org/terms/Terms_Use.cfm

Flow Regimes and Drag Characteristics of Yawed Elliptical Cavities With Varying Depth

Thomas Hering
Research Engineer
e-mail: thering@uwo.ca

Eric Savory
Associate Professor
e-mail: esavory@eng.uwo.ca

Department of Mechanical and Materials Engineering,
The University of Western Ontario,
Spencer Engineering Building,
London, ON, N6A 5B8 Canada

The effect of yaw angle and cavity depth on the resulting flow field of cavities with elliptical planform areas embedded in a low velocity turbulent boundary layer was investigated experimentally. A 2:1 elliptical cavity with depth to minor axis ratios ranging from 0.1 to 1.0 was tested in a wind tunnel facility. Surface pressure measurements and wake velocity measurements, using hot-wire anemometry, were conducted to examine the resulting flow regimes. The results indicated several different flow regimes for the different yaw angle and cavity depth configurations. Cellular structures were observed when the minor axis was aligned with the streamwise direction. Yawing the cavity with respect to the streamwise direction resulted in a highly asymmetric flow regime. This flow regime was also associated with high drag for certain cavity depth configurations. A nominally two-dimensional flow regime was observed for large yaw angles, when the major axis of the cavity was aligned with the streamwise direction. The yaw angle had only a minor effect on the flow regimes associated with the shallowest and deepest cavities examined. A strong resemblance was found between the flow regimes associated with elliptical and rectangular cavities for similar yaw and depth configurations. This similarity was also observed in the lift and drag coefficients for the different yaw angles and cavity depths. This indicated that the wall radius of curvature of elliptical cavities has a negligible effect on the resulting flow regimes when compared to rectangular cavities. [DOI: 10.1115/1.2801365]

1 Introduction

Cavities are a special type of surface irregularity, which may arise from manufacturing and assembly limitations on aerodynamic vehicles. Some examples include landing gear wells, weapon bays, flap recesses, rivet depressions, and recessed windows on airplanes [1]. In the case of depressions or cavities, simple geometries have been investigated to examine the effects of different cavity dimensions on the resulting cavity drag. Highly complex flow regimes are associated with simple cavity geometries, which may play a role in creating high drag flow regimes.

Charwat et al. [2] were the first to introduce the terms "closed" and "open" cavity flow to categorize flow regimes of idealized two-dimensional cavities. The closed term refers to a shallow cavity where the shear layer separates at the leading edge, impinges on the cavity base, and then separates again to pass over the downstream cavity sidewall. As the cavity depth is increased, an open flow regime occurs. In this flow pattern, the shear layer bridges the cavity and causes a captive vortical structure to form along the span of the cavity [3]. The trapped vortex is driven by the separated shear layer spanning the cavity, as mentioned by Roshko [3] and Ukeiley and Murray [4]. A transitional region exists between the two different flow types.

Although these flow regimes were introduced to explain idealized two-dimensional cavity flow, three-dimensional effects have been found to exist in large aspect ratio cavities far from the cavity sidewall. Maull and East [5] were the first to identify such three dimensionalities in large aspect ratio rectangular cavities. Maull and East [5] found that the separation line near the upstream wall on the cavity base appeared to form a "wave like" pattern as opposed to a straight line, creating cellular structures along the span of the cavity. The number of cells present was dependent on the aspect ratio and cavity depth. A later study by Kistler and Tan [6] showed that the flow within these cellular structures affects the vertical location of the shear layer on the downstream cavity wall, creating local in- and outflows from the cavity. Kistler and Tan [6] found that the shear layer deflects upward near a cell boundary and downward at a cell centerline.

The effects of yawing a cavity with respect to the streamwise direction has received little attention compared to the drag of different aspect ratio cavities aligned with the flow. The effects of aspect ratio have led to the identification of high drag configurations. Square and circular cavities have been known to show a peak in drag at certain cavity depths, which are not seen for aligned rectangular and elliptical cavities [1,7].

High drag regimes have also been found for yawed rectangular [8,9] and elliptical [10] cavities at certain depths and aspect ratios. The flow regimes of yawed rectangular and elliptical cavities contain a captive vortex aligned with the yawed major axis of the cavity. Czech [8] found that for yawed high aspect ratio rectangular cavities, flow is entrained near the upstream cavity end. This results in a vortical structure of helical shape along the primary axis of the rectangular cavity. An outflow region exists in the downstream region of the cavity, which ejects the entrained flow. Czech [8] found this structure to be dependent on yaw angle, aspect ratio, and cavity depth. Similar flow patterns have also been found in elliptical cavities [10], but due to the limited aspect ratios and depths studied, the effects of depth and yaw angle are not fully understood. However, these similarities do suggest a similar structure forming inside elliptical cavities. Thus, the radius of curvature seems to have negligible effects on the resulting flow regimes for elliptical cavities when compared to rectangular cavities.

Although some similarities have been found between rectangu-

Contributed by the Fluids Engineering Division of ASME for publication in the Journal of Fluids Engineering. Manuscript received January 20, 2007; final manuscript received June 13, 2007. Review conducted by Phillip M. Ligrani.

Copyright © 2007 by ASME

Downloaded 03 Jun 2010 to 171.66.16.156. Redistribution subject to ASME license or copyright; see http://www.asme.org/terms/Terms_Use.cfm

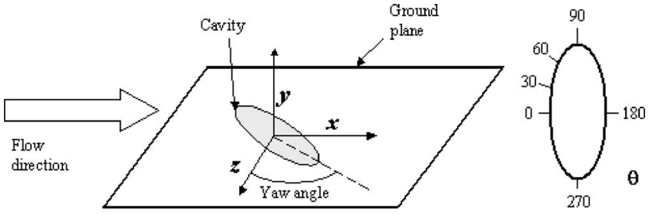

Fig. 1 Experimental coordinate system and θ variable

lar and elliptical cavity flow regimes, the effect of the radius of curvature is not fully understood as only limited number of yaw angles and cavity depths have been investigated so far. One aspect of the current work is to identify the flow regimes associated with elliptical cavities, as well as the effects of altering the flow direction on the resulting lift and drag of elliptical cavities.

2 Experimental Approach

2.1 Wind Tunnel Facility and Model Dimensions. The experiments were carried out in a dual fan closed loop wind tunnel at the Boundary Layer Wind Tunnel Laboratory at the University of Western Ontario. The tunnel working section dimensions were 6500 mm length × 611 mm width × 214 mm height. Due to limited access to the floor of wind tunnel working section, the elliptical cavity was mounted on the roof of the tunnel. A transformation was applied to display the results as if the cavity was originally embedded in the tunnel floor. A right handed coordinate system was used for the transformed results. The origin was located at the center of the cavity, as seen in Fig. 1.

The 2:1 elliptical cavity model was machined from acrylic with its minor axis equal to 53.8 mm. The minor axis length D was used as the reference length scale. The model contained a movable base to examine the effects of cavity depth on the resulting flow field. The cavity was mounted on a turntable made of aluminum, which allowed the yaw angle to be altered.

Pressure taps were placed on one side of the cavity model and turntable, which were then rotated by 180 deg in order to capture the entire pressure field during the course of the experiments. The pressure taps had an inner diameter of 0.8 mm and were concentrated in regions of expected high pressure gradients. The sidewall contained eight rows of pressure taps, spaced approximately the same circumferential distance apart. Due to manufacturing constraints, the first row of taps on the sidewall was placed on an angle, 0.8 mm from the cavity rim along the vertical direction.

A wide range of yaw angles and cavity depths was examined. The yaw angle was defined as yaw 0 deg when the minor axis was aligned with the streamwise direction. The yaw angle increased as the cavity was rotated counterclockwise until the major axis was aligned with the freestream direction (yaw 90 deg), seen in Fig. 1. Mean surface pressure measurements were taken for depth to length (h/D) ratios of 0.1, 0.2, 0.35, 0.5, 0.7, and 1.0 for all yaw angles ranging from yaw 0 deg to yaw 90 deg in 15 deg intervals. Due to time constraints, only the wake measurements for h/D ratios of 0.2, 0.5, and 0.7 with yaw angles of 0 deg, 45 deg, and 90 deg were undertaken.

2.2 Experimental Conditions. The approaching turbulent boundary layer parameters are given in Table 1, which are based on a freestream velocity of 27 m/s used throughout all the experiments. The freestream velocity varied by ±1.5% and the freestream rms turbulence intensity was approximately 1.8% across the span of the tunnel. The Reynolds number based on the ellipse minor axis length and freestream velocity was equal to 9.07×10^4.

2.3 Pressure Measurements. Mean pressure measurements were completed using 13 Honeywell DC001NDR4 ultralow differential pressure transducers with a range of ±1 in. H_2O. The pressure transducers were sampled by a National Instruments PCI-6052E data acquisition card at 500 Hz for 30 s time periods and were calibrated each day with a liquid manometer. The 13 transducers were rotated through all the pressure taps on the cavity model. A pitot-static tube placed in the freestream was used to measure the reference dynamic and static pressures used in the pressure coefficient calculations. The accuracy of the measurement setup was estimated to be $\pm 0.0034 C_p$.

Pressure coefficient contours were created for the measured cavity surfaces and surrounding ground plane. A new variable θ was introduced, which represented a length along the circumference of the ellipse ranging from 0 to 360, seen in Fig. 1. The cavity sidewall was "unwrapped" with the most upstream point located at $\theta=0$ and the furthest downstream point located at $\theta=180$. The variable θ increased in a clockwise direction, when looking down onto the cavity on the tunnel floor. For yawed cavities, the location of $\theta=0$ and 180 was considered to be the intersection of the upstream and downstream cavity edges with the streamwise axis through the center of the cavity, respectively. Pressure coefficients were extrapolated on the sidewall to the cavity rim and cavity depth, using a second order polynomial surface extrapolation scheme. The extrapolated data were then added to the base to show the continuous pressure variation in that region.

The drag coefficient, based on the planform area of the cavity, was computed by integrating the surface pressure coefficients, obtained from the measured data, on the cavity sidewall and resolving the resulting force coefficients in the streamwise direction. The friction drag of the cavity walls and base were not included in the drag coefficient since Roshko [3] found them to be two orders of magnitude lower than the pressure drag coefficient. The net drag coefficient (ΔC_D) due to the presence of the cavity was determined by subtracting the ground plane skin friction coefficient from the total drag coefficient. The lift coefficient was calculated in a similar manner to the drag and was also based on the planform area of the cavity. The lift coefficient of the ground plane was subtracted from the total lift to determine a net lift coefficient (ΔC_L) due to the presence of the cavity. The errors associated with the net lift and drag coefficients were ±0.0031 and ±0.0035, respectively.

2.4 Velocity Measurements. Crossed hot-wire anemometry was used to examine the cavity wake velocities. The miniature constant temperature anemometry system from Dantec Dynamics, MiniCTA 54T30, was connected to a Dantec Dynamics 55H25 straight probe holder, which held a 55P61 cross wire probe. The platinum plated tungsten wires were 5 μm in diameter and 1.25 mm in length. A 1 mm gap separated the two wires on the tip of the cross wire probe. With the use of a two axis traverse system, accuracy of ±0.2 mm in both directions, velocity measurements were completed over a plane perpendicular to the streamwise direction. In the spanwise direction, 15 evenly spaced data points were taken ranging from +2 D to −2 D, referenced from

Table 1 Boundary layer parameters at a freestream velocity of 27 m/s

Boundary layer parameter	δ (mm)	δ_* (mm)	δ_θ (mm)	μ_* (m/s)	c_f	H
Value	57.8	7.8	5.7	0.981	0.0026	1.37
Uncertainty (±)	4.9	0.8	0.6	0.021	0.0002	0.20

Downloaded 03 Jun 2010 to 171.66.16.156. Redistribution subject to ASME license or copyright; see http://www.asme.org/terms/Terms_Use.cfm

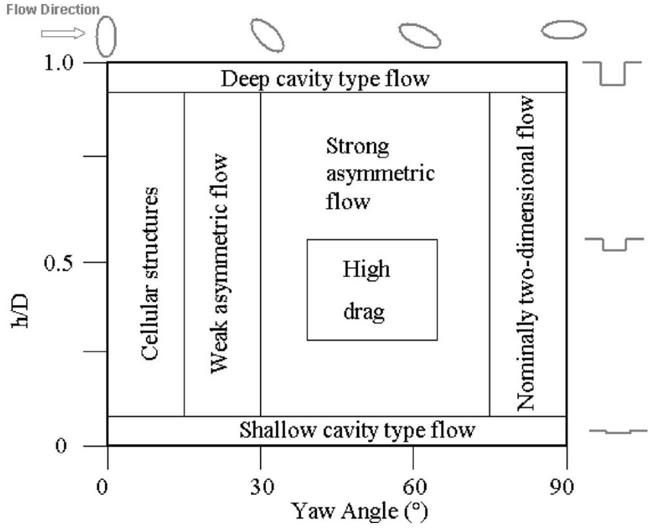

Fig. 2 Resulting flow regimes of yawed elliptical cavities

the cavity center. Seven evenly spaced data points ranging from 0.07 D to 0.75 D from the ground plane were taken in the vertical direction. Two sets of wake velocities were completed, one at the furthest downstream cavity lip and one at 2.6 D downstream of the cavity center.

The hot-wire system was sampled at 5000 Hz for 30 s at each grid point with a National Instruments PCI-6071E card. A pitot-static tube, located at the same location as in the pressure measurements, was connected to a Honeywell DC002NDR4 pressure transducer, which was used to monitor the dynamic pressure in the freestream. A mercury thermometer was used to temperature correct the data obtained from the hot wires, although the temperature fluctuations were less than ±1 °C throughout the course of each wake velocity measurement. To examine the effect of the cavity, the velocity field without the cavity in place was subtracted from the wake velocity field containing the cavity. This was also necessary as the velocity defect was small compared to the approaching undisturbed flow. A no slip boundary condition was applied to the ground plane in the velocity contour plots. The hot-wire setup was calibrated in situ before each experiment and the error associated with the hot-wire measurements was estimated to be ±0.34 m/s.

3 Results and Discussion

3.1 Yawed Elliptical Cavity Flow Regimes. Mean surface pressure contour plots were created to examine the key features of the flow field. Shear layer impingement and separation can be identified by high and low pressure regions, respectively [11]. It has been shown that a captive vortex, a key characteristic of open cavity flow [3], may be properly identified by an approximately circular low pressure region [12]. The minimum pressure at the center of the circular pressure pattern corresponds to the vortex center of rotation, which is followed by increasing pressure in the radial direction.

The resulting flow regimes were grouped according to similar trends observed in the mean surface pressure and wake velocity measurements. These included location of shear layer impingement on the sidewall, existence of a captive vortex, location and size of the velocity defect in the streamwise direction, lift and drag coefficients, and the existence of asymmetric flow. According to these observations, the different cavity configurations were grouped into corresponding flow regimes by approximate boundaries, as shown in Fig. 2. The resulting flow regimes will be further discussed in the following sections.

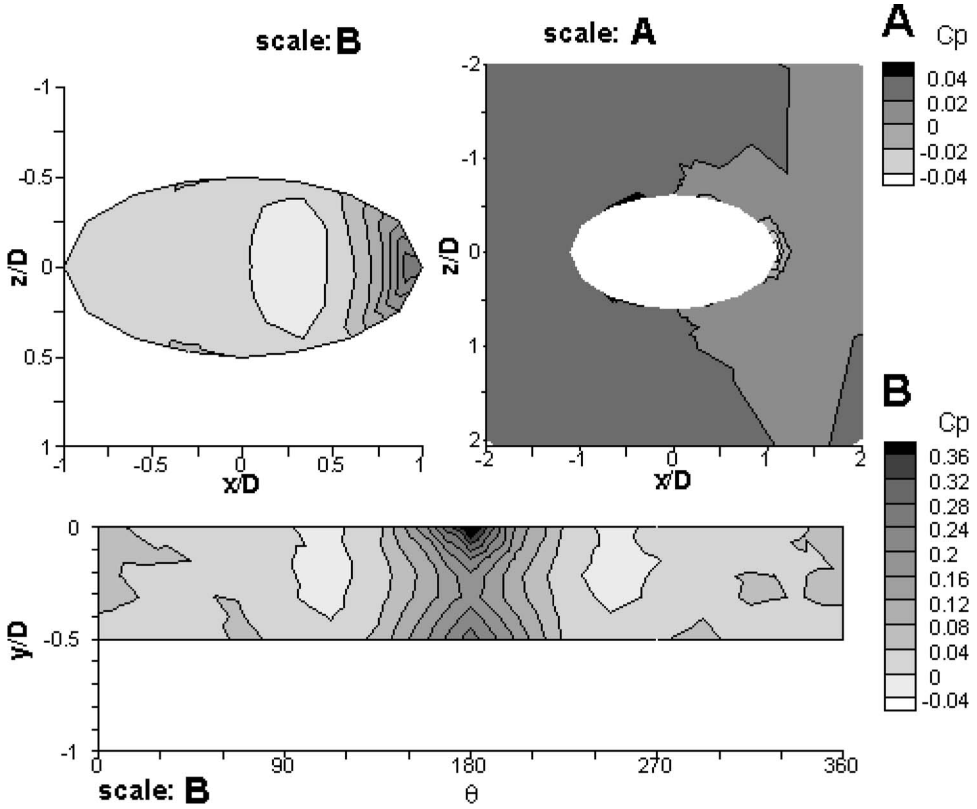

Fig. 3 Pressure coefficient distribution for $h/D=0.5$, yaw 90 deg; base (top left), ground plane (top right), and sidewall (bottom)

Downloaded 03 Jun 2010 to 171.66.16.156. Redistribution subject to ASME license or copyright; see http://www.asme.org/terms/Terms_Use.cfm

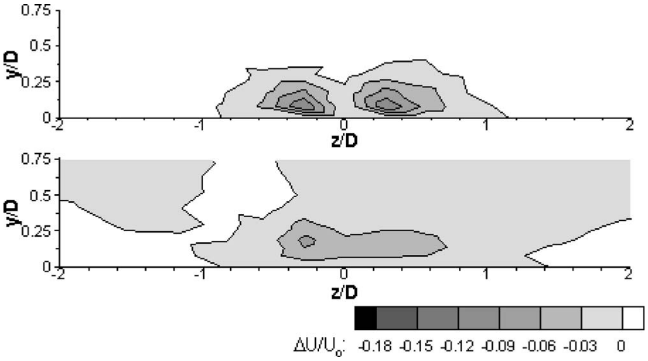

Fig. 4 Streamwise velocity defects for *h*/*D*=0.5, yaw 90 deg; *x*/*D*=1.0 (top) and *x*/*D*=2.6 (bottom)

3.2 Nominally Two-Dimensional Flow Regime. This flow regime occurred for large yaw angles where the major axis is aligned with the streamwise direction. Weak end effects due to the cavity sidewall were seen in the mean pressure distribution on the cavity base. The flow regime showed good agreement with the flow types found for idealized two-dimensional rectangular cavities, even though this yaw angle had the smallest spanwise length to effective cavity length (D') ratio. The centerline profiles showed similar trends as for rectangular cavities by Plentovich et al. [13]. Open and closed flow cavity flows were observed at similar h/D' ratios as found by Plentovich et al. [13] for rectangular cavities.

An open cavity configuration, with a large captive vortical structure along the span of the cavity, was observed to appear initially at $h/D=0.5$. The low pressure region on the cavity sidewall indicates the location of the vortex axis, seen in Fig. 3. The vortex was initially located in the downstream region of the cavity and moved upstream to the cavity center as the cavity depth was increased. This has also been observed for rectangular cavities by Savory et al. [9] and Ashcroft and Zhang [14]. The closed cavity configuration occurred for $h/D=0.1$ only, indicated by the high pressure region in the middle of the cavity base. The low pressure region on the ground plane near the downstream cavity sidewall region was also apparent, indicating the secondary shear layer separation at the downstream wall.

Figure 4 shows two large streamwise velocity defects in the wake velocity measurements. These defects were most likely caused by side vortices due to the close resemblance to rectangular cavity flow regimes. Surface oil visualization techniques for rectangular cavities showed that flow is entrained into the cavity along the sidewalls once the shear layer flows over the leading cavity edge, indicated in a review of rectangular cavities [15]. For rectangular cavities with small width to length ratios, the entrainment over the sidewall increases, which may lead to the formation of these side vortices. In the current experiment, these side vortices were only observed for this configuration as it had a low cavity width to streamwise length ratio.

3.3 Cellular Structure Flow Regime. A three-dimensional flow field was observed when the minor axis was aligned with the streamwise direction. Cellular structures were found inside the cavity volume for open cavity flows ($h/D=0.35$ to 0.7), which have also been observed in large aspect ratio rectangular cavities [5,6,8]. This flow regime occurred only for this yaw angle of 0 deg, although a further test revealed that cellular structures were still present with the cavity yawed to 5 deg but did not exist once the yaw angle reached 15 deg. The cellular structures were symmetric along the span of the cavity and contained two shear layer impingement zones on the cavity sidewall located at approximately $\theta=135$ and 225, seen in Fig. 5. Two shear layer impingement regions were also observed by Czech [8] for a 2:1 rectangular cavity, which contained the same number of cellular structures

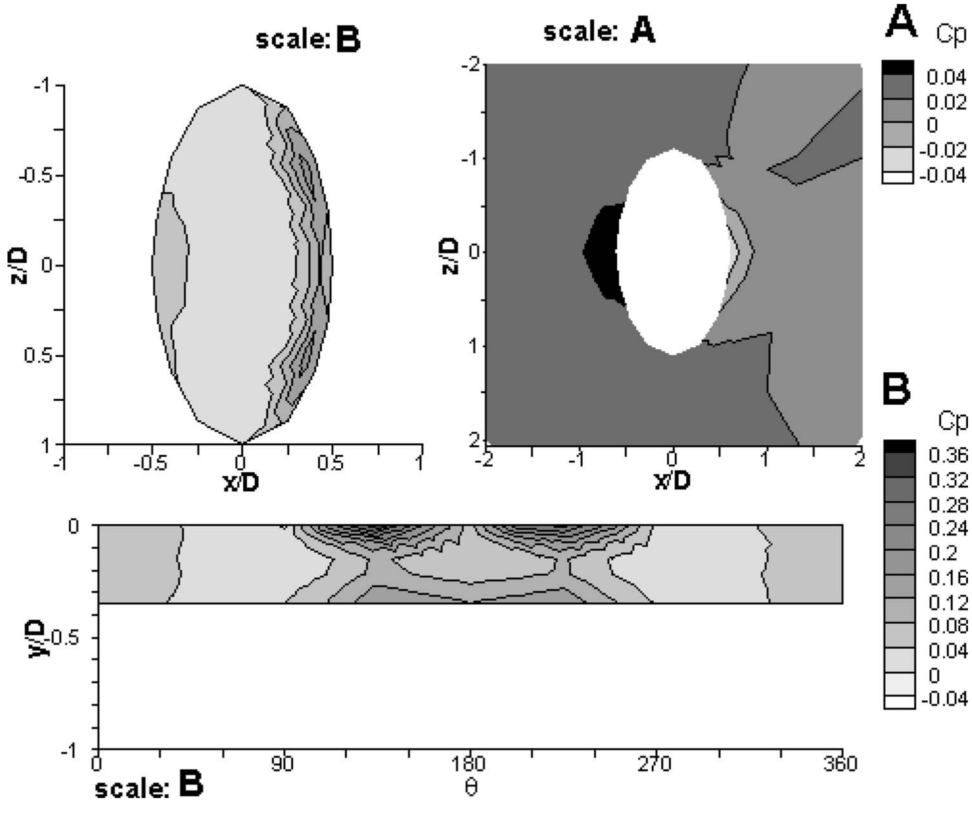

Fig. 5 Pressure coefficient distribution for *h*/*D*=0.35, yaw 0 deg; base (top left), ground plane (top right), and sidewall (bottom)

Downloaded 03 Jun 2010 to 171.66.16.156. Redistribution subject to ASME license or copyright; see http://www.asme.org/terms/Terms_Use.cfm

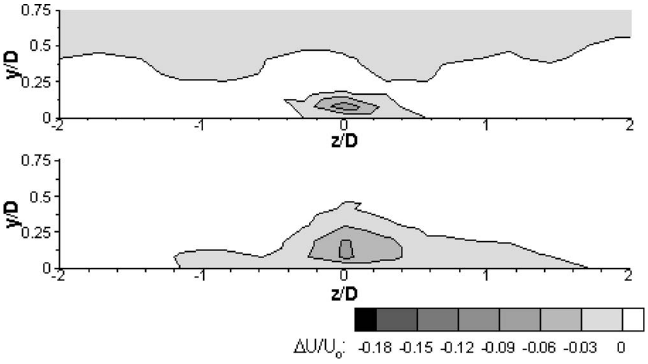

Fig. 6 Streamwise velocity defects for $h/D=0.5$, yaw 0 deg; $x/D=0.5$ (top) and $x/D=2.6$ (bottom)

(as defined by Maull and East [5]) as in the current experiment. Two low pressure regions on the cavity base found in the same spanwise location from the cavity center as the two shear layer impingement zones make up this cellular structure, seen in Fig. 5. This indicates the wave like pressure variation along the span of the cavity, as mentioned by Maull and East [5].

The wake velocity profiles showed a single velocity defect region near the cavity centerline, which was weaker than for the yaw 90 deg case, seen in Fig. 6. This single velocity defect is caused by the local outflow created by the cellular structures described by Kistler and Tan [6]. One should note that Kistler and Tan [6] defined a "unit cell" as a repetition of itself. This means that according to their definition, the current experiment contained only two cells as opposed to four, as defined by Maull and East [5]. Assuming that there are only two cells, the wake velocity defect at the cavity centerline corresponds to an outflow, which is exactly at the cell boundary, as observed by Kistler and Tan [6]. The two shear layer impingement zones also correspond well with inflow locations, as they are located at the two cell centerlines. The outflows at the outer edges of the cells are weak compared to that located at the centerline. This may be due to the diminishing effective streamwise length in those regions.

3.4 Asymmetric Flow Regime. A weak asymmetric flow regime resulted as the yaw angle was increased to yaw 15 deg. Increasing the yaw angle results in a trailing vortex configuration. The curved downstream cavity sidewall, now yawed to the flow direction, forces the separated shear layer to one side and creates an asymmetric flow regime. Examining the pressure coefficients along the cavity walls revealed that the shear layer entrained into the cavity created a helical structure along the major axis of the cavity similar to that described by Czech [8] for rectangular cavities. After the shear layer impinges on the cavity sidewall near the lip of the cavity at approximately $\theta=170$, seen in Fig. 7, it is redirected downward as well as along the sidewall, creating a secondary impingement region on the cavity base. This process creates the helical structure along the major axis of the cavity.

As the yaw angle is increased, the positive pressure on the cavity base, caused by the deflected shear layer, forces the helical structure to exit the cavity near the downstream region of the cavity. The pressure data on the sidewall in this region display a semicircular pressure pattern, indicating the exiting trailing vortex. This is also indicated on the ground plane by a low pressure zone in the same region. The velocity defect caused by this trailing vortex configuration is stronger than any of the other different flow regime types. Although the trailing vortex is yawed to the streamwise direction, the spanwise velocity component of the vortex is very small compared to the freestream velocity as the velocity defect is in the same spanwise location at both measurement planes. At $h/D=1.0$, the vortex is once again contained inside the

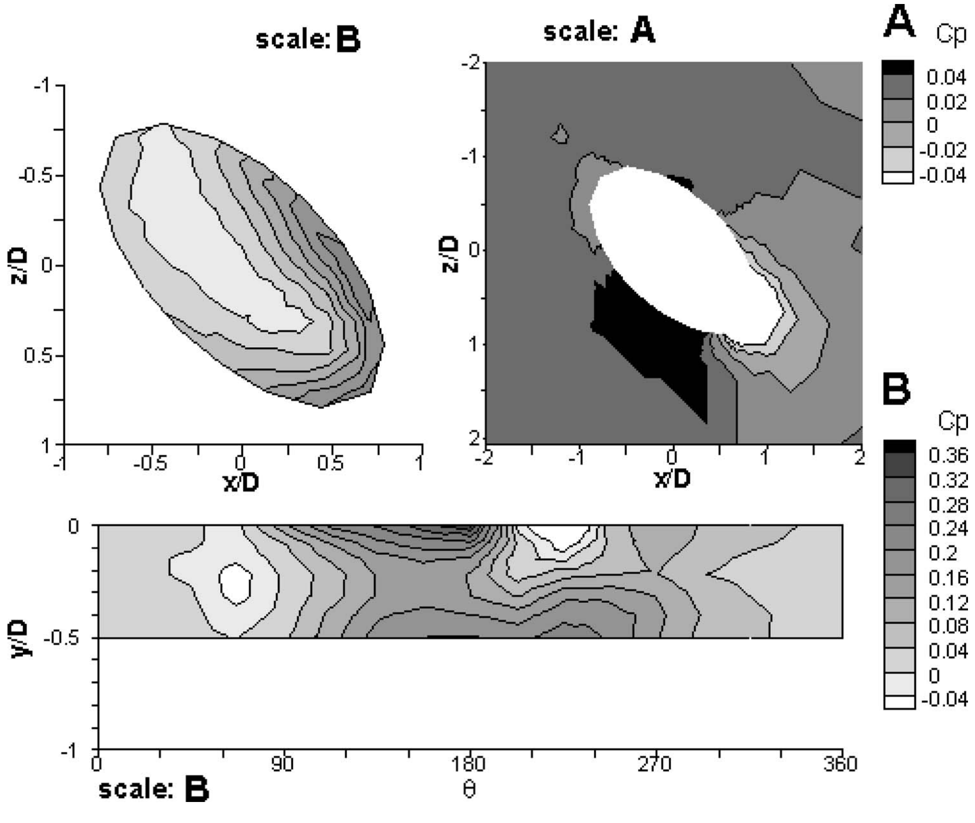

Fig. 7 Pressure coefficient distribution for $h/D=0.5$, yaw 45 deg; base (top left), ground plane (top right), and sidewall (bottom)

Downloaded 03 Jun 2010 to 171.66.16.156. Redistribution subject to ASME license or copyright; see http://www.asme.org/terms/Terms_Use.cfm

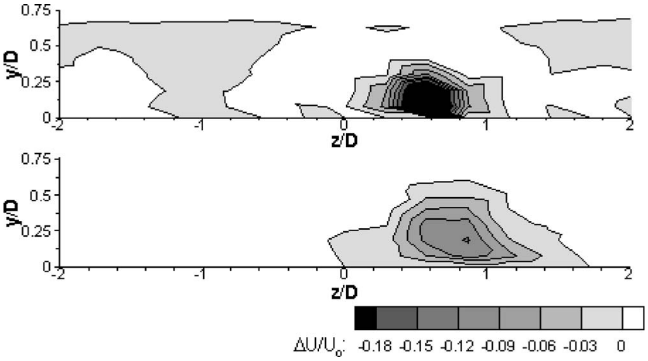

Fig. 8 Streamwise velocity defects for $h/D=0.5$, yaw 45 deg; $x/D=0.7$ (top) and $x/D=2.6$ (bottom)

cavity, as the stagnation pressure on the base is not strong enough to force out the vortical structure. The axis of the captive vortex is misaligned with the major axis and is once again normal to the flow direction as for the yaw 0 deg and 90 deg cases. The high drag flow regime occurred for cavities with yaw angles of 45 deg and 60 deg and h/D ratios of 0.35 and 0.5. These configurations created the largest wake velocity defect when compared to the yaw 0 deg and yaw 90 deg cases, seen in Fig. 8. The largest C_p values in the shear layer impingement region on the cavity sidewall were also observed for these configurations. This indicated that higher velocity fluid further away from the cavity in the vertical direction is being entrained into the cavity.

3.5 Deep and Shallow Flow Regime. The flow regimes described so far are applicable for $h/D=0.2-0.7$. The effect of yaw angle is negligible for cavities with h/D ratios greater than this range. For shallow cavities, $h/D=0.1$, a transitional cavity regime is found except for the yaw 90 deg case, where a closed cavity flow was observed. The initial shear layer impingement on the sidewall occurs at the cavity centerline near the lip for all yaw angles. The shear layer impinges at the same location for deep cavities, $h/D=1.0$. Deep cavities have an open cavity configuration where the axis of the captive vortex is normal to the streamwise direction, independent of the yaw angle.

3.6 Lift and Drag Coefficients. The lift and drag coefficients were also used to group the different flow regimes for elliptical cavities. The net drag, where the skin friction of the ground plane is subtracted from the total drag, was compared to other data found for yawed elliptical cavities in Fig. 9. Good agreement was found between the current results and previous studies in terms of the overall trends for three different yaw angles. Some of the differences in the magnitude may be attributed to the different boundary layer thickness used in the two experiments. Although the skin friction coefficients were of the same magnitude between the two studies, the boundary layer thickness compared to the minor axis of the cavity (δ/D) was smaller in the present study, 1.1 compared to 4.6 in Ref. [10]. A thinner boundary layer has been shown to cause a higher drag coefficient [16]. The pressure coefficient distributions for the current study were also overall approximately $0.05C_p$ higher compared to Savory and Toy [10].

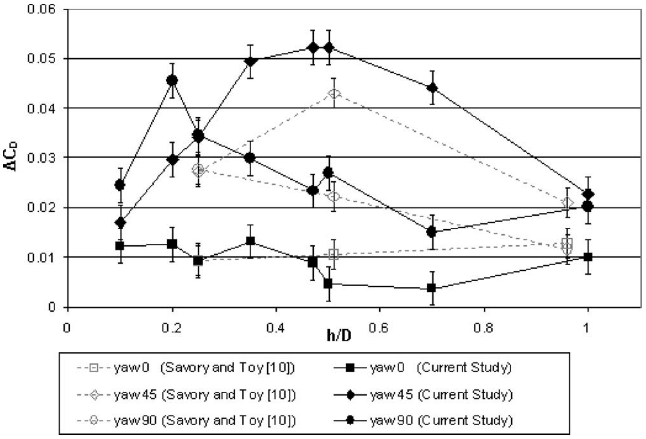

Fig. 9 Normalized net drag coefficient of elliptical cavities at different yaw angles

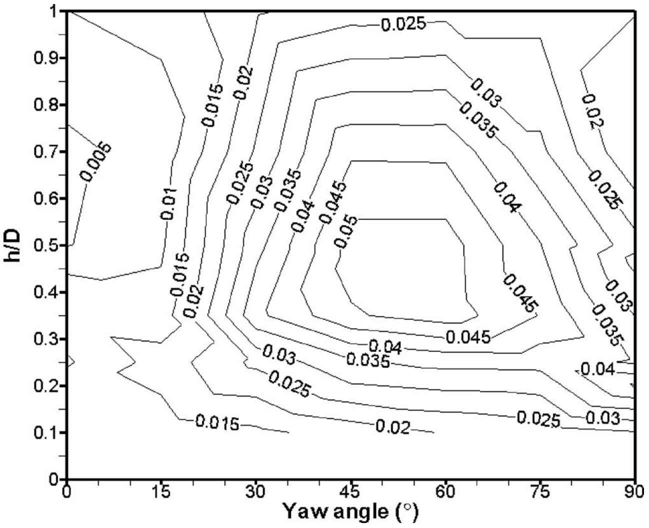

Fig. 10 Net drag coefficient

The effect of yaw angle and cavity depth on the net drag is shown in Fig. 10. As mentioned before, the highest drag occurs for yaw angles of 45 deg and 60 deg for h/D ratios of 0.35 and 0.5. The largest variation of drag was also seen for the asymmetric flow regime. Figure 11 shows the net lift coefficient, where the lift coefficient of the ground plane has been subtracted from the overall lift coefficient. Nearly all the configurations examined are subject to a downward thrust force. As seen in the figure, the lift coefficient for shallow cavities is nearly constant until about 45 deg. The largest downward forces are observed for shallow cavities at high yaw angles, due to the closed cavity configurations where the shear layer impinges on the cavity base. The con-

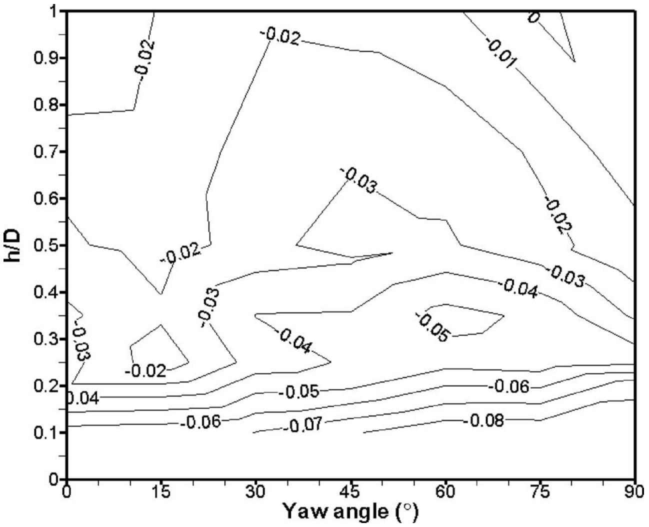

Fig. 11 Net lift coefficient

Downloaded 03 Jun 2010 to 171.66.16.156. Redistribution subject to ASME license or copyright; see http://www.asme.org/terms/Terms_Use.cfm

tour plots of the drag and lift coefficient were similar to those found by Savory et al. [9] for 2:1 rectangular cavities, which indicate that the effect of radius of curvature is negligible for such aspect ratio cavities. The minor effect of the radius of curvature is also apparent in Friesing's [1] data between a square and circular planform cavity. A similar trend is observed in the drag coefficient as the cavity depth is increased for both planform areas.

4 Conclusions

The flow regimes of yawed 2:1 elliptical cavities with varying depths were identified. When the minor axis was aligned with the streamwise direction, cellular structures were found inside the cavity volume. These cellular structures were symmetrical along the span of the cavity and resulted in a low drag coefficient when compared to the other configurations. Increasing the yaw angle forced the captive vortex, originally normal to the flow, to be yawed to flow direction as well. A helical structure was set up along the major axis of the cavity. This created an asymmetric flow regime, which resulted in a trailing vortex configuration. This trailing vortex configuration caused the largest wake velocity defect and also produced the largest drag coefficient of all the different yaw angles. The highest drag coefficient was observed for yawed cavities between yaw 45 deg and 60 deg for h/D ratios ranging from 0.35 to 0.5. At higher yaw angles, the major axis was aligned with streamwise direction and a nominally two-dimensional flow regime occurred. Negligible effects of yaw angle were observed for h/D ratios of 0.1 and 1.0.

The flow regimes of 2:1 yawed elliptical cavities are very similar to those found for yawed rectangular cavities. Similarities in the lift and drag were also found for varying yaw angles and cavity depth between the two different cavity geometries. The similarities indicated that the radius of curvature of elliptical cavities has a negligible effect on the resulting flow regimes, for this aspect ratio.

Preliminary results indicated negligible effect of yaw angle for deep cavities. Further work should examine deeper cavities as multiple vortex structures may be present, which have been observed in deep rectangular cavities.

Acknowledgment

The current work was funded by the Natural Sciences and Engineering Research Council of Canada (NSERC).

Nomenclature

C_p = pressure coefficient $(P-P_s/q)$
ΔC_D = incremental drag coefficient
c_f = local skin friction coefficient
ΔC_L = incremental lift coefficient
D = cavity minor axis
D' = effective streamwise cavity length
h = cavity depth
H = boundary layer shape factor, $\delta * / \delta_\theta$
P = surface pressure on model
P_s = freestream static pressure
q = freestream dynamic pressure
rms = root mean square, e.g., $\sqrt{\overline{u}^2}$
U = mean velocity in the freestream direction
U_0 = freestream velocity
$u*$ = friction velocity
x = streamwise length coordinate
y = vertical length coordinate
z = lateral (spanwise) coordinate
δ = boundary layer thickness (based on $U=0.99U_0$)
$\delta *$ = boundary layer displacement thickness
δ_θ = boundary layer momentum thickness
θ = circumferential length coordinate

References

[1] Friesing, H., 1936, "Measurement of the Drag Associated With Recessed Surfaces: Cut-Outs of Rectangular and Elliptical Planform," ZWBFB Report No. 628 (RAE Library Translation No. 1614, 1971).
[2] Charwat, A. F., Roos, J. N. Dewey, Jr., F. C., and Hitz, J. A., 1961, "Investigation of Separated Flows, Part I: The Pressure Field," J. Aerosp. Sci., **28**(6–7), pp. 457–470.
[3] Roshko, A., 1955, "Some Measurement of Flow in a Rectangular Cutout," NACA TN Report No. 3488.
[4] Ukeiley, L., and Murray, N., 2005, "Velocity and Surface Pressure Measurements in an Open Cavity," Exp. Fluids, **38**, pp. 656–671.
[5] Maull, D. J., and East, L. F., 1963, "Three-Dimensional Flow in Cavities," J. Fluid Mech., **16**, pp. 620–632.
[6] Kistler, A. L., and Tan, F. C., 1967, "Some Properties of Turbulent Separated Flows," Phys. Fluids, **10**(9), pp. S165–173.
[7] Young, A. D., and Paterson, J. H., 1981, "Aircraft Excrescence Drag," NATO Report No. AGARD-AG-264.
[8] Czech, M., 2000, "The Acoustics and Aerodynamics of Turbulent Flow Over Yawed, Rectangular Cavities," Ph.D. thesis, University of Surrey, Guildford, England.
[9] Savory, E., Toy, N., Disimile, P., and Dimicco, R., 1993, "The Drag of Three-Dimensional Rectangular Cavities," Appl. Sci. Res., **50**, pp. 325–346.
[10] Savory, E., and Toy, N., 1993, "The Flows Associated With Elliptical Cavities," *Symposium on Separated Flows, ASME Fluids Engineering Conference*, Washington, DC, FED Paper No. 149, pp. 95–103.
[11] Adams, E. W., and Johnston, J. P., 1988, "Effects of the Separating Shear Layer Reattachment Flow Structure Part 1: Pressure and Turbulence Quantities," Exp. Fluids, **6**(7), pp. 400–408.
[12] Dubief, Y., and Delcayre, F., 2000, "On Coherent-Vortex Identification in Turbulence," J. Turbul., **1**(11), pp. 1–22.
[13] Plentovich, E. B., Stallings, R. L., and Tracy, M. B., 1993, "Experimental Cavity Pressure Measurements at Subsonic and Transonic Speeds," NASA TP Report No. 3358.
[14] Ashcroft, G., and Zhang, X., 2005, "Vortical Structures Over Rectangular Cavities at Low Speed," Phys. Fluids, **17**(1), pp. 1–8.
[15] ESDU, 2004, "Aerodynamics and Aero-Acoustics of Rectangular Planform Cavities. Part I: Time-Averaged Flow," ESDU International, Data Item No. 02008.
[16] Haugen, R. L., and Dhanak, A. M., 1966, "Momentum Transfer in Turbulent Separated Flow Past a Rectangular Cavity," ASME J. Appl. Mech., **33**, pp. 641–646.

Downloaded 03 Jun 2010 to 171.66.16.156. Redistribution subject to ASME license or copyright; see http://www.asme.org/terms/Terms_Use.cfm